Topological phases in polar oxide nanostructures

Javier Junquera

Departamento de Ciencias de la Tierra y Física de la Materia Condensada,
Universidad de Cantabria, Avenida de los Castros s/n, 39005 Santander, Spain

Yousra Nahas, Sergei Prokhorenko, and Laurent Bellaiche

Physics Department and Institute for Nanoscience and Engineering,
University of Arkansas, Fayetteville, Arkansas 72701, USA

Jorge Íñiguez

Materials Research and Technology Department, Luxembourg Institute of Science and
Technology, 5 avenue des Hauts-Fourneaux, L-4362 Esch/Alzette, Luxembourg
and Department of Physics and Materials Science, University of Luxembourg, 41 Rue du Brill,
L-4422 Belvaux, Luxembourg

Darrell G. Schlom

Department of Materials Science and Engineering, Cornell University,
Ithaca, New York 14853, USA,
Kavli Institute at Cornell for Nanoscale Science, Ithaca, New York 14853, USA,
and Leibniz-Institut für Kristallzüchtung, Max-Born-Straße 2, 12489 Berlin, Germany

Long-Qing Chen

Department of Materials Science and Engineering, Materials Research Institute,
The Pennsylvania State University, University Park, Pennsylvania 16802, USA

Sayeef Salahuddin

Department of Electrical Engineering and Computer Sciences, University of California,
Berkeley, Berkeley, California 94720, USA and Lawrence Berkeley National Laboratory,
1 Cyclotron Road, Berkeley, California 94720, USA

David A. Muller

School of Applied and Engineering Physics, Cornell University, Ithaca, New York 14853, USA
and Kavli Institute at Cornell for Nanoscale Science, Ithaca, New York 14853, USA

Lane W. Martin

Department of Materials Science and Engineering, University of California,
Berkeley, Berkeley, California 94720, USA and Materials Sciences Division,
Lawrence Berkeley National Laboratory, Berkeley, California 94720, USA

R. Ramesh[*]

Department of Physics and Department of Materials Science and Engineering,
University of California, Berkeley, Berkeley, California 94720, USA
and Materials Sciences Division, Lawrence Berkeley National Laboratory,
Berkeley, California 94720, USA

(published 20 April 2023)

The past decade has witnessed dramatic progress related to various aspects of emergent topological polar textures in oxide nanostructures displaying vortices, skyrmions, merons, hopfions, dipolar waves, or labyrinthine domains, among others. For a long time, these nontrivial structures (the electric counterparts of the exotic spin textures) were not expected due to the high energy cost associated with the dipolar anisotropy: the smooth and continuous evolution of the local polarization to produce

---

[*]Present address: Rice University, Houston, Texas 77005, USA.

topologically protected structures would result in a large elastic energy penalty. However, it was discovered that the delicate balance and intricate interplay between the electric, elastic, and gradient energies can be altered in low-dimensional forms of ferroelectric oxide nanostructures. These can be tuned to manipulate order parameters in ways once considered impossible. This review addresses the historical context that provided the fertile background for the dawning of the polar topological era. This has been possible thanks to a fruitful, positive feedback between theory and experiment: advances in materials synthesis and preparation (with a control at the atomic scale) and characterization have come together with great progress in theoretical modeling of ferroelectrics at larger length and timescales. An in-depth scientific description to formalize and generalize the prediction, observation, and probing of exotic, novel, and emergent states of matter is provided. Extensive discussions of the fundamental physics of such polar textures, a primer explaining the basic topological concepts, an explanation of the modern theoretical and computational methodologies that enable the design and study of such structures, what it takes to achieve deterministic, on-demand control of order-parameter topologies through atomically precise synthesis, the range of characterization methods that are key to probing these structures, and their thermodynamic field-driven (temperature-driven, stress-driven, etc.) susceptibilities are included. The new emergent states of matter join together with exotic functional properties (such as chirality, negative capacitance, and coexistence of phases) that, along with their small size and ultrafast dynamical response, make them potential candidates in multifunctional devices. Finally, some open questions and challenges for the future are presented, underlining the interesting future that is anticipated in this field.

CONTENTS

I. INTRODUCTION

Over the years, the complex interplay of spin, charge, orbital, and lattice degrees of freedom has provided for a plethora of exotic phases and physical phenomena in transition metal oxides (Tokura and Nagaosa, 2000). In contrast to semiconductors, which are typically materials with a rigid structure where only the charge (semiconducting electronics) or the interaction between charge and spin (spintronics) degrees of freedom are of relevance, in transition metal oxides the energies of various interactions (Coulombic repulsion, orbital bandwidth, crystal-field splitting, elastic strain, Hund's exchange, etc.) tend to be of a similar order of magnitude. Moreover, in most cases they are coupled, giving rise to strong electron-phonon, spin-phonon, spin-orbit, electron-spin, or polarization-strain couplings (Rondinelli and Spaldin, 2011).

As a consequence of the delicate balance among these interactions, many systems exhibit a large variety of phase transitions, leading to a spectrum of competing phases. Small external perturbations (driven by temperature, strain or pressure, electric or magnetic fields, doping, chemical composition, etc.) are then able to induce phase transitions, giving rise to tunable order and properties and/or giant responses that can be used in the design of multifunctional devices. Thus, it is not surprising that some of the key discoveries of condensed-matter physics in the past few decades have emerged in the fertile field of complex transition metal oxides. Among the most prominent examples is high-temperature superconductivity (Dagotto, 1994), which was discovered by Bednorz and Müller (1986) in ceramic copper oxides. A few years later, in another family of oxides (mixed-valence manganites) colossal field-driven magnetoresistance responses were found (Jin *et al.*, 1994; Uehara *et al.*, 1999) whereby the application of a magnetic field changes the electrical resistance of the material by orders of magnitude. Giant electromechanical

responses have also been reported at morphotropic phase boundaries (Noheda *et al.*, 1999; Bellaiche, García, and Vanderbilt, 2000), providing a continuous path for the ferroelectric polarization displayed by some oxides to rotate and yielding large piezoelectric responses. In addition, different mechanisms for metal-insulator transitions, including the formation of electronic quantum liquid-crystal phases (Kivelson, Fradkin, and Emery, 1998), have been discussed in d-electron oxide systems (Imada, Fujimori, and Tokura, 1998). Other oxides display multiferroism (that is, they present two or more primary ferroic properties united in the same phase, for instance, magnetic and ferroelectric) and exhibit unusual physical properties as a result of the coupling between their coexisting order parameters (Wadhawan, 2000; Fiebig, 2005; Spaldin and Ramesh, 2019). Even more, beyond the fascinating physics of complex oxides at the bulk level, interesting new perspectives were opened upon the observation of unusual phenomena at oxide interfaces, boosted by the possibility of growing them epitaxially with a control at the atomic level (Zubko *et al.*, 2011). Interfaces break the translational symmetry and potentially allow new coupling between adjacent layers that are of utmost importance and ultimately govern the properties of the heterostructures. Sometimes totally new and unexpected phenomena emerge, exhibiting novel functionalities that can be completely different than those of the respective bulk materials. These include the appearance of a two-dimensional electron gas at the interface between two large band-gap insulating oxides ($LaAlO_3$ and $SrTiO_3$) (Ohtomo and Hwang, 2004; Thiel *et al.*, 2006; Reyren *et al.*, 2007) and the emergence of improper ferroelectricity due to coupling of the oxygen octahedra rotations (primary order parameter) with the polarization (dependent order parameter) in short-period $PbTiO_3/SrTiO_3$ superlattices (Bousquet *et al.*, 2008).

One of the recent breakthroughs in this field of multifunctional complex oxides is related to ferroelectricity, which was first discovered by Valasek 100 years ago, who observed that Rochelle salt possesses a spontanenous polarization that can be reversed in a sufficiently large external electric field, yielding hysteresis loops similar to those known for magnetization versus magnetic field in ferromagnets (Valasek, 1921). Ferroelectric materials have a tendency to form domains (local regions of uniform polarization) as a means of reducing the depolarization fields that occur at surfaces. Uniform domains are by far the most common arrangement. However, in recent years complex polarization patterns have been discovered, including flux-closure (Jia *et al.*, 2011; Tang *et al.*, 2015), vortex (Naumov, Bellaiche, and Fu, 2004; Yadav *et al.*, 2016), skyrmion (Nahas *et al.*, 2015; Das *et al.*, 2019; Pereira Gonçalves *et al.*, 2019; Nahas, Prokhorenko *et al.*, 2020), meron (Nahas, Prokhorenko *et al.*, 2020; Wang *et al.*, 2020; Shao *et al.*, 2023), and hopfion (Luk'yanchuk *et al.*, 2020) patterns, among others. Some of this progress has already been reviewed (Gregg, 2012; Seidel, Vasudevan, and Valanoor, 2016; Zheng and Chen, 2017; Das *et al.*, 2018, 2020; Hlinka and Ondrejkovic, 2019; Ramesh and Schlom, 2019; Nataf *et al.*, 2020; Chen *et al.*, 2021; Tang, Zhu, and Ma, 2021; Tian *et al.*, 2021; Fernandez *et al.*, 2022; Guo *et al.*, 2022; Wang *et al.*, 2023).

Topology has played a key role in our understanding of many physical systems (Mermin, 1979), from the role of dislocations in crystalline solids and its influence on the

strength and malleability of a metal under stress to the existence of vortex lines in the order-parameter field of superconductors and superfluids, a topic first studied in the middle of the 20th century (Halperin, 2020). In other ferroic systems, especially ferromagnets, complex spin topologies such as magnetic flux-closure domains (Runge *et al.*, 1996), vortices (Shinjo *et al.*, 2000; Wachowiak *et al.*, 2002; Park *et al.*, 2003), and skyrmions (Rößler, Bogdanov, and Pfleiderer, 2006; Mühlbauer *et al.*, 2009; Neubauer *et al.*, 2009; Pappas *et al.*, 2009; Yu *et al.*, 2010) were observed more than a decade ago. In most cases, these spin textures originate from the delicate balance between the exchange interaction (which tends to align the spins in a colinear way), the relativistic Dzyaloshinskii-Moriya (DM) interactions (which tend to tilt the spins by a rotation around the DM vector and produce chiral structures), and the long-range magnetic dipolar interactions, often in the presence of thermal activation and external fields (Nagaosa and Tokura, 2013). Since their first observation, these spin textures have attracted a lot of interest. Particularly attractive is their potential application in novel spintronic devices (Fert, Cros, and Sampaio, 2013), benefiting from their stability in high-density data storage (Parkin, Hayashi, and Thomas, 2008), or of the controlled motion of these particlelike magnetic nanostructures in logic devices (Omari and Hayward, 2014). Furthermore, a dedicated road map has been created to capture the present state of the art and the wide range of research directions and strategies currently under way (Back *et al.*, 2020).

The quest to establish the existence of complex topological arrangements of electric dipoles in ferroelectrics, the electric counterparts of the exotic spin textures, has been a popular topic of research since the beginning of this century. These polar topological structures have the potential to be more advantageous than their magnetic analogs for ultrafast (phonon frequencies typically in the terahertz regime) and high-density storage (due to their smaller sizes) devices. But the determination of how to create topologically nontrivial ferroelectric textures turned out to be far from obvious. Common wisdom was that such nontrivial structures would have a prohibitive energy cost in ferroelectric materials. The main reason is that the primary order parameter (the polarization) is strongly coupled to the lattice, leading to a strong role of structural and dipolar anisotropy. Therefore, the smooth and continuous evolution of the local polarization to produce a topologically protected structure would result in a large elastic energy penalty (Das *et al.*, 2020; Martin, 2021). However, theoretical predictions, eventually followed by an experimental synthesis and characterization of materials, have allowed us to overcome the barriers, and nontrivial polarization patterns are now frequently observed in ferroelectric nanostructures, where the electric, elastic, and gradient energies of the materials compete in an extraordinarily balanced way. Indeed, this is a particularly exciting problem in nanoscale physics, as the experimental advances in materials preparation and characterization have come together with great progress in theoretical modeling of ferroelectrics. Both theorists and experimentalists are finally now able to work on the same length scales. This allows real-time feedback between theory and experiment, with new discoveries routinely made both in the laboratory and via computer (Ahn, Triscone, and Mannhart, 2003; Ahn, Rabe, and Triscone, 2004).

In this review we summarize the efforts undertaken during the last two decades to unravel the existence of emergent nontrivial polar topologies. A summary of the initial steps in this research endeavor is presented in Sec. II. A primer on the topological concepts required to understand important ideas discussed in this work (homotopy classes and their characterization by indices, novel toroidal characteristics, topological phase transitions, etc.) is provided in Sec. III. The nontrivial textures emerge as the result of a delicate balance between different interactions. The most important ones, and their relative importance in the stabilization of the novel phases, are reviewed in Sec. IV. These discoveries were made possible by the advent of new experimental synthesis and characterization techniques, developed simultaneously with improved theoretical frameworks. An overview of the key methods is given in Sec. I of the Supplemental Material (472). The design and study of novel topological states of matter and emergent phenomena in ferroic superlattices and other low-dimensional forms (films, wires, and dots), whereby the innate competition between energy scales is taken advantage of to perch materials at or near the boundary between different states, is considered in Sec. V. Despite these efforts, a vast design space and potential for the development of novel functionalities, emergent properties, unprecedented effects, and exotic physics remains essentially untapped. Possible future directions of the field are outlined in Sec. VI.

II. OVERVIEW OF THE DAWN OF NONTRIVIAL TEXTURES IN FERROIC MATERIALS

Vortexlike structures appear in significantly different contexts in nature, including spiraling galaxies, massive storms and hurricanes, stirred fluids, whirlpools, and smoke rings, among others. They have attracted the interest of scientists and philosophers alike, from ancient Greeks to René Descartes, who introduced them in his book *The World or Treatise on the Light* to describe the orbits of planets around the Sun. Vortices are also interesting phenomena in condensed-matter physics. Quantum vortices representing a quantized flux circulation of some physical quantity (quantized angular momentum) were predicted by Onsager in 1949 in connection with superfluid helium (Onsager, 1949). A few years later, Abrikosov applied them to explain the magnetic phase diagram of type-II superconductors (quantized magnetic flux) (Abrikosov, 1957). Geometrical configurations of domains where magnetic flux circuits lie almost completely within the specimen were already predicted to exist in thin ferromagnetic films in the 1930s (Landau and Lifshitz, 1935) and 1940s (Kittel, 1946).

The underlying physics for the formation of such vortices is different in each of the previous examples. In most cases, the fundamental element is the velocity field (for example, in the case of fluid vortices in the bathtub). In the case of magnetic vortices, it is the arrangement of spins that is presented as a vortex pattern. Furthermore, the length scales of all previous vortexlike structures differ by orders of magnitude, indicating a similar range of energy scales that drive the formation of such patterns.

Here we explore the existence of similar states in ferroelectrics, a topic first explored at the beginning of this century. Conventional wisdom had pointed to the fact that localized

electron spins in magnetic crystals, which are a fundamental quantum mechanical quantity, are fixed. In contrast, electric dipole moments are the result of local symmetrywise polar lattice distortions, whose amplitude can vary continuously. Indeed, past work (Meyer and Vanderbilt, 2002) cited this "mutability" of the dipole moment as the spontaneous polarization changes directions across a ferroelectric Ising domain wall where the polarization axis does not change orientation but instead simply decreases in size, changes sign, and increases again. However, it has become increasingly apparent that such a "mutable" picture of the ferroelectric spontaneous dipole may not capture the behavior of many ferroelectrics. Prime among them has been the well-studied multiferroic $BiFeO_3$, which exhibits a large spontaneous polarization (~ 90 $\mu C/cm^2$) accompanied by an equally large spontaneous distortion. The early work of Kubel and Schmid (1990) pointed to some puzzling aspects, namely, that the polarization rotated instead of going through the high symmetry state with a vanishing polarization during switching. Indeed, this was directly confirmed through experimental measurements and first-principles theoretical calculations (Heron *et al.*, 2014). Subsequently, several other instances of such polarization rotation were discussed for other ferroelectric systems [for example, $PbTiO_3$ (Wojdeł and Íñiguez, 2014)]. Thus, in hindsight it should not be a surprise that ferroelectrics, especially in constrained dimensions, can exhibit such rotating patterns, in this case of the spontaneous polarization.

A. The problem involving screening depolarization fields in nanosized ferroelectrics

The transition between the 20th and 21st centuries gave witness to many breakthroughs in the synthesis of complex oxide heterostructures which brought the field to an entirely new level of sophistication (Dawber, Rabe, and Scott, 2005; Schlom *et al.*, 2007; Mannhart and Schlom, 2010), as discussed in Sec. I.A.1 of the Supplemental Material (472). The availability of single-crystal oxide substrates with atomically flat surfaces and the tremendous amount of progress achieved in the epitaxial growth of thin films were crucial to growing high-quality multilayers and superlattices (Posadas *et al.*, 2007), due to which complex artificial oxide structures can now be realized with an atomic-level precision comparable to that of semiconductor heterostructures. This progress paved the way to combine, at the nanoscale, compounds with different functional properties (ferroelectrics, high-T_c superconductors, and magnets), thus offering tremendous new possibilities for creating artificial multifunctional materials and devices, as well as for engineering radically new properties by fully relying on interfacial effects.

Regarding polar ferroelectric materials, for many years the focus was on the size dependence of the polarization. The main challenge was to determine whether a high-quality nanodot or nanodisk [zero-dimensional (0D)], nanowire [one-dimensional (1D)], or thin ferroelectric [two-dimensional (2D)] film with a characteristic size of only a few nanometers could sustain a switchable polar state in a monodomain configuration. Common wisdom was that the depolarization field arising from unscreened bound charges at the surface of the ferroelectric would be strong enough to suppress the monodomain polarization state completely. Indeed, survival of the polar state critically depends on whether or not this deleterious field is screened. Screening by free charges provided by metallic electrodes (Batra and Silverman, 1972; Batra, Wurfel, and Silverman, 1973; Mehta, Silverman, and Jacobs, 1973; Dawber *et al.*, 2003), atmospheric absorbates (Spanier *et al.*, 2006; Wang *et al.*, 2009), ionic screening whereby the electrodes share the ionic displacements of the ferroelectric (Chisholm *et al.*, 2010), oxygen vacancies (Wang *et al.*, 2009; Chisholm *et al.*, 2010), and mobile charges considering the ferroelectric as a semiconductor by itself (Watanabe, 1998) (likely to be the dominant mechanism on the macroscale) were contemplated (Lichtensteiger *et al.*, 2012). But even considering perfect metallic electrodes the screening charges will spread over a small but finite interfacial region (Junquera and Ghosez, 2003; Bratkovsky and Levanyuk, 2009), giving rise to a nonzero effective screening length that will dramatically alter the properties of an ultrathin film. To further reduce the depolarization field within a monodomain configuration, it is critical to decrease the normal component of the polarization to the surface, as this would translate immediately into a decrease of the bound charges. This can be done using a rotation of the electric dipoles close to the surface to point along an in-plane direction or, if the development of such an in-plane component of the polarization is not favorable, directly by a total suppression of the ferroelectricity.

B. Ferroelectric vortices in zero-dimensional nanodots and nanodisks (0D)

Competing with these mechanisms, another possibility is the formation of complex patterns of polarization in real space that avoids the formation of a net polarization charge. Within this context, groundbreaking simulation works based on models derived from first principles and focusing on stress-free ferroelectric nanodots and nanodisks (0D) made of $BaTiO_3$ and $Pb(Zr, Ti)O_3$ (PZT) were conducted in the early 2000s (Fu and Bellaiche, 2003; Naumov, Bellaiche, and Fu, 2004). These dots, under open-circuit electrical boundary conditions (i.e., no screening of the polarization-induced surface charges), were predicted to adopt polar vortices. Before these works, the general thinking was that the high anisotropy energy inherent to ferroelectric materials (much larger than the equivalent one in ferromagnets; see Sec. IV.D) would inhibit a continuous polarization rotation in ferroelectric nanostructures and, therefore, the formation of nontrivial polarization states. The key contribution made by Fu and Bellaiche (2003) and Naumov, Bellaiche, and Fu (2004) was to refute this assumption.

Although the net polarization of the predicted vortices vanishes, new parameters describing the swirling order emerge. The *toroidal moment*, which reflects the sense of rotation of the polarization, and the *hypertoroidal moment* (Prosandeev and Bellaiche, 2008b), which captures subtle local features such as the distance between vortex centers and the magnitude of their electric dipoles for pairs of vortices having opposite electric toroidal moments, were introduced. Notably in some systems these characteristics were shown to exhibit dynamical signatures (Gui and Bellaiche, 2014)

expected from conventional order parameters. Rigorous definitions and applications of both are discussed in Sec. III. Besides, atomistic computations were combined with analytical developments to determine the existence of new tensors in systems possessing electrical vortices (Prosandeev, Kornev, and Bellaiche, 2007): one called a piezotoroidic tensor, which relates stress and electric toroidal moment (direct piezotoroidic effect) or strain and curl of electric field (converse piezotoroidic effect), and a second one named electric toroidal susceptibility, which connects toroidal moment and the curl of the electric field. These two tensors can naturally be considered a generalization of the well-known piezoelectric and dielectric susceptibility tensors in usual ferroelectrics (possessing electrical polarization, rather than a toroidal moment, as their order parameters). Furthermore, in addition to being of fundamental importance by bringing ferroelectrics within the class of materials that can manifest vortices, these pioneering works also suggested interesting potential applications (Naumov, Bellaiche, and Fu, 2004). At this level, it is essential to control the "sense of rotation" of these vortices from clockwise to counterclockwise and vice versa, so as to revert the electric toroidal moment. Several pathways were rapidly proposed based on atomistic simulations, involving curled electric fields (Naumov and Fu, 2008), transverse inhomogeneous static electric fields (Prosandeev *et al.*, 2006), or even homogeneous electric field in the case of asymmetric ferroelectric nanorings (Prosandeev, Ponomareva, Kornev, and Bellaiche, 2008). All of them are further described in Sec. V.A.5.

The previous theoretical predictions on the stabilization of polar vortices opened a completely unexplored field of research and triggered a flurry of activity. Complex polarization patterns, depending on their size and surface termination, were also predicted in ferroelectric nanoislands based on a phenomenological Landau model (Xue, Gao, and Liu, 2009) or in $BaTiO_3$ (Stachiotti, 2004) and $PbTiO_3$ nanoparticles (Stachiotti and Sepliarsky, 2011) from shell-model simulations. Similar results were obtained by analytical calculations and numerical solutions within the Ginzburg-Landau formalism coupled with electrostatic equations (Lahoche, Luk'yanchuk, and Pascoli, 2008). Other examples include investigations of the dependency of polar vortices in ferroelectric nanodots as a function of their size, shape, material, and temperature (Prosandeev and Bellaiche, 2007b), the topological-phase transitions from the vortex phase to trivial polarized states under homogeneous electric fields (Naumov and Fu, 2007), and the interaction between the ferroelectric nanodots with a polarizable medium in nanocomposites (Prosandeev and Bellaiche, 2006), with the emergence of the new *antiferrotoroidic* phases that consist of adjacent vortices having opposite electric toroidal moments. Prosandeev and Bellaiche (2007b) also revealed associated unusual strain characteristics, such as an axial ratio lower than unity in tetragonal nanodots or inhomogeneous strains having large magnitudes near the center of the vortex, as a result of elastic deformation of the domains forming this vortex. Analytical developments were also carried out, yielding the formula of the electric field produced by the dipole vortex outside the dot and of the energy characterizing the interaction between two vortices.

Some experimental efforts were devoted to the detection of these vortex states in micrometer-size $PbZr_{0.2}Ti_{0.8}O_3$ circular capacitors during switching (Gruverman *et al.*, 2008) (i.e., *transient* vortices). The observed evolution of the out-of-plane component was in agreement with theoretical simulations based on micromagnetic equations of motion for a Heisenberg magnet, which predicted the occurrence of vortices for the in-plane components of the polarization. The piezoresponse force microscopy (PFM) technique used in the characterization made the unambiguous detection of the in-plane components of the polarization difficult. Nevertheless, the existence of a vortex state texture in such structures was supported by a theoretical model considering a ferroelectric with a weak, anisotropic free energy and subject to an axially symmetric electric field induced by circular electrodes (Baudry *et al.*, 2011). The development of further thermodynamic theories for restricted geometries (ferroelectric cylinders with top and bottom electrodes under the presence of external fields) demonstrates the existence of nontrivial mathematical solutions induced by the boundary conditions at the perimeter of the cylinder, which can be interpreted as the precursors of the skyrmions that are discussed in Sec. V.B (Scott *et al.*, 2008; Baudry *et al.*, 2014). Later using the same PFM technique as Gruverman *et al.* (2008), Rodriguez *et al.* (2009) studied smaller tetragonal nanodot arrays (<100 nm in diameter) of $PbZr_{0.4}Ti_{0.6}O_3$ under compressive strain. On the one hand, vertical PFM signals showed how some of the dots presented ring or bubble domains, wherein the outer diameter of the dot corresponds to a negatively polarized domain, and the inner portion is positively polarized. On the other hand, lateral PFM revealed the presence of multiple in-plane domains in other nanodots, suggesting the presence of a vortex polarization state. A few years later, changing the composition to $Pb(Zr_{0.2}Ti_{0.8})O_3$ (more in the ferroelectric side of the phase diagram), Ding *et al.* (2019) observed the appearance of abundant domain defects including flux-closure domains, center-divergent vortices, center-convergent vortices, and antivortices having a quadrilateral shape with concave center nanodots of PZT on a Nb-doped $SrTiO_3$ substrate.

After the works by Gruverman *et al.* (2008) and Rodriguez *et al.* (2009), the next step in the experimental characterization of the polar vortices was undertaken by Schilling *et al.* (2009), who observed symmetric quadrants containing bundles of 90° stripe domains regularly formed in freestanding single-crystal nanodots of $BaTiO_3$. Scanning transmission electron microscopy (STEM) measurements using high-angle annular dark-field (HAADF) detectors showed how the polarization within each quadrant were oriented more accordingly to an antivortex, i.e., either directly toward or away from the quadrant "core"; see Figs. 2 and 6 of Schilling *et al.* (2009). A clearer, more detailed visualization of a mesoscopic vortex was reported by McQuaid *et al.* (2011) by PFM of freestanding single-crystal lamellae of $BaTiO_3$ deposited between Pt electrodes. Every quadrant forming the flux-closure state was composed of 90° stripe domains. The novel mesoscale domains (on the length scale of microns) appeared on a timescale of hours after removal of a uniform poling electric field due to the depolarization fields within the lamellae (the Pt electrodes presented a relatively low conductivity and poor electrical screening of the polarization). These experiments

underlined the difficulty to observe static vortices in ferro-electrics: simple quadrant arrangements generate enormous disclination strains. Above a critical size, the elastic energy would be released by the formation of ferroelastic shape-conserving 90° stripe domains within each quadrant (Catalan *et al.*, 2012). Schilling *et al.* (2011) combined dark-field STEM with Monte Carlo simulations and an original phenomenological model in order to investigate the unusual quadrant domain structures observed in freestanding single-crystal platelets made of $BaTiO_3$. Modifying the shape of these platelets results in a symmetry breaking of the quadrant domain pattern that has been ascribed to a second-order phase transition, driven by the length-to-width ratio of the platelet sidewalls (rather than the temperature, as for usual transitions in ferroelectrics) and for which the order parameter is the degree of off-centering of the domain pattern (rather than the electrical polarization, as in typical ferroelectric transitions). It was further proposed that controlling the direction along which the domain pattern moves off-center, along with the resulting spontaneous macroscopic electrical polarization and toroidal moment, may be taken advantage of for memory storage.

Finally, note that the presence of a skyrmion was speculated by Dawber, Gruverman, and Scott (2006) to explain the nanodomain ejection in front of advancing large domain walls in lead germanate, and vortexlike textures have been predicted in $BaTiO_3$ and $PbTiO_3$ nanoparticles embedded in a dielectric media for particle diameters larger than a critical value (Mangeri, 2017).

C. Topological phases in ferroelectric nanowires (1D)

The atomistic first-principles-based effective Hamiltonian simulations were rapidly extended to cover other low-dimensional ferroelectrics, such as one-dimensional infinite nanowires. Again the interplay between strain and electrical boundary conditions was essential for stabilizing the complex polarization patterns, and both of them must be properly included in the simulations (Ponomareva *et al.*, 2005b). Using this technique, exotic metastable phases including arrays of vortices where the local polarization successively rotates in opposite fashion in the (x, z) planes were predicted in $Pb(Zr_{0.4}Ti_{0.6})O_3$ nanowires under open-circuit and tensile strains (z is the infinite direction of the nanowires) (Ponomareva, Naumov, and Bellaiche, 2005). The formation of this configuration is driven by the requirement of the wire to have nonzero components of the dipole in both the x and z directions, as dictated by the tensile strain, while minimizing the depolarization field inside the wire. This unusual pattern then transforms under compressive strains within the (x, z) planes into nanoscale domains with dipoles now being up or down along the y axis in the (y, z) planes, with vorticeslike domain walls forming in between.

This interplay between mechanical and electrical boundary conditions was emphasized, and taken advantage of, in the computational study by Pappas, Fthenakis, and Ponomareva (2018). The application of a uniaxial stress allows nanowires made of $PbTiO_3$ and under open-circuit-like electrical boundary conditions to switch their dipolar pattern from a flux-closure state, having no macroscopic electrical polarization, to a phase having a polarization along the axis of the nanowire.

Large piezoelectricity and mechanical responses naturally accompany this phase transition.

More complex dipolar textures, with large winding numbers of the point defect (a topological related concept that is discussed in Sec. III), were predicted in BaO-terminated $BaTiO_3$ nanowires from first-principles simulations (Hong *et al.*, 2010). Multivortex states were also reported in long ferroelectric cylinders (Lahoche, Luk'yanchuk, and Pascoli, 2008; Di Rino, Sepliarsky, and Stachiotti, 2020). The topological landscape of the polarization field in nanostructures could be more complex than hitherto assumed.

D. Ferroelectric nanodomains in two-dimensional ferroelectric thin films (2D)

Beyond all previous approaches, most experimental endeavors were focused on the growth and characterization of ultrathin epitaxial films (2D) grown on different substrates. The presence of satellites around the Bragg peaks in x-ray scattering revealed nanoscale 180° stripe domains in $PbTiO_3$ ultrathin films epitaxially grown on $SrTiO_3$ (Streiffer *et al.*, 2002; Fong *et al.*, 2004). These stripe domains are periodic nanometer-scale regions of alternating polarization that lead to overall charge neutrality at the surfaces, and minimize the free energy of the system. A direct visualization of the atomic structure was still missing at that time due to the lack of resolution in the available techniques. However, calculations based on phenomenological theories (Bratkovsky and Levanyuk, 2000, 2001; De Guerville *et al.*, 2005; Stephenson and Elder, 2006; Bratkovsky and Levanyuk, 2009; Luk'yanchuk, Lahoche, and Sené, 2009), shell models (Tinte and Stachiotti, 2001), first-principles-based effective Hamiltonians (Kornev, Fu, and Bellaiche, 2004; Wu *et al.*, 2004, 2007; Prosandeev and Bellaiche, 2007a), and first principles (Aguado-Puente and Junquera, 2008, 2012; Shimada, Tomoda, and Kitamura, 2010a) supported the existence of such narrow and ordered stripe domains. As discussed in Sec. IV.A.1, the widths of the domains scale as the square root of the thickness of the films, following the Landau-Kittel law. Moreover, all the previous theoretical simulations agreed on the fact that the dipole texture can be characterized by a continuous rotation of the polarization close to the surfaces and interfaces in order to minimize the divergence of polarization at every point in space. (In the absence of free carriers, we expect $\nabla \cdot \mathbf{P} = 0$ according to Maxwell's equations.) The predictive power of the simulations is noteworthy, anticipating by more than a decade (Kornev, Fu, and Bellaiche, 2004) a feature that was later experimentally confirmed in the form of flux-closure quadrants by Tang *et al.* (2015) and later by the continuous rotation of the polarization in vortices (Yadav *et al.*, 2016). These flux-closure domain structures (also known as closure domains) in ferroic materials were first predicted by Landau and Lifshitz (1935), then one decade later by Kittel (1946, 1949) in his studies on ferromagnetic domains. They can be considered as tubes of vortices: for instance, the vortices seen in (x, z) planes propagate along the y axis.

The next step further was foreseen in 2004, when it was predicted using effective Hamiltonians that a variation of the electrical boundary conditions by moving the system toward a short-circuited condition resulted in the generation of peculiar

dipolar configurations (Kornev, Fu, and Bellaiche, 2004). They are characterized by the formation of nanodomains having local dipoles that are aligned in an opposite direction with respect to the macroscopic polarization. These "bubble" nanodomains, which are defined in Sec. III.B.4 and which extend throughout the thickness of the film but are laterally confined, were experimentally observed in 2017 as electric bubbles (Zhang *et al.*, 2017). They can be considered the precursors of the polar skyrmions (Das *et al.*, 2019). These bubbles were also found in subsequent atomistic simulations, and their field evolution predicted, when dc electric fields are applied to ultrathin films [made of $Pb(Zr_{0.5}Ti_{0.5})O_3$ or $BaTiO_3$] possessing nanostripe domains. They act as intermediate states before these 2D systems transform into monodomains (Lai *et al.*, 2006, 2007b). The differences between (001) $Pb(Zr, Ti)O_3$ and $BaTiO_3$ thin films, such as the direction along which stripes alternate and the existence of zigzag domain walls in $BaTiO_3$ under fields, were emphasized by Lai *et al.* (2007b).

Other effects were computationally investigated in ferroelectric ultrathin films, such as the effect of the growth direction on properties (Ponomareva and Bellaiche, 2006). The latter study resulted in the prediction of novel dipolar textures, including 90° nanodomains for (110) and (111) $Pb(Zr_{0.4}Ti_{0.6})O_3$ films under open-circuit-like electrical boundary conditions, to be compared to 180° nanostripes for their (001) counterpart.

In many cases, surfaces are not flat but rather present steps in their morphology (Shimada, Tomoda, and Kitamura, 2010b). A first-principles-based approach was also used to investigate the effect of crystallographic steps on the characteristics of the nanostripe domains in ultrathin $Pb(Zr_{0.4}Ti_{0.6})O_3$ films (Prosandeev and Bellaiche, 2007c). New stripe configurations were predicted to occur as a result of being pinned by these steps.

The interplay between polar and antiferrodistortive (oxygen octahedral tilting) motions, together with alloying and strain degrees of freedom, was computationally studied in ultrathin $Pb(Zr_{0.52}Ti_{0.48})O_3$ films under different electrical boundary conditions by Sichuga and Bellaiche (2011). The original features were found there too, including phases exhibiting both dipolar nanodomains and oxygen octahedral tilting, chemical pinning of domain walls in Zr-rich regions, and enhancement of antiferrodistortive distortions near the domain walls. The existence of cylindrical dipolar chiral bubbles and dipolar waves was also predicted for the first time there and was experimentally confirmed years later (Zhang *et al.*, 2017; Lu *et al.*, 2018).

E. Novel topological phenomena in ferroelectric nanocomposites

Motivated by the aforementioned work of Prosandeev and Bellaiche 2006) on ferroelectric nanodots embedded in a polarizable medium, computational investigations of nanocomposites made of $BaTiO_3$ nanowires embedded in a $SrTiO_3$ matrix were pursued in the search for novel dipolar textures and phenomena starting in the 2010s. Three major striking effects were predicted.

The first effect was the emergence of *chirality* (Louis *et al.*, 2012), which is further discussed in Sec. V.D.1. First-principles-based effective Hamiltonians showed how these nanocomposites spontaneously have both a vortex and a macroscopic spontaneous polarization, with this polarization aligned along the normal of the plane containing the vortex. All vortices display the same sense of rotation in every wire because of their pairing with antivortices, thereby resembling the phase-locking phases observed in magnets (Ruotolo *et al.*, 2009). Therefore, these systems exhibit an electric toroidal moment parallel to the polarization. Similar phases where found by Chen, Zheng, and Wang (2015). Subsequent analytical derivations and Landau-type phenomenological developments demonstrated that this chirality results in natural optical activity: the plane of polarization of linearly polarized light rotates by a fixed amount per unit length when it goes through the material. This effect can be quantified using the gyrotropic coefficients (Prosandeev *et al.*, 2013). The sense of rotation can be switched by an electric field applied via an induced transition between the dextrorotatory and laevorotatory forms. The gyrotropic coefficient was further optimized at room temperature for some applied dc electric field (Walter *et al.*, 2016).

The second breakthrough in nanocomposites was the prediction of the stabilization of polar electrical skyrmions defined in Sec. III.B.3, down to a few nanometers in size, along an electric-field-induced path (Nahas *et al.*, 2015). The third major step forward predicted in the nanocomposites was the interplay between geometrical frustration and the ordering of topological defects (Nahas, Prokhorenko, and Bellaiche, 2016). It was found that different self-assembled ordered structures, inside which point topological defects condense, fluctuate down to the lowest temperatures. This fluctuation gives rise to several fingerprints of geometric frustration that were previously reported in a variety of materials (Anderson, 1987; Laughlin, 1988; Wen and Niu, 1990; Harris, 1999; Lee *et al.*, 2002; Hemberger *et al.*, 2005; Moessner and Ramirez, 2006; Castelnovo, Moessner, and Sondhi, 2008), such as a residual configurational entropy, ground state degeneracy, and broad dielectric response. Related complex orderings and spatial organization, with novel stripe and spiral phases, topological defects, and curvature, were reported by Choudhury *et al.* (2011) in compositionally graded ferroelectrics, for which the Ba and Sr compositions of $(Ba, Sr)TiO_3$ layers periodically change along the [001] direction (Damodaran *et al.*, 2017b).

F. Experimental breakthrough for the characterization of the structures with subangstrom resolution

In parallel, experimental breakthroughs were boosted by the development of novel techniques such as phase-contrast high-resolution transmission electron microscopy (HRTEM) or the aberration-corrected annular dark-field *Z*-contrast HAADF STEM, to directly visualize the atomic structure (and therefore to obtain atomic-scale quantitative maps of the electric polarization) with subangstrom resolution. These techniques were applied for the first observations of electric dipole configurations involving regions of continuous polarization rotation to screen the depolarization field. That was the case for the triangular-shaped vortex nanodomains providing polarization closure in insulating 109° domain walls at the interface between $BiFeO_3$ thin films grown on $TbScO_3$ (Nelson *et al.*, 2011). For other domain configurations (such

as the 71° domain pattern) the interfaces were metallic, and standard stripe domains were formed with a much smaller polarization rotation. The same year, Jia *et al.* (2011) demonstrated the existence of flux-closure structures at a 180° domain wall in epitaxial thin films of $Pb(Zr_{0.2}Ti_{0.8})O_3$ on $SrTiO_3$. Near the interface region, the local dipoles rotate continuously through a well-defined area of triangular shape (maximum width of around four unit cells) connecting two 180° domains. At the upper interface, no flux-closure structure was observed. The observation of periodic flux-closure quadrants was first detected in $PbTiO_3/SrTiO_3$ multilayer films grown under tensile strain on a $GdScO_3$ substrate (Tang *et al.*, 2015). The thicknesses of the $PbTiO_3$ layers in which the closure quadrants occur were in the range of 15–36 nm. At the center of the $PbTiO_3$, 180° domain walls were observed in the HAADF-STEM images, with a continuous rotation of the polarization happening in the neighborhood of the interface, forming 90° domain walls. Substantial nonuniform disclination strains (including giant strain gradients related to flexoelectric effecs; Sec. IV.B) resulted from the configuration of these flux closures. Flux closures were also observed in tunnel junctions made of $PbTiO_3$ ultrathin films sandwiched between Co and $La_{0.7}Sr_{0.3}MnO_3$ electrodes (Peters *et al.*, 2016) or associated with chiral Néel-like domain walls in Ti-rich $Pb(Zr, Ti)O_3$ single crystals (Wei *et al.*, 2016).

The critical step toward the first experimental realization of a complex polarization pattern where the local polarization continuously rotates around a core to form a polar-vortex state was undertaken by Yadav *et al.* (2016) in a $PbTiO_3/SrTiO_3$ superlattice grown on a $DyScO_3$ substrate. When the thickness of both the $PbTiO_3$ and $SrTiO_3$ layers is reduced to ten unit cells (~4 nm), the dipolar configuration evolves from the flux-closure to the vortex structure, as discussed in Sec. V.A.

All these efforts required the convergence of a precise materials synthesis (in this case, oxide superlattices or nanostructures) in which thermodynamic boundary conditions are imposed on a ferroelectric phase and directly studied with state-of-the-art materials characterization and simulation tools. With this as the background, this review focuses on the advances and breakthroughs over the past decade (and particularly in the past five years) in the growth, characterization, and computations of model ferroelectric heterostructure systems and topological structures that have emerged within them. We focus on polar vortices, polar skyrmions, and the recently observed associated functionalities. A timeline with some important milestones is shown in Fig. 4 of the Supplemental Material (472), which is inevitably reduced in the number of examples due to size constraints. Reviews on unusual electric dipole textures that summarized activities on that field of research from about 2003 to 2015 were given by Ponomareva *et al.* (2005a), Kornev, Fu, and Bellaiche (2006), Kornev *et al.* (2008), Prosandeev, Ponomareva, Naumov *et al.* (2008), Prosandeev and Bellaiche (2009), and Prosandeev *et al.* (2016).

III. PRIMER ON TOPOLOGY

Topology is the branch of mathematics concerned with the properties of geometric objects that are preserved under continuous deformations. A set of operations is allowed

within this "continuous deformations" family, including the stretching, twisting, crumpling, or bending of a given structure. However, operations involving the cutting and pasting of different parts of the structure are forbidden for the topological characterization of a system. The quest for physical properties that remain invariant under these continuous deformations is boosting interest in the field, permeating many different areas in condensed-matter physics, from electronic-structure theory to dislocations, superconductivity, and superfluidity. Ramirez and Skinner (2020) referred to this as the "dawning of the topological age.".

The goal of this section is to provide for a nonexpert in the field the basic definitions of topologically related concepts (topological invariants, homotopy class, topological-phase transitions, defects, and solitons, etc.), particularly of the polar systems that constitute the topic of this review. A rigorous definition of all of them is beyond the scope of this review; see Mermin (1979), Toulouse (1980), Dubrovin, Fomenko, and Novikov (1985), Chaikin and Lubensky (2000), Nakahara (2003a), and Manton and Sutcliffe (2004) for more information.

A. Homotopy classes and groups

Two objects that can be continuously transformed from one into the other are said to be homotopy equivalent or to belong to the same homotopy class (Mermin, 1979; Dubrovin, Fomenko, and Novikov, 1985; Pontryagin, 1986; Mineev, 1998; Monastyrsky, 1999; Nakahara, 2003a; Manton and Sutcliffe, 2004; Bick, Bick, and Frank, 2005). Homotopy classes thereby gather objects that have common features preserved under continuous transformations. These invariant properties are called topological invariants.[1]

The prototypical example of a topological invariant is the number of handles on the surface of a geometrical shape, i.e., the *genus* g (Dubrovin, Fomenko, and Novikov, 1985), related to the Euler characteristic $\chi = 2(1-g)$ of the shape (Ramirez and Skinner, 2020). For instance, a doughnut and a coffee mug belong to the same homotopy class since the number of handles on both shapes is equal to 1.

Another example is related to the problem of enumerating possible positions of a closed loop on a a given surface (Monastyrsky, 1999). For instance, imagine an elastic band (a closed loop made of rubber) wrapped around an infinitely long cylinder. The band can wind around the cylinder one or several times, as shown in Fig. 1(a). Various homotopy equivalent band placements can be obtained by continuously deforming the band. It can be moved along the cylinder axis, rotated, stretched, and deformed [Fig. 1(b)], but cutting and regluing are not allowed. Can any band position be matched by deforming a simple, untwisted band [the green loop in Fig. 1(a)]? The answer becomes obvious once we notice that the infinite extent of the cylinder prevents one from freeing the band or wrapping it around an additional time without cutting.

---

[1]In physics, the term homotopy invariant or class is often replaced by topological invariant or class, albeit the latter definition imposes more stringent constraints on the allowed transformations between objects (Dubrovin, Fomenko, and Novikov, 1985; Monastyrsky, 1999).
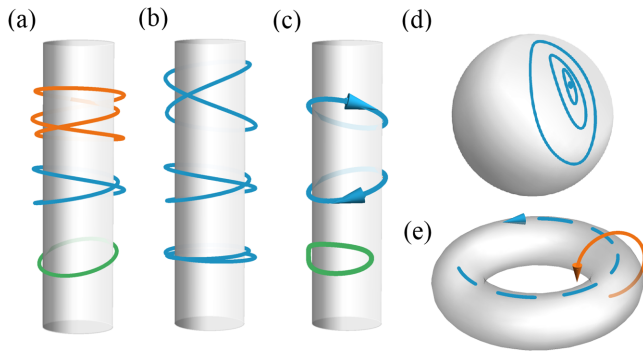
FIG. 1. (a) Elastic band wrapped around an infinite cylinder. Green (lower), blue (middle), and orange (upper) bands wind around the cylinder one, two, and three times, respectively. (b) Examples of homotopy equivalent band placements that wind twice around the cylinder. These configurations can be continuously transformed into one other and belong to the same homotopy class. (c) The green (lower) band does not wrap the cylinder and belongs to a class of trivial loops that can be contracted to a point. Bands that wind the cylinder clockwise and counterclockwise [blue (dark gray) arrows] cannot be continuously matched. Their respective classes are labeled with winding numbers of opposite signs. (d) Any loop on a sphere can be continuously contracted to a point. The sequence of contracting loops is shown with blue (dark gray) lines. (e) Loops on the surface of a torus are characterized by a combination of winding numbers in the poloidal (orange solid arrow) and toroidal (blue dashed arrow) directions.

In other words, the number of times that the band winds around the cylinder is invariant under continuous transformations. In mathematics (Dubrovin, Fomenko, and Novikov, 1985; Monastyrsky, 1999) and physics of topological defects (Mermin, 1979; Chaikin and Lubensky, 2000), such a topological invariant is termed as the winding number w. Here w is a unique invariant, and as such it unambiguously determines the homotopy class of a specific band placement: all configurations with equal winding numbers can be continuously deformed from one into the other and thus belong to the same homotopy class.

Note that we can also define band configurations with $w = 0$, as well as negative w values. The zero w configuration can be described as a band lying on the surface of the cylinder without encircling it [the green band in Fig. 1(c)]. The sign of w can be defined by the sense of rotation (clockwise or counterclockwise) of the band [Fig. 1(c)].

If we replace the cylinder with a different shape having a different Euler characteristic χ (such as a sphere or torus), we will see a drastically different picture. For instance, any closed loop on the surface of a sphere [Fig. 1(d)] can be contracted to a point (Dubrovin, Fomenko, and Novikov, 1985; Monastyrsky, 1999). For this reason, all bands wrapped around a sphere can be continuously matched and belong to the same unique homotopy class. In contrast, two different winding numbers are required to describe all types of closed loops placed on a surface of a torus (Dubrovin, Fomenko, and Novikov, 1985) [Fig. 1(e)].

The ensemble of all band classes labeled by w is an illustration of what mathematicians call the first, or

fundamental, *homotopy group* π_1 (Mermin, 1979; Dubrovin, Fomenko, and Novikov, 1985; Chaikin and Lubensky, 2000; Nakahara, 2003a). This group classifies topologies of closed loops that can be placed in a space $\mathcal{X}$. The π_1 group and its extensions π_n play an important role in topology (Dubrovin, Fomenko, and Novikov, 1985) and are at the core of the theory of topological defects (Toulouse and Kléman, 1976; Volovik and Mineev, 1977; Mermin, 1979; Toulouse, 1980; Trebin, 1982; Chaikin and Lubensky, 2000) and solitons (Rajaraman, 1987; Manton and Sutcliffe, 2004). In Secs. III.B–III.F, we describe the main aspects of this theory, with a particular focus on the complex patterns of electric polarization.

B. Topological defects and solitons

Topological properties of a material are defined mainly by its dimensionality D and the topology of its order-parameter space $\mathcal{X}$. The latter is defined as a set of all possible values of the order parameter at any given point in the material (Mermin, 1979; Chaikin and Lubensky, 2000).

For instance, in the Ising magnets the spins have a fixed magnitude and always point along a given direction. As a result, $\mathcal{X}$ is made of only two points that correspond to the "up" and "down" spin values [Fig. 2(a)]. In the XY model, the spins can be directed along all the possible directions of the plane. In this example, the fixed spin magnitude means that $\mathcal{X}$ is a circle $\mathbb{S}^1$ [Fig. 2(b)]. In the Heisenberg magnets, the spin can point in any direction of a three-dimensional space, sweeping all the points of the surface of a sphere [Fig. 2(c)]. The same considerations apply to the Ising-, XY-, and Heisenberg-like ferroelectrics in their polar states. For these systems, the dipoles with zero magnitude are practically improbable and can be continuously normalized.

In all aforementioned examples the nontrivial topology of $\mathcal{X}$ allows for various topological defects and solitons. Both are swirling order-parameter patterns that feature a core region where the order is destroyed, and a far field region where the order parameter changes slowly in space (Chaikin and Lubensky, 2000; Manton and Sutcliffe, 2004). For instance, for the Ising model shown in Fig. 2(d) part of the sample presents a domain where all the local dipoles are pointing up, and a second domain where the domains are pointing down. The separation of both is the domain wall, the core region where the order parameter is not defined. In this example, the domain wall is a topological defect. Domain walls typically appear when $\mathcal{X}$ is not simply connected, for instance, it consists of several disconnected parts or points [Fig. 2(a)]. Typical topological defects in the XY model ($\mathcal{X} = \mathbb{S}^1$) are vortices and vortex lines [Fig. 2(e)]. In this case, the defect is localized in a core region where the orientation of the dipole changes abruptly between consecutive lattice points. Far from the core, these variations are strongly reduced. A three-dimensional analog of a vortex is a hedgehog pattern [Fig. 2(f)]. Hedgehogs and antihedgehogs are the defects appearing in the 3D Heisenberg model.

Vortices and hedgehogs are classical examples of topological defects. The second type of topological patterns is topological solitons or topological textures. A widely known example of solitons are skyrmions that are also typical of the
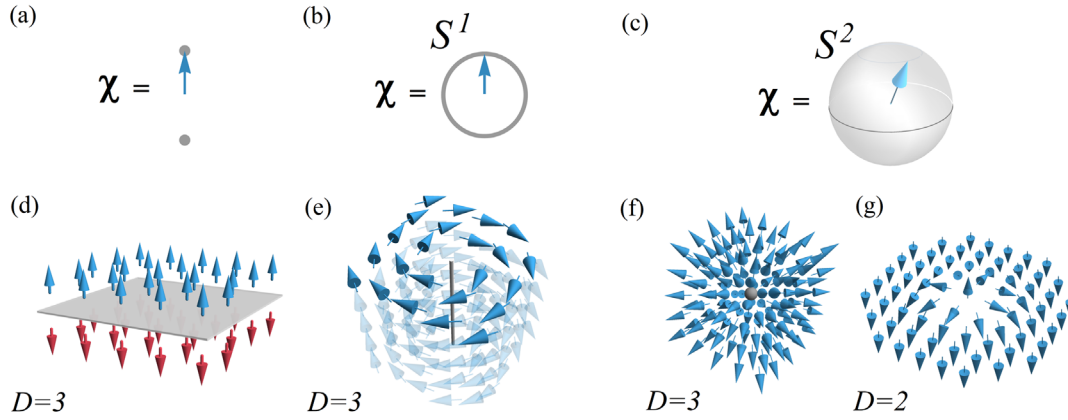
FIG. 2. Order-parameter spaces $\mathcal{X}$ for (a) the Ising, (b) XY, and (c) Heisenberg models. The arrows indicate examples of orientations of the spin vector. The locus of all possible spin tip positions constitute the order-parameter space. The relevant topological defects in three dimensions for the Ising, XY-, and Heisenberg models are (d) domain walls (e) vortex lines, and (f) hedgehogs or Bloch points. The Heisenberg model also allows for various topological solitons in $D = 1, 2$, and 3 dimensions. (g) Néel skyrmion, which is an example of such a soliton. This can be considered the stereographic projection of (f) taken from the south pole.

Heisenberg model ($\mathcal{X} = \mathbb{S}^2$), but this time in two dimensions. A Néel flavor of this topological texture is shown in Fig. 2(g). The skyrmionic case is a bit more subtle. In contrast to topological defects, solitons do not feature an order-parameter singularity at the core (Manton and Sutcliffe, 2004).

Another important difference between topological defects and solitons resides in the behavior of the order parameter in the far field region. In the case of stand-alone defects, the order-parameter distribution is inhomogeneous even at an inifinite distance from its core while stand-alone solitons always converge to a homogeneous order at their periphery.

Defects and solitons are characterized (Chaikin and Lubensky, 2000) by their topological charge. Additionally, defects can be described by the dimension of their core d. The latter determines the dimensionality of the locus of singular points. For point defects the core has zero dimension ($d = 0$). The order-parameter distribution of these patterns features a singularity or vanishes at a single point (for instance, the vortex in two dimensions). Domain walls, also known as kinks, are planar defects ($d = 2$) in three dimensions, line defects ($d = 1$) in two dimensions, and point defects ($d = 0$) in one dimension (Fig. 3). A domain-wall vertex (intersection of two domain walls) in three dimensions is another example of a line defect with $d = 1$.

The topological charge[2] is computed by associating the order-parameter pattern with an element of the homotopy group π_n, where $n = D - d - 1$ for the case of defects and $n = D$ for solitons. The general procedure is rather technical and can be found elsewhere (Mermin, 1979; Manton and Sutcliffe, 2004). Several important properties of topological charges ought to be mentioned. One is that topological charges are additive quantities. A given order pattern can be globally characterized by the sum of charges of individual defects or solitons. Such additivity stems from the group operation in π_n. For defects, it can also be linked to the

singular nature of defect cores through the Poincaré-Hopf theorem (Dubrovin, Fomenko, and Novikov, 1985). The latter theorem constrains the sum Σ of all topological charges in the system to be equal to the Euler characteristic of the embedding space. For instance, an infinite bulk crystal with $D = 2$ or 3 is described by $\chi = 0$, and any defect is bound to appear in pair with its negatively charged counterpart. In Sec. III.B.1 we focus on the most relevant defect and soliton cases, where we
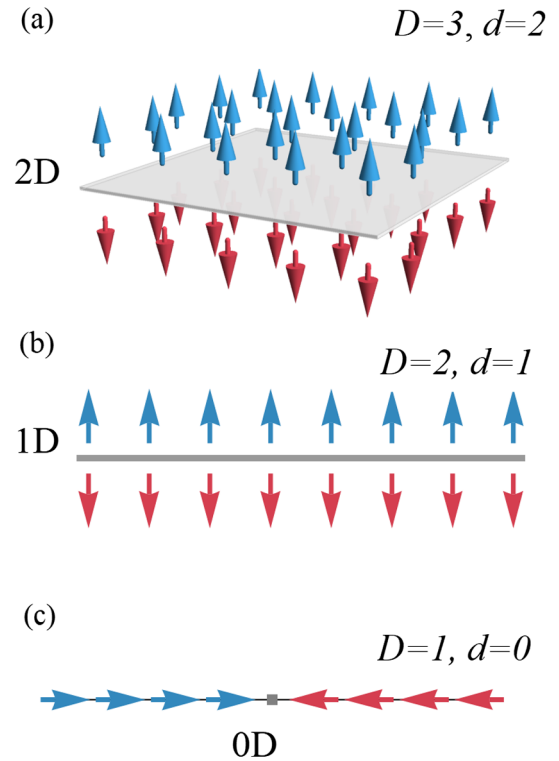

FIG. 3. A domain wall in (a) three-dimensional ($D = 3$), (b) two-dimensional ($D = 2$), and (c) one-dimensional ($D = 1$) spaces is a planar, line, and point defect, respectively. The core dimension d of a domain wall is always equal to $D - 1$.

---

[2]The topological charge can be equivalently referred to as the topological index or topological number.
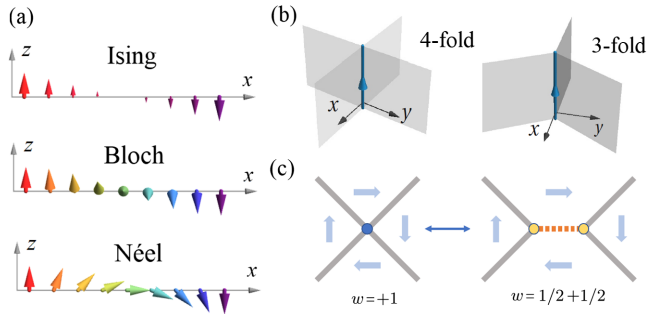
FIG. 4. (a) Ising, Bloch, and Néel domain-wall structures. (b) Schematic illustration of fourfold and threefold domain-wall vertices. (c) Splitting of a vortexlike domain-wall vertex [blue (dark gray) circle at the left] into two threefold vertices [yellow (light gray) circles at the right]. The domain wall shown by the dashed-orange line carries $w = +1/2$ half vortices at its end points.

1. Domain walls and domain-wall vertices

Domain walls are commonly encountered in ferroic materials. Depending on how the order parameter changes across the wall, one distinguishes Ising, Bloch, or Néel domain-wall structures [Fig. 4(a)]. Topologically, these states are an exceptional case in the family of defects and solitons: their topological properties are related to the continuous space partitioning (such as tiling in two dimensions) rather than the continuity of the order-parameter field. Domain walls are classified by the zeroth homotopy set π_0 that lacks the group structure. Consequently, in a general case one cannot assign a topological charge to a domain wall.

As a subregion of space, domain walls can themselves host topological defects and solitons. Common examples include Bloch and Ising lines as well as Bloch points (Malozemoff and Slonczewski, 1979) and domain-wall skyrmions (Cheng *et al.*, 2019). Intersections of domain walls are called vertex lines (Catalan *et al.*, 2012) [Fig. 4(b)]. These can be topologically equivalent to vortex and antivortex lines (Sec. III.B.2). However, in contrast to the latter vortexlike vertices can be easily deformed. For instance, a fourfold vertex can be split into Kittel closure domains with an additional domain wall carrying half-vortex structures at its end points [Fig. 4(c)]. A 180° Néel or Bloch wall surrounding a cylindrical domain is topologically equivalent to a skyrmion (Malozemoff and Slonczewski, 1979; Bogatyrev and Metlov, 2018) (Sec. III.B.3). An ensemble of meronlike domain-wall vertices topologically equivalent to a skyrmion were also reported in ferroelectric nanocomposites (Nahas *et al.*, 2015).

2. Vortices and antivortices

Vortices are ubiquitous topological defects in materials with a two-dimensional order parameter and underlying continuous rotational symmetries (the global rotations of dipoles or spins by any angle does not change the energy) (Kosterlitz and Thouless, 1973; Toulouse and Kléman, 1976; Mermin, 1979).
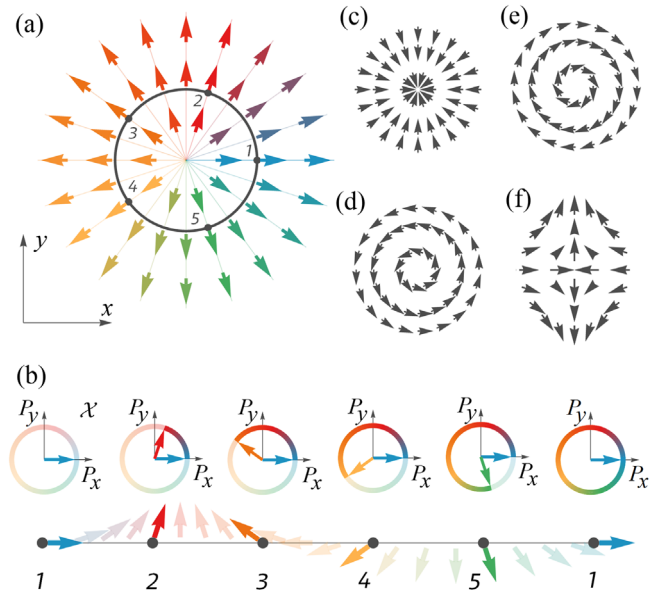
FIG. 5. (a) Two-dimensional center-divergent vortex. The arrows represent the 2D polarization vectors **P** and are colored according to their x Cartesian component. The black circle is a loop surrounding the defect core. Moving counterclockwise along this loop from point 1 to point 5 generates a counterclockwise rotation of polarization, as shown in (b). Consequently, the tip of the polarization vector draws a loop wrapping around **P** = 0. The winding number w of configuration (a) is equal to 1 since one full turn around the vortex core yields a 360° polarization rotation. (c)–(e) Topologically equivalent vortex configurations with $w = 1$. (f) Antivortex configuration with $w = -1$.

The order-parameter space of such systems is equivalent to a circle $\mathbb{S}^1$ or an infinite cylinder [Fig. 1(a)]. The winding number introduced in Sec. III.A plays the role of the topological charge.

An example of a center-divergent vortex is shown in Fig. 5(a). Its central point features a singularity and constitutes the defect core. To compute the topological charge of this state we first need to trace the values of the order parameter along a path of dimension $n = 1$ enclosing the defect core (according to the rule described at the beginning of this section, $n = D - d - 1 = 2 - 0 - 1 = 1$). An example of such a path is shown as a black circle in Fig. 5(a). With counterclockwise motion along the indicated path from point 1 to point 5 and back to point 1, the order parameter will continuously rotate, making a full turn around the origin in the observer reference frame [Fig. 5(b)]. Note that the order-parameter values on this path form a closed loop in the order-parameter space that is similar to the rubber band in Sec. III.A. The topological charge of the order-parameter pattern can thus be assigned to the homotopy class of such a loop and is given by its winding number; see Sec. III.A. In the physics of magnetic materials, the topological charge of a vortex is most commonly called vorticity (Chaikin and Lubensky, 2000). This charge has a simple geometric interpretation: it is equal to the number of full 360° turns of the order parameter along a given closed path. For the considered pattern, one counterclockwise turn along the path produces a single 360°

counterclockwise rotation of spins. Therefore, the winding number w and the topological charge of the configuration shown in Fig. 5(a) is equal to 1. Here w can be formally defined as a line integral over a closed loop L,

$$w = \frac{1}{2\pi} \int_L \frac{d\theta}{d\mathbf{l}} \cdot d\mathbf{l}, \qquad (1)$$

where θ denotes the inclination angle of the order parameter from the x axis.

In general, point topological defects classified by elements of π_1 are called vortices or antivortices, depending on the sign of w. In three dimensions ($D = 3$) elements of π_1 define topological charges of vortex and antivortex lines (Chaikin and Lubensky, 2000) [Fig. 2(e)].

For $\mathcal{X} = \mathbb{S}^1$ the computed winding number w is topological invariant and does not change under continuous transformations of the order-parameter field. A trivial example of a continuous transformation is a global rotation of all spins. For example, the consequent counterclockwise rotation by 90° of all vectors in Fig. 5(a) allows other prototypical vortex configurations to be obtained [Figs. 5(c)–5(e)]. Despite obvious geometric and physical differences, all these states are homotopy equivalent. An example of an antivortex pattern with $w = -1$ is shown in Fig. 5(f).

3. Skyrmions, antiskyrmions, and merons

In contrast to vortices and antivortices, skyrmions and antiskyrmions are topological solitons. They are common attributes of two-dimensional systems with a spherical order-parameter space ($\mathcal{X} = \mathbb{S}^2$).

Two canonical examples of such topological textures called Néel and Bloch skyrmions (Rößler, Bogdanov, and Pfleiderer, 2006) are shown in Figs. 6(a) and 6(b), respectively. The topology of the skyrmions is related to the $\mathbb{S}^2 \to \mathbb{S}^2$ mapping (Manton and Sutcliffe, 2004; Nagaosa and Tokura, 2013). As a result, skyrmionic textures are associated with nontrivial elements of the second homotopy group π_2. The topological charge of these patterns can be obtained by mapping the order-parameter values within the area covered by the defect to the order-parameter space (Manton and Sutcliffe, 2004; Nagaosa and Tokura, 2013). For the Néel skyrmion, such a mapping is illustrated in Figs. 6(c)–6(e). Taking all order-parameter values within the area of an increasing diameter [bottom images in Figs. 6(c)–6(e)] creates an expanding two-dimensional surface in the order-parameter space [top images in Fig. 6(c)–6(e)]. Since topological solitons are required to have constant order-parameter distribution away from the defect core, the created surface will eventually close and fully cover the order-parameter space an integer number of times. This integer number will label the homotopy class or, equivalently, will correspond to the skyrmion's topological charge. The topological charge of a skyrmion is called the skyrmion number N (Manton and Sutcliffe, 2004; Nagaosa and Tokura, 2013). It can be computed as

$$N = \frac{1}{4\pi} \int \int \mathbf{n} \cdot \left(\frac{\partial \mathbf{n}}{\partial x} \times \frac{\partial \mathbf{n}}{\partial y} \right) dx\,dy, \qquad (2)$$
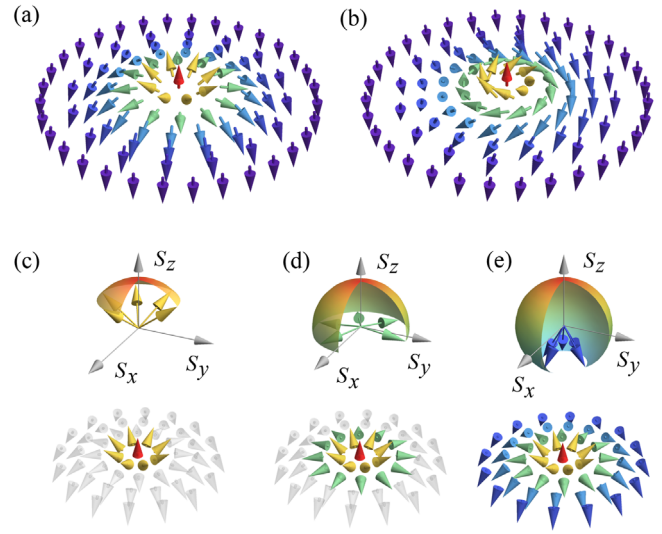
FIG. 6. (a) Néel and (b) Bloch skyrmions. The arrows represent spins and are colored according to their out-of-plane Cartesian component. The topological charge of a skyrmion (the skyrmion number) is computed by mapping the spin values within a disk containing the skyrmion core to the order-parameter space. (c)–(e) Schematic of the skyrmion number calculation for the Néel skyrmion texture. Increasing the diameter of the mapped area [bottom images in (c)–(e)] eventually creates a closed surface [top images in (c)–(e)] that fully covers the order-parameter space $\mathbb{S}^2$ one time.

where $\mathbf{n}(\mathbf{r})$ is the normalized order-parameter vector field and the integrand is called the Pontryagin charge density. In 3D systems, skyrmions can form so-called skyrmion tubes, which are similar to vortex lines.

Integer-charged skyrmions can be broken into subparticles that carry a fractional skyrmion number (most often $\pm 1/2$). These particles are called merons. They do not satisfy the requirement of a homogeneous order parameter at their periphery and are not topological solitons. However, in ferroic systems merons often have features of π_1 defects such as vortices, antivortices, and disclinations.

4. Bubbles, bubble skyrmions, and hopfions

Another type of structure related to skyrmions is polar bubbles [Fig. 7(a)] (Lai *et al.*, 2006; Zhang *et al.*, 2017) and polar bubble skyrmions [Fig. 7(b)] (Das *et al.*, 2019). These solitons have an up (or down) polarized core surrounded by a toroidal-vortex pattern. In both cases, the soliton is embedded in a homogeneous matrix domain with an opposing down (or up) polarization. Such 3D structures generate Néel-like rotations of the order parameter at the top and bottom planes. A distinctive feature of bubble skyrmions is an additional Bloch component related to an in-plane circumferential vortex [the orange arrow in Fig. 7(b)]. Most often polar bubbles and bubble skyrmions form in ultrathin tetragonal ferroelectric films, or in ferroelectric-dielectric superlattices, and span the total thickness of the ferroelectric layer along the polar axis.

Topologically, the skyrmion tubes and both types of bubbles are characterized by an integer skyrmion number N of their in-plane cross sections. At their bottom and top
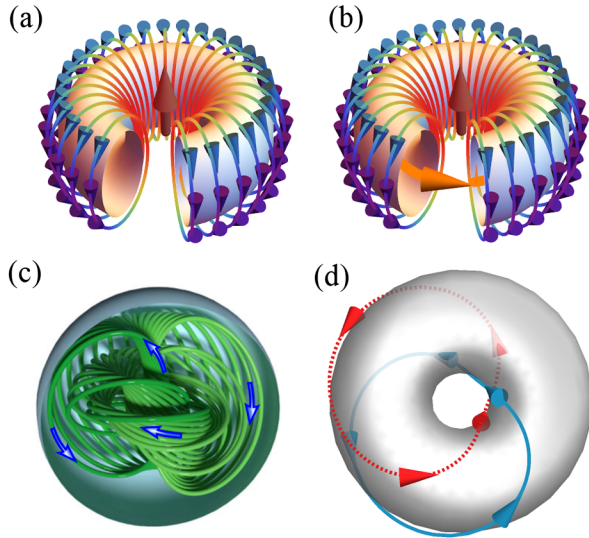
FIG. 7. Schematic structures of (a) a polar bubble, (b) polar bubble skyrmion, and (c) polar hopfion. Lines indicate the polarization flux lines, while arrows show the orientation of the local dipoles. The in-plane polar vortex of a bubble skyrmion is indicated by an orange (light gray) horizontal curled arrow in (b). (d) Linking of two polarization flux lines (shown in solid blue and dashed red) on a toroidal surface. (c) From Luk'yanchuk *et al.*, 2020.

planes, polar bubbles and bubble skyrmions feature two Néel skyrmions [see Figs. 28(g) and 28(h)] that can terminate at a Bloch point (Han *et al.*, 2022). In the latter case, these skyrmions bear similarity to the so-called spin and polar bobbers. These Néel rotations extend up to six unit-cell layers toward the middle plane, depending on the diameter of the soliton, and ensure an integer skyrmion number $N = \pm 1$.

In the case of bubble skyrmions, the Néel component gradually transforms into Bloch rotations and eventually yields a circular 180° Bloch wall in the middle layers of a bubble skyrmion [Fig. 7(b)]. The corresponding cylindrical domain structure with a circular Bloch wall (known in the magnetic community as magnetic bubbles) is topologically equivalent to a skyrmion. Bubble skyrmions are thereby characterized by an integer skyrmion number in all cross sections.

The latter is also true in the case of spherical polar bubbles (Nahas, Prokhorenko *et al.*, 2020). When the in-plane bubble diameter of the bubble is equal to its thickness along the out-of-plane direction, all in-plane cross sections of the bubble are characterized by an integer skyrmion number $N = \pm 1$. At the same time, elongating this bubble in the direction of its polar core results in a cylindrical Ising domain with half-bubble top-bottom terminations.

Note that albeit bubbles carry an integer skyrmion number, the conservation of this 2D topological index for vector fields in 3D space is not guaranteed. Additionally, since the corresponding polarization patterns are defined on a finite thickness slab within $\mathbb{R}^3$, the constraints on the polarization at the boundary will have a crucial impact on topology. These points, as well as mathematically rigorous topological characterizations of bubblelike patterns, constitute an important (but still open) question. Additional arguments on this topic were offered in a recent perspective article (Govinden, Prokhorenko *et al.*, 2023).

Adding an inhomogeneous Bloch component throughout the full volume of a bubblelike soliton can result in an intricate hopfion structure (Arnold and Khesin, 1998; Luk'yanchuk *et al.*, 2020) [Fig. 7(c)]. A detailed description of this construction was given by Luk'yanchuk *et al.* (2020). Note that, unlike bubble skyrmions, hopfions feature Bloch rotations at their outer boundary as well as the top and bottom poles. Moreover, in contrast to bubbles and bubble skyrmions, the polarization lines are closed and divergenceless in a hopfion structure. The extra Bloch rotations make the polarization flux lines wind around the hopfions' core and links them like links of a chain [Fig. 7(d)]. This linking can be characterized by the Hopf invariant N_{H}. N_{H} can be computed as (Arnold and Khesin, 1998; Luk'yanchuk *et al.*, 2020)

$$N_{\mathrm{H}} = \int \mathbf{P} \cdot \mathrm{curl}^{-1} \mathbf{P}\, dV, \tag{3}$$

where $\mathbf{P}$ is the polarization and the gauge field $\mathbf{A} = \mathrm{curl}^{-1} P$ is defined as $\mathbf{P} = \nabla \times \mathbf{A}$. Notably N_{H} can take noninteger values (Arnold and Khesin, 1998) but is invariant under volume-preserving deformations. An integer topological charge of a hopfion called the Hopf invariant can be computed using the Whitehead integral formula (Whitehead, 1947):

$$N_{\mathrm{H}} = \int \mathbf{F} \cdot \mathrm{curl}^{-1} \mathbf{F}\, dV, \tag{4}$$

where $F_i = \varepsilon_{ijk} \mathbf{n} \cdot \partial \mathbf{n}/\partial x_j \times \partial \mathbf{n}/\partial x_k$, with $\mathbf{n}$ the normalized polarization. Equation (4) is the three-dimensional analog of the skyrmion number [Eq. (2)]. Like skyrmions, hopfions can have multiple geometric realization related to each other by smooth deformations. A more detailed discussion on the relation between bubble, skyrmion bubble and hopfion structures was given by Govinden, Prokhorenko *et al.* (2023).

5. Physical characteristics of polar topological states

Notice [see Figs. 5(c)–5(e) and 6(a)–6(b)] that topologically equivalent patterns can often have distinct geometries, and consequently significantly different physical properties. Such states can be distinguished using nontopological characteristics that are defined in this section. These include polarity and helicity or macroscopic order parameters, such as average polarization, toroidal, and hypertoroidal moments.

The two- and three-dimensional vortex structures can be characterized using the toroidal (Prosandeev and Bellaiche, 2009) and hypertoroidal moments (Dubovik and Tugushev, 1990; Prosandeev and Bellaiche, 2008b, 2009). The toroidal moment, commonly denoted as $\mathbf{T}$ or $\mathbf{G}$, is equal to

$$\mathbf{G} = \langle \mathbf{R}_i \times (\mathbf{p}_i - \mathbf{P}) \rangle_i, \tag{5}$$

where $\mathbf{p}_i$ is the local electric dipole of the unit cell i located at $\mathbf{R}_i$ from a chosen origin and $\langle \cdots \rangle_i$ denotes the average over the volume of the crystal. The polarization vector $\mathbf{P}$ is introduced to make $\mathbf{G}$ independent of the chosen origin of the coordinate system (Prosandeev and Bellaiche, 2009). At the same time, for periodic systems the value of $\mathbf{G}$ was found to depend on the choice of the unit cell. The multivalued nature of $\mathbf{G}$ was suggested to be analogous to that of electric

polarization since only the differences of **G** are physically meaningful and do not depend on the unit-cell shift.

The term toroidal moment arguably comes from the definition of the toroidal and poloidal angles of a torus. For instance, vortices winding along the poloidal angle [Fig. 7(a)] of a toroidal structure do not contribute to **G**, in contrast to circumferential vortices winding along the toroidal angle [the orange arrow in Fig. 7(b)]. A nonzero toroidal moment **G** is also characteristic of structures bearing vortex line features [Fig. 2(c)].

The emergence of unusual electric dipolar configurations in zero-dimensional ferroelectric nanostructures led to the introduction of the hypertoroidal moment **h** (Prosandeev and Bellaiche, 2008b, 2009). It can be used to physically characterize multivortex patterns, such as the double vortex state in so-called ferroelectric hysterons (Prosandeev and Bellaiche, 2008a).

Systems possessing nonzero **G** and **h** can strongly couple to inhomogeneous electric and magnetic fields (Prosandeev and Bellaiche, 2008b, 2009). The displacement currents in electrotoroidic systems were linked to the dynamical magnetoelectric tensor and optical activity (Prosandeev *et al.*, 2013).

Additional geometric characteristics of skyrmions include polarity and helicity. The polarity p is assigned based on the orientation of the order parameter at the center of the skyrmion (Nagaosa and Tokura, 2013). For parallel and antiparallel alignment with the z axis, the polarity is equal to $+1$ and -1, respectively. For a Bloch or Néel skyrmion, polarity coincides with its topological charge (skyrmion number). However, for antiskyrmions polarity and charge always have the opposite signs.

The skyrmion helicity angle γ is usually defined as the phase angle of the base vortex (Nagaosa and Tokura, 2013). The vortex phase is equal to the angle between polarization and the x axis passing through the core at zero polar angle ϕ. For instance, if the in-plane skyrmion projection were to look like Figs. 5(a), 5(c), 5(d), or 5(e), the helicity would be equal to 0, π, $\pi/2$, or $-\pi/2$, respectively. Equivalently, helicity can be defined as the angle of global rotation around the z axis relating a given skyrmion to a Néel skyrmion. According to the latter definition, the helicity of a Néel skyrmion is always zero. The product of the polarity times the sign of the helicity angle defines the chirality (or handedness) of the structure (van der Laan, Zhang, and Hesjedal, 2021). Note that the concept of helicity can also be borrowed from fluid dynamics (Moffatt and Ricca, 1992), with the sign of helicity directly related to the handedness and chirality of the system. This is further discussed in Sec. V.D.1. As a summary of the concepts developed in this section, we represent in Fig. 8 the most important topological defects and textures that are discussed in this review.

C. Topological protection

In the context of symmetry-breaking transitions, topological protection usually refers to a certain resistance of the state to changing its homotopy class under external perturbations. For example, topological protection can mean that a weak bias field, a slight change of temperature, or any other external stimulus will neither destroy nor create a topological defect or soliton (vortex, skyrmion, etc.) but rather move, deform, or split it into fractionally charged pieces.

Topological protection is a direct consequence of topological invariance and holds only as long as the evolution induced by the driving force does not break the continuity of the order-parameter distribution. Consequently, topological protection is usually associated with an energy barrier intrinsic to a particular system. Perturbations that drive the system over such a barrier induce discontinuities and are said to break the topological protection.

To illustrate the origin of topological protection and the related energy barrier, we consider an example of a 2D vortex; see Fig. 9. In the case of a two-dimensional order parameter **n** with a fixed magnitude, a vortex belongs to the $w = 1$ homotopy class, while the ordered state is a member of the trivial $w = 0$ class. As these two states belong to different homotopy classes, both are topologically protected. The vortex can be neither "smoothly" destroyed nor created. In other words, to destroy a vortex the perturbation will have to break its continuity.

An example of such a "discontinuous" transformation is shown in Fig. 9(a). Starting with an initial vortex state [top left panel of Fig. 9(a)], the order parameter at each point is continuously rotated clockwise so as to align along the x direction at the end of the transformation [top right panel of Fig. 9(a)]. Since we have assumed a fixed sense of rotation, the vectors with different orientations will, at the end, rotate by different angles. For example, vectors that were slightly tilted toward the positive y direction (small $n_y > 0$) will rotate by a small angle, while similarly oriented vectors slightly tilted toward the $-y$ direction (small $n_y < 0$) will make almost a full 360° turn. Such a mismatch of rotation speed will inevitably create a discontinuity in the order-parameter distribution, an infinite head-to-head domain wall [top middle panel in Fig. 9(a)] extending from the center of the vortex to infinity along the y axis. While the considered transformation is not unique, it is possible to show that any transformation between a $w = 1$ and a $w = 0$ state will create an extended head-to-head or tail-to-tail 180° domain wall.

In the order-parameter space, destroying a vortex is equivalent to contracting a closed loop to a point. However, on a unit circle such a transformation is impossible unless the loop has been cut. In our case the incision happens at the first instant of the pattern evolution on the n_x axis [bottom left panel of Fig. 9(a)]. The consequent contraction of the created circular arch leads to a pattern where the order-parameter orientations cover only half of the full 180° angle [bottom middle panel of Fig. 9(a)]. Independent of the transformation details, such an intermediate state will necessarily contain points where **n** vectors adopt head-to-head or tail-to-tail orientations.

It is worthwhile to consider a counterexample, i.e., a nonprotected state. For instance, we consider the same vortex configuration, but this time with a spherical order parameter. The homotopy theory predicts that a two-dimensional vortex and a perfectly ordered state will now belong to the same homotopy class. Therefore, adding 1 degree of freedom should allow us to smoothly eliminate a vortex. Indeed, the
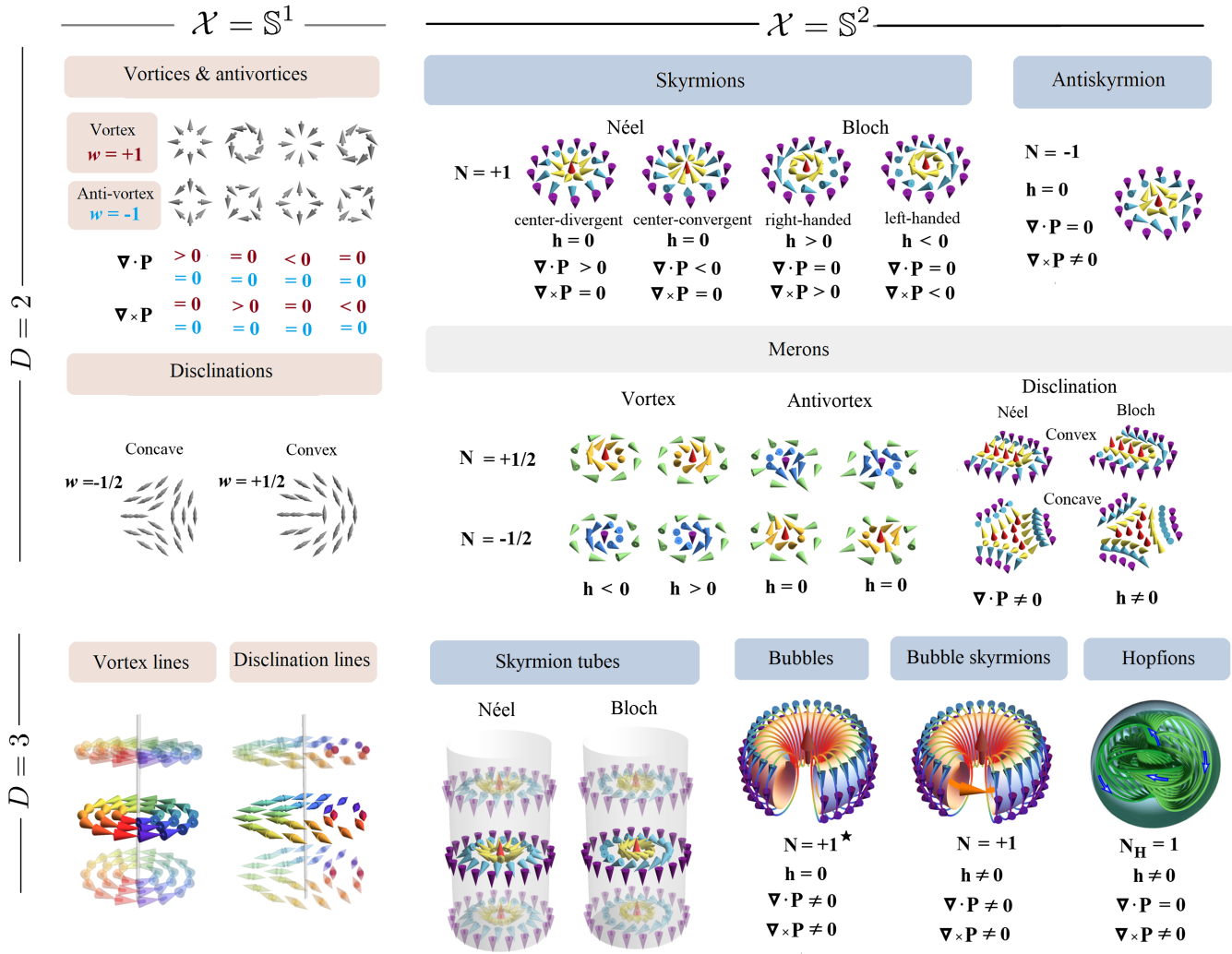
FIG. 8.   Table of the relevant topological structures in two-dimensional (the $D = 2$, top row) and three-dimensional (the $D = 3$, bottom row) systems with the circle-equivalent (left $\mathcal{X} = \mathbb{S}^1$ column) and sphere-equivalent (right $\mathcal{X} = \mathbb{S}^2$ column) order-parameter spaces. Structures belonging to the families of topological defects and solitons are found below the pink and blue labeled boxes, respectively. The most frequently encountered meron structures are shown below the gray labeled boxes. For vortices, skyrmions, bubbles, bubble skyrmions, and hopfions the structure schematics are complemented with indications of physical properties (chirality h, as well as the divergence and curl of the polarization field). Merons and skyrmion tubes (antiskyrmion tubes; not shown) have the same physical properties as the corresponding skyrmion (antiskyrmion) structures, while vortex lines (antivortex lines; not shown) inherit their properties from 2D vortices (antivortices). For the antivortices the local value of the curl is not zero, but it vanishes when the surface integral is taken (the circulation over circular contours surrounding the core vanishes). ★ As discussed in Sec. III.B.4, polar bubbles can be split into two half-bubble structures featuring $N = \pm 1$ layers using a cylindrical Ising domain wall characterized by $N = 0$. Schematic hopfion illustration from Luk'yanchuk *et al.*, 2020.

additional degree of freedom allows the **n** vectors to escape into the third dimension by rotating around the in-plane–oriented axes [top panels of Fig. 9(b)]. The representation of this transformation in the order-parameter space looks like a contraction of a closed loop on the surface of a sphere [bottom panels of Fig. 9(b)].

The $\mathbb{S}^1$ and $\mathbb{S}^2$ order-parameter spaces are traditionally associated with continuous symmetries. For instance, any 2D rotation of **n** vectors in the XY model does not change the total energy resulting in $\mathcal{X} = \mathbb{S}^1$. However, Prokhorenko, Nahas, and Bellaiche (2017) realized that such $\mathcal{X}$ topologies can emerge even from discrete symmetry groups, as long as local continuous rotations of the dipoles are accessible by thermal fluctuations. This protection mechanism was predicted to

occur in $BaTiO_3$. Owing to the strong cubic anisotropy, local dipoles in $BaTiO_3$ are always preferentially oriented along the $\langle 111 \rangle_{pc}$ directions. However, in the tetragonal and orthorhombic phases, thermal fluctuations are strong enough to allow for continuous rotations between distinct $\langle 111 \rangle_{pc}$ orientations.

In finite systems, the topological defects and solitons can both also be "pushed over the edge," i.e., eliminated at the boundary. The topological protection barrier for the annihilation at the boundary is typically much smaller than the barrier related to the collapse in the bulk. For example, the values of 10 vs 100 meV were reported for magnetic skyrmions (Cortés-Ortuño *et al.*, 2017). For polar bubbles, the bulk collapse is associated with internal energies on the order of 200 meV (Prokhorenko *et al.*, 2023).
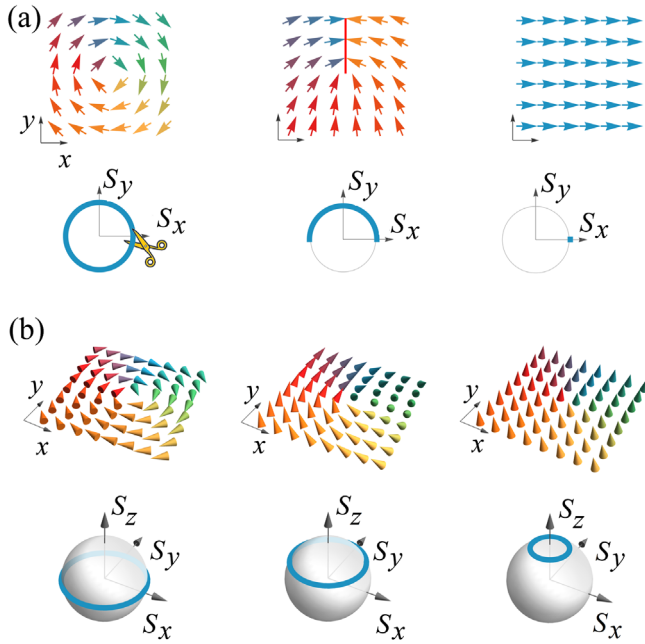
FIG. 9. (a) Unwinding of a vortex in a two-dimensional order-parameter field. In the order-parameter space, a vortex (top left panel) and a perfectly ordered state (top right panel) corresponds to a closed loop (bottom left panel) and a point (bottom right panel), respectively. The transformation between the two states is therefore impossible without making a cut. Such a "surgery" with a consequent contraction of the circular arch creates a midpoint state (middle panels) with a characteristic head-to-head 180° domain wall. (b) Allowing out-of-plane rotations of the order parameter (top subpanels) opens the door to smoothly eliminate a vortex. The order-parameter space representation of such a transformation looks like a contraction of a loop on a sphere (bottom subpanels).

D. Topological-phase transitions

Topological-phase transitions lie beyond spontaneous symmetry-breaking concepts and Landau's classification of transitions. These transitions were introduced by Berezinskii (1972) and Kosterlitz and Thouless (1972) in 1972, leading to their Nobel Prize in 2016. As later discussed, the Berezinskii-Kosterlitz-Thouless (BKT) transition is usually the attribute of two-dimensional systems with short-range interactions and continuous symmetry. While the BKT transition is mediated by a change in the behavior of defects in two-dimensional systems, i.e., the unbinding of a defect-antidefect pair, more general topological transitions are reported whenever not only the ordering or behavior but also the nature of the defects themselves is altered. As discussed, topological protection is lifted whenever the energy injected into the system surmounts the topological energy barrier. As a result, the order-parameter field structure can be profoundly altered, and a transition between topologically distinct phases can set in. In ferroelectrics, for example, varying the screening in ultrathin $Pb(Zr, Ti)O_3$ heterostructures can drive the system from exhibiting a labyrinthine phase to a bubble-skyrmion phase (Zhang *et al.*, 2017), while varying the external electric field, mechanical boundary conditions, or temperature can lead to the destruction of skyrmions (Pereira Gonçalves *et al.*,

2019; Nahas, Prokhorenko *et al.*, 2020; Das *et al.*, 2021; Zhu *et al.*, 2022). Moreover, topological defects can readily compose or decompose, leading to composite or elementary defects, and in some instances can also interact and annihilate. Some examples of such transitions are discussed in Secs. V.C and V.E.2.

To characterize these topological-phase transitions, the *universality principle* is an invaluable tool. This principle focuses on the behavior of the order parameter (or any of its moments) as a function of the external perturbation (temperature, electric field, etc.) close to the critical point where the phase transition takes place. The singular behavior in the vicinity of the critical point is characterized by a set of critical exponents that describe the nonanalyticity of various thermodynamic functions. The equivalence based on the universality principle connects seemingly different systems that share fundamental symmetries but that cannot be straightforwardly mapped onto each other. For instance, when studying the critical properties of the transition in an Ising ferromagnet, one learns about the nature of the liquid-gas transition, and similarly the critical behavior of a superconductor with its complex order parameter falls in the same universality class (identical set of critical exponents) as the two-component (or *XY*) ferromagnet. Many properties are immune to the microscopic details of physical models and their various possible representations, as near the critical point correlations of the order parameter depend only on general features such as (i) the spatial dimension D, (ii) the order-parameter dimension n, (iii) the symmetries, and (iv) the range of the interactions.

These four fundamental features intricately condition the strength of long-range collective excitations, which in turn determine the ordering process. For example, fluctuations are geometrically enhanced in low-dimensional systems, and below a lower critical dimension d_c^- fluctuations obliterate long-range order. In contrast, above an upper critical dimension d_c^+ the mean-field theory appears to be internally consistent. For $d_c^- < D < d_c^+$, although long-range order is not suppressed, the critical behavior in the vicinity of a second-order phase transition, i.e., in the critical regime, departs from mean-field theory. In the case of systems endowed with short-range interactions and continuous symmetry, Landau's theory loses its validity near the transition for dimensions below $d_c^+ = 4$, while long-range order is suppressed at or below $d_c^- = 2$.

In this sense, $D = 2$ stands out as a marginal case that can nevertheless display an *essential phase transition* of a topological nature. The temperature range within which the recently discovered intermediate BKT phase in ultrathin $BaTiO_3$ films decreases with increasing film thickness (Nahas *et al.*, 2017).

1. Mermin-Wagner-Hohenberg theorem

Prior to the discovery of the BKT topological-phase transition, the analysis initiated by Peierls (1935) showed the possible absence of long-range order as a result of the enhanced disordering effect of thermal fluctuations. In this first formalization, Peierls demonstrated that two-dimensional crystalline order is destroyed by the thermal motion of long-wavelength phonons. This conclusion is a particular case of a

more general result known as the Mermin-Wagner-Hohenberg theorem (Mermin and Wagner, 1966; Hohenberg, 1967; Mermin, 1967) [or the Coleman-Weinberg theorem in field theory (Coleman and Weinberg, 1973)]. This theorem was proven by Mermin and Wagner (1966), and independently by Hohenberg (1967). While Mermin and Wagner considered ferromagnetism and antiferromagnetism in one and two dimensions, Hohenberg considered Bose quantum liquids and Cooper pairs in superconductors. Their conclusions were similar and stated that, for a system of $d \leq 2$ with short-range interactions, there cannot be spontaneous continuous symmetry breaking at any finite temperature. Descriptions of the theorem were given by Herbut (2007) and Mudry (2014).

The absence of long-range order in the 2D *XY* case is demonstrated by the fact that the finite-temperature correlation decays to zero at long distances (albeit as a power law), and thus there is no net magnetization in the system. Note that, while the condition on the dimensionality being effectively smaller or equal to 2 is essential for the manifestation of the Mermin-Wagner-Hohenberg theorem and associated topological phenomena such as BKT physics, the ones relating to the range of interactions and symmetry are less stringent.

2. Berezinskii-Kosterlitz-Thouless transitions

As discussed, owing to the Mermin-Wagner theorem, in two-dimensional systems with continuous symmetry and short-range interactions, smooth wavelike fluctuations prevent the formation of long-range order. Rather than a spontaneous symmetry breaking, a topological-phase transition driven by the unbinding of vortex-antivortex pairs can occur, the so-called Berezinskii-Kosterlitz-Thouless (BKT) transition (Berezinskii, 1972; Kosterlitz and Thouless, 1973). Lying beyond Landau classification, it is an infinite-order phase transition (José, 2012) in that the free energy displays an essential singularity; i.e., it remains infinitely differentiable, but nonanalytic at the transition. It is paradigmatically captured by the two-dimensional *XY* model [and its dual 2D Coulomb gas model (Fröhlich and Spencer, 1981)], which has attracted much interest since it astutely describes, among other subjects, two-dimensional melting (Nelson and Halperin, 1979; Young, 1979), the physics of superfluid helium (Bishop and Reppy, 1978), superconductors (Beasley, Mooij, and Orlando, 1979; Hebard and Fiory, 1980; Wolf *et al.*, 1981), Josephson junction arrays (Resnick *et al.*, 1981), nematic liquid crystals (Lammert, Rokhsar, and Toner, 1993), and recently ferroelectrics (Nahas *et al.*, 2017; Villanova, Kumar, and Barraza-Lopez, 2020; Xu *et al.*, 2020; Gómez-Ortiz *et al.*, 2022a).

A crucial feature of the BKT transition in the paradigmatic *XY* model is its intricate relationship with topological defects, namely, vortices and antivortices (Kosterlitz and Thouless, 1973). The seminal heuristic argument of Kosterlitz and Thouless points to a subtle logarithmic competition between the energy and entropy of defects, the balance point of which, marked by T_{BKT}, insulates two different modes of their behavior (Kosterlitz and Thouless, 1973). Below this transition temperature, lone defects are inhibited due to their logarithmically divergent energy with the system size, and hence vortices or antivortices are expected to occur not in
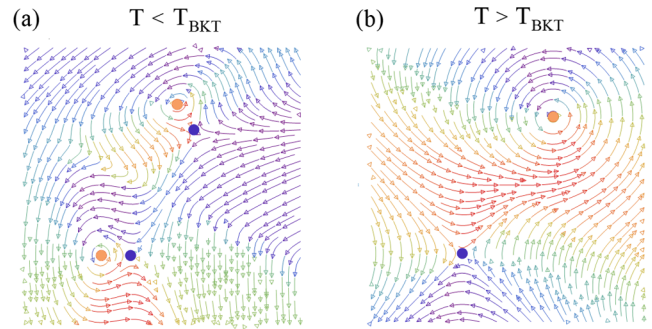

FIG. 10. (a) For $T < T_{BKT}$ tightly bound pairs of vortices [orange (light gray) circles] and antivortices [blue (dark gray) circles] are formed. (b) For $T > T_{BKT}$ the vortex-antivortex pairs unbind.

isolated form but instead within tightly bound vortex-antivortex pairs as local excitations, due to the finite pair energy scaling with its radius rather than with the system size. These bound pairs appear to be topologically neutral from a large-scale perspective, as they confine and mutually cancel their orientational disturbance, thereby allowing for algebraic decay of correlations and quasi–long-range order. Indeed, winding numbers are additive, and the two oppositely charged defects within pairs compensate each other such that the resulting texture can be immersed in a uniform background (Fig. 10), yielding a power-law decay of dipolar correlations. As the temperature is raised, the number of pairs increases and larger ones start forming, screened by other smaller pairs that lie in between. The average separation between a vortex and an antivortex becomes comparable to the separation between pairs. These loose pairs thus effectively unbind at T_{BKT}, whereupon entropy balances the interaction, allowing for single topological defects to wander in the system and causing correlations to decay exponentially in the high-temperature disordered phase. While a large chemical potential supports a dilute phase of defect pairs, for higher temperatures a smaller chemical potential is expected, as it becomes thermally easier to create many pairs (the presence of which decreases the free energy by increasing the entropy), leading to increased screening and effective dissociation when the paraelectric phase is reached. This phase transition is characterized by the onset of out-of-equilibrium dynamics and ergodicity breaking, with dynamical annihilation and generation of defects.

One of the features reflecting the particularity of the BKT phase transition thus lies in the quasi–long-range order that it can sustain at low enough temperatures. This quasi–long-range–ordered phase is characterized by the slow algebraic decay of the order-parameter correlation function and its continuously varying critical exponent η (Kosterlitz and Thouless, 1973). The power-law falloff of the correlation function arises from the logarithmic growth of angular fluctuations, which is specific to two dimensions and is similar to that of an isolated critical point while not being confined to a single temperature. The BKT phase can thus be regarded as a phase consisting of critical points, distinct from the high-temperature disordered phase with rapid exponential decay of the correlation function, while being weaker than a truly long-range–ordered one.

Note that crystalline solids can also exhibit BKT physics. While in $d \geq 3$ melting is a first-order phase transition between crystal and liquid, in $d = 2$ the mechanisms for melting and the transition from the solid state [with only quasi–long-range translational order, which is consistent with the Peierls argument (Peierls, 1935) and the Mermin-Wagner theorem, and long-range orientational order] to liquid (with both short-range translational and orientational order) involve topological defects. Crystalline solids can have two types of topological defects characterized by closed loops (point defects in two dimensions or line defects in three dimensions), known as dislocations and disclinations, associated with translational and rotational symmetry breaking, respectively. The dislocation has a vector-valued topological charge called the Burgers vector and can be thought of as a row of misaligned atomic bonds within an otherwise regular lattice. The energy of the dislocation scales as the modulus of this vector squared. The disclination is characterized by an angle corresponding to a wedge of superfluous or deficient material. In the late 1970s Halperin and Nelson (1978) and Young (1979) suggested a two-step melting scenario in two dimensions. The unbinding of dislocation pairs at a temperature T_m causes the system to lose the quasi–long-range translational order, while a quasi–long-range orientational order survives. In this anisotropic liquid phase (also known as the *hexatic* phase), there is a rapid exponential decay of translational correlations but only a slow, algebraic decay of orientational correlations. At a temperature $T_i > T_m$ another phase transition of BKT type, where the disclination pairs that make up the dislocations unbind, drives the anisotropic fluid phase to melt into a true isotropic liquid with neither positional nor orientational order. Thus, free dislocations should appear only once the solid is melted into the anisotropic liquid phase, whereas free disclinations should be excited across the anisotropic liquid–isotropic liquid melting.

The situation described by the 2D XY model conventionally applies only to two-dimensional degenerate systems with local interaction and is scarcely met in experiments involving ferroelectric systems. In these systems, the presence of a dipole-dipole interaction, nonlocal in nature, significantly reduces fluctuations, thereby altering the low-temperature properties of the XY model (Maier and Schwabl, 2004). Indeed, it is well known that the dipolar interaction tends to stabilize the long-range order against thermal fluctuations, and the ground state may thus be spontaneously polarized (Maleev, 1976; Maier and Schwabl, 2004) or may acquire various structures. However, while the low-temperature properties substantially depend on the dipolar interaction, at higher temperatures this interaction is of lesser significance (Feigelman, 1979), and its contribution has been demonstrated to be irrelevant in the treatment of the dipolar XY model (Maier and Schwabl, 2004; Vasiliev *et al.*, 2014), in which the characteristic logarithmic interaction of defects within a pair was shown to be restored.

Anisotropic variants of the XY model can also be evoked to assess systems that are subject to symmetry-breaking crystalline fields, such as those at play in ferroelectrics, in addition to isotropic coupling (Maleev, 1976; Maier and Schwabl, 2004), and those that lie in between the limiting cases of the XY model and the p-state clock model. Within the last model,

the spins are restricted to two dimensions and can point along p directions distributed uniformly. Ortiz, Cobanera, and Nussinov (2012) showed how if $p \leq 4$ only a second-order phase transition between the ordered and the disordered phase as a function of temperature can be observed. However, for $p \geq 5$ there exists an intermediate phase separating the ferromagnetic and paramagnetic ones characterized by its BKT behavior (Ortiz, Cobanera, and Nussinov, 2012).

The discovery of BKT physics in ferroelectrics was demonstrated through effective Hamiltonian simulations and a finite-size-scaling analysis of $BaTiO_3$ ultrathin films subjected to tensile strain (Nahas *et al.*, 2017) for a narrow temperature region being located between the ferroelectric and paraelectric phases. Owing to an effectively reduced spatial dimensionality and a lesser number of dominant contributing polarization components, the transitional region of tensile strained $BaTiO_3$ ultrathin films is enhanced into a critical phase exhibiting BKT features. Indeed, owing to tensile strain, local dipole moments are confined to the film plane, and thus polarization can be regarded as a two-component order parameter. Moreover, while the fourfold anisotropy is relatively irrelevant in the intermediate critical BKT phase where the two-dimensional XY model properties are recovered and a quasicontinuous symmetry is observed, it reasserts itself by suppressing fluctuations and restoring the fourfold rotational symmetry at low temperatures. In contrast to short-range isotropic systems, the anisotropic dipolar interactions ineluctably drive ferroelectric long-range order at low temperatures. This endows the system with a three-phase structure: a truly ordered ferroelectric phase, a quasi–long-range–ordered phase substantiated by an algebraic decay of spatial correlations and supported by an emergent continuous symmetry that allows for stable topological defects to condense in the distortion-confining form of vortex-antivortex bound pairs, and a disordered, paraelectric phase with exponentially falling correlations. A BKT phase was then further numerically suggested in another two-dimensional ferroelectric system, namely, one made of one-unit-cell-thick SnTe, with epitaxial strain allowing the control of the BKT stability temperature region and even possibly making it the ground state (Xu *et al.*, 2020), or in $PbTiO_3/SrTiO_3$ superlattices under tensile strain (Gómez-Ortiz *et al.*, 2022a). Vortex-antivortex pairs have also been reported in one-unit-cell-thick SnSe films from molecular dynamics simulations (Villanova, Kumar, and Barraza-Lopez, 2020).

E. Spins versus electric dipoles: Differences and analogies at the level of the topological properties

Localized spins in magnetic crystals most often have a fixed magnitude. For this reason, spin patterns are intrinsically nonlinear fields and are likely to exhibit stable topological solitons (Manton and Sutcliffe, 2004). In contrast, the amplitude of polar displacements is not restricted. However, from this perspective, spin and dipole fields can still be seen as topologically equivalent when vanishing electric dipoles are unlikely to occur. Indeed, the latter assumption allows each electric dipole to be continuously normalized (Toulouse and Kléman, 1976; Gómez-Ortiz, 2018) and the polar pattern to be treated as a distribution of spins.

More substantial differences come into play once symmetries are taken into account. Spin rotations and polar displacements are governed by interactions of a distinct physical nature. Because of this, restrictions on possible values (such as order-parameter spaces) of spin and electric dipoles can drastically differ. For instance, magnets often exhibit continuous rotational symmetries, while in bulk ferroelectrics dipoles tend to align only along a few preferred crystallographic directions. In other words, the role of crystalline anisotropy is much more pronounced in ferroelectrics. Owing to such orientational rigidity, the order-parameter space of polar materials might seem to have a finite set topology [such as Ising or Potts models; see Fig. 2(a)], which explains the long-lasting belief of domain walls being the only possible polar topologies.

However, even this consideration does not prevent the existence of nontrivial polar counterparts of magnetic-topological patterns. For instance, the underlying quasicontinuous symmetries enabled the prediction of polar-vortex lines [Fig. 2(e)] in improper ferroelectrics in the late 1980s (Tagantsev and Sonin, 1989). In improper crystals the magnitude of the order parameter is small, which diminishes the role of higher-order energy terms responsible for orientational anisotropy. As a consequence, the domain-wall vertices (Fig. 4) start behaving much like vortex lines, albeit the symmetry stays formally discrete: hence the term quasicontinuous symmetry (Tagantsev and Sonin, 1989).

Moreover, quasicontinuous symmetries emerging in the vicinity of the critical temperature in both improper (Griffin *et al.*, 2012; Artyukhin *et al.*, 2014; Lin *et al.*, 2014) and proper ferroelectrics (Nahas *et al.*, 2017; Xu *et al.*, 2020) were found to be responsible for nontrivial topological transitions. Spinlike point and line topological defects and solitons were predicted to exist even in symmetry-broken phases of bulk ferroelectrics (Nahas *et al.*, 2015; Stepkova, Marton, and Hlinka, 2015; Prokhorenko, Nahas, and Bellaiche, 2017), and a novel topological protection mechanism in proper ferroelectrics was proposed (Prokhorenko, Nahas, and Bellaiche, 2017). These works demonstrated that the constraints imposed by the symmetry of the Hamiltonian on the possible values of local dipoles do not restrict (Prokhorenko, Nahas, and Bellaiche, 2017) the topology of the order-parameter space if one follows the original theory by Toulouse and Kléman (1976).

Currently the theory of topological patterns in low-dimensional ferroelectrics is at an early development stage. Recent works suggest that the origin of topological patterns in these systems can instead be linked to topologies emerging in the flows of incompressible fluids (Luk'yanchuk *et al.*, 2020) and phase separation processes (Nahas, Prokhorenko *et al.*, 2020). The former approach is based on the natural tendency of ferroelectric materials to avoid bound charges $\sim \nabla \cdot \mathbf{P}$, thereby making polarization patterns akin to divergence-free flows (Luk'yanchuk *et al.*, 2020). The discovery of this analogy opens a door to build upon a well developed theory of topological hydrodynamics (Arnold and Khesin, 1998). The analogy with separation kinetics (Nahas, Prokhorenko *et al.*, 2020) concerns the arrays of vortex-antivortex lines [Fig. 2(e)] (also refered to as nanostripe domains) in partially screened $Pb(Zr, Ti)O_3$ films and their relation to merons, bimerons, and

bubble arrays [Fig. 7(a)]. It rests on the order-parameter conservation driven by the depolarition field and allows one to make a link of polar topologies with a large family of Turing patterns (Turing, 1952).

F. Relationship with related topological properties in other fields

One of the beauties of topology is that, once a given problem is expressed in its language, unexpected bridges with other *a priori* unrelated fields can be discovered. One example is the case of skyrmion quasiparticles, which were named after the British nuclear physicist Tony Skyrme. He developed a nonlinear field theory for interacting pions in the 1960s and showed that topologically stable field configurations occur as particlelike solutions that can be modeled as topological solitons (Skyrme, 1961). It is surprising how, despite the fact that there are orders of magnitude of difference in the typical energy scales between nuclear physics and condensed-matter physics, the underlying theories can be transposed between the two fields.

This is not an isolated case. As summarized by Nobel laureate F. Wilczek in his review "Particle physics and condensed matter: The saga continues" (Wilczek, 2016), many ideas from quantum field theory and topology (spontaneous symmetry breaking, gauge structures, etc.) have proved to be fertile in suggesting new phenomena in the quantum physics of condensed matter. And reciprocally other concepts like quasiparticles or superconductivity made their way in the opposite direction.

During the last decade, topological analyses of band structures have played a primary role. Links with mathematical concepts related with geometric phases (Berry phases, Berry curvatures, Chern numbers, etc.) readily apply. Some physical observables (such as the anomalous Hall conductivity in a 2D insulator) in systems that have a topological character are quantized. See Vanderbilt (2018) for more details. One difference between this theory and the topic of this review is that the parameter space in electronic-structure theory is in the *reciprocal space* (wave vector $\mathbf{k}$ and the corresponding occupied Bloch functions). The topological nature of the problem emerges because the first Brillouin zone can be regarded as a closed manifold, so closed paths can be defined within it. The *Chern number* can be defined from the surface integral over the surface of the first Brillouin zone of the Berry curvature of a given band. This Chern number or Chern index of the surface can be regarded as a topological index attached to the manifold of states defined on the surface.

It can be proved that the skyrmion number of a magnetic skyrmion exactly corresponds to the Chern number, bridging the topology of the band structure with the nontrivial swirling of the spins. Assume a spin $1/2$ particle whose wave function can be described by a spinor under the effect of an external magnetic field whose direction is determined by an unitary vector $\hat{n}$. If the corresponding interacting Hamiltonian is diagonalized, then the Berry curvatures computed from the eigenstates are formally equivalent to the Pontryagin density, whose integral is the skyrmion number (Nagaosa and Tokura, 2013; Gómez-Ortiz, 2018).

In the case of polar skyrmions, we can define similar topological indices as in their magnetic counterparts (vorticities, skyrmion numbers, etc.). Despite these similarities, there

are also differences: in the case of polar nontrivial textures, the local dipoles are defined in real space, and it is not certain that we can define a quantum mechanical (2×2) Hamiltonian that can be diagonalized, as happened with the case of magnetic skyrmions.

Links can also be established with fluid mechanics, where physical quantities such as vorticities and helicities are naturally defined (Moffatt and Ricca, 1992). However, in this case, these characteristics are related to flux tubes defined from movements of the particles within the liquid, and therefore with their velocities. Here again the mathematical formulation is similar, allowing an easy exchange of ideas for cross-fertilization. But we have to keep in mind that the nature of our polarization profile is static; i.e., neither the nuclei nor the electrons are free to move within our insulating materials.

Melting and dislocations in 2D crystals, or disclinations in the previously discussed 2D liquid crystals, have also shown topological BKT transitions like the ones described in Sec. III.D.2. As in Sec. VI, the same kind of hexatic phases and phases transitions are expected in the polar-skyrmionic materials.

IV. PHYSICAL INGREDIENTS TO DEVELOP TOPOLOGICAL PHASES IN POLAR SYSTEMS

A. Electrostatic interactions

Electrostatics is the most important driving force behind the formation of nontrivial topological phases in polar oxides. More precisely the requirement to minimize the electrostatic energy cost associated with the depolarization fields arising from any discontinuity (divergence) of the polarization. This depolarization field depends on several factors, such as the dimensionality and the characteristic size of the system, the polarizability of the surrounding medium (typically a dielectric in the case of nanocomposites or ferroelectric-dielectric superlattices), the periodicity (in the case of superlattices), or the electrostatic boundary conditions (from open circuit to short circuit), whose control is essential for the stabilization of the novel topological phases.

1. Formation of nanodomains

It is well known from elementary electrostatics that the bound charge density in the presence of a spatially varying polarization field is given by $\rho_{\text{bound}}(\mathbf{r}) = -\boldsymbol{\nabla} \cdot \mathbf{P}(\mathbf{r})$, where $\rho_{\text{bound}}(\mathbf{r})$ and $\mathbf{P}(\mathbf{r})$ are fields coarse grained over a length scale much larger than a lattice constant. In the case of a free insulating surface in a nanoparticle or thin film, the surface normal component of the polarization leads to a surface bound charge given by $\sigma_{\text{bound}} = \mathbf{P} \cdot \hat{\mathbf{n}}$, where $\hat{\mathbf{n}}$ is the unitary vector normal to the surface [Fig. 11(a)]. These classical concepts were firmly routed in the modern theory of polarization (used in most first-principles codes) by Vanderbilt and King-Smith (1993) and Resta and Vanderbilt (2007). These bound polarization charges are responsible for the appearance of large depolarization fields $\mathbf{E}_{\text{dep}}$. The electrostatic energy resulting from the coupling of the polarization and the depolarization field is generally strong enough to suppress the polarization completely in the usual proper ferroelectrics driven by the softening of a transverse-optic mode. This energy has to be reduced in one of a number of ways if the polar state is to be preserved (Wurfel, Batra, and Jacobs, 1973). As shown in Fig. 11(b), one of the possible mechanisms is the formation of domains (Catalan *et al.*, 2012): small spatial regions with different polarities separated by a boundary, referred to as the domain wall, that in ferroelectrics is narrow (typical widths of the order of the lattice constant). Opposite polarized domains lead to overall charge neutrality at the surfaces, reducing the depolarization field and the associated electrostatic energy. However, the formation of domains is not for free, since the modification of the short-range interactions resulting from the change of the dipole moments when passing through a domain wall give rise to an energy cost known as *domain-wall energy*, introduced in phenomenological models through a *gradient energy* term. The delicate balance between the electrostatic and gradient energies at the domain wall yields Landau-Kittel's scaling law in systems with straight-walled domains, which states that the width of the domains scales as the square root of the thickness of the film (Lines and Glass, 1977; Catalan *et al.*, 2012), so they can be of the order of a few nanometers. As a result, 180° stripe domains are formed in which the polarization forms a transverse wave with alternating signs between adjacent lamella. As shown in Sec. III, these domain walls can be thought of as 2D topological defects. For simplicity, here we have focused on planar domain walls. However, other morphologies of nanoscale domains in ferroelectrics are possible (Hlinka and Ondrejkovic, 2019), including needles, small
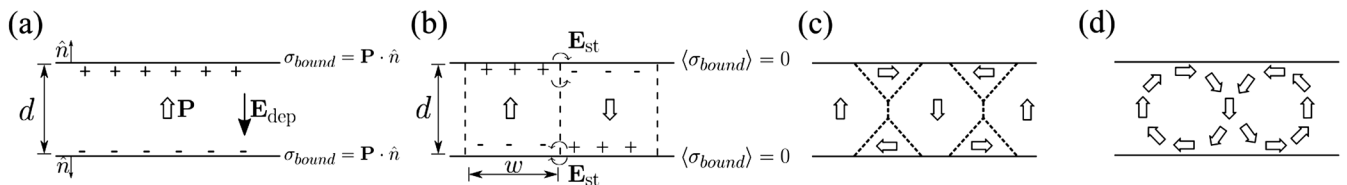
FIG. 11. Formation of nanodomains in ferroelectric thin films under open-circuit boundary conditions. (a) Uniformly polarized ferroelectric of thickness d. The normal component of the polarization gives rise to surface polarization charges $\sigma_{\text{bound}} = \mathbf{P} \cdot \hat{\boldsymbol{n}}$, where $\hat{\boldsymbol{n}}$ is the unitary vector perpendicular to the surface. These polarization charges generate a depolarization field $\mathbf{E}_{\text{dep}}$. (b) One way to screen the depolarization energy is the formation of stripe domains: regions with different orientations of spontaneous polarization. w stands for the width of the domain, which according to Landau-Kittel's law scales as $w \propto d^{1/2}$. (c) To further screen the stray field $\mathbf{E}_{\text{st}}$, 90° domain walls are formed at the near-surface shell, yielding flux-closure domains or (d) vortices depending on the thickness d. In the vortices the polarization continuously rotates, in contrast to the flux-closure domains, where at some regions 180° domain walls between the up and down domains are present.

domains of cylindrical shape (equivalent to the so-called bubble domains in ferromagnets), and laterally confined domains of a nanoscale ball shape.

Although under these conditions the depolarization field is drastically reduced in the interior of the domains, some stray field components are still present near its surface. The first calculations of the emergent stray fields in ferroelectric domains were done on the basis of the Kittel model by Bratkovsky and Levanyuk (2000, 2001, 2009), and then within the more exact Ginzburg-Landau model by De Guerville *et al.* (2005) and Luk'yanchuk, Lahoche, and Sené (2009). These stray fields are large enough to overcome the energy cost associated with the large crystalline anisotropy in ferroelectrics, where the primary order parameter (the polarization) is strongly coupled to the lattice. Therefore, despite the large cost in polarization gradient, polarization anisotropy, and elastic energy, in order to minimize the electrostatic energy the near-surface shell is polarized in the direction perpendicular to the one determined by the domains [Fig. 11(c)], forming 90° domain walls still preserving the constraint that the normal component of the polarization should be continuous across the boundary so that no net charge is present. This is a stronger condition than the one imposed for the straight 180° domains, and it comes from the fact that the polarization charges (i.e., the divergence of the polarization) have to vanish to minimize electrostatic energies (De Guerville *et al.*, 2005; Luk'yanchuk, Lahoche, and Sené, 2009). The polar flux-closure configuration plotted in Fig. 11(c) contains multiple short segmented 90° and 180° domain walls with mutual interactions. The pronounced Néel character in the vicinity of the domain-wall interface terminations leads to domain broadening (De Guerville *et al.*, 2005; Stephenson and Elder, 2006; Eliseev *et al.*, 2009). The structure is similar to the closure domains proposed by Landau and Lifshitz (1935) and Kittel (1946) for magnetic systems. Nevertheless, keep in mind that narrow 90° domains should be unfavorable due to the large anisotropy energy in ferroelectric materials. This is especially relevant if the system is grown under compressive strain epitaxial conditions. A progressive rotation of the polarization to minimize the anisotropy energy is expected, forming the arc-shaped rotation of the polarization vector at the domain wall between the up and down domains, forming the vortex shown in Fig. 11(d). In summary, the different panels in Fig. 11 show how ideal Ising domains [Fig. 11(b)] in a hypothetical model system could be gradually turned into vortex arrays [Fig. 11(d)] by tweaking various interactions. Note that in the original theoretical prediction of vortices in ultrathin PZT films (Kornev, Fu, and Bellaiche, 2004), vortex arrays in PZT are referred to as "nanostripes," which underlines the relationship between the two structures. Moreover, Nahas *et al.* (2020) and Nahas, Prokhorenko *et al.* (2020) referred to the vortex structures in Fig. 11(d) as stripe domains.

Here it is noteworthy how atomistic simulations based on first principles have been used to verify Landau-Kittel's law in (001) Pb(Zr, Ti)O$_3$ (Lai *et al.*, 2007a), in multiferroic BiFeO$_3$ ultrathin films (Prosandeev, Lisenkov, and Bellaiche, 2010), and in PbTiO$_3$/SrTiO$_3$ superlattices (Gómez-Ortiz *et al.*, 2023). This law was found to be valid for thicknesses above 1.6 nm (more than four unit cells), even in the presence of a vortexlike dipole arrangement near the domain walls and a
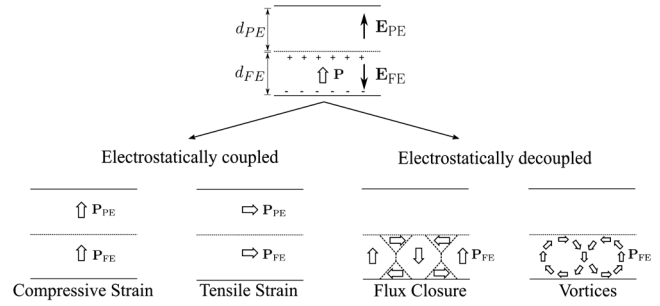

FIG. 12. Different regimes for the polarization coupling in a ferroelectric-dielectric interface. For a sufficiently thin ratio of the dielectric layer with respect to the ferroelectric (left panels) and under compressive epitaxial strain, the dielectric is expected to polarize with nearly the same spontaneous out-of-plane polarization as the ferroelectric layer, resulting in a roughly homogeneous polarization throughout the structure. The two layers are said to be electrostatically coupled. Under tensile epitaxial strain, the polarization might rotate to in plane. For a thick enough layer of the dielectric, the polarization is confined within the ferroelectric layer, breaking into domains to minimize the electrostatic energy (right panels). The two layers are said to be electrostatically decoupled. Depending on the thickness of the ferroelectric, the local polarization can rotate continuously to impose a vanishing divergence of the polarization (vortices) or a 180° domain might appear at the central layers of the ferroelectric (flux-closure domains).

substantial proportion of in-plane surface dipoles. Below 1.2 nm (fewer than three unit cells), the domains disappeared. In BiFeO$_3$, the interactions between the tilting of oxygen octahedra around the domain walls and magnetoelectric coupling near the surface (and away from the domain walls) play an important role in the observance of this law in multiferroic films. Moreover, an unusual pattern consisting of an array of vortices at the surfaces was found in these simulations. This pattern was later experimentally confirmed (Nelson *et al.*, 2011; Mundy *et al.*, 2022). A Ginzburg-Landau free-energy model including the full electrostatic expression (Bennett, Muñoz Basagoiti, and Artacho, 2020) suggested that Landau-Kittel's law is verified for large enough values of the thickness of the ferroelectric layer. But the thinner the ferroelectric, the smaller the width of the domains, which reach a minimum and then diverge to a monodomain phase. The model assumes infinitely thin domain walls, and therefore is not expected to be reliable for film thickness in the nanometer scale.

2. Role of periodicity in superlattices

Although the previous reasoning is valid for nanoparticles or thin films with free surfaces, it can be trivially generalized to the case of insulating interfaces, such as those present in ferroelectric-dielectric superlattices. In this case, the difference in the interface-normal components of the polarization leads to an interface bound charge given by $\sigma_{\text{bound}} = (\mathbf{P}_2 - \mathbf{P}_1) \cdot \hat{\mathbf{n}}$. Therefore, any discontinuity in the polarization will give rise to strong electric fields that tend to both suppress the polarization in the ferroelectric layers $\mathbf{E}_{\text{FE}}$ and polarize the dielectric layers $\mathbf{E}_{\text{PE}}$ (Bousquet, Junquera, and Ghosez, 2010). The electrostatic energy cost associated

with these fields is large, and thus the system will look for a more favorable ground state.

For short enough periodicities, one possibility is to adopt a state of quasiuniform, out-of-plane polarization throughout the structure whereby the dielectric layers become polarized (left panels of Fig. 12). In this case the two materials are "electrostatically coupled." The value of the polarization will depend only on the relative fraction of the ferroelectric material (Dawber *et al.*, 2007) and the mechanical boundary conditions. Alternatively, as discussed in Sec. IV.B, under tensile strain epitaxial conditions for such short-period superlattices, the net polarization can rotate to the plane within the ferroelectric layers, thereby forming a_1/a_2 domains.

As the individual layers become thicker, however, domain formation becomes a more effective mechanism for eliminating the depolarization fields and lowering the total energy of the superlattice (right panels of Fig. 12). The polarization is confined mainly to the ferroelectric layers, with domains of opposite polarization screening the depolarization field. The ferroelectric and the dielectric are "electrostatically decoupled" in this case. At relative large length scales, the balance between electrostatic and domain-wall energy results in the formation of classical flux-closure domain patterns. The period of the closure quadrant array might differ from that in Kittel's law [for instance, Tang *et al.* (2015) had it as linearly dependent on the thickness of the $PbTiO_3$ layer, with a slope equal to $\sqrt{2}$]. At intermediate length scales, such superlattices are the perfect background for the appearance of clockwise-counterclockwise vortices confined within the ferroelectric layer, where the local polarization continuously rotates. The transition from strong to weak interlayer coupling and the associated changes in the domain structure as a function of the periodicity were first quantitatively described in $KNbO_3/KTaO_3$ strained-layer superlattices by Stephanovich, Luk'yanchuk, and Karkut (2003) and Stephanovich, Luk'yanchuk, and Karkut (2005) and were later experimentally studied in $PbTiO_3/SrTiO_3$ superlattices by Zubko *et al.* (2012), by Lisenkov and Bellaiche (2007) from first-principles-based effective Hamiltonians, by Aguado-Puente and Junquera (2012) from first principles, and by Hong *et al.* (2017) from phase-field modeling, as shown in Fig. 13. The phase transition from the coupled nanostripes to the monodomain phase as a function of dc and ac electric fields applied on long-period $BaTiO_3/SrTiO_3$ superlattices has also been studied using effective Hamiltonian methods (Lisenkov, Ponomareva, and Bellaiche, 2009).

Controlling the thickness ratio between adjacent $PbTiO_3$ layers is important for controlling the configurations of flux-closure array in $PbTiO_3/SrTiO_3$ superlattices. When the $PbTiO_3$ thickness is fixed in the multilayer (the thickness ratio of the adjacent $PbTiO_3$ layers is 1), a periodic V-type flux-closure array (with 180° domain walls perpendicular to the interfaces) is observed in each $PbTiO_3$ layer. When the thickness ratio of adjacent $PbTiO_3$ layers ranges from 0.4 to 0.7, a periodic V-type flux-closure array is identified in the thicker $PbTiO_3$ layer and a horizontal H-type flux-closure array (with 180° domain walls parallel to the interfaces) is found in the thinner $PbTiO_3$ layer (Liu, Wang *et al.*, 2017).
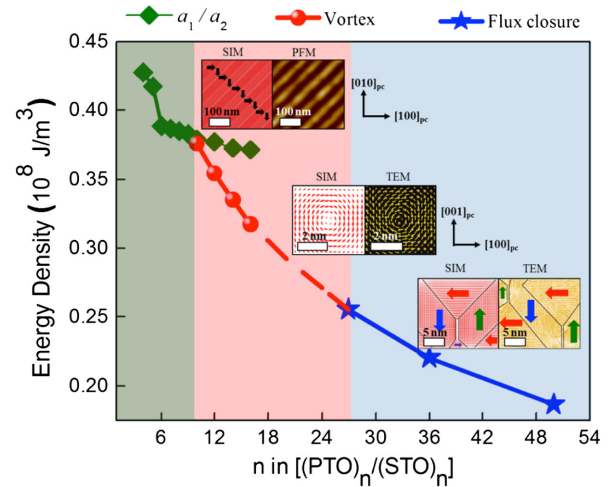

FIG. 13. Phase diagram and total energy density for the $(PbTiO_3)_n/(SrTiO_3)_n$ superlattice grown on the $DyScO_3$ substrate, as calculated using the phase-field simulations and verified experimentally. Top left inset: simulation and planar STEM result of an in-plane view of the a_1/a_2 twin-domain structure for $n = 6$. Middle left and right insets: vortex structures for $n = 10$ from simulation and experimental TEM mapping, respectively. Bottom left and right insets: cross sections of flux-closure structure for $n = 50$ from phase-field simulation and experimental TEM vector mapping, respectively. SIM, simulation; TEM, transmission electron microscopy. From Hong *et al.*, 2017.

Finally, note that, due to the incomplete screening of the depolarization fields, periodic arrays of flux-closure domains can form in ferroelectric thin films with symmetric electrodes, as theoretically predicted by first principles (Aguado-Puente and Junquera, 2008) and as experimentally observed (S. Li *et al.*, 2017). This has an influence on the formation of supercrystals described in Sec. V.A.7.

B. Elastic interactions

Coupling between polar and lattice degrees of freedom is known to be strong in ferroelectric perovskites. In cubic perovskites, the ferroelectric phase transition not only involves the condensation of a spontaneous polarization but also is accompanied by the appearance of a macroscopic strain, i.e., a spontaneous lattice distortion. This polarization-strain coupling is at the origin of the large piezoelectric properties of the polar phases, a property that is fundamental to the PFM techniques discussed in Sec. I.A.3 of the Supplemental Material (472) and in a wide range of applications (such as refocusing the Hubble telescope and 3D ultrasound imaging and sonar). More broadly it also reflects a strong sensitivity of ferroelectricity to mechanical boundary conditions, unlike in ferromagnets.

There are different pathways to apply strain to a ferroelectric film. The advent of advanced synthesis techniques, which is reviewed in detail in Sec. I.A.1 of the Supplemental Material (472), opens the door for the fabrication of high-quality oxide heterostructures with control at the atomic scale. Single-crystal perovskite oxides can currently be grown fully coherently, with a low density of threading dislocations.

Substrates that are chemically and structurally compatible with perovskites can be prepared with a controlled termination and a small roughness (atomically flat on terraces that are hundredths of nanometers wide). In these high-crystalline-quality heterostructures, the thin films are coherently matched to the substrate; that is, the epilayers are forced to grow with the same in-plane symmetry and lattice constant as the underlying substrate, even if this may not be their most stable phase in the bulk. The lattice constants of commercial substrates span a range that would allow both compressive and tensile biaxial strains of typical perovskite thin films [such as $BaTiO_3$, $PbTiO_3$, $Pb(Zr, Ti)O_3$, and $SrTiO_3$]. On top of the epitaxial strain imposed by the substrate, there are other sources of strain, such as the different thermal expansion coefficients between the film and the substrate or the presence of crystalline defects that give rise to inhomogeneous strain fields.

The functional properties of a thin film clamped to a substrate but free to relax in the out-of-plane direction may dramatically change as a result of the biaxial strain imposed by the substrates. Indeed, *strain engineering* of ferroelectric properties has become a powerful generic concept (Rabe, 2005; Schlom *et al.*, 2007, 2014). Experimentally, it has been shown how the physical quantities can be tuned to a desired value by controlling the lattice mismatch between a ferroelectric film and its substrate, providing an alternative to the traditional substitution and alloying of the *A* and *B* cations ("chemical pressure"). Strain engineering has its limitations since epitaxial strain will be preserved only up to a critical film thickness beyond which misfit dislocations or twins form.

Large shifts in the paraelectric-to-ferroelectric phase transition temperature have been reported for $BaTiO_3$ grown on $GdScO_3$ and $DyScO_3$ substrates (Choi *et al.*, 2004). Similar enhancements of the transition temperature have been observed for $PbTiO_3$ thin films grown on insulating (001)-oriented $SrTiO_3$ substrates (Streiffer *et al.*, 2002). As discussed in Sec. V, this will have an impact on the stabilization of the topological phases in higher temperature regimes. Furthermore, new phases not present in the bulk phase diagram might be stabilized. For instance, a spontaneous polarization can be induced by strain in $SrTiO_3$ at room temperature, whose bulk, pure, unstressed form remains paraelectric down to 0 K (although it is considered an incipient ferroelectric) (Haeni *et al.*, 2004).

Assuming a single, homogeneous domain state, and as a general rule for the usual bulk perovskites on a (001) substrate, sufficiently large epitaxial compressive (tensile) strains will favor a ferroelectric *c* phase (*aa* phase) with out-of-plane (in-plane) polarization, together with a concomitant enhancement (shrinking) of the out-of-plane lattice constant. Distinct behaviors are predicted for the different compounds in the intermediate regime, but the most typical one is a continuous polarization rotation from out of plane to in plane (Kornev, Fu, and Bellaiche, 2004). If the ferroelectric thin film is allowed to form domains, then ferroelastic 90° domain walls, in either $c/a/c/a$ (where *c* and *a* are the out-of-plane- and in-plane-oriented domains, respectively) or $a_1/a_2/a_1/a_2$ (where a_1 and a_2 are in-plane, orthogonally oriented domains), can be stabilized by means of epitaxial strain engineering. This fact will have a profound impact on the phase diagrams of topological phases in ferroelectric-dielectric superlattices. For the same periodicity and under the same electrostatic
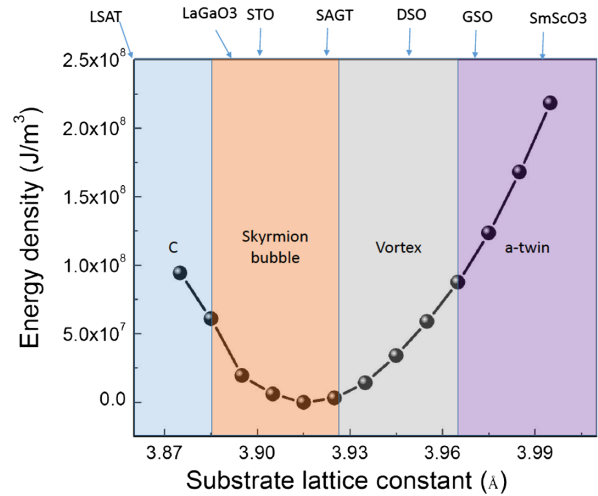

FIG. 14. Phase diagram of a $(PbTiO_3)_{16}/(SrTiO_3)_{16}$ super-lattice under short-circuit electrical boundary conditions obtained from phase-field simulations, as described in Sec. I.B.3 of the Supplemental Material (472). For a particular value of the in-plane lattice constant, three independent calculations were carried out, starting with a random configuration of the local polarization. After a minimization of the energy, the three calculations converged to a similar ground state. The "*a*-twin" phase corresponds to the a_1/a_2 domain structure. In the top *x* axis, the lattice constants of some of the available commercial substrates are represented. LSAT, $(LaAlO_3)_{0.29}$-$(SrAl_{0.5}Ta_{0.5}O_3)_{0.71}$; STO, $SrTiO_3$; SAGT, $Sr_{1.04}Al_{0.12}Ga_{0.35}Ta_{0.50}O_3$; DSO, $DyScO_3$; GSO, $GdScO_3$. Courtesy of Z. Hong.

boundary conditions, different phases can be found by changing the biaxial strain: from the tetragonal *c* phase to skyrmions, vortices, and finally a_1/a_2 ferroelectric twin boundary phases when the lattice constant is increased from compressive to tensile strains, as shown in the phase diagram obtained with phase-field methods in Fig. 14.

The evolution of flux-closure domain arrays in $PbTiO_3/SrTiO_3$ superlattices with misfit strain was studied by Li *et al.* (2019). Reversible phase transitions can be induced in $PbTiO_3/SrTiO_3$ superlattices by mechanical forces, such as a compressive stress stimulation via a scanning probe tip used as an indenter, that causes a transition from the vortex to the *a*-domain phase with polarization in plane (P. Chen *et al.*, 2020) that might coexist with the tetragonal *c* phase in *a/c* domains (Li *et al.*, 2020). Moreover, as discussed in Sec. V.E.2, epitaxial strain also plays a role in the competition and transition from skyrmion to meron lattices (Wang *et al.*, 2020).

Like piezoelectricity, flexoelectricity is an important coupling property (Stengel and Vanderbilt, 2016). While the former describes the linear coupling between electric polarization and homogeneous strain and arises only in noncentrosymmetric materials, the latter relates to the linear coupling between electric polarization and a strain gradient and is always symmetry allowed. Flexoelectric effects may be large in thin films, where large strain gradients, far exceeding those possibly accommodated in bulk phases, can arise. Flexoelectricity's effect is expected to be particularly strong in the polar-vortex topology since it inherently hosts a set of

large, correlated strain and polarization gradients (Shimada *et al.*, 2021). The nontrivial role of flexoelectricity in the generation of emergent complex polarization morphologies was discussed by Q. Li *et al.* (2017), whose experimental images showed good agreement with phase-field simulations once the longitudinal and shear flexoelectric coefficients of the $PbTiO_3$ layers are activated. In addition, the influence of the shear component of the flexoelectric tensor of $PbTiO_3$ on the shear strain at domain walls in $PbTiO_3$ flux-closure quadrants in tensile strained was analyzed by Tang *et al.* (2015). The interplay between the inhomogeneous strain present at atomic steps on the substrate of a ferroelastic thin film and twin walls were proposed to be the source of half vortices due to flexoelectric effects (Lu *et al.*, 2021). These can be closed by mobile half vortices generated by the interaction of an atomic force microscopy (AFM) tip with the upper surface of the thin film, whose position is controlled by the movement of the tip. The dynamic change of the polar structures underneath the AFM tip would produce displacement currents and weak magnetic fields. The role of inhomogeneous strain and strain gradients produced by surface trenches in $PbTiO_3/SrTiO_3$ superlattices has been analyzed from first principles (Baker and Bowler, 2021). The influence of the flexoelectric coupling on the spatial distribution and temperature behavior of the spontaneous polarization for several types of stable domain structure in thin $BaTiO_3$ ferroelectric thin films, including stripe domains and vortices, was analyzed by means of finite-element modeling and the Landau-Ginzburg-Devonshire phenomenological approach, combined with electrostatic equations and elasticity theory, by Morozovska, Eliseev *et al.* (2021). A correlation between the flexocoupling and the formation of chiral polar vortices in thin ferroelectric films and cylindrical ferroelectric nanoparticles, forming the so-called flexon polarization configuration, was also inferred from simulations (Morozovska, Hertel *et al.*, 2021). Finally, Sánchez-Santolino *et al.* (2023) recently reported on Moiré bilayers formed by stacking thin slabs of $BaTiO_3$ (≈ 15 nm). They showed that the interlayer couplings cause spatially modulated strains that yield tunable (twist-angle dependent) vortex-antivortex dipole patterns via a flexoelectric effect. Moiré structures thus appear to be a unique way to obtain topological states with controlled periodicity.

Last, some works have appeared where the ground state of some topological structures has been studied without any interference from the mechanical boundary conditions by lifting off ferroelectric-dielectric superlattices from the substrate (Shao *et al.*, 2023). When the temperature is increased, a phase transition from a skyrmion state (with a topological charge of $+1$) to a two-dimensional meron square lattice (with a topological charge of $+1/2$) is found. Li *et al.* (2022) investigated freestanding $PbTiO_3/SrTiO_3$ superlattices with a $SrRuO_3$ bottom electrode. For thin enough $SrTiO_3$ layers, releasing the superlattice film from the substrate leads to a reorientation of the polarization into the plane of the film due to the sudden change in the balance between the electrostatic and elastic interactions with respect to the superlattice clamped by the substrate. In turn, this polarization rotation modifies the lattice parameter mismatch between the superlattice and the thin $SrRuO_3$ layer, causing the heterostructure to curl up into microtubes.
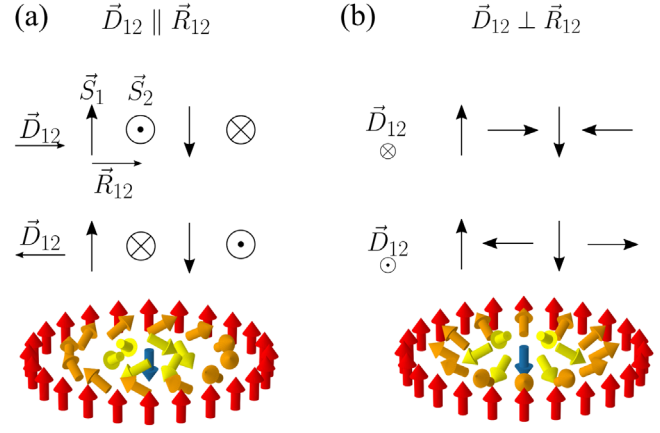

FIG. 15. Schematic sketch of the effect of the antisymmetric Dzyaloshinskii-Moriya interaction in the alignment of neighboring spins. The order parameter rotates around an axis parallel to the Dzyaloshinskii-Moriya vector $\mathbf{D}_{12}$. (a) If $\mathbf{D}_{12}$ is parallel to the relative position between the two neighboring spins $\mathbf{R}_{12}$, then the appearance of chiral helices and Bloch-like skyrmions, such as the one shown at the bottom, are favored. (b) If $\mathbf{D}_{12}$ is perpendicular to $\mathbf{R}_{12}$, then a nonchiral spin texture and a Néel-like skyrmion are supported.

C. Sources of noncollinear polarization

The origin of the complex whirling spin textures of magnetic skyrmions is in most cases the Dzyaloshinskii-Moriya interaction (DMI) (Dzyaloshinsky, 1958; Moriya, 1960). This antisymmetric interaction between two spins $\mathbf{S}_1$ and $\mathbf{S}_2$ whose relative position is $\mathbf{R}_{12}$ typically appears in systems with strong spin-orbit coupling, and its Hamiltonian is given by

$$H_{\mathrm{DM}} = -\mathbf{D}_{12} \cdot (\mathbf{S}_1 \times \mathbf{S}_2), \qquad (6)$$

where $\mathbf{D}_{12}$ is known as the Dzyaloshinskii-Moriya vector, which measures the interaction between the two spins and depends on the material and the distances between the spins. Considering only the DMI, it is clear that the energy is minimized for a configuration where neighboring spins are orthogonal to each other. If $\mathbf{D}_{12}$ is parallel to $\mathbf{R}_{12}$, the spin texture of the ground state looks like the helix that is schematically represented in Fig. 15(a). This helical state is chiral, and therefore it has an associated handedness. If $\mathbf{D}_{12}$ is perpendicular to $\mathbf{R}_{12}$, the resulting pattern does not exhibit chirality, as depicted in Fig. 15(b). From these schematic representations, it is inferred how the spins rotate around an axis parallel to $\mathbf{D}_{12}$. If $\mathbf{D}_{12} \| \mathbf{R}_{12}$, the DMI favors the appearance of a Bloch domain wall between the up and down spins, while a $\mathbf{D}_{12} \perp \mathbf{R}_{12}$ is at the origin of Néel-like domain walls. This interaction is at the root of the stabilization of topological patterns such as vortices, skyrmions, and merons in magnetic systems (Strkalj *et al.*, 2019; Tian *et al.*, 2019).

For a long time, the electric analog of the DMI describing the interaction between two polar displacements has remained elusive. The reason can be traced to the physical origin of the DMI. In magnetism, it arises from the interplay between the spin-orbit coupling and the superexchange. It is not possible to
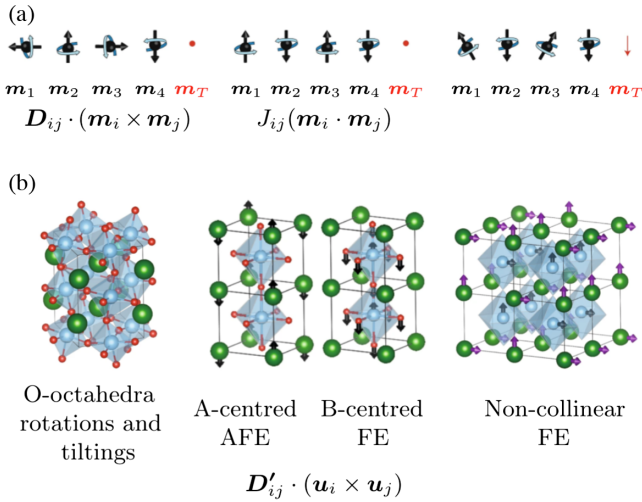
(a)

$m_1 \quad m_2 \quad m_3 \quad m_4 \quad \boldsymbol{m_T}$ $m_1 \quad m_2 \quad m_3 \quad m_4 \quad \boldsymbol{m_T}$ $m_1 \quad m_2 \quad m_3 \quad m_4 \quad \boldsymbol{m_T}$

$$\boldsymbol{D}_{ij} \cdot (\boldsymbol{m}_i \times \boldsymbol{m}_j) \qquad\qquad J_{ij}(\boldsymbol{m}_i \cdot \boldsymbol{m}_j)$$

(b)

O-octahedra rotations and tiltings   A-centred AFE   B-centred FE   Non-collinear FE

$$\boldsymbol{D}'_{ij} \cdot (\boldsymbol{u}_i \times \boldsymbol{u}_j)$$

FIG. 16. (a) Sketch showing how the combination of (left images) the DMI (which favors a 90° rotation between neighboring magnetic moments i and j) and (center images) the Heisenberg interaction (which favors, depending on the coupling constant J_{ij}, 0° or 180° angles between neighboring magnetic moments i and j, such as in the antiferromagnetic configuration) produces weak ferromagnetism in (right images) an antiferromagnetic crystal. $\mathbf{m}_i$ and $\mathbf{m}_j$ are the localized magnetic moments in neighboring atoms. The straight arrow represents the spin and the curled arrow indicates the angular momentum of an electron on a given site, highlighting the fact that the Dzyaloshinskii-Moriya vector $\mathbf{D}_{ij}$ stems from spin-orbit coupling. $\mathbf{m}_T$ stands for the total magnetization of the corresponding configuration. (b) Sketches showing different distortions in a ABO_3 perovskite structure. The trilinear coupling between oxygen octahedra rotations and tilts (left image) with two antiferroelectric (center left image) or ferroelectric modes (center right image) leads to the appearance of noncollinear (anti)ferroelectricity (right image). A, B, and O atoms are represented by green, blue, and red balls, respectively. The arrows represent the atomic displacements from the reference centrosymmetric positions, $\mathbf{u}_i$. The electric DMI $\mathbf{D}'_{ij} \cdot (\mathbf{u}_i \times \mathbf{u}_j)$ is formally equivalent to the magnetic counterpart $\mathbf{D}_{ij} \cdot (\mathbf{m}_i \times \mathbf{m}_j)$, but the $\mathbf{D}'_{ij}$ vector depends on the octahedral tilts, which play the role of the spin-orbit coupling. From Junquera, 2021, and Zhao *et al.*, 2021.

simply identify these two contributions by inspection of ferroelectric distortions, allowing the nature of an electric DMI analog to remain unknown.

Recently a systematic symmetry analysis on the 212 species of structural phase transitions was carried out (Erb and Hlinka, 2020). For three of the species, the existence of a term in the bulk free-energy density analogous to the DMI in magnetic systems was predicted, but its strength could not be anticipated. Therefore, although these energy contributions can induce electric Bloch skyrmions in the same way as the DMI induces bulk magnetic Bloch skyrmions in chiral magnets, the absence of experimental evidence of these phenomena driven by this kind of interaction in ferroelectrics suggests that it is a weak effect, with other interactions dominant.

A major step forward was recently taken by Zhao *et al.* (2021), who used a combination of group theoretical symmetry analysis and first-principles simulations to prove that electric DMI does exist in perovskites, with a one-to-one correspondence with the magnetic counterpart. The strength and coupling of the electric DMI is mediated by oxygen octahedral tilting, which plays an equivalent role to the spin-orbit coupling in the magnetic counterpart (Fig. 16). Up to 12 different contributions to the energy expression where three distortions combine in a product (trilinear coupling) were identified. The products involve an in-phase or antiphase tilting of the oxygen octahedra with two kinds of ferroelectric or antiferroelectric motions for the A and B cations. The symmetry relationships among these three modes are such that, if two of them are allowed, the third one will spontaneously appear to reduce the energy. These new invariant terms in the energy expansion generate noncollinear electric dipole patterns, playing the role of an electric DMI interaction. The microscopic origin of this electric Dzyaloshinskii-Moriya interaction was further investigated by Chen, Zhao *et al.* (2022).

Nevertheless, note that it is not necessary to have DMI-like interactions to produce Bloch-like domain walls in ferroelectrics. Wojdeł and Íñiguez (2014) showed that the common 180° domain walls in $PbTiO_3$ have a Bloch-like character at low temperatures, with a spontaneous electric polarization confined within the domain-wall (DW) plane. First-principles calculations further revealed how they originate from the large displacements of Pb atoms and the Pb-O hybridization at the DWs, which reduce the domain-wall energies up to 10% (Wang *et al.*, 2014; Wojdeł and Íñiguez, 2014; Wang, Zhu, and Ma, 2017). The ferroelectric instability of $PbTiO_3$ is largely driven by the off-centering of the Pb cations to form chemical bonds with some of the surrounding oxygen. Within the ferroelectric domains, the off-centering occurs along a certain direction and the atoms reach their optimal configuration. The Pb cations at the domain walls do not "forget" this tendency to off-center; in fact, while it is weakened by several factors [such as reduced dimensionality and unfavorable strain conditions (Wojdeł and Íñiguez, 2014; Wang, Zhu, and Ma, 2017)], the tendency survives and eventually yields the Bloch-like component of the polarization. The development of these Bloch-like domain walls is at the core of the condensation of polar Bloch skyrmions when columnlike domains are written in a single phase material such as $PbTiO_3$ (Pereira Gonçalves *et al.*, 2019). This is also the ultimate origin of the room-temperature skyrmions discovered in $PbTiO_3/SrTiO_3$ heterostructures (Das *et al.*, 2019).

D. Magnetic versus polar systems: Differences and analogies at the level of the physical interactions

Ferroelectrics have traditionally been viewed as dominated by long-range dipolar interactions and short-range anisotropy energies. In contrast, ferromagnets are typically characterized by a strong short-range exchange energy that overcomes any other magnetic coupling (notable exceptions are materials containing rare-earth ions, which tend to present large anisotropies, because of the large spin-orbit coupling, and small exchange couplings, because of the spatial localization of the unpaired electrons). We provide in Table I the orders of magnitude of the most relevant magnetic and electric interactions as estimated for two systems that are relevant to our discussion: Fe/Ir(111) [one of the classic examples for

TABLE I. Orders of magnitude of the most relevant magnetic and electric interactions in typical magnetic and ferroelectric materials.

	Magnetic (J)	Electric (J)
Dipolar (at 1 nm)	5×10^{-26}	1×10^{-20}
Short-range	1×10^{-21}	5×10^{-21}
Anisotropy	5×10^{-25}	5×10^{-21}
DMI	5×10^{-22}	5×10^{-22}

magnetic skyrmions caused by interface-related DMIs (Seki and Mochizuki, 2016)] and $PbTiO_3$ (the platform for many of the electric topological patterns presented here).

In the magnetic case, all mentioned interactions pertain to bulk iron and have been taken from classic references (Kittel, 1966) except the DM coupling, for which we cite the maximum (large) values estimated by electronic-structure calculations of the $Fe/Ir(111)$ interface (Dupé *et al.*, 2018). In the electric case the dipole-dipole energy is evaluated based on standard polarization and volume data for $PbTiO_3$ (Bilc *et al.*, 2008) and recalling that $\epsilon_\infty \approx 8.6$ for this compound (Zhong, King-Smith, and Vanderbilt, 1994); the short-range interaction energy is evaluated taking into account the harmonic interatomic constants reported by Ghosez *et al.* (1999) for nearest neighbor Pb cations; the anisotropy energy is derived from the computed energy difference between the tetragonal and rhombohedral ferroelectric polymorphs of $PbTiO_3$; see King-Smith and Vanderbilt (1994). Finally, for the electric DM-like interaction, which was recently introduced by Zhao *et al.* (2021), we cite an estimate from a first-principles calculation of perovskite $LaFeO_3$. The general significance of the values in Table I is arguable; nevertheless, they reflect the main differences between most ferromagnetic and ferroelectric compounds, namely, the relatively small influence that dipolar and anisotropy energies have in the magnetic case.

As an immediate manifestation of the differences in the order of magnitude of all these interactions, the domain-wall width (which is directly related to the trade-off between the dipolar and anisotropic energies) is small in ferroelectrics (a few unit cells wide) since anisotropy dominates. In contrast, domain-wall widths in classical ferromagnets (such as iron and cobalt) are much larger than the unit-cell dimensions since exchange dominates. As a direct consequence of the strong role of anisotropy energy in ferroelectrics, rotations of the dipoles away from the crystallographic easy axes (for instance, [001] in tetragonal $PbTiO_3$) have always been thought to be challenging.

V. NOVEL TOPOLOGICAL PHASES: RECENT PROGRESS

Sections I–IV have provided a perspective of the world of ferroelectrics, how it has evolved over the past century, and a primer on topology. We now transition to a full description of the dramatic progress that has occurred over the past decade that relates to various aspects of topological polar textures. In this section, we review the first experimental realizations and theoretical simulations of complex polarization patterns where the local polarization continuously rotates in space forming polar vortices, skyrmions, merons, dipolar waves, hopfions, or labrynthine domain structures. We emphasize the key role of the confluence of experimental tools, probes, and theoretical treatments that have come together to describe the richness of

such topological structures. We also explore the coexistence of complex polar textures with other phases. Finally, a detailed summary of their functional properties, including chirality and negative capacitance, is presented together with different mechanisms to control them with external electric fields or stresses.

A. Polar vortices

1. Experimental realization in superlattices

As summarized in Sec. II, the milestone theoretical works predicting that, under appropriate electrical and mechanical boundary conditions, polarization rotation is possible in ferroelectric systems were carried out in freestanding nanoparticles and nanowires (Fu and Bellaiche, 2003; Naumov, Bellaiche, and Fu, 2004). The experimental confirmation had to wait for some years due mostly to (i) the difficulty to grow with control at the atomic level such nanostructures and (ii) the challenge of visualizing the polarization pattern at the atomic scale. Steady improvements in the experimental techniques reviewed in Sec. I of the Supplemental Material (472) have allowed both of them to be overcome. Another important step forward was taken when a change in the kind of system to be studied was considered, putting the focus on ferroelectric superlattices. The confluence of advances in RHEED controlled layer-by-layer growth, the similarity of in-plane lattice parameters of $PbTiO_3$ and $SrTiO_3$, and advanced microscopy techniques have shown how superlattices are ideal model systems to study the effects of the competition among various components of the ferroelectric Hamiltonian, in a manner that is not present in the bulk form.

On the synthesis side, the most important recognition came with the realization that having an excess of lead in the
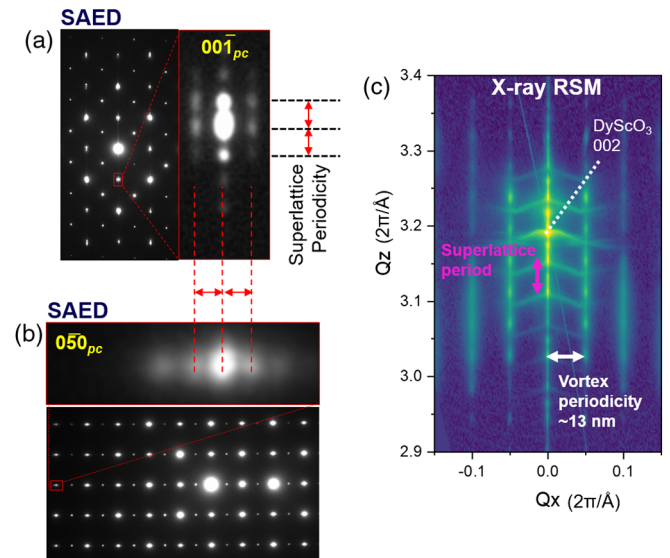
FIG. 17. (a) Selected area electron diffraction (SAED) patterns of the $n = 18$ $PbTiO_3/SrTiO_3$ superlattice grown on $DyScO_3$ showing the existence of superlattice reflections for both the (a) $00l$ and (b) $0l0$ parent reflections. (c) Synchrotron scattering-based reciprocal-space map of the same superlattice as in (a) and (b) that captures the scattering from the superlattice period as well as the vortex lattice, which has a periodicity of ~ 13 nm. Adapted from Yadav *et al.*, 2016.
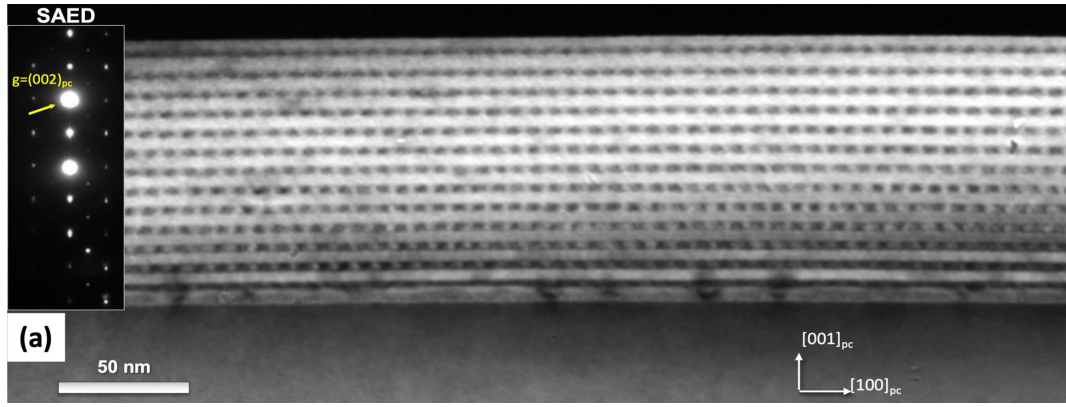
FIG. 18. A dark-field image obtained from a cross section of the $PbTiO_3/SrTiO_3$ superlattice using the $(002)_{pc}$ reflection that shows periodic intensity modulation corresponding to the location of the vortices in the $PbTiO_3$ layer. From Yadav *et al.*, 2016.

target is beneficial to the layer-by-layer growth of the $PbTiO_3$ layers in the superlattices grown by pulsed laser deposition (Yadav *et al.*, 2016). As outlined in Sec. I.A.1 of the Supplemental Material (472), in molecular beam epitaxy (MBE) the individual cationic and anionic species can be independently controlled. As a direct consequence, such a growth mode can be maintained up to even 200 nm of total thickness. Indeed, high-quality $(PbTiO_3)_{10}/(SrTiO_3)_{10}$ superlattices were first grown using MBE on (001) $SrTiO_3$ substrates in 1999 (Jiang *et al.*, 1999). Although they were studied using XRD and TEM and found to be atomically abrupt, this was long before polarization mapping was possible in TEM, and the polar skyrmions that they presumably contained were completely missed.

The first indication of an unusual, emergent structure came from both selected area electron diffraction (SAED) and synchrotron-based reciprocal-space maps (RSMs) (Fig. 17). The SAED patterns [Figs. 17(a) and 17(b)] show the presence of additional reflections that are reminiscent of superlattice reflections. Similarly, the RSMs reveal streaks that correspond to structural features with a real-space spacing of ~13 nm [Fig. 17(c)]. Armed with the reciprocal-space data, one can now look at the same superlattice structures in real space, i.e., using TEM and STEM imaging (Fig. 18). This low-resolution, dark-field image shows the existence of periodic intensity modulations in the $PbTiO_3$ layer. At higher resolution, atomically sharp chemical interfaces can be observed in cross-section STEM images [Fig. 19(a)]. Such chemically
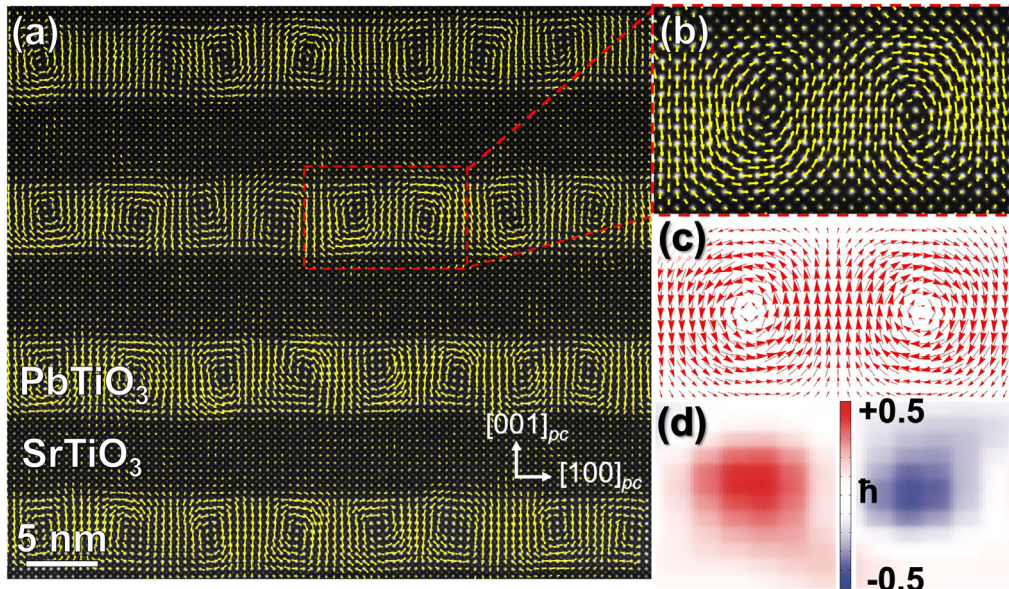
FIG. 19. Observation of clockwise and counterclockwise vortex pair structures. (a) Cross-section HRSTEM image with an overlay of the polar displacement vectors ($\mathbf{P}_{PD}$), indicated by yellow (light gray) arrows for a $(SrTiO_3)_{10}/(PbTiO_3)_{10}$ superlattice, showing that an array of clockwise-counterclockwise vortex pairs is present in each $PbTiO_3$ layer. (b) A magnified image of a single clockwise-counterclockwise vortex pair, showing the full density of data points (one for each atom) and the continuous rotation of the polarization state within such pairs. (c) Polarization vectors from a phase-field simulation of the same $(SrTiO_3)_{10}/(PbTiO_3)_{10}$ superlattice, which predicts pairs that closely match the experimental observations. (d) Orbital angular momentum transferred to the electron beam. (a)–(c) From Yadav *et al.*, 2016. (d) From Nguyen *et al.*, 2020.

FIG. 20. 3D visualization of the vortex array in the $PbTiO_3/SrTiO_3$ superlattice. The front of the left side is the vector map from a HAADF-STEM image, while the top is a dark-field image showing the vortex "tubes." The front of the right side is the phase-field simulation, and the side view gives the 3D perspective. From Yadav *et al.*, 2016.

sharp interfaces (i.e., with a minimum of interfacial interdiffusion) are critical to imposing the relevant electrostatic and elastic boundary conditions on the superlattice.
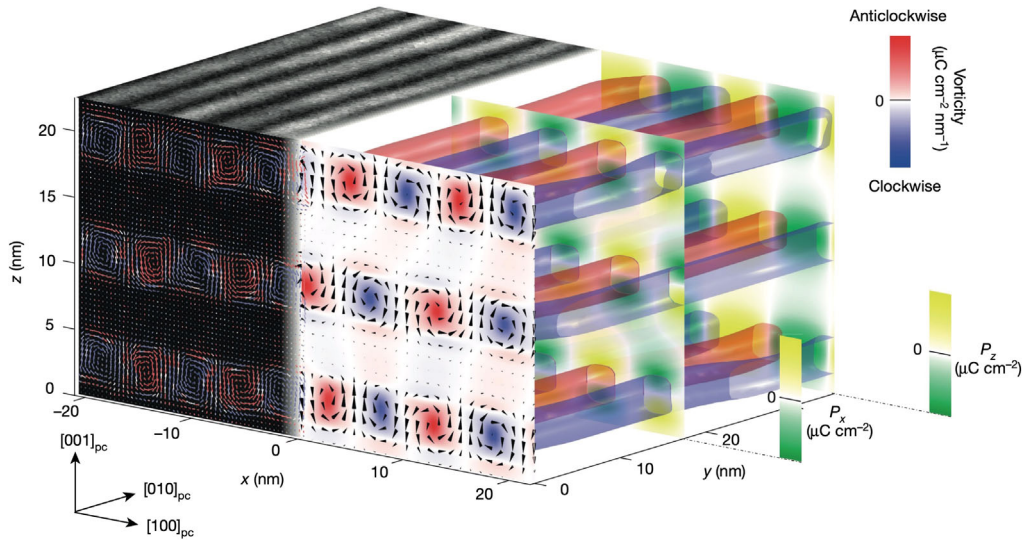
If these high-resolution STEM (HRSTEM) atomic-resolution images are analyzed using vector-mapping algorithms, then the resulting atomic polar displacements P_{PD} enable the measurements of the local noncentrosymmetry of the lattice. The vector map of these polar displacements indicates the formation of long-range arrays of clockwise and counterclockwise vortex pairs in each $PbTiO_3$ layer [Fig. 19(a)]. The lateral periodicity of these vortex pairs is ~10 nm [Fig. 19(b)] (and scales with the superlattice periodicity). The polarization distribution of individual ferroelectric vortices at the subunit cell level has been also measured using the atomically resolved integrated differential phase contrast imaging in an aberration-corrected STEM (Sun *et al.*, 2019). Such pairs of clockwise and counterclockwise vortices have been confirmed by first principles (Shimada, Tomoda, and Kitamura, 2010b; Aguado-Puente and Junquera, 2012), second principles (Kornev, Fu, and Bellaiche, 2004; Shafer *et al.*, 2018), and phase-field simulations (Yadav *et al.*, 2016) [Fig. 19(c)].

The 3D structure of a clockwise and counterclockwise array of vortex in a $(PbTiO_3)_{10}/(SrTiO_3)_{10}$ superlattice from phase-field simulation is shown in Fig. 20. In the 3D structural model, the polarization rotation is mapped onto the front plane of the structure alternating clockwise (blue) vortices and counterclockwise (red) vortices according to the curl of the polarization, which extends along $[010]_{pc}$ as long tubes, indicating the ordered vortices. The red and blue regions correspond to the curl of the polarization extracted from the phase-field model and the HRSTEM polar displacement map. The phase-field models indicate the formation of a clockwise and counterclockwise array of a vortex ground state bearing a close resemblance to the experimental observations from HRSTEM studies. On the basis of both the experimental results and the phase-field simulations, one can conclude that the vortex structure results from competition among three

energies: (i) elastic energy [the $PbTiO_3$ layers are under tensile strain on the $DyScO_3$ (110) substrate], (ii) electrostatic energy from built-in fields (arising from the large polar discontinuity at the interfaces from $PbTiO_3$ to $SrTiO_3$ layers), and (iii) strain gradient (flexoelectric coupling) and polarization gradient energies that dictate the energy cost of the polarization rotation in the system.

2. Influence of the periodicity of the superlattice

Building on the initial observation and understanding of the nature of the vortex structures, subsequent studies on the dependence of the structural properties of the $(PbTiO_3)_n/(SrTiO_3)_n$ superlattices on $DyScO_3$ $(110)_o$ substrates with a period n revealed a number of important observations.

For short-period superlattices ($4 < n < 6$ unit cells), structures consistent with traditional ferroelectric domain structures (so-called a_1/a_2 domain patterns) with fully in-plane oriented polarization were observed. This was also evident in both PFM and synchrotron-based 3D RSM studies (Damodaran *et al.*, 2017a). On transitioning to intermediate-period superlattices ($6 < n < 10$), however, more complex RSM patterns are observed showing the presence of both the ferroelectric a_1/a_2 phase and peaks for a new phase. The mixed-phase coexistence for superlattices in this layer thickness range are confirmed by both phase-field simulations and cross-section TEM images (Fig. 21) (Hong *et al.*, 2021). For superlattices with periodicities from 12 to 18 unit cells, we observe an almost exclusively vortex phase ensemble, which is sensitive to the number of repeat units in the heterostructure. For example, a $SrTiO_3/PbTiO_3/SrTiO_3$ trilayer with a layer thickness of 16–18 unit cells is essentially all vortex phase (this is also discussed in Sec. VI.A.4, Fig. 42), while for the sample layer thickness a superlattice (i.e., one that has multiple repeat units) evolves into a mixed ferroelectric a_1/a_2-vortex phase. This once again demonstrates the sensitivity of the phase stability in this system to the fine scale magnitudes of the elastic
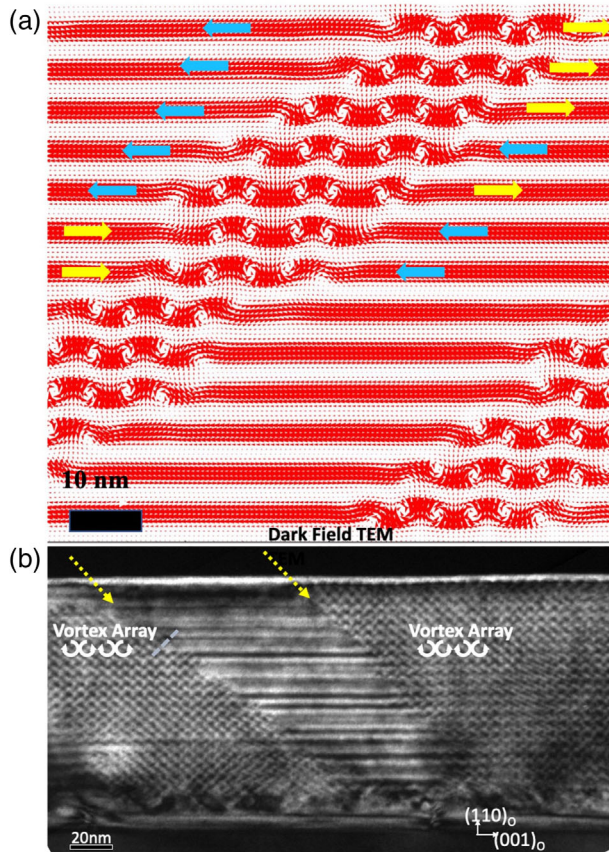
FIG. 21. (a) Phase-field cross-section simulation of a mixed vortex-ferroelectric phase ensemble showing how the vortex phase accommodates the in-plane head-to-head or tail-to-tail domains. (b) Dark-field image of an $n = 8$ SrTiO$_3$/PbTiO$_3$ superlattice that also exhibits the mixed phase; the ferroelectric phase is identified by the yellow dashed arrows. Adapted from Hong *et al.*, 2021.

FIG. 22. (a) Lateral piezoresponse image for a SrTiO$_3$/PbTiO$_3$ superlattice with $n = 16$ revealing stripelike order in which alternating stripes exhibit high (checkered white and black) and low or zero [brown (gray)] piezoresponse with a periodicity of ~300 nm along the $[010]_{pc}$. (b) Variations in the surface topography. (c) Changes in the lateral piezoresponse amplitude. (d) Line trace across the topography (green dashed line) and lateral piezoresponse images (red dashed line) revealing opposite and dramatic modulations in surface topography and lateral piezoresponse between the a_1/a_2 and vortex phases. These measurements in combination with RSM x-ray diffraction studies confirm that the vortex phase corresponds to protruding features in surface topography with low piezoresponse, while the a_1/a_2 phase is recessed in topography with large lateral piezoresponse. (e) 3D phase-field calculated image of the mixed vortex-ferroelectric a_1/a_2 phase ensemble. Adapted from Damodaran *et al.*, 2017a.

and electrostatic boundary conditions, which is also consistent with the notion of phase competition and coexistence. Finally, for superlattices with larger periods, i.e., ($n \gtrsim 20 - 25$), the stable structure is a classical flux-closure pattern. All these experimental findings are in good agreement with phase-field simulations (Hong *et al.*, 2017), as discussed in Fig. 13 in Sec. IV.A.2.

3. Mixed-phase structures and tunable properties

As described, RSM and TEM studies point to the coexistence of a classic ferroelectric phase and a new vortex phase for periodicities ranging between $n = 12$ and 18. This coexistence can be visualized using PFM, as in Fig. 22 for a superlattice with $n = 16$. The resulting self-assembled, hierarchical structure reveals stripelike order in which alternating stripes exhibit high (checkered white and black) and low or zero (brown) piezoresponse with a periodicity of ~300 nm along the in-plane pseudocubic [100] [Fig. 22(a)]. The high-response regions are the ferroelectric a_1/a_2 phase [Figs. 22(b) and 22(c)], and the low-response regions are the vortex structures. Ultimately these data indicate that at room temperature the coexisting vortex and ferroelectric phases
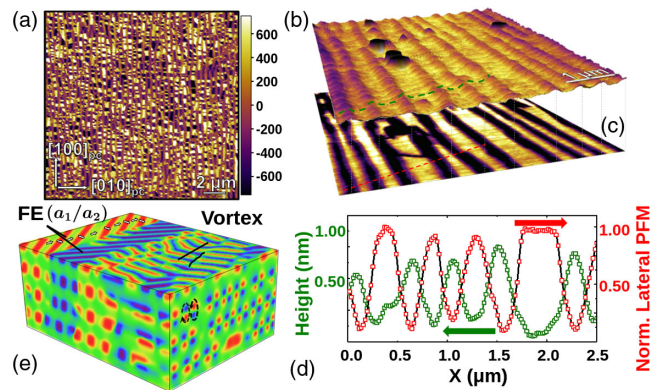
spontaneously assemble in a mesoscale, fiber-textured hierarchical superstructure. This structure was also replicated in large-scale phase-field models [Fig. 22(e)].

The previous approach allows one to track the evolution of the polarization across the boundary between the ferroelectric and vortex phases. Surprisingly it was found that the polarization component along the length of the vortex tube does not go to zero. This was confirmed by PFM studies that showed the presence of in-plane polarization in the vortex phase. This means that the vortices are not simply tubes of wrapped polarization (like a rolled-up piece of paper) but rather more like a spiral with an axial component of polarization. Therefore, within the vortex phase, these systems are characterized by a multiorder-parameter state, with the electric toroidal moment [Eq. (5)] parallel to the net polarization. Numerical estimations of the electric toroidal moment indicate that it ultimately saturates to values of 0.2 e Å^{-1} (Damodaran *et al.*, 2017a). This 3D polarization texture in turn presents interesting possibilities for other emergent functions, including chirality, which is discussed in Sec. V.D.1.

Arrays of polar vortices have been engineered in (PbTiO$_3$)$_{10}$/(SrTiO$_3$)$_{10}$ after fabricating lamellae from topologically trivial (a_1/a_2)-domain architectures in superlattice films (Tan *et al.*, 2021). Beyond superlattices, periodic vortex-antivortex pairs have been observed in tensile strained PbTiO$_3$ films (Y. T. Chen *et al.*, 2020). And phase coexistence and an unusual transformation between an a_1/a_2 phase and a flux-closure phase in SrTiO$_3$/PbTiO$_3$ thin films grown on GdScO$_3$

substrates upon irradiation of electron beams in a TEM was recently reported (Ma *et al.*, 2020). In the process, some dislocations consisting of only flux-closure domain pipes might appear. Phase-field simulations suggest that the partial screening by accumulation of free charges are the driving force for the phase transition.

4. Electric-field control of toroidal-vortex and ferroelectric order

The presence of the axial component of polarization has other important implications, namely, that with this axial polarization component dc electric-field manipulation of the vortex phase should be possible. To probe this concept, Damodaran *et al.* (2017a) explored the evolution of the mixed-phase ferroelectric-vortex structures under applied out-of-plane dc electric fields using PFM. For example, the as-grown mixed-phase structure for an $n = 16$ superlattice again reveals the spontaneously assembled mesoscale, fiber-textured, hierarchical superstructure for ferroelectric and vortex regions [Fig. 23(a)]. Upon application of a positive dc bias to a specific area of the sample [orange box, Fig. 23(a)], however, the mixed-phase structure is transformed into a pure vortex phase with uniformly low piezoresponse [Fig. 23(b)]. This transition was also confirmed via nanoscale x-ray diffraction experiments [Fig. 23(d)]. The resulting pure vortex phase can in turn be switched back to have a mixture of ferroelectric and vortex phases with application of a negative dc bias [Fig. 23(c)]. Reversing the

FIG. 23. Lateral piezoresponse amplitude images for an $n = 16$ superlattice. (a) As-grown mixed-phase structure. (b) Conversion to a uniformly low-piezoresponse state corresponding to the vortex phase following application of a positive 15 V bias. (c) Reversal of portions of region back into a mixed-phase structure following application of a negative 15 V bias. (d) These results are confirmed by nanodiffraction studies showing the intensity of the a_1/a_2 002_{pc} diffraction peak. (e) Ti-absorption edge, x-ray linear-dichroism-based photoemission electron microscopy image of the region in (c) showing the difference in XLD between the vortex and ferroelectric phases. (f) SHG polar plots obtained from regions with the as-grown mixed-phase structure [solid orange (light gray)], the electrically poled pure vortex structure [solid blue (dark gray)], and that of the volume normalized signal from the a_1/a_2 phase (red dashed ellipse) revealing a large SHG intensity change after transitioning to the vortex phase. Adapted from Damodaran *et al.*, 2017a.

applied field (i.e., a negative bias followed by a positive bias) produces similar effects. This reversible electric-field control of ferroelectric and electric toroidal order provides a number of novel opportunities for applications. For example, regions of pure vortex order exhibit order-of-magnitude-lower piezoresponse and nonlinear optical effects, indicating that one can electrically manipulate and dramatically change materials properties. The ability to write vortex regions and control the electric toroidal order with an applied electric field suggests a coupling between the toroidal and ferroelectric order parameters that can be exploited to control other materials properties, namely, the chirality. Electric control of the chirality, as described in Sec. V.D.1, and other coupled properties would open a new frontier in condensed-matter physics and the construction of multifunctional devices.

5. Switching of the toroidal moment

As discussed in Secs. II and III, a new order parameter (the toroidal moment) has been introduced to characterize the polar vortices. Since the original work (Naumov, Bellaiche, and Fu, 2004), it has been recognized how the vortex state is bistable: for instance, the energy of the vortices where the local polarization in space continuously rotates clockwise or counterclockwise is degenerate. But for a practical realization of this emergent order parameter, it is essential to find the mechanism for a systematic and efficient switch of the electric toroidal moment. Here we review some of the different mechanisms proposed in the literature using electric-field manipulation or strain engineering to control this order parameter.

a. Switching with electric fields

In principle, the conjugate field that would couple with the polar dipoles that continuously rotate around the topological defect of the vortex core is the electric field. But the required interacting electric field should have a non-vanishing curl that, according to the Maxwell equations, is produced not by static charges but by a temporal change of a magnetic field [$\mathbf{\nabla} \times \mathbf{E} = -(1/c)\,d\mathbf{B}/dt$]. This mechanism was theoretically explored by Naumov and Fu (2008) in $Pb(Zr_{0.5}Ti_{0.5})O_3$ nanoparticles from first-principles-based effective Hamiltonians. One important result was that such a reversal is possible and involves the formation of a new vortex nucleated around the center of the nanoparticle that has a perpendicular (rather than opposite) electric toroidal moment with respect to the initial and final ones. However, from a practical point of view this proposal seems impractical since the magnitude of the magnetic field necessary to switch the electric toroidal moment is large, although it can be greatly reduced by means of a combined action with an homogeneous electric field. If the topological defect at the core is suppressed, for instance, in a ferroelectric *nanotube*, then phase-field simulations suggest that the reversal of the toroidal moment is driven by the nucleation and growth of local vortices with the opposite toroidal moment. The difference with respect to the previous mechanism (where $+\mathbf{G}$ and $-\mathbf{G}$ never coexist) is attributed to the absence of topological defects in nanotubes and, therefore, the impossibility of
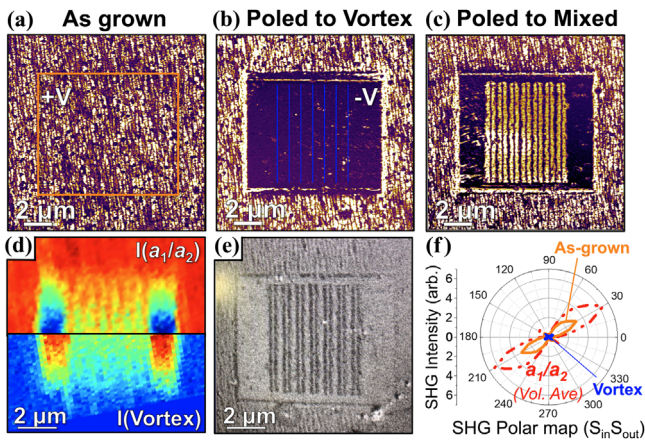
nucleating new vortices with a perpendicular toroidal moment (Wang and Kamlah, 2009).

Another explored model for an efficient control of the direction of the macroscopic toroidal moment includes the application of a transverse inhomogeneous static electric field, such as those that can be generated by an external dipole. This was tested within an effective Hamiltonian approach in stress-free $Pb(Zr_{0.4}Ti_{0.6})O_3$ nanodots under open-circuit-like electrical boundary conditions (Prosandeev *et al.*, 2006). When the dipolar source of the inhomogeneous field rotates, the toroidal moment switches its direction.

Sweeping of a biased tip (like the ones used in AFM) has also been postulated as an efficient method to dynamically switch the toroidal moment of vortices in nanoparticles of different shapes and sizes and nanocomposites (Ma *et al.*, 2018). Phase-field simulations unraveled how the inhomogeneous electric field generated by the tip shrinks the original vortices and pushes its center toward the side of the nanoparticles. This vortex annihilation (happening at the front zone of the tip) is followed by a vortex creation driven by the depolarization field (occurring behind the tip). The new vortex nucleation is driven by the depolarization field, and its sense of rotation is controlled by the polarity of the tip field.

A fourth possibility was to use a homogeneous electric field but for asymmetric ferroelectric nanorings (Prosandeev, Ponomareva, Kornev, and Bellaiche, 2008). In that case, the electric vortex was found to be controllable, via the formation of intermediate states (consisting of two vortices of opposite rotations) and thanks to two novel interaction energies involving a vector characterizing the asymmetry, the applied field, and the electric toroidal moment. The latter possibility also explained why a reversal of vortices has also been observed in magnetic nanostructures (Chien, Zhu, and Zhu, 2007).

b. Switching with strain and stress fields

Chen *et al.* (2018) proposed using the trilinear coupling between the shear stress and the two polarization components that lie in the shear strain plane. Integrating the coupling energy density over the volume of the vortex structure results in a total energy contribution that couples the toroidal moment, the polarization, and the shear stress. Therefore, for a fixed shear stress, a change in the sign of the polarization (which can be controlled by an external electric field) can lead to a change in the sign of the toroidal moment. Another possible path is to fix the sign of the polarization with an external field, and then change the sign of the shear stress; in this case, a reversal of the toroidal moment is produced. Note that in both paths a polar-toroidal state ($G_z \neq 0$, $P_z \neq 0$) is required.

Mechanical loads were also investigated by phase-field simulations as a method to control the vortex domain structure in $PbTiO_3$ nanoplatelets under open-circuit boundary conditions (Chen, Zheng, and Wang, 2012). Although it was shown how vortex domain structures with more (fewer) vortices can generally be obtained by applying compressive (tensile) surface traction to the ferroelectric nanoplatelet with a strong interplay with the temperature, nothing could be determined regarding the systematic control of the sense of rotation of the polarization. The effects of voids in the feasibility of switching the vorticity with stress in these nanoplatelets were also explored (Yuan *et al.*, 2018; Peng *et al.*, 2021).

6. Interplay between electronic and atomic structure

Since the milestone work by Cohen (1992) on the origin of ferroelectricity in perovskite oxides, first-principles simulations have contributed to the exploration and rationalization of the energy landscape and the microscopic mechanism of the instabilities of ferroelectric oxide perovskites. Although ABO_3 perovskites can be classified as dominantly ionic compounds, it was already highlighted by Cohen that partial hybridization between the O-$2p$ and B-d states plays a key role in the condensation of a polar (ferroelectric) mode. These interactions might be particularly intricate in cases where the local polarization continuously rotates around a core, such as in the polar vortices. Electron energy loss spectroscopy (EELS) in the STEM mode is a powerful tool to check the interactions between the atomic and the electronic structure of the materials. It uses inelastically scattered electrons to probe the core-shell excitations (empty density of states) of transition metals at atomic resolution.

Torres-Pardo *et al.* (2011) performed the first characterization of $(PbTiO_3)_6/(SrTiO_3)_6$ superlattices showing 180° ferroelectric domains using this technique. The energy splittings were resolved with a high accuracy in the $PbTiO_3$ and $SrTiO_3$ layers across the superlattice. The observed continuous evolution of the spectral features were semiquantitatively correlated with the local ferroelectric distortions and tetragonality by means of first-principles simulations and charge transfer multiplet calculations. The results pointed to an inhomogeneous strain and polarization profile within the ferroelectric and paraelectric layers that had never before been detected by direct methods. EELS measurements revealed the presence of broad interfacial regions with reduced tetragonality and polarization extending over five to six unit cells into the $PbTiO_3$ layers that are compatible with the presence of dipolar patterns with continuous polarization rotation (flux closures and vortices) (Zubko *et al.*, 2012). However, in the first two works only average signals over the domains within the thickness of the TEM specimen could be recorded, and the comparison with first principles required to take the root-mean-square polarization and average tetragonality for each (001) layer of the superlattice. The latest step in this direction (Susarla *et al.*, 2021), where the EELS spectra were recorded with atomic resolution, was recently taken. It was shown how the peaks in Ti L-edge EEL spectra shift systematically depending on the position of the Ti^{4+} cations within the vortices, i.e., with the direction and magnitude of the local dipole.

Note how Ti^{4+} can possibly be reduced to Ti^{3+}, especially under reducing (or oxygen deficient) conditions. However, this can be readily checked with spectroscopic methods such as EELS (Susarla *et al.*, 2021). Similar $PbTiO_3/SrTiO_3$ superlattices grown under slightly different conditions might be prone to display oxygen vacancies and larger concentrations of Ti^{3+} close to the vortex core. Signatures of this electron concentration, such as energy splittings of the L_3 and L_2 edges at the vortex core lower than that in other regions of the $PbTiO_3$ layer, were found by Du *et al.* (2019). The role of

such electronic defects that arise either due to doping of the transition ion site (i.e., Ti^{+4} to Ti^{+3}) or through the replacement of the Ti^{+4} by other transition metal ions that carry electrons (for example, Fe^{+3}, which is in the d^5 state) could be of interest for single spin manipulation studies. This is elaborated upon in Sec. VI.

Another important physical property that is susceptible to change within these structures showing a complex pattern of polarization is the band gap. This is particularly important since it modifies the optical properties or the absorption of above-band-gap photons. An *ab initio* scheme was developed by Gui, Wang, and Bellaiche (2015) in order to determine the effect of electrical vortices on electronic properties in $BaTiO_3/SrTiO_3$ nanocomposites. This scheme sheds some light on the observed current activated at low voltages in systems possessing electrical vortices (Balke *et al.*, 2012). It also pointed out a novel phenomenon, namely, a technologically important control of the so-called type-I versus type-II band alignment (Yu, McCaldin, and McGill, 1992; McDonald *et al.*, 2005) within the same material via the occurrence (disappearance) of electrical vortices when cooling down (heating up) the system below (above) some critical temperature. This new scheme was also further used to predict that varying the temperature within the stability region of electrical vortices provides a substantially larger range of control of the band gap and band alignment than the field control of the electrical skyrmion (Walter *et al.*, 2018).

7. Ultrafast manipulation of polar vortices

a. Supercrystals

Ultrafast light pulses (shorter than 1 ns in the time domain) can help create and manipulate the vortex states with emergent structural, electronic, and magnetic phenomena. These nonequilibrium phases are often transient, and the challenge is to stabilize them as persistent states. The vortex arrays can be converted to a supercrystal phase by subpicosecond optical pulse excitations with light above the band gap (Fig. 24) (Stoica *et al.*, 2019). This phase is stable under ambient conditions but can be erased by heating. X-ray scattering and microscopy show that this unusual phase consists of a coherent three-dimensional structure with polar, strain, and charge-ordering periodicities of up to 30 nm. Phase-field modeling describes this emergent phase as a photoinduced charge-stabilized supercrystal formed from a two-phase equilibrium state. The good agreement between experiments and phase-field modeling gives strong support to a formation mechanism dominated by reduction of the depolarization field via photocarrier excitation. In contrast to the photoexcitation of bulk crystals or crystalline thin films that show no new phases, the creation of a polar supercrystal with a subpicosecond optical pulse highlighted the role of the local spatial confinement of the ferroelectric order parameter. While photocarrier excitation occurs in the $PbTiO_3$ layer, the $SrTiO_3$ interlayers act as nanoscale heat sinks to promptly spread out the thermal excitations, which may quench the optically stimulated transient states by exploiting nonadiabatic conditions to develop long-range order in a way that might not be accessible by equilibrium pathways. This also highlights routes to stabilizing these polar phases via tuning of the
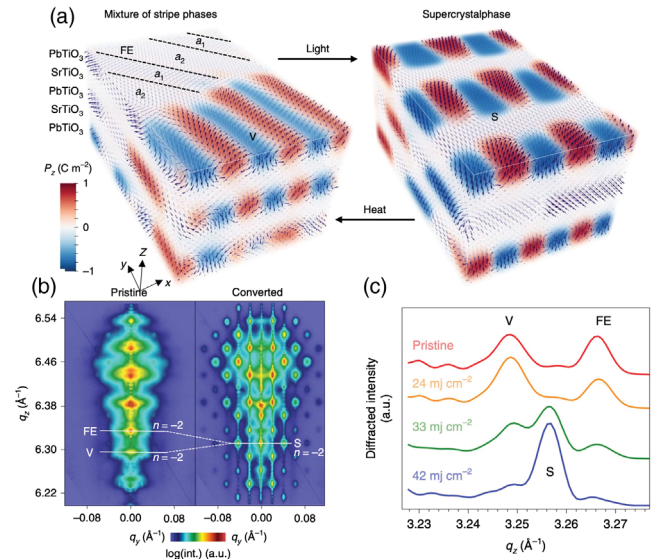

FIG. 24. (a) A two-phase mixture of in-plane ferroelectric-ferroelastic a_1/a_2 domains (FE) and polar vortex (V) is converted to a single 3D supercrystal (S) phase by subpicosecond optical pulses in a $PbTiO_3/SrTiO_3$ superlattice. The S phase contains ferroelectric, ferroelastic, and polar-vortex subregions ordered in three dimensions. Thermal annealing reverses this transition. The arrows in (a) indicate the local polar displacements obtained from a phase-field model. The red and blue color contrasts illustrate the up and down z components of the polarization. The white regions correspond to in-plane polarization. (b) Diffraction along the K-L ($q_y - q_z$) plane near the 004_{pc} peak for the mixed-phase (FE + V) pristine sample shows evidence of order only along the z direction, with distinct peaks due to the FE and V phases, as indicated by the horizontal lines. (c) Superlattice peaks near 002_{pc} (pseudocubic notation) showing two distinct diffraction peaks, corresponding to the V and FE phases in the pristine sample, that transform into a single uniform S phase with single-shot optical excitation above a certain threshold energy density. a.u., arbitrary units. From Stoica *et al.*, 2019.

boundary conditions through alteration of the dielectric spacer material or environmental conditions. Much remains to be learned about the formation of such "supercrystals." Why did it form the specific lattice? How does that relate to the underlying perovskite lattices in $SrTiO_3$ and $PbTiO_3$ as well as the superlattice periodicity. The role of band-gap light seems to be critical; in the case of $SrTiO_3/PbTiO_3$ superlattices, both $SrTiO_3$ and $PbTiO_3$ have band gaps that are close to each other, so there could be the possibility of photoexcitation in either or both layers. Replacing $SrTiO_3$ with a layer that has a different band gap would throw light on the specific role of the electronic structure in the $PbTiO_3$ layer. The stability of these supercrystals with respect to changes in temperature and under the influence of electric fields was recently analyzed (Dai *et al.*, 2022).

Different supercrystals can be stabilized in oxide superlattices where the dielectric $SrTiO_3$ is replaced by a metallic $SrRuO_3$ layer, without the need of optical excitation (Fig. 25) (Hadjimichael *et al.*, 2021). The proposed structure consists of "horizontal" and "vertical" flux-closure domains with 180° walls in the plane of the film and perpendicular to it, respectively. The supercrystal phase forms in response to
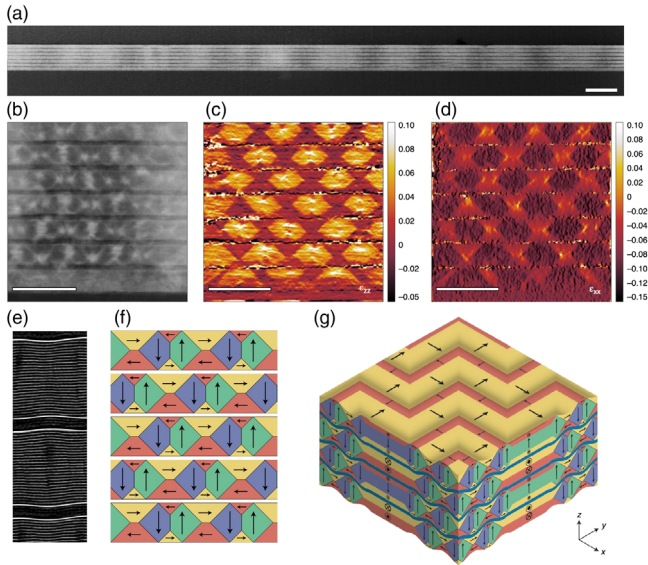
FIG. 25. Electron microscopy characterization of the supercrystal phase. (a) Cross-section HAADF-STEM image of the $(PbTiO_3)_{27}/(SrRuO_3)_5$ superlattice showing the full superlattice structure with well-defined periodicity. Scale bar, 100 nm. (b) Higher magnification image revealing a complex periodic arrangement of horizontal and vertical flux-closure domains. (c) Out-of-plane strain (ϵ_{zz}) with respect to the substrate (DyScO$_3$, $c = 3.946$ Å) extracted using geometric phase analysis (GPA). (d) In-plane strain (ϵ_{xx}) extracted using GPA. Scale bars in (b)–(d), 30 nm. (e) Laterally compressed HAADF-STEM image that has been Fourier filtered to retain only the out-of-plane periodicity. White curves superposed over atomic planes near the PbTiO$_3$–SrRuO$_3$ interfaces are included as guides for the eye to highlight the large bending of the lattice. PbTiO$_3$ layers are found to exhibit periodic expansion and contraction along the out-of-plane direction with opposite deformation in neighboring PbTiO$_3$ layers, while the SrRuO$_3$ layers bend to accommodate this distortion. (f) 2D sketch of the domain pattern deduced from the TEM measurements. (The absolute directions of the polarization may be reversed in the experimental image.) (g) 3D sketch of the overall domain pattern deduced from XRD, PFM, and TEM studies. From Hadjimichael *et al.*, 2021.

two simultaneous constraints: the moderately tensile strain imposed by the substrate [orthorhombic $(110)_o$ DyScO$_3$ substrates], and the poor screening of the PbTiO$_3$ polarization. Indeed, the same kind of supercrystal structures are stabilized when the metallic layer is replaced by alternating blocks of PbTiO$_3$ (21 unit cells thick) separated by a fine-period spacer structure made from the repetition of one-unit-cell SrTiO$_3$/one-unit-cell PbTiO$_3$ superlattice (up to five unit cells in total).

b. Collective dynamics

In contrast to magnetic skyrmions, where current effort is indeed focused on exploring skyrmion dynamics, in polar vortices and skyrmions this is in its early stages. The collective dynamics of topological structures (Choe *et al.*, 2004; Naumov, Bellaiche, and Fu, 2004; Nagaosa and Tokura, 2013; Büttner *et al.*, 2015; Huang and Cheong, 2017) are of interest from both the fundamental and applied
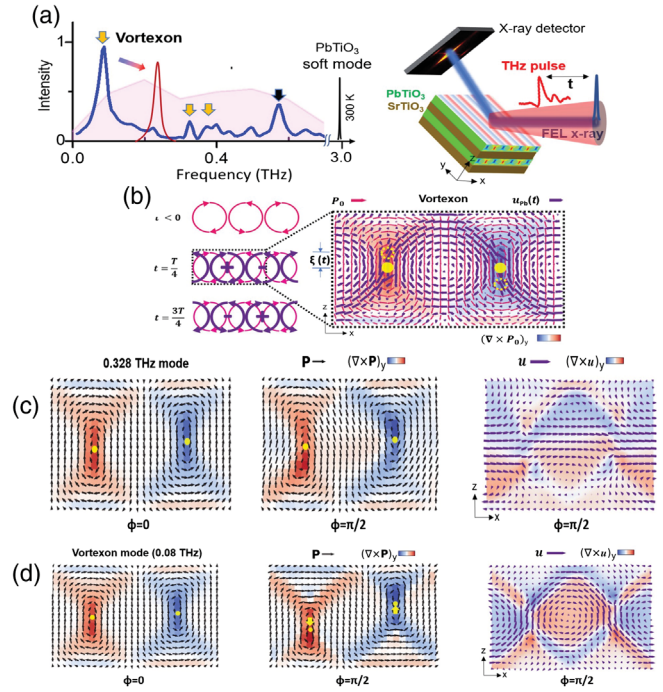

FIG. 26. (a) Fourier spectra (blue) of calculated time-dependent response of polar vortices on terahertz-field excitation. The spectrum of the terahertz pulse is shown as a broad pink background. The collective modes of polar vortices (orange arrows) are shown as a separate set of modes with respect to the known superlattice acoustic modes (black arrow) and the soft mode of PbTiO$_3$ at room temperature. The vortexon mode shifts to higher frequency (red peak; note that this is not the calculated peak but rather a schematic peak to show the temperature dependence) as the sample temperature increases. To the right is a schematic of the terahertz-pump and x-ray-diffraction-probe experiment using an x-ray free-electron laser (FEL). The colored stripes on the $(PbTiO_3)_{16}/(SrTiO_3)_{16}$ superlattice film represent in-plane vortex orders with opposing polarization vorticities. (b) Emergence and evolution of the vortexon (atomic displacement vortices, purple circles) during its oscillation period τ, overlaid with the static polarization vortices (magenta circles). $+$ and $-$ are signs for the vortexon vorticities, which reverse dynamically. Right panel: enlarged view of the region of the dashed box with the calculated static polarization (magenta arrows) and lead-cation displacement (purple arrows) in each unit cell of the vortexon mode at $t = \tau/4$. (c),(d) Snapshots of the two types of coherent deformation modes that are observed in the vortexons at two different frequencies: (c) 0.328 and (d) 0.08 THz. From Li *et al.*, 2021.

perspectives. Studies of dynamical properties of magnetic vortices and skyrmions have not only deepened our understanding of the fundamental physics but also provided directions for potential applications. Terahertz excitation and femtosecond x-ray diffraction measurements have provided insight into the ultrafast collective polarization dynamics in polar-vortex arrays, with orders-of-magnitude-higher frequencies and smaller lateral sizes than those of experimentally realized magnetic vortices. A coherent collective mode, called a vortexon (Fig. 26), was observed that emerges in the form of transient arrays of nanoscale circular patterns of atomic displacements, which reverse their vorticity on picosecond timescales (Li *et al.*, 2021). Its frequency is

considerably reduced at a critical strain, indicating a condensation (freezing) of structural dynamics. This could provide us with pathways for phonon engineering, or could perhaps even explore the much sought-after phonon localization. Since this is literally the first measurement of such collective modes, several open questions remain. Can the width of the vortexon mode be used as a measure of the thermal evolution of the degree of long-range order within the vortex lattice? If yes, how does it change with temperature? Would this be a pathway to study the nature of the vortex lattice phase transition (i..e, classical versus topological) into the a_1/a_2 ferroelectric phase? A recent analytical model has been proposed to derive the equations of motion of the ultrafast collective polarization dynamics. The effective mass, spring constants, and mode frequencies were extracted consistently with the former experimental measurements and phase-field simulations (Yang *et al.*, 2021). Rijal *et al.* (2023) investigated dynamics of polar-vortex crystallization and determined that such crystallization is driven by the softening of a peculiar and specific phonon mode. They also predicted a new effect that may lead to the development of novel low-power electronic technologies, namely, the reorientation of the vortex lattice by an ac-field-driven resonant switching.

B. Polar skyrmions

Thus far we have discussed the appearance of complex polarization patterns (vortices) in oxide nanostructures. However, as summarized in Sec. III, topological solitons (such as skyrmions and merons) have been added to the quest. First-principles-based model Hamiltonian approaches predicted the existence of polar skyrmions in BaTiO$_3$ nanowires embedded in a SrTiO$_3$ matrix (Nahas *et al.*, 2015) [Fig. 27(a)]. They were also foreseen in a single phase material (nanocolumns written in bulk PbTiO$_3$) thanks to the condensation of a Bloch component of the polarization at the domain wall (Pereira Gonçalves *et al.*, 2019) [Fig. 27(b)].
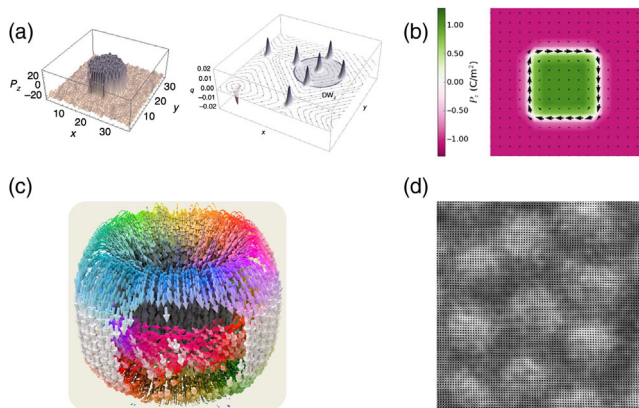

FIG. 27. Theoretical predictions of the formation of polar skyrmions from second-principles simulations in (a) BaTiO$_3$/SrTiO$_3$ nanocomposite, (b) skyrmion tubes written in nanocolumns of PbTiO$_3$, and (c) polar bubble skyrmions in PbTiO$_3$/SrTiO$_3$ superlattices. (d) Planar section HRTEM image showing the locally ordered arrays of skyrmions. (a) From Nahas *et al.*, 2015. (b) From Pereira Gonçalves *et al.*, 2019. (c),(d) From Das *et al.*, 2019.

The first steps in the experimental characterization were taken by Zhang *et al.* (2017). In Pb(Zr$_{0.2}$Ti$_{0.8}$)O$_3$ ultrathin films sandwiched with a SrTiO$_3$ thin film, laterally confined bubbles of sub-10-nm size were observed. In the bubbles, the local dipoles self-aligned in a direction opposite to the macroscopic polarization of a surrounding ferroelectric matrix. But the visualization of the atomic positions with subangstrom resolution, especially the Bloch component at the domain wall, and a proper characterization of the topological invariant were not achievable in these experiments. *Ab initio*–based simulations (Zhang *et al.*, 2017, 2019) revealed that imperfect screening conditions as well as built-in electric bias were essential ingredients for the stabilization of polar bubbles. The computations showed the existence of incommensurate phase and symmetry breaking in the bubble domains, resulting in strong fluctuations of the local polarization responsible for a mixed Néel-Bloch-like dynamical character of the bubble domain walls.

The final experimental visualization of a polar-skyrmion bubble, such as the ones described in Sec. III.B.4, came a couple of years later [Figs. 27(c), 27(d), and 28] (Das *et al.*, 2019) based on (PbTiO$_3$)$_n$/(SrTiO$_3$)$_n$ superlattices. The interplay of elastic, electrostatic, and gradient energies provides an opportunity to produce such nontrivial topological phases, the electric counterparts of the magnetic skyrmions. It was discovered that the (PbTiO$_3$)$_n$/(SrTiO$_3$)$_n$ heterostructures have to be grown under a slight compressive strain, for instance, on SrTiO$_3$ (001) substrates, to tip the balance of energies in the right manner to induce these new structures. Looking down at the surface of a (PbTiO$_3$)$_{16}$/(SrTiO$_3$)$_{16}$ superlattice, plane-view STEM images reveal long-range ordered arrays of circular features with a size of 8 to 9 nm, suggesting that this polar order extends through the film over many hundreds of nanometers length scale [Fig. 27(d)]. Low-resolution, cross-section dark-field-TEM imaging [Fig. 28(a)] in turn revealed a pseudo–long-range periodic array of intensity modulations along both the in- and out-of-plane directions of the superlattice. Atomic-scale polarization mapping using a displacement vector-mapping algorithm on both plane-view and cross-section HAADF-STEM images was used to extract the local polarization structures [Figs. 28(a) and 28(b)]. The reverse titanium-displacement vector mapping [Fig. 28(a), top image] based on a high-resolution plane-view HAADF-STEM image [Fig. 28(a), bottom image] reveals a single skyrmion bubble. The reversed titanium displacement is converging from the edge to the center, corresponding to a Néel-like skyrmion structure. To complement this, a vector displacement mapping of cross-section HAADF-STEM imaging [Fig. 28(b)] shows a cylindrical polar region with antiparallel (up-down) polarization. The polarization vector rotates at the boundaries near the PbTiO$_3$/SrTiO$_3$ interfaces, which is consistent with the divergence of polarization observed in plane-view images. The combined plane-view and cross-section vector displacement mapping reveals a Néel-like structure at the top of the PbTiO$_3$ layer. Along these lines, four-dimensional (4D) STEM with an electron microscope pixel array detector (EMPAD) provides information about the central PbTiO$_3$ layers. In 4D STEM, the full momentum distribution (that is, the electron diffraction pattern) can be collected at every scan
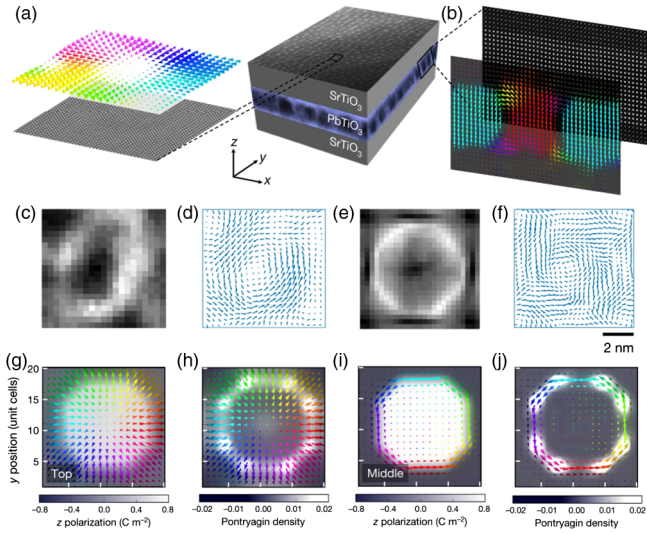
FIG. 28. (a) Reversed Ti-displacement vector map (top image) based on the atomically resolved plane-view HAADF-STEM image (bottom image) of a single skyrmion bubble showing the Néel-like skyrmion structure. The sketch of the superlattice in the central top panel is overlaid with the planar-view dark-field TEM image and gives a top view of the superlattice. (b) Ti-displacement vector map (front image) based on the atomically resolved cross-section HAADF-STEM image (back image) showing a cylindrical domain with antiparallel (up-down) polarization. The sketch in the central top panel is overlaid with the cross-section dark-field TEM image and shows the cross-section view of the superlattice. (c),(d) 4D STEM image of a $[(PbTiO_3)_{16}/(SrTiO_3)_{16}]_8$ superlattice giving the (c) ADF image and (d) maps of polar order using the probability current flow, which were reconstructed from the same 4D dataset. (e),(f) Multislice simulations of the beam propagation through the model structure from Fig. 27(c) showing (e) the ADF image and (f) the probability current flow, which were analyzed using the same process as the experimental data. The signals are not simple projections but are instead weighted by electron-beam channeling toward the middle of the skyrmion bubble, where the polarization exhibits a Bloch-like character. (g) Néel-like skyrmion at the top interface between $SrTiO_3$ and $PbTiO_3$. (i) Bloch-like skyrmion at the central plane in $PbTiO_3$. The up and down domains are represented as white and gray regions, respectively. (h),(j) Corresponding Pontryagin densities. The arrows represent the normalized electric dipole moments in the *x-y* plane. From Das *et al.*, 2019.

position by the EMPAD. From the diffraction patterns collected on the EMPAD, the reconstructed low-angle annular dark-field (ADF) image [Fig. 28(c)] and the probable current flow in *x* and *y* giving the vector components of polar order [Fig. 28(d)] can be obtained. This is largely weighted toward the Bloch-like skyrmion in the middle of the $PbTiO_3$ layer. The combination of Néel and Bloch skyrmions is further confirmed by second-principles calculations [Fig. 27(c)]. As mentioned in Sec. III.B.4, the mathematically rigorous topological characterization of bubblelike patterns constitutes an important (but still open) question. However, considering the fact that there is always a danger in correlating the objects from different dimensionalities, Das *et al.* (2019) carried out layer-by-layer projections of the local electric dipoles
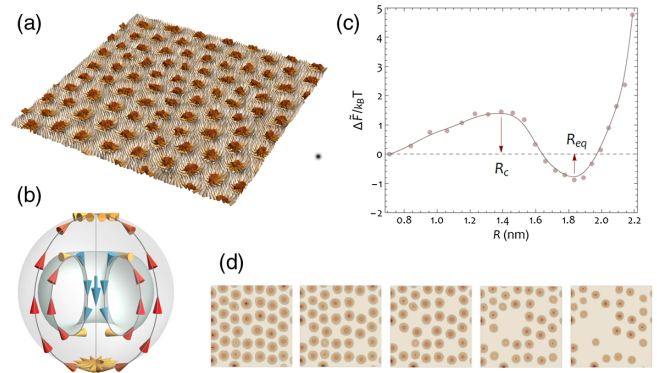

FIG. 29. (a) In-plane cross section of the simulated dipolar structure of the hexagonal bubble lattice wherein each bubble is topologically equivalent to a Néel skyrmion. (b) Schematic illustration of the equilibrium structure of a spherical polar bubble averaged over thermal fluctuations (c) Calculated dependence of the free energy on the polar bubble size indicative of a constrained nucleation process. R_c and R_{eq} denote the critical and equilibrium radii. (d) Field-induced sublimation of polar bubbles and formation of the bubble gas. The distribution of the out-of-plane polarization displays increasing bias field magnitudes from left to right. From Nahas, Prokhorenko *et al.*, 2020.

obtained from the second-principles calculations. This shows how the three-dimensional structure can be described as an evolution of two-dimensional skyrmionlike structures along the film normal. The analysis of the polarization texture in a plane at the top and bottom $PbTiO_3/SrTiO_3$ interface reveals Néel-like skyrmion structures with a positive or negative divergence of the polarization pattern [Fig. 28(g)]. But in a plane at the center of the $PbTiO_3$ layer, the local order parameter has a full rotational component and resembles a Bloch-like skyrmion [Fig. 28(i)]. Within this evolution, one must notice how these structures are topologically equivalent, since they can be transformed from one into the other by a continuous deformation. Indeed, for every layer we can compute the topological charge N [Eq. (2)], where the integral is taken on the corresponding two-dimensional plane. The topological charge is found to be equal to $+1$ in every layer [Figs. 28(h)–28(j)].

Further characterization of polar bubbles in $Pb(Zr_{0.4}Ti_{0.6})O_3/SrTiO_3/Pb(Zr_{0.4}Ti_{0.6})O_3$ sandwiches (Nahas *et al.*, 2020) have revealed similar topological features. Namely, the in-plane distribution of local electric dipoles averaged over thermal fluctuations was shown to closely match the Néel skyrmion texture [Fig. 29(a)], with the calculated skyrmion number in each dipolar plane equal to the number of bubble domains. This result confirmed that polar bubbles in these heterostructures also have a skyrmionic nature.

At the same time, the current understanding implies that the physical nature and properties of polar bubbles in PZT- and bubble skyrmions in $PbTiO_3$-based heterostructures are distinct in that (Nahas, Prokhorenko *et al.*, 2020) (i) the Néel nature of their stationary polar structure [Fig. 29(b)] makes polar bubble skyrmions in PZT achiral; (ii) much like magnetic skyrmions, polar bubbles in PZT are stabilized by a symmetry-breaking field and tend to form hexagonal domain lattices; (iii) the out-of-equilibrium formation of polar bubbles in PZT

can be described as a nucleation process [Fig. 29(c)], wherein the domain growth is constrained by the depolarization field; and (iv) external bias field can be used to trigger a sublimation of bubbles (Nahas *et al.*, 2020; Nahas, Prokhorenko *et al.*, 2020) prior to the transition to the homogeneously polarized state [Fig. 29(d)]. Recently, polar bubbles were also experimentally found in freestanding $PbZr_{0.2}Ti_{0.8}O_3/SrTiO_3$ multilayers (Bakaul *et al.*, 2021), while bubblelike structures were observed in $PbTiO_3/SrTiO_3$ bilayers (Han *et al.*, 2022) and epitaxial $BiFeO_3/SrTiO_3$ superlattices (Govinden *et al.*, 2022).

C. Polar labyrinth

The self-patterning and nonequilibrium dynamics in PZT ultrathin films subjected to compressive misfit strain were analyzed through extensive Monte Carlo and molecular dynamics effective Hamiltonian simulations (Nahas, Prokhorenko *et al.*, 2020). This study revealed that, due to the crystalline anisotropy introduced by compressive strain, the system behaves as an electrically manipulable phase-separating system. Upon abruptly cooling the system under a low external electric field, long-wavelength spinodal instability entails the emergence of a labyrinthine pattern, while under high field values localized fluctuations lead to the nucleation of a quasihexagonal bubble lattice. For intermediate electric fields, additional mesophases were discovered: the disconnected or self-avoiding labyrinth phase and the mixed meron-bubble pattern called the bimeron-skyrmion phase. These phases are all topologically distinct (see Sec. III) and can be obtained either in nonequilibrium conditions by abruptly cooling the system in certain electric-field and temperature ranges or through the application of a gradually increasing electric field on the labyrinth phase through progressive disconnection of the labyrinthine pattern. These results are encompassed in the nonequilibrium phase diagram of compressively strained lead zirconate titanate (Fig. 30).

The labyrinth pattern consists of meandering and interconnected domains with sharp interfaces and is highly degenerate. It is only weakly unstable and has an internal energy that is only 0.6% higher than that of the ground state (vortex stripes obtained upon slowly cooling the system). The labyrinth is kinetically arrested and effectively frozen at low temperatures. It retains high-temperature properties (like the common local structure exhibited by glasses and their liquid phases), such as the overall absence of long-range orientational order at the mesoscale mirrored by its structure factor, which has a ring-shaped spectral weight. Moreover, there is a local tendency of adjacent domains to order by adopting one of the two lower equilibrium states of the Hamiltonian (with either horizontal [100] or vertical [010] local periodicity of parallel stripes). The labyrinthine state inherently features frustration and can be seen as a mosaic pattern consisting of a spatial mixture of tiles with different realizations of local order. Upon slowly heating the labyrinthine state, thermal activation effects come into play, and the resulting kinetic unfreezing elicits the phenomenon of inverse transition (Nahas *et al.*, 2020), whereby a state with higher symmetry transforms into a lower symmetry one. These inverse transitions were predicted to occur in ultrathin PZT films and were experimentally observed in $BiFeO_3$ thin films (Nahas *et al.*, 2020). During such transition in PZT, the more symmetric labyrinthine phase experiences a lessening of its junctions, resulting in a transient reordering and the occurrence of the less symmetric nano stripe state at $T_{inv} \sim 200$ K, before transitioning to the paraelectric state at a transition temperature of $T_c \sim 380$ K. The coarsening of structures is conveyed by the diffusion and relaxation of topological defects localized at the junction of different tiles and reconciling discrepancies in their prevailing local orientations and/or wavelengths. The straightening of the labyrinthine pattern involves recombination or annihilation of defects, whereby a pair of meron-antimeron rebinds into a diffusing dislocation. The occurrence
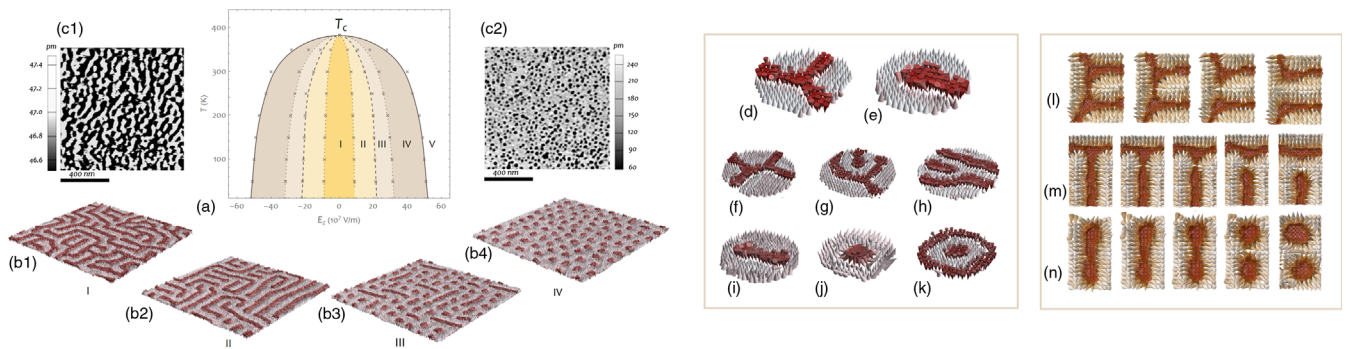
FIG. 30.   (a) Temperature-electric-field phase diagram of a $Pb(Zr_{0.4}Ti_{0.6})O_3$ ultrathin film. Phases I and II correspond to (b1) connected and (b2) disconnected labyrinthine patterns, respectively, while phases III and IV denote (b3) the mixed bimeron-skyrmion phase and (b4) the bubble phase, respectively. Light gray [red (dark gray)] dipoles are oriented along the [001] ([00$\bar{1}$]) pseudocubic direction. Phase V corresponds to a homogeneously polarized state. The dashed line separating phases II and III marks the spinodal-like boundary, while the solid line separating phases IV and V marks the binodal-like boundary. (c1),(c2) Experimental PFM amplitude images of PZT films with a one-unit-cell $SrTiO_3$ spacer and labyrinthine and bubble morphologies, respectively. (d)–(k) Elementary and composite topological defects within the predicted dipolar modulated phases in $Pb(Zr_{0.4}Ti_{0.6})O_3$ ultrathin film, namely, a threefold junction or (d) an antimeron, (e) meron, (f) saddle or fourfold junction, (g) the handle or meron-antimeron pair, (h) dislocation, (i) the bimeron or meron-meron pair, (j) the polar bubble, and (k) the target skyrmion pattern. (l)–(n) Numerical onsets of the disconnection processes of domains via the removal of a fourfold junction or saddle defect and of a threefold junction or antimeron, as well as the cleavage of an elongated bimeron into two bubbles. From Nahas, Prokhorenko *et al.*, 2020.

of topological defects in response to frustration has already been reported in ferroelectric relaxors (Nahas *et al.*, 2016), where hedgehogs and antihedgehogs (see Sec. III) were found at the boundaries of polar nanoregions in ferroelectric relaxors (Nahas *et al.*, 2016). Similarly, vortices and antivortices appear in a ferroelectric nanocomposite consisting of a square array of $BaTiO_3$ nanowires embedded in a $Ba_{1-x}Sr_xTiO_3$ matrix (Nahas, Prokhorenko, and Bellaiche, 2016). Therein, different arrangements of the wires' chiralities geometrically frustrate the matrix, which in response exhibits point topological defects featuring self-assembled ordered structures spatially fluctuating down to the lowest temperatures.

The labyrinthine pattern hosts a variety of topological defects, the classification of which can be made by considering two elementary point topological defects, the antimeron (or threefold junctions of $-1/2$ charge) and the meron (or stripe end points of $+1/2$ charge). Merons and antimerons can combine differently, yielding a plethora of composite defects such as saddle defects (superposition of two antimerons or a fourfold junction), handle defects (meron-antimeron pair), bimerons (elongated meron-meron pair), bubbles (contracted meron-meron pair), target skyrmions, and dislocations. Upon applying a homogeneous out-of-plane field, the labyrinthine pattern features topological junction instabilities and sequential topological transitions. The predicted evolutive topology of these self-patterned polar textures was confirmed by PFM experiments and is captured by the disconnection of domains via the removal of saddle defects (or fourfold junctions), antimerons (or threefold junctions), and the cleavage of elongated bimerons into two skyrmions (Nahas, Prokhorenko *et al.*, 2020).

AFM measurements further revealed that elementary point defects (meron and antimeron) are characterized by enhanced conduction that can be up to 50 times larger than the conduction at straight segments of domain walls. It was found that the typical current level is 0.2 pA in domains, 0.5–1.0 pA at domain walls, 15 pA at the meron, and 50 pA at the antimeron (Nahas *et al.*, 2020). Additionally, the transition from the hexagonal bubble lattice to the homogeneous state with increasing electric field exhibits hysteretic behavior associated with the dependence of the z component of polarization on the external electric field. Such history-dependent behavior can be leveraged to devise memristor-based solid-state synapses for unsupervised machine learning circuits. Further confirmation of the memristor behavior is provided by an estimate of the tunneling conductance dependence on the field magnitude and shows that the upper branch of this dependence corresponding to switching toward the monodomain state upon increasing field magnitude exhibits up to ~250% higher conductance than that of the inverse-path switching branch (Nahas, Prokhorenko *et al.*, 2020). Moreover, it was found that polar modulated phases (such as nanostripes, labyrinths, and hexagonal bubble lattices) are endowed with memory. Upon applying an out-of-plane electric field, the nanostripe domain transforms into a nano bubble lattice before yielding a monodomain state at high-enough electric-field values. The labyrinthine state exhibits an equivalent sequence of electric-field-induced morphological transitions. The two bubble states obtained from either the parallel stripe domains or the

labyrinthine ones are energetically equivalent. However, upon releasing the stabilizing external field, each of the two bubble states relaxes back to its parent state morphology, which was obtained before any electric-field treatment. This history-dependent behavior is rooted in a complex energy landscape and attests to an intrinsic memory effect (Nahas *et al.*, 2020). The topological phase transitions between polar labyrinth and bubble structures were further studied by Govinden *et al.* (2021), and these transitions were linked (Govinden, Rijal *et al.*, 2023) to the conservation of the residual depolarization field.

D. Physical phenomena and functional properties of vortices and skyrmions

1. Emergent chirality

When an object is not superimposable on its mirror image (i.e., it imparts a handedness), we call it a chiral object. Chirality is a geometrical property that is ubiquitous in nature: from the strength of the weak interactions according to the electroweak theory to its essential roles in the spontaneous symmetry breaking in subatomic particle physics, biophysics (the aminoacids and sugars in our bodies), and materials science (natural chirality in quartz crystals).

One of the most exotic and unexpected properties displayed by the nontrivial topological defects and textures discussed in this review is the occurrence of natural chirality. In this section, we analyze its origin, how to demonstrate its existence and measure the degree of chirality of the samples, and how to switch it with simple methods based on the applications of electric fields.

a. Origin of chirality

The topological patterns presented so far (dipolar vortices and electric skyrmions in superlattices or nanocomposites) are not expected *a priori* to be chiral, since the constituent elements are by themselves not chiral. However, when these polar textures form in an orderly manner within a superlattice, they are found to exhibit chirality. Therefore, the first question that has to be addressed is, what is the origin of the chiral behavior when such nonchiral materials are brought together? Is this an interface phenomenon or is it through the bulk of the superlattice?

Note that the presence of a vortex, i.e., a nonzero toroidal moment, does not immediately imply that the system would be chiral in three dimensions. As shown in Fig. 31(a), depending on the mirror plane such a structure can be directly superimposed onto its image or can require only a rigid translation of half a unit cell. These vortices would be chiral only in two dimensions, where we restrict ourselves to transformations that always retain the dipoles in the plane.

Chirality can arise in ensembles of such polar vortices and skyrmions as a consequence of a few symmetry-breaking pathways that are schematically illustrated in Figs. 31(b)–31(e). Chiral behavior can arise in polar vortices from the coexistence of the axial component of polarization (perpendicular to the plane defined by the vortices) with the vorticity of the clockwise and counterclockwise vortices, as predicted from first-principles-based effective Hamiltonians
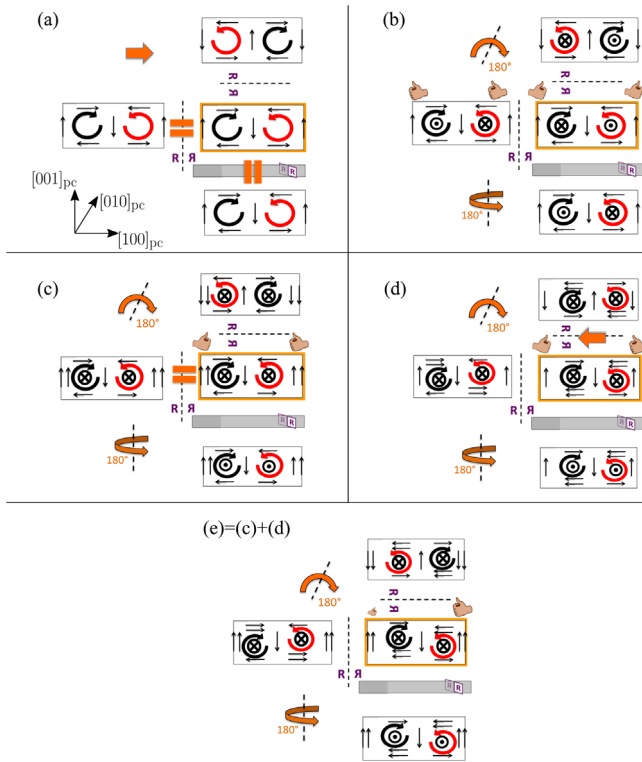
FIG. 31. Key features defining the chiral character of polar vortices. Straight arrows point along the direction of the local polarization. Clockwise (counterclockwise) vortices are represented as black (dark gray) [red (light-gray)] curled arrows. Circles represent the direction of the axial component of the polarization, with the sign indicated by a cross or dot. The original dipolar configuration in every panel is surrounded by a orange box. Three orthogonal reflections are then examined for each of the configurations. The mirrors are perpendicular to (left) $[100]_{pc}$, (upper) $[001]_{pc}$, and (bottom) $[010]_{pc}$. If the reflections can be mapped onto each other but not to the original one by means of rotations and translations, then the structure is chiral in three dimensions. If not, the configuration is achiral. (a) Vortices without an axial component of polarization (achiral in three dimensions). (b) Vortices coexist with antiparallel axial components of the polarization in neighboring vortices (chiral; the handedness is indicated in the original configuration and in the reflection in the left panel). (c) Vortices coexist with parallel axial components of the polarization in neighboring vortices. The sizes of the up and down domains differ (achiral). (d) Buckled vortices (nonzero offset between its centers) coexist with parallel axial components of the polarization in neighboring vortices. This favors a net polarization along the $[100]_{pc}$ direction, as represented by the horizontal double arrow. The structure is achiral; the mirror images can be superimposed on the original one by a rigid translation of half a unit cell (indicated by the horizontal orange arrow at the center of the upper mirror). (e) Combination of the cases sketched in (d) and (e). This structure is chiral since the handedness of one of the vortices is larger than the other, as indicated by the size of the hands.

in BaTiO$_3$/SrTiO$_3$ nanocomposites (Louis *et al.*, 2012). In a Bloch skyrmion, chirality originates naturally from the coexistence of the closed contour of the in-plane Bloch polarization and the out-of-plane polarization at the skyrmion core. Chirality can be quantified through the helicity,

whose mathematical expression is borrowed from fluid dynamics as (Moffatt and Ricca, 1992)

$$\mathcal{H} = \int \mathbf{p} \cdot (\mathbf{\nabla} \times \mathbf{p}) d^3 r, \tag{7}$$

where $\mathbf{p}$ is the local value of polarization. The integrand of Eq. (7) is a pseudoscalar quantity that changes its sign under a mirror symmetry operation. At a polar-vortex core, its sign depends on whether the direction of the curl is parallel ($\mathcal{H} > 0$, right-handed) or antiparallel ($\mathcal{H} < 0$, left-handed) to the axial component of the polarization. In an electric skyrmion, the curl of the polarization is determined by the direction of rotation of the Bloch component at the skyrmion wall. Qualitatively, the handedness can be assigned using the right-hand rule: curl the fingers of your right hand following the direction of the vortices. If the thumb points in the same direction as the axial component, then it is right-handed. If it points in the opposite direction, then it is left-handed. To have a global nonvanishing chirality, the axial component of the polarization must point in opposite directions at the center of consecutive clockwise and counterclockwise vortices (Shafer *et al.*, 2018) [Fig. 31(b)]. The evolution of this vortex structure and the chirality of the vortices in a pure vortex phase as a function of temperature was theoretically analyzed by Gómez-Ortiz *et al.* (2022b). Otherwise, in the case of a parallel alignment of the axial component of the polarization, the helicities coming from two consecutive topological defects cancel each other.

But even from such an achiral structure a second source of chirality can be triggered by combining two nonchiral symmetry-breaking distortions. The first one is related to the increase of one of the domains at the expense of the other, such that the up and down domains do not equally match in size [Fig. 31(c)]. This can be easily controlled by applying an electric field along the z-pseudocubic direction. In fact, in most experimental realizations there is always a small built-in field that makes this happen. The second one is the existence of a buckling affecting the core of the vortices [Fig. 31(d)]. These misalignments lead to a mismatch in the polarization pointing along the x-pseudocubic direction (left or right). None of the symmetry-breaking operations shown in Figs. 31(c) and 31(d), by themselves, are chiral. But the combination of the two generates an excess (deficit) of the clockwise (counterclockwise) rotations, making the entire system chiral [Fig. 31(e)]. Again the degree of chirality can be captured by the helicity modulus defined in Eq. (7), whose values for this second mechanism [Fig. 31(e)] are 2 orders of magnitude smaller than the ones produced in the first scenario [Fig. 31(a)]. However, as we soon discuss, this mechanism for chirality has a definite advantage, as it provides us with a relatively straightforward way to potentially control the handedness in a deterministic way.

b. Measuring chirality

One way to look for chirality in condensed-matter systems is to measure the interaction with circularly polarized electromagnetic radiation, i.e., circular dichroism, or optical rotation-absorption phenomena. In the case of $(PbTiO_3)_n/(SrTiO_3)_n$ superlattices, recent resonant soft x-ray diffraction (RSXD)

Chirality from RSXD in polar vortices

Chirality from RSXD in polar skyrmions
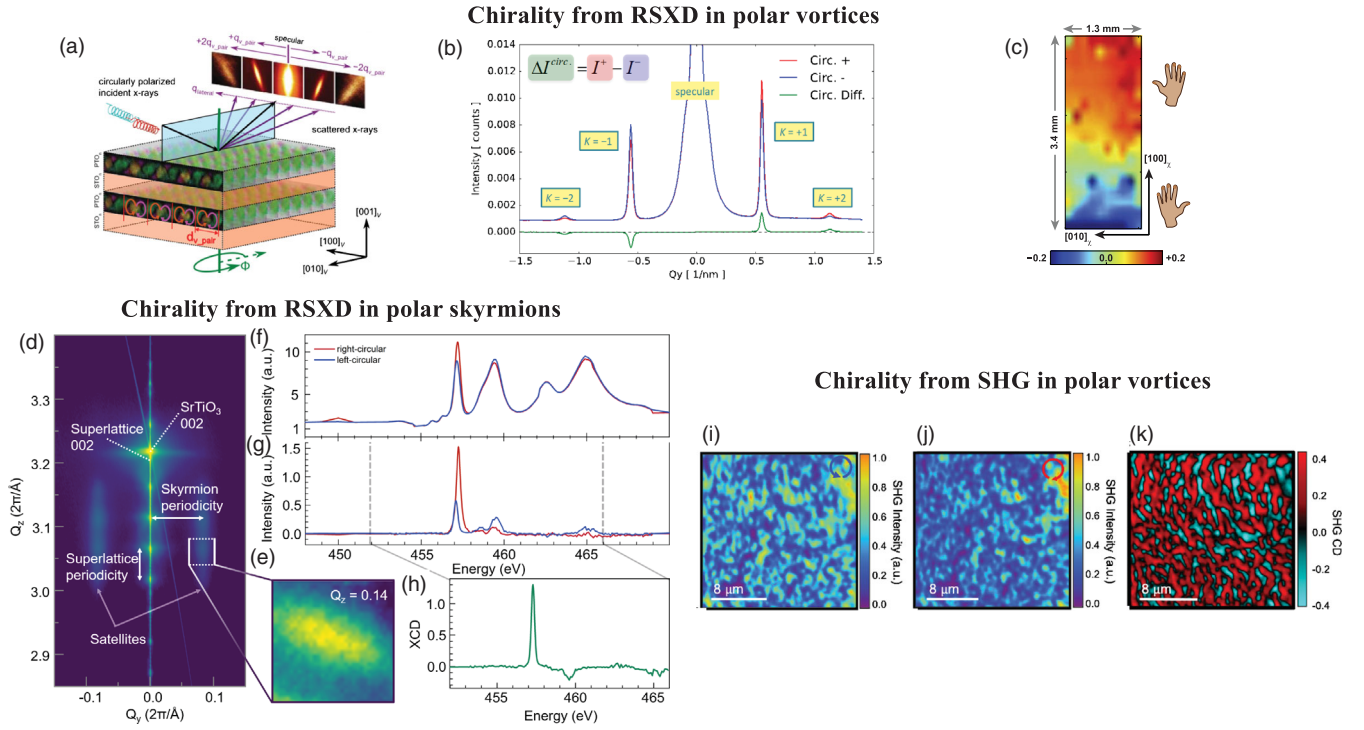
Chirality from SHG in polar vortices

FIG. 32. Different experimental techniques to characterize chirality in topologically nontrivial polar systems. (a) Schematic illustrating the experimental setup for the RSXD studies in polar vortices in $PbTiO_3/SrTiO_3$ superlattices. The data on the top right are actual images of the specular beam and various higher-order satellite peaks that can be observed. (b) Linecut of the scattered intensity vs lateral momentum transfer using right- (red) and left-circularly (blue) polarized x rays for an $n = 16$ superlattice. The difference in intensity between the two helicities is shown in green, displaying a significant dichroism at the vortex peaks, indicative of the chiral nature of the polar-vortex phase. (c) Map of XCD intensity at $q_{lateral} = +q_{pair}$ across an $n = 14$ sample. Regions of positive (negative) XCD indicate where chiral polar arrays have positive (negative) helicity. (d) Hard-x-ray reciprocal-space mapping about the $SrTiO_3$ (002) peak for a $[(PbTiO_3)_{16}/(SrTiO_3)_{16}]_8$ superlattice shows superlattice peaks along the Q_z direction, corresponding to an out-of-plane periodicity of about 12 nm, and satellite peaks along the Q_y direction, corresponding to an in-plane periodicity of about 8 nm. (e) Image from the CCD used to collect RSXD data, where the resonant diffraction peak is clearly visible. (f),(g) Spectra from a satellite peak for right- (red) and left-circularly (blue) polarized light. (h) The XCD difference spectrum (right-circular minus left-circular x-ray absorption spectrum) shows a clear circular dichroism peak at the titanium L_3 t_{2g} edge. (i) SHG images taken with right-circularly and (j) left-circularly polarized excitation in $PbTiO_3/SrTiO_3$ trilayers. (k) SHG CD calculated from the images shown in (i) and (j). (a)–(c) From Shafer *et al.*, 2018. (d)–(h) From Das *et al.*, 2021. (i)–(k) From Behera *et al.*, 2022.

studies have shown that the polar vortices (Shafer *et al.*, 2018) and polar skyrmions (Das *et al.*, 2021) do indeed exhibit strong circular dichroism (Fig. 32), which is also reminiscent of magnetic-topological structures. In hard-x-ray RSM studies, lateral satellites appear due to the regular spacing of the vortex [Fig. 32(b)] and skyrmion structures [Fig. 32(d)], where the spacing is $d(x_{pair})$ ($\sim$8 nm for skyrmions and $\sim$10 nm for vortices). These satellites occur at q vectors equal to $\pm n \times q(x_{pair})$, where $q(x_{pair}) = 2\pi/d(x_{pair})$. By tuning the energy of the x rays through the titanium $L_{3,2}$ edge (where electronic transitions from the $2p$ to $3d$ levels occur), absorption spectra are collected at q values corresponding to the satellite peaks. At the titanium $L_{3,2}$ resonance, effects from the electronic structure (specifically, the d-orbital configuration) are strongly enhanced. If the spiraling polar distortions that create the skyrmion or vortex phase are chiral, this will manifest as a nonzero circular dichroism since chiral objects interact differently with left- and right-circularly polarized light (Shafer *et al.*, 2018). By measuring the spectra with both right- and left-circularly polarized light [Figs. 32(b), 32(f), and 32(g)], subtracting the background fluorescence,

and taking the difference between the two [Figs. 32(b) and 32(h)], x-ray circular dichroism (XCD) is indeed observed, which is strongly indicative of chirality. Furthermore, resonant-scattering intensity is asymmetric with respect to the scattering vector and the sign of the circular dichroism as a function of the lateral scattering vector (Q_y). The origin of this circular dichroism has been attributed to the periodic modulation of anisotropic tensors due to the parity-even charge quadrupole moments that form in these heterostructures. While there is no charge quadrupole moment in the spherically symmetric $3d^0$ valence state of Ti^{4+}, the excited state $2p^5 3d^1 t_{2g}$ at the Ti L_3 resonance is known to have a quadrupole moment (Lovesey and van der Laan, 2018). Resonant elastic x-ray scattering was recently proposed as a promising application to elucidate the chiral structure of electrical polarization emergent in a ferroelectric oxide superlattice, through the interaction between the x-ray polarization vector and electromagnetic multipoles in a sample (Kim *et al.*, 2022). This method has the advantage of contributions from electric and magnetic channels simultaneously, making it especially suitable for multiferroic material structures.

Despite this progress in experimentally characterizing chirality, two aspects require further exploration. First, despite its intellectual sophistication, RSXD circular dichroism (CD) requires access to a synchrotron source. While there are several state-of-the-art beam lines worldwide, these experiments by design are not meant for rapid throughput. Second, and perhaps more important, they are limited in terms of spatial resolution (currently of the order of 100 μm); this will undoubtedly change with newer, brighter, and more coherent sources [such as those intended at the Advanced Light Source (ALS)]. This imposes a constraint in terms of pathways to characterize and manipulate the chirality. Therefore, optical approaches to probe chirality, as is conventionally done in the case of chiral molecules, would be fruitful. Specifically, optical second-harmonic-generation- (SHG-) based circular dichroism shows promise, and the preliminary results are encouraging. Behera *et al.* (2022) were able to observe regions of opposite CD in a sample that is made up only of vortices in $(SrTiO_3)_{20}/(PbTiO_3)_{20}/(SrTiO_3)_{20}$ trilayers [Figs. 32(i)–32(k)]. These measurements, done with a confocal optical microscope, yield a spatial resolution of ∼500 nm, which can be improved with an oil immersion lens down to ∼300 nm.

c. Switching the chirality

An aspect that is of fundamental interest is whether this chirality can be manipulated with an electric field. For practical applications, it would be essential to switch the handedness in a controlled, reversible way in mesoscale regions.

If the origin of chirality comes from the presence of antiparallel axial components of the polarization at the center of the counterrotating vortices [Fig. 31(b)], both the right- and left-hand enantiomers belong to the same homotopy class. Therefore, a continuous transition to transform one into the other might be envisaged. Here we propose three different paths, as sketched in Fig. 33. The first one (top row in the central panel) consists of a continuous 180° rotation of all the dipoles that form the vortices. However, there is one midpoint along the path where energetically costly head-to-head and tail-to-tail domain walls appear. Thus, although topologically allowed, such a transition implies a large energy barrier, which makes it unlikely. The second mechanism consists of a continuous approximation of the vortex cores, as sketched in the central panel of Fig. 33. But again the energy barrier to overcome is large: one of the domains along the z direction increases its volume at the expense of the other, and this translates into large depolarization fields. Moreover, the Néel components of the polarization would form head-to-head and tail-to-tail domains. The third path (bottom row in the central panel of Fig. 33) can be described as a homogeneous reduction of the axial Bloch component within the two vortex cores. At some point along the path, the axial component of the polarization vanishes, giving rise to an achiral structure. Beyond this point, a polarization at the center of the vortices opposite to the original one can be developed, changing the sign of the helicity. However, this procedure seems to be impractical, due to the difficulty of applying a spatially dependent external field that change its value over the length scale of the separation of the vortex cores (around 8 nm).
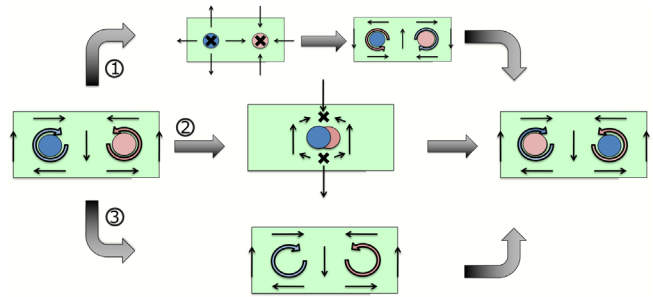

FIG. 33. Different paths to switch the helicity of the vortices when the chirality is due to the opposite direction of the axial polarization at the cores of neighboring counterrotating vortices. Straight arrows represent the direction of the local polarization in the *x-z* plane, while the curled arrows indicate the sense of rotation of the vortices. Orange (light gray) and blue (dark gray) circles represent different directions of the axial component of the polarization. The crosses are the points where head-to-head and tail-to-tail domains are formed. From Behera *et al.*, 2022.

Phase-field simulations have predicted alternative methods for switching the chirality in ferroelectric skyrmions (Tikhonov *et al.*, 2020) and polar vortices (Chen *et al.*, 2022) by applying homogeneous electric fields or with local surface charges (Liu, Wang *et al.*, 2022). The calculations of Tikhonov *et al.* (2020) were carried out in nanometric-size disks. The protocol implies the destruction of the skyrmion through a phase transition to a monodomain phase under high-enough fields, and the later nucleation of a new one after the gradual reversal of the field [Fig. 34(a)]. Since the applied field does not possess its own chirality, the handedness of the skyrmions that are formed depends on local fluctuations. They are included in the simulations through a new term in the energy functional that couples the polarization with its rotation. But experimentally these fluctuations might be out of control, and even the slightest one that would arise randomly would push the system into either of the degenerate "left" or "right" free-energy minima. Therefore, this mechanism would not be smooth (i.e., it would require the destruction of the system), not be uniform in space, and not be deterministic. Chen *et al.* (2022) also showed atomically resolved *in situ* STEM results, in this case in vortex arrays in $PbTiO_3/SrTiO_3$ superlattices. The rotation of the vortices could be changed, accompanied by the concomitant chirality reversal of the individual vortices, after the application and removal of the external field [Fig. 34(b)]. However, as in the previous case, the process requires the destruction of the vortex state. Neither the rotation reversal nor the position of the center of the vortices could be well controlled, since during the spontaneous back-switching the nucleation of the new vortices could be disturbed by random fields. Therefore, although the source of chirality proposed in Fig. 31(b) gives large values of the helicity density, it appears to be difficult to switch.

The question of how to connect chiral enantiomers in a controlled, deterministic, and reversible way using simple methods (application of homogeneous electric fields) becomes easier if the chirality is generated through a mechanism such as the one proposed in Fig. 31(e). In this case, the buckling of the vortices that control the chirality can be trivially controlled by means of an electric field applied along the $[100]_{pc}$ direction.
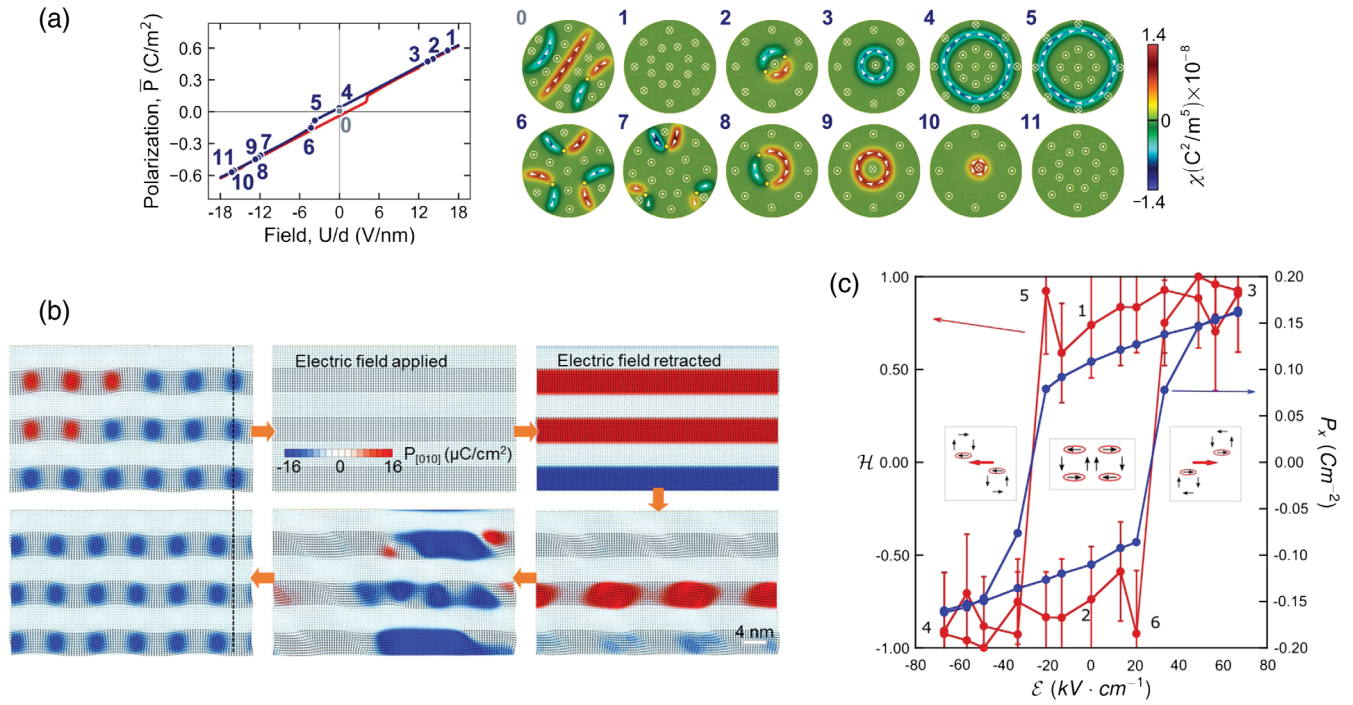
FIG. 34. Different mechanisms to switch the chirality of topologically nontrivial polar structures. (a) Distribution of the polarization and chirality for different homogeneous applied fields in a ferroelectric skyrmion. Left panel: hysteresis behavior of the polarization of the nanodot as a function of the applied field. The blue and red branches correspond to the up-down and down-up sweeps of the applied field. The numbers mark the different topological states of the polarization. From Tikhonov *et al.*, 2020. (b) Chirality switching of vortices by an electric field in $PbTiO_3/SrTiO_3$ superlattices. The blue and red in the pristine vortex array indicate the direction of the axial component of the polarization. The handedness can thus be determined for an individual vortex. From Chen *et al.*, 2022. (c) Helicity (red, left axis) and polarization (blue, right axis) for a $PbTiO_3/SrTiO_3$ trilayers as a voltage is applied along $[100]_{pc}$. Insets schematize the direct coupling between the sense of the buckling and the $[100]_{pc}$ component of the polarization. From Behera *et al.*, 2022.

Behera *et al.* (2022) demonstrated the existence of well-defined and repeatable hysteresis loops of both the in-plane polarization and the chirality [Fig. 34(c)] following this recipe in polar vortices in $PbTiO_3/SrTiO_3$ trilayers under epitaxially strained mechanical boundary conditions.

2. Negative permittivity

The phenomenon of negative capacitance has garnered extensive interest due to its exotic physics, as well as for its promise in applications in next-generation electronics (Salahuddin and Datta, 2008; Theis and Solomon, 2010; Khan *et al.*, 2011; Zubko *et al.*, 2016), specifically to overcome the "Boltzmann tyranny" in electronics. The origin of this negative capacitance, in addition to its connection with the ferroelectric multidomain state, has been theoretically discussed (Bratkovsky and Levanyuk, 2001; Luk'yanchuk, Sené, and Vinokur, 2018; Íñiguez *et al.*, 2019) and experimentally demonstrated (Zubko *et al.*, 2016; Yadav *et al.*, 2019; Das *et al.*, 2021). In essence, under certain open-circuit-like electric boundary conditions, ferroelectrics may be below their Curie point but fail to develop their homogeneous polarization. In this situation, the free energy of the ferroelectric is higher than it would be under more favorable (short-circuit) boundary conditions. In fact, this frustrated state can be thought of as if regions of the ferroelectric were at a maximum of its Landau-Devonshire-Ginzburg potential G. The high-energy regions can extend to the entire volume

of the ferroelectric (when the frustrated state is paraelectric-like, with no local polarization) or be restricted to the domain walls (if the ferroelectric adopts a multidomain configuration). Regardless, these high-energy regions are characterized by being locally unstable upon changes in the displacement vector D, so we have $\epsilon \propto \partial^2 G/\partial D^2 < 0$; hence, a local negative capacitance emerges [Fig. 35(a)].

Note that the entire volume of a sample in equilibrium cannot exhibit such a negative permittivity (Íñiguez *et al.*, 2019), since in that case it would spontaneously evolve to a state where the curvature of the free-energy landscape is positive. Hence, in the illustrative case of ferroelectric-dielectric superlattices (e.g., those formed by $PbTiO_3$ and $SrTiO_3$), the ferroelectric layers may display a local negative permittivity, but the permittivity of the dielectric layers is positive, making the overall permittivity positive as well. The electrostatic theory of ferroelectric-dielectric superlattices and the relationship between the negative permittivity of the ferroelectric layers and the voltage amplification in the dielectric ones were analyzed by Graf *et al.* (2022), where amplification up to tenfold has been predicted. A negative permittivity can also be achieved by bringing the ferroelectric out of equilibrium in the temporal regime (Khan *et al.*, 2015).

A direct measurement of the spatially resolved, equilibrium (steady-state) negative capacitance is rare in nature and was first observed microscopically in a vortex structure of $(PbTiO_3)_n/(SrTiO_3)_n$ superlattices (Yadav *et al.*, 2019). The existence of negative permittivity at the vortex core
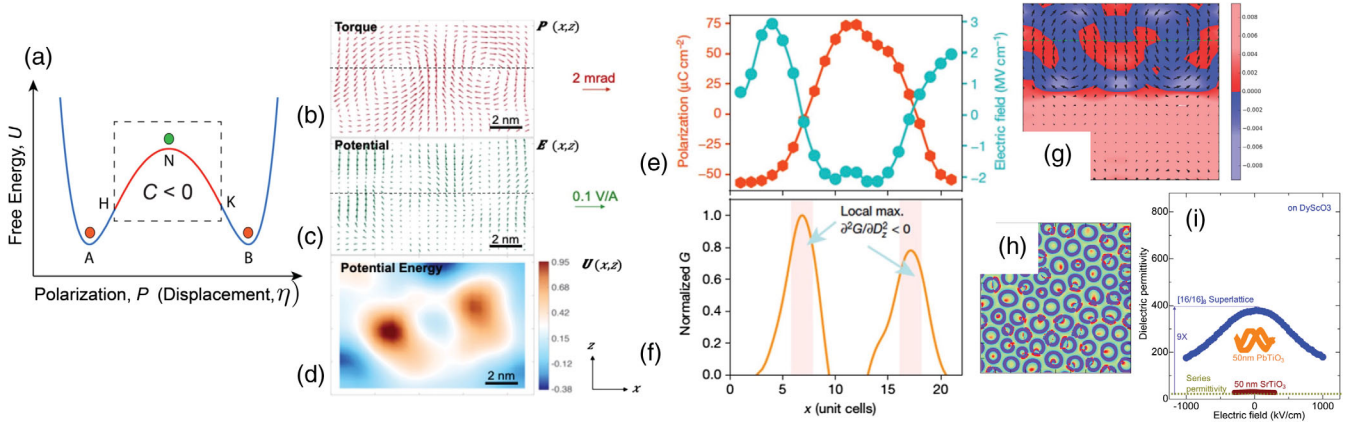
FIG. 35. (a) Schematic of the classical double-well-energy landscape for a ferroelectric. *A* and *B* denote the stable polar states, and the regions shaded in red denote areas with negative curvature, i.e., negative permittivity. (b) Polarization vector map from a subregion of a PbTiO$_3$ layer embedded within a $(SrTiO_3)_{12}/(PbTiO_3)_{12}$ superlattice as measured using STEM. (c) Local electric field in a PbTiO$_3$ layer corresponding to the region shown in (b). (d) Local potential-energy map in the same region as shown in (a) and (b). (e) Variation in the *z* components of local polarization (P_z, red hexagons) and electric field (E_z, blue circles) along a horizontal line [indicated by the horizontal lines in (b) and (c) that pass through the core of the vortices]. (f) Local energy density estimated from the variation in P_z and E_z along the same line. Regions around the core (marked with arrows) have negative curvature $\partial^2 G/\partial D^2 < 0$. (g) Second-principles calculation of the inverse of the local dielectric constant in the vortex structure (blue for negative and red for positive regions). (h) Phase-field calculation of a cross section of an array of skyrmions showing the regions of negative permittivity (identified by the dark blue rings). (i) Macroscopic dielectric permittivity as a function of electric field for vortices in $(SrTiO_3)_{16}/(PbTiO_3)_{16}$ superlattices with different periodicities. (a)–(g) From Yadav *et al.*, 2019. (h)–(i) From Das *et al.*, 2021.

and the potential-energy landscape across the vortex structure were directly probed via 4D STEM. These imaging experiments were carried out in cross-section samples and show the clockwise-counterclockwise vortex pair [Fig. 35(b)]. The long-range electric fields can be mapped out from the deflection of the electron-beam pattern due to the Lorentz force [Fig. 35(c)] (Kittel, 1966). The spatial distribution of the polarization (P_z) and the electric field (E_z) [Fig. 35(e)] are measured by focusing along the dashed horizontal line profile [Figs. 35(b) and 35(c)], which goes through the vortex core [the magnitude of the measured polarization was calibrated using the polarization of PbTiO$_3$ as a reference (Watanabe, 2005)]. With both the measured electric field and polarization, one can calculate the local potential energy of the system using $dG = EdD$, where $D_z = \epsilon_0 E_z + P_z$. The estimated potential energy (G) as a function of P_z across the vortex reveals the existence of a local potential-energy maxima $\partial^2 G/\partial D^2 < 0$ at the location of the vortex core, where P_z is small [Fig. 35(f)], thus illustrating that the negative capacitance exists in clockwise-counterclockwise vortex core (Yadav *et al.*, 2019). Second-principles and phase-field simulations corroborate that the regions displaying a negative capacitance are those significantly more responsive that the system as a whole, i.e., those with the higher local energy and the higher electronic susceptibility. Those regions are located at the domain walls (center of the vortices) and at the interfaces between SrTiO$_3$ and PbTiO$_3$ [Fig. 35(g)]. The existence of such regions of negative capacitance in the material actually leads to an enhancement of the effective dielectric permittivity that can then be probed even by macroscopic measurements (Das *et al.*, 2021). This phenomenon is not restricted to polar vortices. In addition, polar skyrmions display an enhancement of the dielectric permittivity due to the appearance of local

negative capacitance regions at the surface of the skyrmion [Fig. 35(h)]. Of greater interest is the fact that such an enhanced dielectric permittivity can be significantly tuned with an electric field [Fig. 35(i)]. This occurs through the destruction of the vortex or skyrmion state under the electric field and the superlattice converts into a "normal" ferroelectric layer, thus representing a topological-phase transition accompanied by a change in the topological charge from a finite value to zero at a finite field. Removal of the electric field restores the skyrmionic state.

Besides these works on polar superlattices, the experimental results of Kim *et al.* (2005) served as motivation for a simulation study of ferroelectric Pb(Zr, Ti)O$_3$ dots, wires, and films (Ponomareva, Bellaiche, and Resta, 2007). Ponomareva, Bellaiche, and Resta computed the external dielectric susceptibility (i.e., the polarization response to the external electric field) and the internal susceptibility (that is, the polarization response to the average internal field) in the nanostructures as a function of the electrical boundary conditions. While the external susceptibility was always positive, as is consistent with the stability requirement (Dolgov, Kirzhnits, and Maksimov, 1981), the internal one was found to be negative over a wide range of boundary conditions for all kinds of these nanostructures, including those that adopt complex electric dipolar patterns (such as vortices). Finally, note that other topological states, like electric hopfions (Luk'yanchuk *et al.*, 2020), have also been predicted to naturally yield a negative capacitance response.

3. Dynamical properties

Ferroelectric nanostructures have been shown to display extremely unusual dynamical properties. For instance, Ponomareva and Bellaiche (2008) found in atomistic

simulations that $Pb(Zr_{0.4}Ti_{0.6})O_3$ films having bubbles or skyrmions respond in an unusual way under picosecond timescale strain pulses: a large change in polarization not only occurs but is also accompanied by a time delay between polarization and strain. In other words, the polarization does not immediately follow the strain pulse via the "usual" (electrostrictive) coupling law. This time delay was revealed to be governed by the "slower breathing" of dipolar inhomogeneities and explained some puzzling experimental data (von Korff Schmising *et al.*, 2007). Dynamics were also computationally studied in a $Pb(Zr_{0.4}Ti_{0.6})O_3$ ultrathin film having nanostripe domains and subject to an ac electric field (Zhang, Herchig, and Ponomareva, 2011). Its domain wall was found to act as an elastic object having a mass that is dependent on the film's thickness. Consequently, these domain walls can induce resonance or relaxational dynamics depending on the film's thickness. A general theory of dynamics in nano-objects, as well as a striking dynamical coupling between the nanostripes and sinusoidal-in-time strain deformations, were reported by Zhang, Herchig, and Ponomareva (2011). Other computations about dynamics predicted the occurrence of pulses of magnetization when (nonmagnetic) $Pb(Zr_{0.4}Ti_{0.6})O_3$ ultrathin films undergo sudden changes in the morphology of their nanodomain structure as a response to an ac gigahertz electric field (Prosandeev *et al.*, 2015) [similar magnetoelectric effects were predicted five years later by Juraschek *et al.* (2019)]. A simple equation relating the time derivative of the electric toroidal moment and the product between the electric polarization and its time derivative was developed to explain these pulses of magnetization in moving ferroelectric domain walls. This prediction appears to be in line with experiments done in the 1980s (Flёrova and Bochkov, 1981, 1982; Popov, Tikhomirova, and Phlerova, 1985).

Moreover, Herchig and Ponomareva (2017) employed an effective Hamiltonian technique to study polar soft mode dynamics in nanowires made of $PbTiO_3$ under open-circuit electric boundary conditions, but subject to different stresses. A phonon mode of high frequency (varying between 200 and 295 cm^{-1}) was found there, unlike in the bulk counterpart and independently of the applied stress. It was proposed to be inherent to the large depolarization field resulting from open-circuit electric boundary conditions. Another computational study aimed at investigating dynamics of vortices in a stress-free nanocomposite made of periodic squared arrays of $BaTiO_3$ nanowires embedded in a "less ferroelectric" $SrTiO_3$ matrix. Toroidic modes resulting from the fluctuations of the electric toroidal moment were found in the terahertz regime, in addition to the usual polar phonon modes that are associated with the fluctuation of the electrical polarization (Gui and Bellaiche, 2014). It was predicted that the resonant frequency of a specific toroidic mode softens via a square-root law when the temperature approaches the paratoroidic-to-ferrotoroidic transition temperature at which electric vortices form, as analogous to the behavior of the so-called soft mode in ferroelectric bulks near the Curie temperature (Scott, 1974; Shirane, 1974). The dynamics of this toroidic mode was further discovered to originate from the fluctuation of the (self-organized within vortices) azimuthal component of individual electric dipoles. Consequently, it was suggested that toroidic modes can be thought of as pendulums, while the

usual polar modes are known to be represented by another type of harmonic oscillators, namely, springs. This analogy raises the question of whether toroidal moments can give rise to a new particle (via the de Broglie correspondence between waves and particles), in the same way that typical oscillations of ions generate phonons. The answer is currently unknown, to our knowledge. Finally, we note that the dynamical response of ferroelectric multidomain structures and its connection to negative capacitance were discussed by Luk'yanchuk, Sené, and Vinokur (2018).

E. Merons, hopfions, and other members of the topological family

Vortices and skyrmions are not the only topological structures that can be found in polar oxide nanostructures and superlattices. In Sec. V.E.1 we describe other nontrivial topological patterns that have received increasing attention during the last few years.

1. Dipolar waves and dipolar disclinations

Dipolar waves where the local polarization behaves like a fluid that changes direction gradually and continuously have been experimentaly observed in $PbTiO_3/SrTiO_3$ multilayer films by means of quantitative HRTEM (Lu *et al.*, 2018) [Fig. 36(a)] and aberration-corrected HAADF-STEM imaging (Gong *et al.*, 2021). Together with the dipolar waves, another interesting feature appears close to the top or the bottom interface under the shape of a "cylindrical chiral bubble"; see the blue circle in Fig. 36(a) for the experimental image, and the red circle in Fig. 36(c) for the theoretical computations. At other parts of the $PbTiO_3$ layer, *dipolar disclinations* similar to those observed in magnetic systems are observed. There the structure breaks in tail-to-tail domains along the *y* direction,

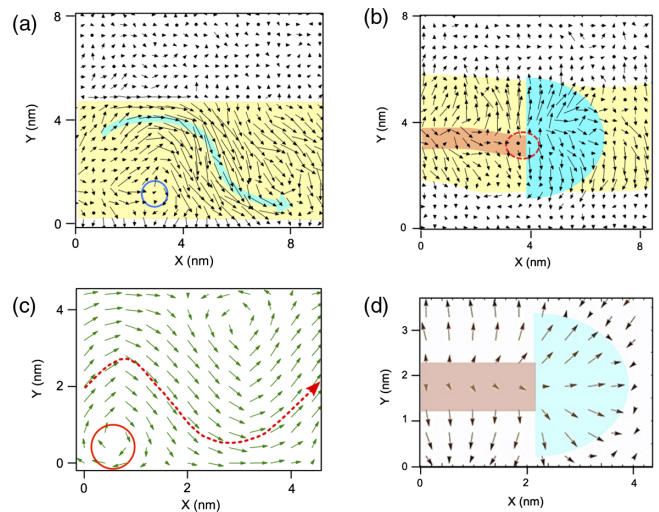FIG. 36. (a) Dipolar waves and (b) dipolar disclination observed by HAADF STEM in $PbTiO_3/SrTiO_3$ superlattices grown on a $SrTiO_3$ substrate. (c) Numerically simulated equilibrium dipolar waves and (d) metastable disclinations in a $PbTiO_3$ film under -0.6% compressive strain show excellent reproduction of the experimental observations in (a) and (b), respectively. From Lu *et al.*, 2018.

tilting to in plane in a domain wall marked as a brown region in Figs. 36(b)–36(d). At the end of the domain wall, the dipole moments of a few unit cells become close to zero. Around this point, another distinct configuration of dipoles is formed (blue area), where the dipoles align essentially along the radius directions and point out, forming a half circle. The observed phases were in good agreement with first-principles-based effective Hamiltonians of $PbTiO_3$ under compressive strain of -0.6% (Lu *et al.*, 2018). This compressive strain is essential for observing the transition from vortices to dipolar waves.

Similar dipolar waves were predicted for $Pb(Zr_{0.52}Ti_{0.48})O_3$ ultrathin films under open-circuit electric boundary conditions, small compressive strains, and low temperatures (Sichuga and Bellaiche, 2011). They are formed as a consequence of the movement of the vortex centers toward the surfaces, a fact that can be controlled with the epitaxial strain. Note that in this system the polar mode coexists with oxygen octahedral tiltings.

2. Merons

Merons (antimerons) are particlelike structures distinct from skyrmions (antiskyrmions) that were originally described in the context of quark confinement (Callan, Dashen, and Gross, 1978, 1994). Merons and antimerons in a magnetic system commonly feature an upward or downward magnetized core and an in-plane spin arrangement at their periphery (Fig. 37). In contrast, skyrmions and antiskyrmions most often feature homogeneous out-of-plane
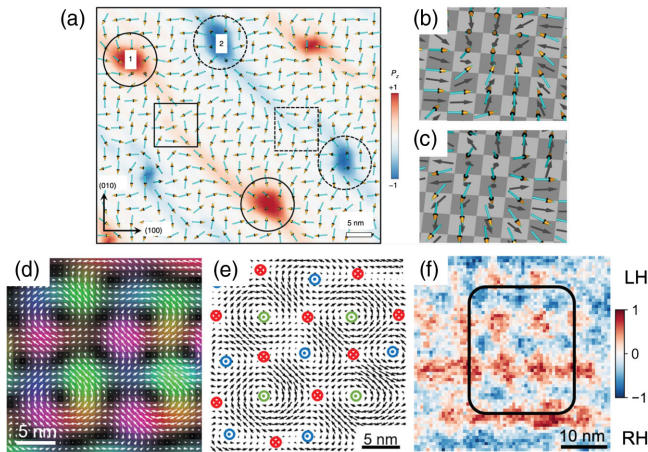

FIG. 37. (a) Polarization vectors in 5 nm $PbTiO_3/SmScO_3$ $(001)_{pc}$ film, obtained from the phase-field simulation with an experiment-inspired lattice model. Convergent and divergent merons are marked with solid and dashed circles. (b),(c) 3D polarization vectors of the two merons marked 1 and 2 in (a), respectively. (d) In-plane polarization mapping exhibiting the local ordered meron textures in $[(PbTiO_3)_{16}/(SrTiO_3)_{16}]_8$ lifted-off membranes at 373 K. (e) Details of (d) where vortices (clockwise, green; counterclockwise, blue) and antivortices (red) are labeled. The dots in the circles represent polarization pointing out of the page, while the cross points into the page. (f) Map of the local regions showing different handedness. The positive (negative) regions indicate the polar textures having left-handed (right-handed) chirality in the meron phase. (a)–(c) From Wang *et al.*, 2020. (d)–(f) From Shao *et al.*, 2023.

order at their boundary. However, note that such a geometry is not a necessary condition to have a meron. For instance, in some cases disclinations can also be characterized as merons (Ezawa, 2011; Hierro-Rodriguez *et al.*, 2017). Topologically, merons are characterized by a rational topological characteristic and are not topologically protected states. For example, in ferroic materials merons typically have a half integer topological charge. For this reason they are presented in many cases as the topologically equivalent structure to one-half of a skyrmion. Merons feature a localized topological charge density distribution. For this reason, merons can be assigned a charge according to Eq. (2). However, this charge is not topologically invariant. The sign of the charge determines whether we have a meron (topological charge of $+1/2$) or antimeron (topological charge of $-1/2$). Magnetic merons were introduced to explain certain anomalies in quantum Hall systems (Moon *et al.*, 1995). Magnetic meron square lattices were discovered in the chiral magnet $Co_8Zn_9Mn_3$ (Yu *et al.*, 2018). More recently single meron pairs were created and stabilized in a continuous in-plane magnetized Permalloy film by local vortex imprinting from a Co disk (Gao *et al.*, 2019). In ferroelectric materials, merons with a fractional charge of $\pm1/6$ were first predicted simultaneously with the skyrmion (Nahas *et al.*, 2015). The first observation of ferroelectric $1/2$-charged merons with a vortexlike geometry typical of spin systems had to wait a couple of years. At that time Wang *et al.* (2020) were able to visualize at the atomic scale such topological structures by aberration-corrected STEM in ultrathin $PbTiO_3$ films under tensile epitaxial strain when grown on an orthorhombic (110)-oriented $SmScO_3$ substrate [Figs. 37(a)–37(c)]. At the same time, Nahas *et al.* (2020) realized that dipolar disclinations observed earlier in $PbTiO_3/SrTiO_3$ multilayers (Lu *et al.*, 2018) also carry $1/2$ of the skyrmion number and, in this sense, are equivalent to merons (Ezawa, 2011; Hierro-Rodriguez *et al.*, 2017). Nahas *et al.* (2020) and Nahas, Prokhorenko *et al.* (2020) also reported emergence of disclinationlike merons in PZT-based heterostructures and $BiFeO_3$ thin films. These merons were associated with enhanced tunneling conductance revealed by conductive atomic force microscopy measurements (Nahas *et al.*, 2020). Nahas *et al.* (2020) also reported a sequence of topological transitions between polar meron, bimeron, and polar-skyrmion states. More recently Shao *et al.* (2023) reported a topological transformation from a skyrmion state (with topological charge of $+1$) to an ordered square lattice of merons (with topological charge of $+1/2$) by varying the temperature and elastic boundary conditions in $[(PbTiO_3)_{16}/(SrTiO_3)_{16}]_8$ lifted off membranes [Fig. 37(d)]. The structural transformation is accompanied by a change in the chirality, which has a well-defined handedness in the room-temperature skyrmionic phase and disappears in the high-temperature meron lattice phase [Fig. 37(f)].

3. Hopfions

Hopfions are another topological formation that appear in a broad variety of natural phenomena, from high-energy physics, cosmology, and astrophysics to biology, magnetodynamics and hydrodynamics, and condensed-matter physics. They are the paradigmatic knotted solitons and can be defined as a

knot in a three-dimensional continuous unit vector field that cannot be unknotted without cutting. Hopfions are classified according to the Hopf invariant [Eq. (3)].

Minimizing a Ginzburg-Landau functional coupled with electrostatic and elastic degrees of freedom, Luk'yanchuk *et al.* (2020) derived their existence in spherical nanoparticles. They would be the result of the delicate balance between developing a local polarization as close as possible to the equilibrium value and minimizing the depolarization energy. This competition yields to a divergence-free polarization field, where **P** is always tangent to the surface of the particle. A vortex texture complies with this condition. But these vortices display a singularity (a position where the polarization is zero) at its center. The tendency to develop a nonvanishing and continuous polarization pattern to minimize the energy induces a continuous deformation of the vector field in the direction perpendicular to the vortex plane. The final picture of the polarization texture can be described as a set of interlinked circles or torus knots: the hopfion state [Fig. 7(c)]. As in the cases of vortices and skyrmions, the hopfions are chiral with a well-defined handedness.

4. Topological eclectons

A novel topological state called topological eclectons (because of the coexistence of a variety of simultaneous defects) has been predicted using first-principles-based effective Hamiltonians when two BaTiO$_3$ conical nanostructures (inverted with respect to each other and connected by their tips) are embedded in a SrTiO$_3$ matrix (Prosandeev *et al.*, 2019). In such structures, the ground state simultaneously possesses vortices, antivortices, hedgehogs, antihedgehogs, and a few skyrmions and is chiral in nature. It was predicted not only to be a ground state but also to have the possibility of readapting itself to form other unusual topological states or phases when temperature is varied or under electric fields. Despite the theoretical interest, it will be difficult to experimentally grow: created conical (or other nonplanar) nanostructures that are embedded in the SrTiO$_3$ matrix are likely to grow with other orientations on the conical sidewalls. Other shapes such as cylinders with square or circular cross sections may be more amenable. Nonetheless, the described study of conical nanocomposite geometry also gives an idea of possible polar structures in ferroelectric nanopillars and nanoneedles.

VI. MOVING FORWARD

Perhaps the most interesting attribute of correlated oxides is the complex interplay of several fundamental effects, each with a different energy scale, as shown in the inset of Fig. 38. This interplay leads to ground states that compete with one another, which consequently leads to large susceptibilities with respect to external stimuli. For example, the electronic
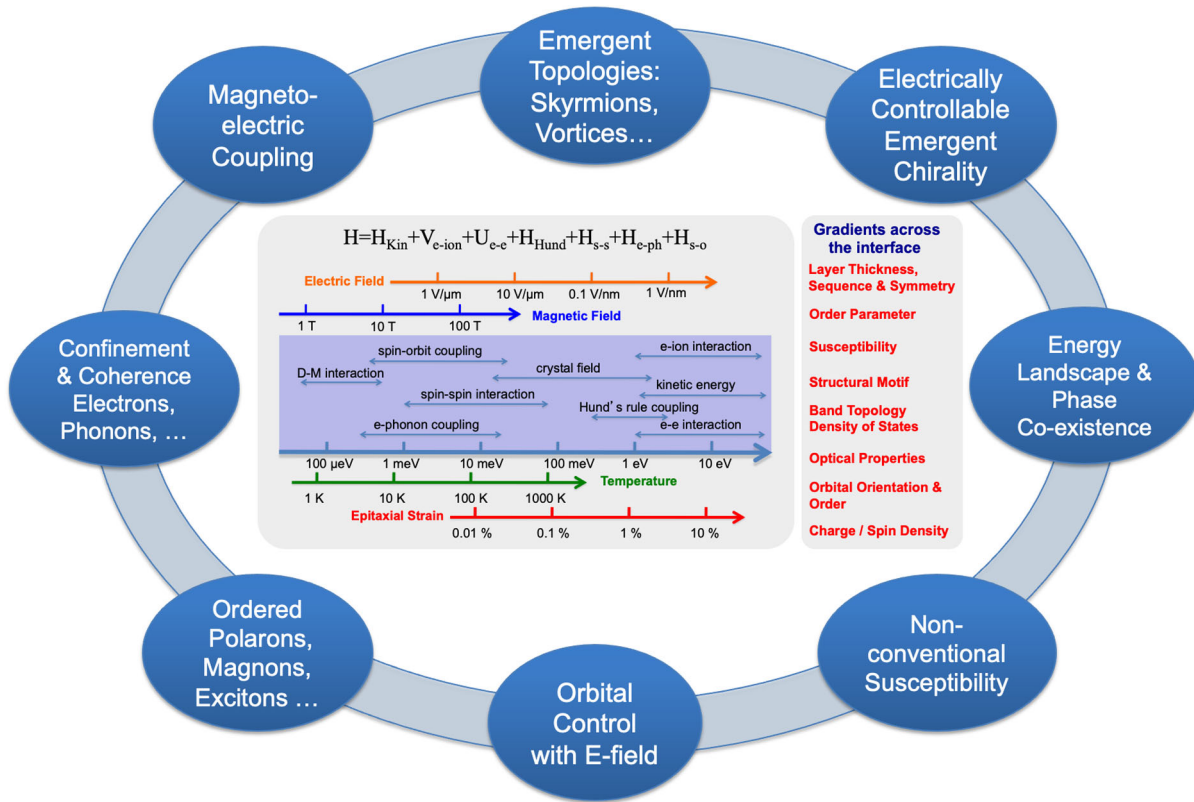
FIG. 38. Some of the possible new directions that can emerge from fundamental phenomena in oxide superlattices in which we can juxtapose the various elements of the Hamiltonian for the system (as shown in the central box). The alignment of energy terms and control parameters on the horizontal scale is intended to show the ranges where each control parameter, within its variability, is effective in tuning the various energy terms in transition metal oxides. The box to the right shows the various fundamental physical properties that could be tuned, leading to the various physical phenomena that manifest in such heterostructures. These are described in the blue oval bubbles in the outer ring.

correlations arising from on-site Coulombic repulsion and spin-orbit interactions have become powerful tools for creating new ground states. When we superimpose on this the power of epitaxy and the ability to artificially engineer the long-range order of the material as well as to create the types of topological patterns that have been discussed thus far, a plethora of new physical effects can arise that await experimental and theoretical study. A sampling of such phenomena is presented in the outer ring of Fig. 38. We now provide descriptions of some of these phenomena, noting that from a broad perspective this is limited only by one's imagination and the ability to translate them using the confluence of theory, synthesis, and measurements.

A. New ground states

1. Beyond PbTiO$_3$-based nanostructures

Progress over the past decade, especially the past five years, has demonstrated the existence of a variety of polar textures, as previously described. It is indeed noteworthy that almost all of the studies (with a few exceptions) have been on one model system, namely, ferroelectric PbTiO$_3$, upon which electrostatic and elastic boundary conditions are imposed to create the polar textures. This immediately begs the following questions: What else is possible? Can we predict new systems where these exotic phases appear? What other ferroelectrics display such polar textures? Using the theoretical framework presented earlier, it now seems possible to systematically describe the criteria for the formation of polar textures. What are the limits on the formation of such textures? How do other degrees of freedom (for example, octahedral tilts and rotations) play into the ability to form them? Can we use this as a framework to explore the possibility of creating other quasiparticles (magnons, excitons, polarons, etc.) that could couple to the polar textures? While these questions permeate the remainder of the review, we focus here on some relevant works.

Wu *et al.* (2012) demonstrated that a BaTiO$_3$/SrTiO$_3$ multilayer stack behaves as a dipole spring ferroelectric, named in analogy to exchange spring magnets in magnetic multilayers that show similar loops. Recently Guo *et al.* (2021) showed that toroidal polar topologies are possible in strained polymeric ferroelectrics as well. Vortex-antivortex domain structures have been stabilized in organic ferroelectrics (Tang *et al.*, 2020) and in a two-dimensional lead iodide organic-inorganic hybrid perovskite ferroelectric (Zhang *et al.*, 2020). Vortex-oriented ferroelectric domain quadrants have been found at the interface between two distinct MBE-grown group-IV chalcogenide monolayers (MLs): an in-plane polarized ferroelectric SnTe ML and a paraelectric PbTe ML (Chang *et al.*, 2021). Polar meron-antimeron networks have been theoretically predicted by first-principles simulations in strained and twisted bilayers of hexagonal boron nitride (Bennett *et al.*, 2023). Polar discontinuities at head-to-head and tail-to-tail domain walls in lead germanate (Pb$_5$Ge$_3$O$_{11}$) are obviated by the generation of characteristic saddle-point domain-wall morphologies with associated novel dipolar topologies due to domain bifurcation along two different axes (Tikhonov *et al.*, 2022). Self-confined

bubble domains with multiple polar topologies have been stabilized in bulk Bi$_{0.5}$Na$_{0.5}$TiO$_3$ ferroelectrics (Yin *et al.*, 2021). Polar and periodic polarization waves have been observed in tensile strained SrTiO$_3$ at room temperature (Tang *et al.*, 2021). Vortices and domain wave spirals were predicted for BiFeO$_3$/SrTiO$_3$ trilayers under different epitaxial strains (Liu, Liu *et al.*, 2022). A single vortex-antivortex pair was created and separated in BiFeO$_3$ through a tip-induced electric pulse using angle-resolved PFM (Kim, You *et al.*, 2019), and spontaneous and reversible topological domain structures have been reported on high-density BiFeO$_3$ nanodots (Z. Li *et al.*, 2017). Antivortices in SrTiO$_3$ have been also reported for PbTiO$_3$/SrTiO$_3$ superlattices (Abid *et al.*, 2021). Prokhorenko, Nahas, and Bellaiche (2017) examined the so-called homotopy theory (Spanier, 1966; Holm and Janke, 1994; Hatcher, 2002; Nakahara, 2003b) can be used to understand and predict the occurrence of specific electric topological defects in specific ferroelectric structural phases. When combining this theory with large-scale effective Hamiltonian simulations (Prokhorenko, Nahas, and Bellaiche, 2017), it was found that proper ferroelectrics, such as BaTiO$_3$, can possess hedgehog or antihedgehog cores in their tetragonal state and line defects made of vortex or antivortex cores in their orthorhombic phase, despite an underlying finite symmetry. The topological protection of such defects was discovered to be related to the nontrivial topology of the internal state manifolds (which is characterized by a specific Euler characteristic) rather than that of the order-parameter space *per se*. Consequently, the stability of these defects resides in an original mechanism of topological protection that is associated with finite-temperature fluctuations of local dipoles.

Other examples of topological structures can be found in hexagonal manganites such as YMnO$_3$, materials that show unique improper ferroelectricity induced by structural trimerization (Choi *et al.*, 2010). There has been a significant amount of research on this system (Fujimura *et al.*, 1996; Fiebig *et al.*, 2002; Cheong and Mostovoy, 2007; Cho *et al.*, 2007; Kumagai and Spaldin, 2013; Das *et al.*, 2014), primarily due to the possibility of using it in nonvolatile memory, as well as the coexistence of ferroelectricity and magnetism. Unlike classical ferroelectrics such as BaTiO$_3$ and PbTiO$_3$, the primary order parameter in such hexagonal systems is a structural trimerization order that couples to a secondary spontaneous dipolar order parameter, leading to an "improper" ferroelectric. One of the consequences of such a ferroelectric state is the discovery of "cloverleaf" patterns of six domains emerging from one point, all distinctly characterized by polarization orientation and structural antiphase relationships (Fig. 39). The ferroelectric domain walls and structural antiphase boundaries are mutually locked, resulting in a topological protection of this state and incomplete poling even with large electric fields. These results reveal the rich physics of the hexagonal system with a truly semiconducting band gap where structural trimerization, ferroelectricity, magnetism, and charge conduction are intricately coupled.

Another example of the formation of such topological patterns is in the case of the Fe$_x$TaS$_2$ system ($x \sim 0.25 - 0.4$), which is shown in Fig. 40. Such Fe$_x$TaS$_2$ crystals with $x = 1/4$ and
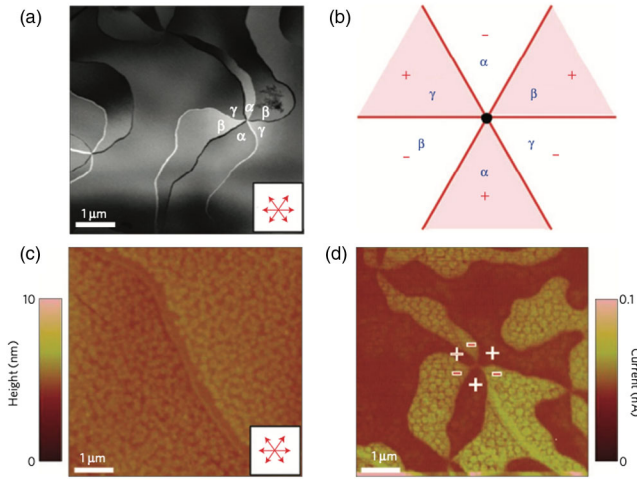
FIG. 39. Topological domain patterns in ferroelectric $YMnO_3$. (a) TEM dark-field image taken using the $1\bar{3}1$ spot, showing six antiphase domains ($\alpha - \beta - \gamma - \alpha - \beta - \gamma$) emerging from one central point. The α, β, and γ antiphase domains correspond to the three options for the origin of trimerization. The red arrows in the insets indicate the anticipated crystallographic directions of antiphase boundaries. (b) Proposed cloverleaf configuration of six antiphase or ferroelectric domains. The presence of three types of antiphase domains (α, β, and γ) and two types of 180° ferroelectric domains ($+$ and $-$) results in the arrangement of six distinct domains meeting at one point. (c) Topography (6×6 μm^2) and (d) conductive atomic force microscopy images simultaneously obtained in contact mode with a tip bias voltage of -2 V, demonstrating the presence of a nanometer-scale smooth surface and striking cloverleaf domains with conductive contrast. The bright (dark) conductive contrast corresponds to a domain with downward (upward) polarization. From Choi *et al.*, 2010.
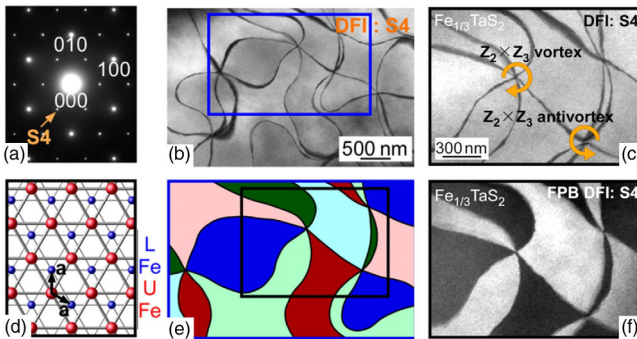

FIG. 40. (a) Electron diffraction patterns of Fe_xTaS_2 with $x = 1/3$. The ($\sqrt{3}a \times \sqrt{3}a$)-type (indicated as $S4$) superlattice spots can be observed in addition to the fundamental spots. (b) Dark-field images taken using the superlattice spot $S4$. (c) Dark-field images of $Fe_{0.43}TaS_2$ taken using the superlattice spot $S4$. (d) Two-dimensional schematics of the $\sqrt{3}a \times \sqrt{3}a$ superstructures of intercalated Fe ions in $Fe_{1/3}TaS_2$. The red and blue spheres depict Fe ions, and small (large) spheres represent the lower (upper) Fe layers. (e) Domain patterns with tensorial proper coloring (first step, dark and light; second step, red, blue, and green) in $Fe_{1/3}TaS_2$. (f) Dark-field image taken under the so-called Friedel-pair-breaking condition exhibiting the presence of chiral domains without centrosymmetry. From Horibe *et al.*, 2014.

1/3 exhibit complicated antiphase and chiral domain structures related to ordering of intercalated Fe ions with $2a \times 2a$ and $\sqrt{3}a \times \sqrt{3}a$ superstructures, respectively. These complex domain patterns have been treated within the framework of the "four-color theorem." The domain topology is closely related to their magnetic properties (Horibe *et al.*, 2014).

2. Manipulating energy-order-parameter landscapes for nonconventional physical responses

Since its conception in 2008 (Salahuddin and Datta, 2008), the negative capacitance (or permittivity) phenomenon and its application in electronic devices has been widely studied. In addition, the possibility of using negative capacitance for supercapacitors and high efficiency batteries has also been discussed (Hoffmann *et al.*, 2019; Braga *et al.*, 2020). As shown in Sec. V.D.2, in the case of a ferroelectric within the classical Landau framework, negative permittivity is associated with regions of the energy versus order-parameter landscape where the curvature is negative, as illustrated by the red shaded portions of the energy landscape in Fig. 35(a).

These proof-of-concept demonstrations establish the notion of engineering the internal energy landscape of ferroic materials and exploiting those for advanced electronic devices to provide functionalities that were not possible otherwise. In the same way as the double-well-energy landscape can be flattened out with an external voltage by placing an ordinary dielectric in contact with a ferroelectric, other pathways can be designed to produce lower energy barriers, multistate energy states in the middle portion of the double-well energy, or squarelike potential profiles (Fig. 41). Some work has already been done to engineer ferroelectric systems having the multiple state energy profile (Khan, Caraveo-Frescas, and Alshareef, 2015; Martelli, Mefire, and Luk'yanchuk, 2015; Quindeau *et al.*, 2015; Lee *et al.*, 2016). Within these configurations, a small voltage can enable a full transition between two states and achieve significant energy efficiency
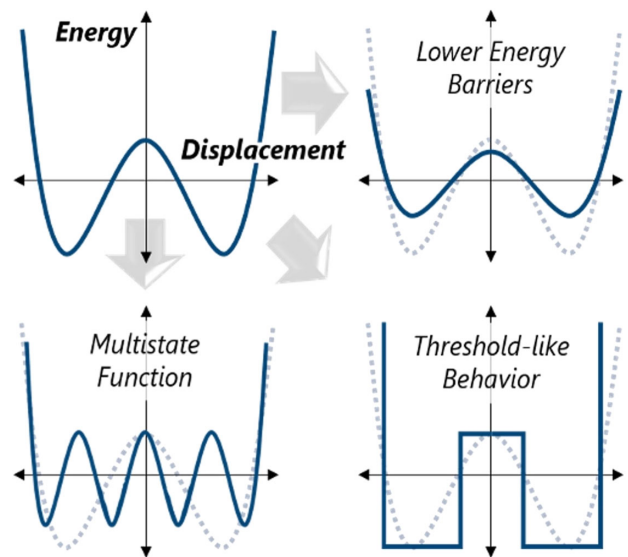

FIG. 41. Manipulating energy landscapes in ferroelectrics. The schematic illustration shows how the energy landscape can be manipulated to create tunable barrier heights, multistates, and thresholdlike behavior.

in logic transistors. The underlying physical concept is not limited to ferroelectrics and can equally be applied to metal-insulator transitions in correlated electron systems. We note that this concept of negative capacitance is currently of significant practical interest as well in exploring pathways to overcome the so-called Boltzmann tyranny in semiconductor electronics, and thus pave the way for highly energy efficient computing.

The small remnant polarization and narrow hysteresis loop due to the multivortex structure in ferroelectric nanowires embedded in nanocomposites can also lead to a large enhancement of energy density and high energy-storage efficiency, making them promising materials for new dielectric capacitors (Liu, Yang *et al.*, 2017). $PbTiO_3/SrTiO_3$ superlattices can also be considered as artificial electrostatically engineered antiferroelectrics whose energy-storage performance (density and release efficiency) can be optimized with respect to different design variables (layer thickness, epitaxial strain, and stiffness of the dielectric layer) (Aramberri, Fedorova, and Íñiguez, 2022).

3. Crystalline orientation effects

One way of changing the energy landscape, as proposed in Sec. VI.A.2, is to change the orientation of the samples. The vast majority of thin-film heterostructures studied to date have been (001) oriented. This has been driven by the fact that high-quality, chemically terminated perovskite substrates have been mainly of this orientation. Changing this to (110)- or (111)-oriented structures can dramatically change the elastic, electrostatic, and gradient terms in the Hamiltonian, as well as introducing anisotropies in the elastic, electrostatic, and piezoelectric susceptibility tensors. Therefore, it can provide another route to manipulate the energy landscape at the atomic scale. Specifically, for rhombohedral systems such as $BiFeO_3$ the polarization points along the [111] direction. Thus, superlattices in (111)-oriented films can provide a route to produce structural and electrostatically similar structures to those we have explored in $PbTiO_3/SrTiO_3$ but that now are built from an intrinsically multi-order-parameter, multiferroic material. Growth in these orientations, however, is complicated by a tendency for faceting, so basic research effort on layer-by-layer growth is required. Specifically, in the case of materials such as $BiFeO_3$, the octahedral tilts about the [111] direction can be an impediment to the formation of polar textures (Shi *et al.*, 2022). In this regard, elimination of the octahedral tilts by alloying (with $BaTiO_3$ or $PbTiO_3$) would be of interest.

Novel coupling between tilting of oxygen octahedra and electrical vortices were found by Sichuga *et al.* (2010) in $BiFeO_3$ stress-free dots under open-circuit boundary conditions. This coupling was predicted to give rise to several new chiral patterns for the tilting of oxygen octahedra, with these patterns requiring other original order parameters to characterize them, including one that can be considered a generalization of the toroidal moment but for oxygen octahedral tiltings. The possibility of novel devices (such as four-state memories) based on the reversals of the latter toroidal moment as well as of the coexisting electric toroidal moment was also suggested.

Density-functional-theory calculations were also carried out on epitaxial $BiFeO_3$ films, but ones that were grown

along the usual $[1\bar{1}0]$ direction (Cruz *et al.*, 2007; Prosandeev, Kornev, and Bellaiche, 2011). These calculations predicted a noncollinear phase that coexists with interpenetrated arrays of ferroelectric vortices and antivortices. Such a phase is an example of a gyrotropic structure that possesses a spontaneous optical activity similar to the chiral vortices and skyrmions in the $PbTiO_3/SrTiO_3$ system. However, there have been few experimental studies in this area, and this should be a focus in the immediate future.

4. Skyrmion and vortex order: How does one obtain a perfectly ordered skyrmion or vortex crystal?

Although skyrmions and vortices comprise individual unit cells, there is a hierarchy of length scales involved in the formation of such topological ensembles. For example, in the vortex lattice shown in Fig. 42, the vortices form a quasi-periodic 2D lattice in which the long-range periodicity is broken up by "vortex" dislocation dipoles, which are indicated as red circles in the right panel of Fig. 42. The second type of defect in the vortex lattice, indicated as yellow arrows in Fig. 42, can be thought of as antiphase boundaries. Recent work has also characterized them as chiral boundaries across which the handedness changes sign (Behera *et al.*, 2022). Geometric frustration stemming from polar chiral boundaries was previously shown to induce checkerboard lattices of vortices and antivortices in ferroelectric nanocomposites (Nahas, Prokhorenko, and Bellaiche, 2016). The vortex arrays shown in Fig. 42 can be thought of as part of a spectrum of patterns that emerge in constrained systems (Radzihovsky and Toner, 1999; Loudet, Poulin, and Barois, 2001; Tadapatri, Krishnamurthy, and Weissflog, 2012; Kamien and Mosna, 2016; Kim, Shin *et al.*, 2019) and manifest themselves in a variety of systems, spanning metals, organic layers, colloidal crystals, and macroscopic desert sand dunes. Figure 43 captures these at various length scales.

In Fig. 43(a) a classical dislocation in a metallic alloy is shown, with the spacing between the dislocation dipoles
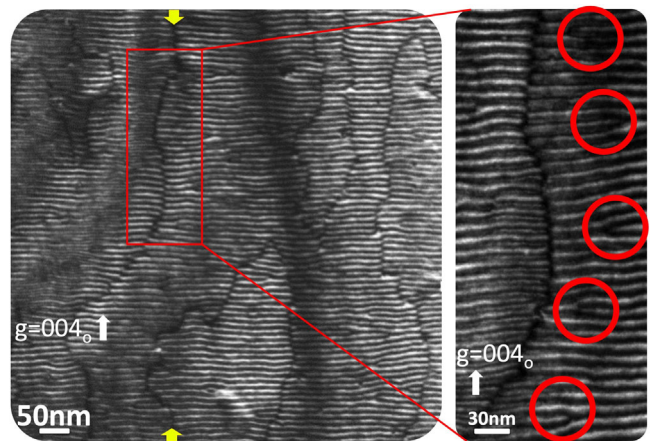

FIG. 42. A weak beam dark-field-TEM image of a $SrTiO_3/PbTiO_3/SrTiO_3$ trilayer sample showing the formation of a quasiperiodic array of vortices (progressing from left to right). The magnified image on the right shows the formation of arrays of edge dislocation dipoles in the vortex lattice as well as the existence of antiphase boundaries. From Behera *et al.*, 2022.
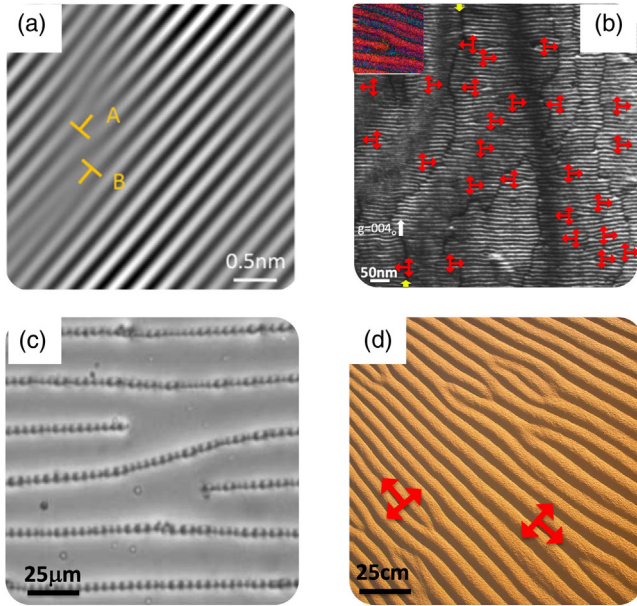
FIG. 43. Topological defects at various length scales. (a) Dislocation dipole in a metal lattice, indicated as a T and an inverted T. From Wu *et al.*, 2019. (b) Dislocation dipoles in the vortex lattice in a $SrTiO_3/PbTiO_3/SrTiO_3$ trilayer structure. From Behera *et al.*, 2022. (c) Dislocation dipoles in a colloidal array. From Loudet, Poulin, and Barois, 2001. (d) Dislocation dipoles in sand dunes. From Bray, 2012. Note the changes in the length scales of these patterns (from nm to cm), although the patterns are self-similar.

(indicated as *A* and *B*) dictated by the binding energy of the dislocations (Wu *et al.*, 2019). Figure 43(b) shows a weak beam dark-field image of the dislocation dipole array in the vortex lattice where the positive and negative dislocations are identified by the left and right T. [A higher magnification image of one dislocation is shown in the inset (Behera *et al.*, 2022).] An example from colloidal chemistry is shown in Fig. 43(c) (Loudet, Poulin, and Barois, 2001), while the coarsest length scale is shown in Fig. 43(d) and corresponds to dislocation patterns in sand dunes. The change in length scales is of many orders of magnitude from Fig. 43(a), which is at the few-angstrom scale, to Fig. 43(d), where the dislocations in the sand dunes are in the several tens of centimeters scale. The topological similarity of these patterns points to a framework that could be common to all of them, with differing energy and length scales. The considerable volume of literature on this pattern evolution, starting with the seminal work of Turing (Turing, 1952; Cross and Greenside, 2009), could provide a convenient framework for understanding the long-range order evolution in the vortex and skyrmion arrays.

On a macroscopic scale, the free energy of a system can be described by the behavior of the order parameter, and phase transitions arise by a spontaneous symmetry breaking. The role of the symmetries, fluctuations, and range of the interactions in eventual phase transitions (including those of the BKT type) was summarized in Sec. III. In the case of three-dimensional systems, the presence of these topological defects can lead to a more complex phase evolution (including vortex liquids and different varieties of vortex-glass phases as in high-temperature superconductors), sometimes reminiscent

of intrinsically 2D phenomena such as the BKT physics (Nelson, 1988; Blatter *et al.*, 1994; Klein *et al.*, 2001; Vasin, Ryzhov, and Vinokur, 2018). Numerical simulations have shown (Nahas *et al.*, 2016) that the dynamics of hedgehogs and antihedgehogs intricately relates to that of bulk relaxors in a defect-mediated relaxation mechanism. Just as vortices and antivortices allow for quasi–long-range order in the two-dimensional BKT model, hedgehogs and antihedgehogs allow for local order to emerge within polar nanoregions by confining the local distortions of the polarization vector field in 3D relaxors. The residual relaxation rate of defects at low temperatures hints at a large density of states for topological excitations at the lowest energies, which is a signature of frustration and glassiness. Moreover, the spin glass formation in the three-dimensional *XY* model with weak quenched disorder was theoretically traced back to the BKT critical behavior of the same model in two dimensions (Vasin, Ryzhov, and Vinokur, 2018). Continuously evolving nature of such systems could support novel transformation pathways not accessible in long-range–ordered solids undergoing symmetry-breaking transformations. Effective Hamiltonian approaches can be used to demonstrate the potential for such BKT-like transitions in ultrathin ferroelectrics. For example, using scaling, symmetry, and topological arguments, it was found that a BKT phase sustained by quasicontinuous symmetry emerges between the ferroelectric and paraelectric phases in ultrathin $BaTiO_3$ under large tensile strains (Nahas *et al.*, 2017), in single unit-cell-thick SnTe (Xu *et al.*, 2020), or in $PbTiO_3/SrTiO_3$ superlattices (Gómez-Ortiz *et al.*, 2022a). The hierarchical nature of such vortex and skyrmion structures points to the possibility that BKT-like phase transitions could be envisioned, not only within the fundamental dipolar lattice (i.e., at the scale of the unit cell) but also at the several nanometer scale of the vortex and skyrmion lattice [as exemplified by Fig. 43(b)].

An aspect that is related to Fig. 43(b) and is just getting noticed by the scientific community is the question of how to induce long-range ordering among the skyrmions and vortices. In both cases some degree of order has been observed, but the underlying physics that could inhibit or promote the emergence of long-range order needs to be understood. In the case of the polar vortices, electron microscopy studies have revealed the formation of dislocation dipoles within the vortex lattice, as illustrated in Fig. 42. These pairs of dislocations are also a key ingredient of the BKT transition (Kosterlitz and Thouless, 1973; Nelson and Halperin, 1979; Kosterlitz, 2016), in which the long-range order in the 2D vortex lattice is inhibited by the formation of topological defects such as dislocation pairs (or dipoles). The melting of the vortex lattice with temperature, a concept that has also been recalled in the explanation of the negative capacitance (Zubko *et al.*, 2016; Gómez-Ortiz *et al.*, 2022b), can then be thought of as the unpinning of such dislocation pairs and the movement of the two components of the dislocation dipole. Given the 2D nature of both the skyrmion ensemble and the vortex arrays, it would seem appropriate to understand these effects in the BKT framework. In a similar vein, the degree of order for the skyrmion ensemble can be described using a Voronoi-poly-hedron construction framework (Donoway *et al.*, 2021) that reveals the interactions among the skyrmions and can be a

powerful pathway to describe the degree of long-range order as well as the phase transitions in this "lattice" in the spirit of the BKT model. Temperature- and strain-driven changes in the degree of order, akin to the 2D transitions in magnetic or superconducting vortex arrays, can be envisioned and could be a fruitful area of future research. It would be valuable to study the potential for topological protection and phase transitions in these materials (i.e., both polar-vortex and polar-skyrmion structures and newly predicted and discovered phases). To do this, a combination of electrical, synchrotron-based *in situ*, field-dependent structural studies and x-ray photon correlation spectroscopy together with time- and field-dependent phase-field simulations, first- and second-principles simulations would be useful. Electrical and synchrotron-based studies will further enable an understanding of the evolution of dielectric order (permittivity and loss) and structure (namely, the correlation length of the emergent polar structures) with temperature. Electric-field-dependent dielectric studies and x-ray diffraction studies can be used to probe other aspects of topological protection. Finally, techniques such as x-ray photocorrelation spectroscopy, which exploits a coherent x-ray source to measure the dynamics of the physical phenomena (such as the fluctuations in the vortex or skyrmion lattice), can be used to probe the temperature- and field-dependent spatiotemporal fluctuations of the topological defects. In other words, one can probe the evolution of the speckle pattern with time and temperature to extract the temperature evolution of the features responsible for the BKT-like transition. Temperature- and field-dependent electron microscopy studies would also provide real-space information on the dislocation dipoles and their thermal stability. Another interesting route to follow is related to thermal excitations of polar skyrmions. For instance, one might wonder whether polar-skyrmion lattices can melt, resulting in dynamical phases akin to skyrmion liquids (Huang *et al.*, 2020) or gases. Prospects of discovering such states are supported by recent effective Hamiltonian simulations (Prokhorenko *et al.*, 2023) that reveal thermally activated motion of polar Néel skyrmions [Fig. 44(a)]. This motion is predicted to occur in depleted skyrmion lattices (Nahas, Prokhorenko *et al.*, 2020) at the low-field boundary of the skyrmion lattice-monodomain state transition line. Ongoing work is now devoted to understanding the origin and properties of this dynamical skyrmion state.

B. From probing ground states to controlling and manipulating emergent structures

Manipulating the dipolar textures at various length scales using external fields and probes (i.e., electric, thermal, and optical) is a rapidly emerging field of condensed-matter physics. Efforts are focused on the microscopic manipulation of skyrmions using electron beams or an AFM tip, the manipulation of emergent chirality over length scales of 50–100 nm, and applied efforts to study pathways to create microwave elements that can be tuned with an electric field over the frequency range from a few megahertz to over 100 GHz are all likely to throw new light on the underlying physics of these topological structures. Needless to say, understanding pathways to do this in a deterministic way in both spatial and temporal domains would be of immense interest.
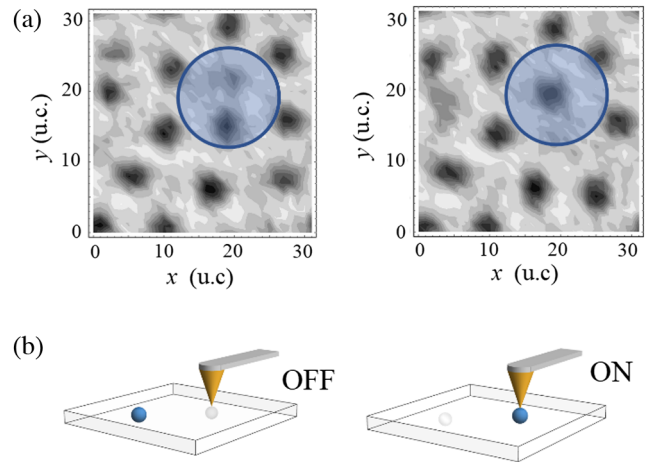

FIG. 44. (a) Two instances of the depleted Néel skyrmion lattice evolution at room temperature obtained from effective Hamiltonian molecular dynamics. Dark (bright) contrast correspond to positive (negative) out-of-plane polarization. The solid blue circles indicate a typical region where thermal skyrmion motion is observed. (b) Schematic illustration of the PFM tip-induced skyrmion "teleportation" in PZT-based heterostructures (Prokhorenko *et al.*, 2023). Application of a local electric field abruptly transports a nearby Néel skyrmion to the position beneath the PFM tip.

1. Probing and manipulating skyrmion dynamics with local fields

Probing skyrmion stability and dynamics in order to establish the limits of the mobility of polar skyrmions, and whether they can be manipulated with low energies (or voltages), can be carried out using a variety of approaches. In particular, we envision electric-field manipulation of the skyrmions to have two major aspects: (i) to be able to move the skyrmions with in-plane electric-field gradients and (ii) to change the diameter or local structure of the skyrmions with out-of-plane electric fields, ultimately leading to a possible topological-phase transition (Das *et al.*, 2021; Zhu *et al.*, 2022). Note that these dipolar textures have two advantages over their magnetic counterparts. First, their innately small size (the dipolar textures have dimensions of 5–10 nm) is smaller than their magnetic analogs. Second, the dipolar textures are stable and remain small laterally at room temperature. These features make them of great interest for a range of practical applications. Beyond this, the fundamental aspects of field-driven phase transitions are of broad interest to the condensed-matter-physics community, and thus it would be of interest to develop methodologies to accomplish this control (both computationally and experimentally) to produce a phase diagram of dipolar texture evolution with field, temperature, stress, and light excitation. To do this, techniques that provide complementary real- and reciprocal-space "pictures" of how these features evolve under applied stimuli need to be developed, which can be directly compared to field-driven simulations (from both first and second principles and the phase field). For example, to probe individual skyrmions at atomic resolution while under the influence of *in situ* electric fields, one can apply 4D STEM to measure polarization, electric fields, and strain in real time over length scales ranging from angstroms to micrometers, yet retaining sub-picometer precision [Figs. 37(d)–37(f)].
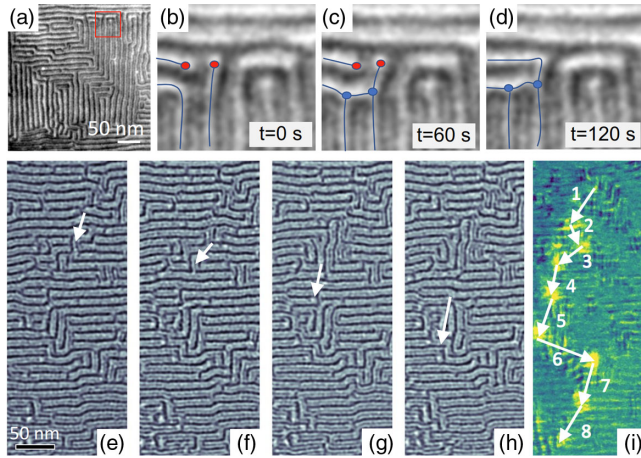
FIG. 45. Moving ferroelectric topological textures with an electron beam. Scanning a subnanometer electron beam across an array of labyrinthine and bubble-shaped textures in a free-standing $SrTiO_3/PbTiO_3/SrTiO_3$ membrane enables the movement of portions of the texture. (a)–(d) Sequence of ADF-STEM images obtained over a period of 120 s showing the creation and annihilation of convex (lower blue circles) and concave disclinations (upper red circles) in the ferroelectric texture. The lower blue and upper red dots denote merons and antimerons with topological charges of $+1/2$ and $-1/2$, respectively. (e)–(h) Electric-field gradient control of polar merons and antimerons, a sequence of images in which the two-dimensional rastering of the electron beam moves the meron cluster. (i) Sum of differences between adjacent frames showing the trajectory of features tracking with the electron-beam parking positions. Adapted from Shao *et al.*, 2021.

For larger fields of view, ensembles of skyrmions can be probed using both ultrahigh-vacuum scanning-probe-based studies and *in situ* synchrotron-based diffraction studies. The latter leverages both the extensive hard-x-ray scattering work on similar structures and pioneering work on *in situ* and *in operando* ac-field-driven studies on ferroelectric materials (Shao *et al.*, 2023). These techniques can be complemented with laboratory-based, indirect modes of characterization, including studies of dielectric responses (e.g., permittivity) that will expand the resources and types of measurements available for probing these effects. Knowing how to move such skyrmions and control this motion could be of significant technological importance. For example, can a local tip or electron beam, generating an inhomogeneous electric field, activate such motion?

Recent simulations (Prokhorenko *et al.*, 2023) support this idea by predicting the possibility of continuously displacing Néel skyrmions using a PFM tip. The applied field magnitude triggering such motion is predicted to be several times lower than the coercive field, thus consolidating the promise of employing polar skyrmions in low-energy electronics. Furthermore, the same work (Prokhorenko *et al.*, 2023) demonstrated a fundamentally new functional phenomenon. Under certain conditions, a PFM tip was shown not only to write (Zhang *et al.*, 2019) but also to simultaneously annihilate another skyrmion in a nearby region [Fig. 44(b)].

Furthermore, preliminary experiments (Fig. 45) point to some interesting possibilities in which polar textures can be manipulated by a localized electron beam. The coupling strength should scale inversely with beam energy, so a low-energy ballistic electron current from a localized point contact should be even more effective. Since skyrmions are neutral, there needs to be a field gradient from the tip across the skyrmion. What is the shape of such an electric-field gradient and what is the preferred distance from such a tip (with respect to the skyrmions) that are the most effective at controlling the motion? How do such parameters affect the speed of the skyrmion motion? Can skyrmions be created and deleted using a mechanical probe or an electron beam? In a similar sense, geometric confinement of these dipolar textures in submicron dimension test structures can also give rise to ordering and novel jamminglike transitions. One might be able to manipulate and drive these features in a manner akin to what has been accomplished with magnetic skyrmions.

Having developed routes to order and control the growth of these features, a second challenge would be to create such skyrmions in test structures that are constrained to submicron dimensions in plane so that we can explore their stimuli-driven response. To accomplish this, standard lithographic approaches (i.e., conventional optical lithography) and *e*-beam lithography will be valuable; He-ion microscope-based lithography and/or focused-ion-beam patterning could further expand this. In all cases, features of varying geometries (i.e., stripes or rectangles, circles or ellipses, etc.) and varying aspect ratios should be created to explore how the lateral boundary conditions affect both the formation and the ordering of the polar-skyrmion structures.

The final aspect should be to push the boundaries of measurement frequency in analyzing these materials. Measurements in the microwave, tertahertz, and higher frequencies have direct implications for a range of applications. The collective dynamics of topological structures such as vortices and skyrmions are also fundamentally of interest as they may unlock a new understanding of many-body interactions where long-range couplings beyond nearest neighbors are crucial. In conventional ferroelectrics, the collective dynamics of soft modes that exhibit a reduction of the mode frequency to zero at a critical point is important to understanding the thermodynamics of phase transitions. Such soft modes have recently been shown to be essential to access hidden ferroelectricity far from equilibrium and to the condensation of metastable polar phases (Li *et al.*, 2021). Whether topological structures host new soft modes and how they behave on ultrafast timescales, however, are unanswered questions for elucidating the fundamental physics and exploring the novel properties in these emergent nanostructures. For example, the study of dynamics of magnetic vortices and skyrmions not only deepens the understanding of many-body physics but also has driven applications in data processing and storage. This said, little is known about the dynamics of such complex extended polar textures, which in turn underlies their functionalities. Terahertz-field excitation and femtosecond x-ray diffraction measurements would be invaluable for observing ultrafast collective polarization dynamics that are unique to polar vortices and skyrmions, with orders-of-magnitude-higher frequencies and smaller lateral size than their magnetic counterparts. These studies should enable us to probe soft modes that may be specific to the vortex or

skyrmion state, and their time dynamics on picosecond timescales. Studying the frequency of these specific soft modes can enable us to look for signatures of the condensation of these mode dynamics close to a structural or topological-phase transition. The discovery of collective dynamics in these dipolar textures (Li *et al.*, 2021) can provide opportunities for applications of electric-field-driven data processing with ultrahigh speed and density. An interesting new avenue may be to create electric topological defects by sending terahertz laser pulses to activate a high-frequency mode that then couple with modes responsible for the formation of such defects (Chen, Paillard *et al.*, 2022; Chen *et al.*, 2023; Gao *et al.*, 2023).

2. Manipulation of chirality with electric field and optics

With the discovery of chiral polar vortices and skyrmions, new studies are warranted to understand if and how we can deterministically manipulate their handedness. We shall need to explore the ability of electric fields, the electrode doping type (hole versus electron as majority carriers), the surface termination, and the valence mismatch across the interface to achieve this control (Baker and Bowler, 2020). The coupling of the chirality to the electric field, ultrafast-optical excitations, and stress or strain need to be understood as well. These studies will require careful scanning force microscopy experiments coupled with SHG CD to investigate the possibility to locally switch chirality with an electric field, as well as larger scale measurements such as electric-field-dependent x-ray diffraction, to monitor field-dependent changes to the polar vortices and skyrmions (and other related textures). Two critical questions relate to the limits of the scaling of the chiral behavior as well as the time dynamics of the switching and/or the lateral movement of such skyrmions.

3. Manipulating capacitive and resonant states

Building on the discovery of negative permittivity in $(PbTiO_3)_n/(SrTiO_3)_n$ vortices (Yadav *et al.*, 2019) and skyrmions (Das *et al.*, 2021), it should now be possible to directly measure trapped "negative permittivity" states at the core of the vortices or the periphery of the skyrmions, which leads to an order-of-magnitude enhancement in the effective permittivity. Application of an electric field drives the topological phases into a uniform polar state in a reversible way with an accompanying large tunability [Fig. 46(a)], a relevant property for tunable phased-array radar and related applications of highly tunable dielectrics. Broadband manipulation of negative capacitance in films and membranes containing arrays of polar vortices or skyrmions would be of both fundamental and practical interest. Preliminary results for the frequency dependence of the dielectric constant up to gigahertz frequencies are available [Figs. 46(b)–46(d)]. Microwave device engineers are particularly interested in novel materials with the potential for application in a range of sensor; electronic warfare; quantum information sciences; position, navigation, and timing; and energy and power systems. Therefore, of particular interest is the development of materials with potentially highly tunable microwave and radio frequency properties, and high-frequency measurements (up to at least 100 GHz, and perhaps even higher) should be carried out as a
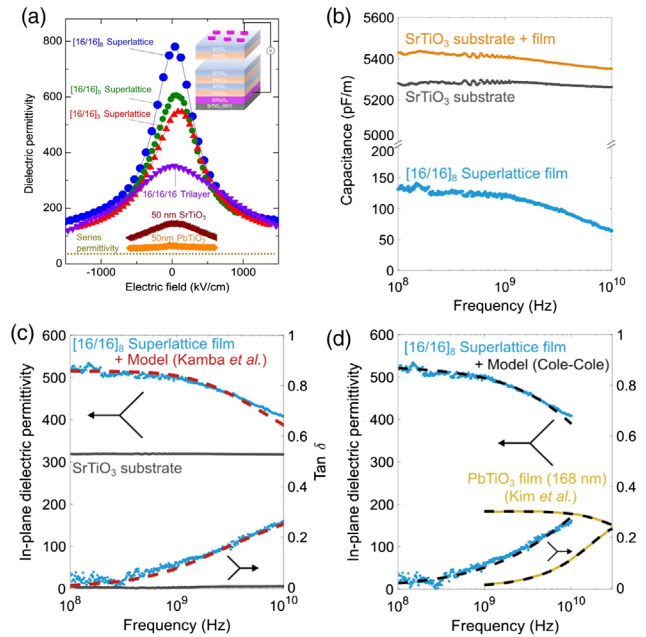

FIG. 46. (a) Dielectric permittivity as a function of electric field (applied voltage divided by the thickness of the sample) for $SrTiO_3/PbTiO_3$ superlattices with different periodicities. (b) Measured capacitance of coplanar wave guide (CPW) transmission lines on the superlattice (upper orange line) and the $SrTiO_3$ substrate (black middle line). Finite-element simulations and the measurements of the bare $SrTiO_3$ substrate are used to analyze and isolate the portion of the total capacitance that is related to the permittivity of the superlattice (bottom blue line). (c) The real part of the in-plane dielectric permittivity (left-hand *y* axis) and the loss tangent (right-hand *y* axis) are determined from the capacitance and conductance measurements via a mapping function obtained from 2D finite-element modeling of the CPW structures. (d) Cole-Cole model of the in-plane complex permittivity of the superlattice from 100 MHz to 10 GHz. From Das *et al.*, 2021.

function of electric field. Besides, such polar textures are likely to display exotic and/or high susceptibility to stimuli such as stress, fields, temperature, and light. Therefore, the knowledge of how to manipulate and control these materials for deterministic response will be essential.

Returning to the manipulation of the energy landscapes, what sets the limits on the electric-field manipulation of the topological state or how tunable this state is? This has obvious implications for practical applications of the large, electrically controllable net dielectric permittivity that is observed.

4. Neuromorphic computing

The systems that are at the heart of neuromorphic architectures and computing are the so-called memristors (which are solid-state synapses), as Torrejon *et al.* (2017) and Romera *et al.* (2018) described. Their structural state, and thus electrical conductance, can be tuned by the application of pulses of electric field or voltage; see Boyn *et al.* (2017) and references therein. Memristors are thus currently experiencing substantial interest. However, thus far their typical frequencies have been below the gigahertz level. Having terahertz frequencies as characteristic for neuromorphic computing

would lead to a revolution in artificial intelligence since it would result in highly desired ultrafast processing data and lower energy consumption (Grollier *et al.*, 2020). The presently unanswered following question is therefore of tremendous importance: As analogous to a recent prediction in a relaxor ferroelectric possessing strongly inhomogeneous electric dipoles that can easily evolve under terahertz external stimuli (Prosandeev *et al.*, 2021), can oxide nano-structures having striking configurations, such as those forming vortices or skyrmions of electric dipoles, also exhibit the three key properties of neuromorphic materials (namely, action potentials, integration, and multiple tunable nonvolatile states) when subject to electric pulses of terahertz frequencies? In other words, can we design terahertz neuro-morphic computing based on electric topological defects? This is an interesting avenue that can be pursued in the coming years (Prosandeev *et al.*, 2022, 2023).

C. Coupling topological patterns with spin: Toward multiferroic skyrmions

The success of the $PbTiO_3$ system in enabling a demon-stration of vortices and skyrmions points to a possible adaptation of the confinement approach to create spin-charge-coupled textures, such as those leading to multiferroic skyrmions. Now that we have a reasonably rigorous theo-retical and experimental synthesis framework coupled with a variety of probes of such polar textures, the next immediate challenge and opportunity is to be able to discover more examples of topological phases in other systems. Given the significant interest in multiferroics, it would indeed be interesting to be able to create such textures in a multiferroic such as $BiFeO_3$, by which one could induce a spin texture through the dipolar texture. Work is currently ongoing to look for topological phases in $BiFeO_3$ (Mundy *et al.*, 2022). It is noteworthy that, unlike the $PbTiO_3$ system, $BiFeO_3$ has a pronounced octahedral tilt, which is somewhat of an impediment to the formation of polar textures (Sichuga and Bellaiche, 2011). Indeed, in the case of $BiFeO_3$, the fact that several crystallographically distinct phases can coexist within close proximity in the energy landscape means that imposing electrostatic and elastic boundary conditions invariably leads to a shift of the phase equilibrium rather than a formation of polar textures. An example of this is the stabilization of an antipolar phase that coexists with the polar $R3c$ phase in this system (Mundy *et al.*, 2022). The power of heteroepitaxy through MBE, laser MBE, atomic-layer deposition, and PVD techniques, combined with the large number of crystal phases in complex oxides along with the wide spectrum of physical phenomena, makes for an interesting combination that could be the framework for the discovery of a large number of such topological phases, with a pathway to coupling the spin and charge textures. Ideally one would start with a multiferroic crystal such as $BiFeO_3$ and impose the same set of boundary conditions, as in the case of the $PbTiO_3/SrTiO_3$ super-lattices, i.e., electrostatic and elastic boundary conditions to manipulate the polar state. Studies to date have shown that when such boundary conditions are imposed on $BiFeO_3$, it

begins to transform into one of these phases, specifically the antipolar, orthorhombic structure, which then coexists with the polar $R3c$ structure (or a distorted version of the polar phase) as a nanoscale ensemble that can be interconverted between each phase with an electric field (Zeches *et al.*, 2009; He *et al.*, 2011; Caretta *et al.*, 2023). Thus, there is an opportunity to create coupled polar and spin textures if the issue of octahedral tilt is resolved. One pathway to do this would be to create solid solutions of $BiFeO_3$ with, for example, $PbTiO_3$ (Narayan *et al.*, 2018). A related pathway would be to interface antiferromagnets, such as the real-space orthoferrites to explore pathways to couple magnons in the antiferromagnet with the skyrmions in the $PbTiO_3/SrTiO_3$ superlattices. Indeed, it would be interest-ing to explore the replacement of $SrTiO_3$ with an insulating antiferromagnet that is still lattice matched to $PbTiO_3$, thus providing a pathway to directly interface the polar textures in $PbTiO_3$ with magnetism in the ferrite. Another phenomenon was predicted by Ren and Bellaiche (2011): applying curled electric fields on $BiFeO_3$ nanodots, resulting in the control of the magnitude and direction of the magnetization due to the field-induced transformation and switching of electrical vortices, which is called the magneto-toroidic effect.

1. Inserting single spins into skyrmions and vortices

The formation of curling polar textures interfaced with the crystal chemistry of the fundamental perovskite building block can provide a new direction to embed isolated ions with spins in the polar-vortex and skyrmion textures in order to manipulate the spin-orbit coupling within the embedded ion, as schematically illustrated in Fig. 47. There was substantial prior work on the role of ionic defects in polar perovskites [such as Fe^{3+} in $PbTiO_3$ or $BaTiO_3$ (Müller and Berlinger, 1986; Laguta *et al.*, 1996; Liu *et al.*, 2021)] in
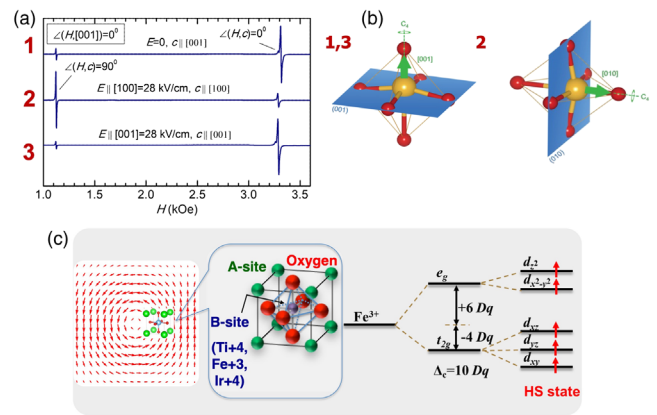
FIG. 47. (a) EPR spectrum from the $[Fe^{+3} - PbTiO_3]$. (b) Left image: schematic of the Fe^{+3}-doped $PbTiO_3$ $[Fe^{+3} - PbTiO_3]$ in the tetragonal perovskite structure, with the green up arrow indicating the polarization direction and the horizontal blue sheet the easy plane of the spins in Fe^{+3}. Right image: graphic showing that the easy plane of the spins rotates as the polarization direction is rotated by 90°. (c) Schematic indicating what happens to the crystal-field splitting and spin-orbit coupling when an impurity is placed within a polar vortex (or skyrmion).

impacting the functional properties (ferroelectric or piezo-electric). However, the spin structure of the ionic defect that is embedded in such a polar environment had not been examined until recently (Liu *et al.*, 2021; Das *et al.*, 2022). Vortex and skyrmion structures with small (less than 1%) dopant concentrations, with a focus on Fe^{3+} (the high spin d^5 state) and Ir^{4+} (the low spin d^5 state) into the Ti^{4+} site of the perovskite lattice or trivalent rare-earth ions into the *A* site could be fruitful directions of research. The first question to resolve would be whether the vortex and skyrmion structures are stable after the inclusion of these ionic defects. If this is successfully demonstrated, the spin structure could be studied using a combination of electron paramagnetic resonance (EPR) and STEM imaging or energy loss spectroscopy. High spin–low spin transitions (and thus magnetoelectric coupling) in both these ions as they are placed in a vortex or a skyrmion with curling dipoles would be interesting potential avenues of research.

2. High-frequency responses of coupled spin-charge textures

Topology combined with multiferroicity is a promising route toward the design of new phenomena. We now take a specific example arising from recent preliminary results to demonstrate the possibility that coupled spin-charge topological patterns in multiferroic systems could induce novel phenomena of fundamental and technological importance. In the last 15 years or so, the cross-coupling between magnetic and ferroelectric ordering in multiferroic materials known as the magnetoelectric effect has attracted significant attention since it can pave the way toward the development of novel sensors, actuators, and low-power logic-in-memory devices (Manipatruni *et al.*, 2019). In recent work (Sayedaghaee *et al.*, 2019; Sayedaghaee *et al.*, 2020), molecular dynamics atomistic simulations have revealed that new quasiparticles can not only be created in monodomains of multiferroics but also generate a resonance (and thus a large increase) in the magnetoelectric coefficients. Similar effects have been observed for mesostructured domain configurations, which enable microwave resonances that cannot be readily accomplished in other ways. These new quasiparticles consist of a mixing between optical and acoustic phonons with magnons and are thus named electroacoustic magnons. Their resonant frequencies were found to be on the order of 100 and 300 GHz in bulk $BiFeO_3$. One may now wonder whether other quasiparticles can be found when specific electric topological defects, namely, vortices and skyrmions, form in a multiferroic (associated with quasiparticles called phasons that can technically couple with magnons). In such a case, one will then be able to create a new quasiparticle (phaso-magnons or, equivalently, localized electromagnons) that has the possibility of inducing a large magnetoelectric response via resonance. Recent atomistic simulations in the $BiFeO_3$ system with 109° ferroelectric domain walls reveal interesting spectroscopic features (Sayedaghaee *et al.*, 2019, 2020). Moreover, applying electric fields should alter the polar textures and thus affect the real-space position of these phaso-magnons and their natural frequencies, consequently allowing for a spatial and frequency control of large magnetoelectric responses. Applications of these polar textures can be classified into two sections: (i) those that build upon known applications of ferroelectrics and dielectrics and (ii) those that uniquely utilize the emergent phenomena in such topological structures. In the first category, the large electric-field tunability of polar vortices and skyrmions in the microwave regime (perhaps upto a few hundred gigahertz) should be of interest for tunable, phased-array radar, filters, and resonators, particularly in 5G and 6G communications.

3. Superlattices based on other crystal structures

While a significant portion of our discussion thus far has been based on the perovskite family of ferroelectrics, complex oxides present a much larger palette of crystal structures and physical phenomena. For example, $PbFe_{12}O_{19}$ is a purported multiferroic with both strong ferroelectric order (its spontaneous polarization is 100 μC/cm^2) (Tan and Li, 2015) and spontaneous magnetization (Pullar, 2012) oriented along its *c* axis. Like $SrTiO_3$, $BaFe_{12}O_{19}$ is an incipient ferroelectric (Mikheykin *et al.*, 2014; Wang and Xiang, 2014; Cao *et al.*, 2015; Rowley *et al.*, 2016). In contrast to $PbTiO_3$ and $SrTiO_3$, however, these hexaferrites are also robustly ferrimagnetic at room temperature, with spontaneous magnetizations of $18.6\mu_B$ and $20\mu_B$ per formula unit for $PbFe_{12}O_{19}$ and $BaFe_{12}O_{19}$, respectively. This combination of ferroelectricity and ferrimagnetism and the possibility of inducing complex and coupled topological states involving both spin and charge make this system enticing. This superlattice combination has never been investigated due to the complexity of the crystal structures (magnetoplumbites) and the lack of isostructural substrates. Nonetheless, $PbFe_{12}O_{19}$ and $BaFe_{12}O_{19}$ are isostructural and lattice matched to each other within 0.3%, suggesting that high-quality superlattices should be possible on an appropriate substrate. In thin-film form, epitaxial hexaferrite heterostructures have not been studied nearly as much as epitaxial perovskite heterostructures. The previously mentioned properties, all measured on bulk samples, underline the opportunity to engineer hexaferrites with atomic-layer control, as has become commonplace for perovskites. These are complex crystal structures and taming and controlling them to be able to create multiferroic skyrmions and related topologies is challenging territory. To master these materials, a powerful combination of theory, synthesis, and characterization will be required. For example, on the synthesis side there are likely to be composition control and interface abruptness issues. The layers may suffer electrical leakage issues similar to what limited $BiFeO_3$ in bulk form, where the true properties of $BiFeO_3$ were not appreciated until the first high-quality and low leakage films were made (Wang *et al.*, 2003). The electrical leakage of bulk $PbFe_{12}O_{19}$ has similarly obfuscated whether or not it is ferroelectric (Rowley *et al.*, 2016) (and thus multiferroic, since its ferrimagnetism is evident). Detailed physical property studies will be needed (including transport, dielectric, pyroelectric, ferroelectric, and magnetic characterization) to fully understand the nature of the multiorder-parameter evolution. Such materials and the potentially unprecedented multiorder-parameter states and coupling can serve as the foundation for a range of device possibilities. Specifically, control over the geometric topological order of polar textures shows promise for low-power sensor and memory devices that are potentially robust to defects. The

discrete nature of topological solitons such as skyrmions lends itself well to a digital world, providing clear binary indicators (creation or annihilation, right- or left-handed, etc.). In addition, the inherent tunability and novel properties (such as negative permittivity and multiferrocity) of the proposed superlattices may reveal a host of applications that were not previously thought of for multiferroic materials. The unprecedented simultaneous control over electric and magnetic polarization present in these materials has the potential to impact a wide array of electronic and spintronic devices.

D. Probing the topological features of skyrmions

1. Photonic topological Hall effects

While the strong interactions of an electron with the medium that it travels through is being explored through several types of Hall measurements (most recently the topological Hall effect arising from the interactions of the electron with magnetic skyrmions) (Kanazawa *et al.*, 2011; Schulz *et al.*, 2012; Li *et al.*, 2013; Nagaosa and Tokura, 2013; Yasuda *et al.*, 2016; Kurumaji *et al.*, 2019; Shao *et al.*, 2019), the photonic analog of this behavior, called the photonic spin Hall effect (PSHE), although predicted theoretically (Onoda, Murakami, and Nagaosa, 2004; Bliokh and Bliokh, 2006), is just beginning to be studied (Hosten and Kwiat, 2008; Shitrit *et al.*, 2013; Yin *et al.*, 2013; Wang *et al.*, 2019). Experimental realization of this effect is challenging for the primary reason that the photon carries much less momentum than the electron, making spin-orbit-type interactions also correspondingly smaller. There have been recent studies of the PSHE in artificially structured metamaterials that have shown promise (Yin *et al.*, 2013). The handedness that is present in the polar vortices and skyrmions could in principle lead to a PSHE and would be a worthwhile direction to pursue.

2. Phononics: Phonon localization and chiral phonons

An aspect that has not received sufficient attention is the behavior of phonons in polar superlattices that exhibit vortices and skyrmions, particularly pathways to localize phonons or to induce chirality in them. Indeed, looking for phonon localization signatures was an original aspiration, stimulated by the observation of a minimum in thermal conductivity in $SrTiO_3/CaTiO_3$ and $SrTiO_3/BaTiO_3$ superlattices at a specific superlattice periodicity corresponding approximately to the dominant phonon main free path, thus prompting the exploration of $(PbTiO_3/SrTiO_3)$-based superlattices to enhance to "acoustic" contrast (or the elastic compliance tensor elements) between the layers. In the past decade, there has been considerable progress in experimentally measuring thermal conductivity of nanostructures using time-dependent thermoreflectance or the $3 - \omega$ measurement (Ravichandran *et al.*, 2014). From the theoretical perspective, the possible effects of phonon localization on thermal transport have been studied using the nonequilibrium Green's function methodology or through molecular dynamics simulations. There appears to be a significant opportunity for some breakthrough research that brings together the power of computationally designing both the composition and the structure in these superlattices such that the phonon behavior is exquisitely

tuned. These computational results can then be fed back to atomically precise synthesis approaches that have been discussed in this review, to attempt to "design" the phonon behavior. Functionally graded superlattices in which electric and chemical gradients are introduced through such an atomically precise synthesis is already trending. Introducing the elastic (and thereby phonon) elements into this framework would be a fruitful endeavor. A corollary to looking at phonon dynamics and localization in such superlattices is to explore the possibility for chiral phonons. While chirality from the electron perspective has been well studied, the same is not true for bosons such as phonons. Indeed, the observation of circular dichroism in the resonant mode for both the skyrmion and vortex structures may already be an indication of the presence of chiral phonons due to the intrinsically strong coupling between the dipoles and the lattice.

E. From the quantization of the topological indices to the quantization of the physical properties

In Sec. III.F we analyzed the relationship between the nontrivial polar textures and the electronic band structure of insulators once both problems are expressed in a topological language. In this context, every 2D insulating crystal is identified by an integer, characterizing the excess numbers of up-crossing versus down-crossing bands on any vacuum terminated edge (Vanderbilt, 2018). This number is called the chirality of the band structure, or the Chern number. The insulator can belong to a class where this integer is zero (the normal or "trivial" class) or nonzero (the "nontrivial" classes). This Chern number is indeed related to a measurable physical quantity: the anomalous Hall effect (AHE). Indeed, the fact that the edge channels are intrinsically quantized implies that the AHE of an insulator is also quantized (Vanderbilt, 2018).

In the case of magnetic skyrmions, it can be proven that the skyrmion number and the Chern number are equivalent (Gómez-Ortiz, 2018). The parallelism starts from the fact that a (2×2) Hamiltonian for spins that depends adiabatically on the magnetic field vector can be defined. The spinors, eigenstates of the former Hamiltonian, depend adiabatically on the position that they occupy in real space. After the computation of the Berry connection, it can be proven how the associated Berry curvature (whose integral is proportional to the Chern number) has exactly the same functional form as the integrand required to compute the skyrmion number (or the Pontryagin density). Depending on the spin texture, this skyrmion number might be zero (trivial topology) or nonzero (nontrivial case). In the latter case, emergent electromagnetic fields arise whose total magnetic flux amounts to $2\pi N$ (Nagaosa and Tokura, 2013), where N is as defined in Eq. (2) and whose effect on the conduction electrons induces the topological Hall effect, experimentally observed.

An interesting question is whether we can walk a similar path for the electric-dipole-based skyrmions. Skyrmion bubbles such as those presented in Sec. III.B.4 display a nonvanishing skyrmion number that is preserved layer by layer. But is this skyrmion number related to something like a Chern number? The polarization is the sum of an electronic contribution (a Berry phase of the electronic band structure) and an "ionic" contribution associated with the classical motions

of the charged nuclei when the atoms are moving during the adiabatic evolution. Is it possible to define the kind of Hamiltonian discussed for the magnetic counterparts? Are there emergent electromagnetic fields with quantized electric fluxes? Is there a physical property that is quantized following the topological index of the class? If the answer is affirmative, is this quantity related with optical, dielectric, or lattice dynamical properties (i.e., phonons)? The answer to this question is extremely important since it would allow the classification of a given texture in the proper homotopy class without the need of an accurate visualization of the atomic position or an extraction of the atomic polar displacements $\mathbf{P}_{PD}$.

Finally, quantum effects can also meet electric topological defects. In another study, once again using an effective Hamiltonian scheme but now within classical but also path-integral Monte Carlo simulations (Ceperley, 1995; Zhong and Vanderbilt, 1996; Íñiguez and Vanderbilt, 2002), the effect of zero-point quantum vibrations on properties of stress-free $KTaO_3$ nanodots under open-circuit electric boundary conditions was modeled (Prosandeev, Akbarzadeh, and Bellaiche, 2009). It was predicted that these vibrations would suppress the formation of an electrical vortex, in analogy with the fact that they annihilate the occurrence of a spontaneous electrical polarization in the bulk counterpart [hence the name incipient ferroelectric or quantum paraelectric (Müller and Burkard, 1979) given for bulks such as $SrTiO_3$ or $KTaO_3$]. In other words, Prosandeev, Akbarzadeh, and Bellaiche (2009) reported the discovery of a new class of materials, called incipient ferrotoroidics, for which the paraelectric-to-ferrotoroidic transition is washed out by quantum effects. Characteristics of this annihilation, such as the saturation of the ferrotoroidic susceptibility at low temperature and the existence of complex local structure exhibiting short-range, needlelike correlations of individual electric toroidal moments, were provided. But an experimental study of the effects that such zero-point vibrations have on electrical labyrinths, skyrmions, bubbles, stripes, etc., is lacking. It would be interesting to know whether such quantum effects destroy the metastable states (for instance,electrical skyrmions) by tunneling to the ground state at low temperatures (for instance, electrical stripes).

VII. CONCLUSIONS

This review has addressed the broad range of fundamental condensed-matter physics embedded in polar textures and the dramatic progress that has occurred in the past five to ten years in this field. While marking the 100 year anniversary of the discovery of ferroelectricity in the solid state, this review also points to the fact that the field of ferroelectrics has evolved dramatically in recent years. The emergent phenomena of the past decade have laid the foundation for the discoveries in the years to come. The confluence of powerful computational approaches, atomically precise syntheses, and a wide spectrum of probes of the physical phenomena with unprecedented energies, lengths, and timescales provides the ideal framework to study such phenomena. As noted, all is not yet known about such topological defects and textures. The search for the unknown should sustain strong interest in the field in the near future.

REFERENCES

Abid, Y. A., *et al.*, 2021, "Creating polar antivortex in PbTiO$_3$/SrTiO$_3$ superlattice," Nat. Commun. **12**, 2054.

Abrikosov, A. A., 1957, "The magnetic properties of superconducting alloys," J. Phys. Chem. Solids **2**, 199–208.

Aguado-Puente, P., and J. Junquera, 2008, "Ferromagneticlike Closure Domains in Ferroelectric Ultrathin Films: First-Principles Simulations," Phys. Rev. Lett. **100**, 177601.

Aguado-Puente, P., and J. Junquera, 2012, "Structural and energetic properties of domains in $PbTiO_3/SrTiO_3$ superlattices from first principles," Phys. Rev. B **85**, 184105.

Ahn, C. H., K. M. Rabe, and J.-M. Triscone, 2004, "Ferroelectricity at the nanoscale: Local polarization in oxide thin films and heterostructures," Science **303**, 488–491.

Ahn, C. H., J.-M. Triscone, and J. Mannhart, 2003, "Electric field effect in correlated oxide systems," Nature (London) **424**, 1015–1018.

Anderson, P. W., 1987, "The resonating valence bond state in La_2CuO_4 and superconductivity," Science **235**, 1196–1198.

Aramberri, H., N. S. Fedorova, and J. Íñiguez, 2022, "Ferroelectric/ paraelectric superlattices for energy storage," Sci. Adv. **8**, eabn4880.

Arnold, V. I., and B. A. Khesin, 1998, *Topological Methods in Hydrodynamics* (Springer, New York).

Artyukhin, S., K. T. Delaney, N. A. Spaldin, and M. Mostovoy, 2014, "Landau theory of topological defects in multiferroic hexagonal manganites," Nat. Mater. **13**, 42–49.

Back, C., *et al.*, 2020, "The 2020 skyrmionics roadmap," J. Phys. D **53**, 363001.

Bakaul, S. R., S. Prokhorenko, Q. Zhang, Y. Nahas, Y. Hu, A. Petford-Long, L. Bellaiche, and N. Valanoor, 2021, "Freestanding ferroelectric bubble domains," Adv. Mater. **33**, 2105432.

Baker, J. S., and D. R. Bowler, 2020, "Polar morphologies from first principles: $PbTiO_3$ films on $SrTiO_3$ substrates and the $p(2 \times \Lambda)$ surface reconstruction," Adv. Theory Simul. **3**, 2000154.

Baker, J. S., and D. R. Bowler, 2021, "Origin of Ferroelectric Domain Wall Alignment with Surface Trenches in Ultrathin Films," Phys. Rev. Lett. **127**, 247601.

Balke, N., *et al.*, 2012, "Enhanced electric conductivity at ferroelectric vortex cores in $BiFeO_3$," Nat. Phys. **8**, 81–88.

Batra, I. P., and B. D. Silverman, 1972, "Thermodynamic stability of thin ferroelectric films," Solid State Commun. **11**, 291–294.

Batra, I. P., P. Wurfel, and B. D. Silverman, 1973, "New Type of First-Order Phase Transition in Ferroelectric Thin Films," Phys. Rev. Lett. **30**, 384–387.

Baudry, L., A. Sené, I. A. Luk'yanchuk, and L. Lahoche, 2011, "Vortex state in thin films of multicomponent ferroelectrics," Thin Solid Films **519**, 5808–5810.

Baudry, L., A. Sené, I. A. Luk'yanchuk, L. Lahoche, and J. F. Scott, 2014, "Polarization vortex domains induced by switching electric field in ferroelectric films with circular electrodes," Phys. Rev. B **90**, 024102.

Beasley, M. R., J. E. Mooij, and T. P. Orlando, 1979, "Possibility of Vortex-Antivortex Pair Dissociation in Two-Dimensional Super-conductors," Phys. Rev. Lett. **42**, 1165–1168.

Bednorz, J. G., and K. A. Müller, 1986, "Possible highT_c super-conductivity in the Ba-La-Cu-O system," Z. Phys. B **64**, 189–193.

Behera, P., *et al.*, 2022, "Electric field control of chirality," Sci. Adv. **8**, eabj8030.

Bellaiche, L., A. García, and D. Vanderbilt, 2000, "Finite-Temperature Properties of $Pb(Zr_{1-x}Ti_x)O_3$ Alloys from First Principles," Phys. Rev. Lett. **84**, 5427–5430.

Bennett, D., G. Chaudhary, R.-J. Slager, E. Bousquet, and Ph. Ghosez, 2023, "Polar meron-antimeron networks in strained and twisted bilayers," Nat. Commun. **14**, 1629.

Bennett, D., M. Muñoz Basagoiti, and E. Artacho, 2020, "Electro-statics and domains in ferroelectric superlattices," R. Soc. Open Sci. **7**, 201270.

Berezinskii, V. L., 1972, "Destruction of long-range order in one-dimensional and two-dimensional systems possessing a continuous symmetry group II, quantum systems," Sov. Phys. JETP **34**, 610, http://www.jetp.ras.ru/cgi-bin/dn/e_034_03_0610.pdf.

Bick, E., S. Bick, and D. Frank, 2005, Eds., *Topology and Geometry in Physics*, Lecture Notes in Physics Vol. 659 (Springer, Berlin).

Bilc, D. I., R. Orlando, R. Shaltaf, G.-M. Rignanese, Jorge Íñiguez, and Ph. Ghosez, 2008, "Hybrid exchange-correlation functional for accurate prediction of the electronic and structural properties of ferroelectric oxides," Phys. Rev. B **77**, 165107.

Bishop, D. J., and J. D. Reppy, 1978, "Study of the Superfluid Transition in Two-Dimensional ^4He Films," Phys. Rev. Lett. **40**, 1727–1730.

Blatter, G., M. V. Feigel'man, V. B. Geshkenbein, A. I. Larkin, and V. M. Vinokur, 1994, "Vortices in high-temperature superconduc-tors," Rev. Mod. Phys. **66**, 1125–1388.

Bliokh, K. Y., and Y. P. Bliokh, 2006, "Conservation of Angular Momentum, Transverse Shift, and Spin Hall Effect in Reflection and Refraction of an Electromagnetic Wave Packet," Phys. Rev. Lett. **96**, 073903.

Bogatyrev, A. B., and K. L. Metlov, 2018, "What makes magnetic skyrmions different from magnetic bubbles?," J. Magn. Magn. Mater. **465**, 743–746.

Bousquet, E., M. Dawber, N. Stucki, C. Lichtensteiger, P. Hermet, S. Gariglio, J.-M. Triscone, and Ph. Ghosez, 2008, "Improper ferroelectricity in perovskite oxide artificial superlattices," Nature (London) **452**, 732–736.

Bousquet, E., J. Junquera, and Ph. Ghosez, 2010, "First-principles study of competing ferroelectric and antiferroelectric instabilities in $BaTiO_3/BaO$ superlattices," Phys. Rev. B **82**, 045426.

Boyn, S., *et al.*, 2017, "Learning through ferroelectric domain dynamics in solid-state synapses," Nat. Commun. **8**, 14736.

Braga, M. H., J. E. Oliveira, A. J. Murchison, and J. B. Goodenough, 2020, "Performance of a ferroelectric glass electrolyte in a self-charging electrochemical cell with negative capacitance and resis-tance," Appl. Phys. Rev. **7**, 011406.

Bratkovsky, A. M., and A. P. Levanyuk, 2000, "Abrupt Appearance of the Domain Pattern and Fatigue of Thin Ferroelectric Films," Phys. Rev. Lett. **84**, 3177–3180.

Bratkovsky, A. M., and A. P. Levanyuk, 2001, "Very large dielectric response of thin ferroelectric films with the dead layers," Phys. Rev. B **63**, 132103.

Bratkovsky, A. M., and A. P. Levanyuk, 2009, "Continuous theory of ferroelectric states in ultrathin films with real electrodes," J. Comput. Theor. Nanosci. **6**, 465–489.

Bray, S., 2012, https://photography.tutsplus.com.

Büttner, F., *et al.*, 2015, "Dynamics and inertia of skyrmionic spin structures," Nat. Phys. **11**, 225–228.

Callan, C. G., R. Dashen, and D. J. Gross, 1978, "Toward a theory of the strong interactions," Phys. Rev. D **17**, 2717–2763.

Callan, C. G., R. Dashen, and D. J. Gross, 1994, "Toward a theory of the strong interactions," in *Instantons in Gauge Theories*, edited by M. Shifman (World Scientific, Singapore), pp. 36–60.

Cao, H. B., Z. Y. Zhao, M. Lee, E. S. Choi, M. A. McGuire, B. C. Sales, H. D. Zhou, J.-Q. Yan, and D. G. Mandrus, 2015, "High pressure floating zone growth and structural properties of ferrimagnetic quantum paraelectric $BaFe_{12}O_{19}$," APL Mater. **3**, 062512.

Caretta, L., *et al.*, 2023, "Non-volatile electric-field control of inversion symmetry," Nat. Mater. **22**, 207–215.

Castelnovo, C., R. Moessner, and S. L. Sondhi, 2008, "Magnetic monopoles in spin ice," Nature (London) **451**, 42–45.

Catalan, G., J. Seidel, R. Ramesh, and J. F. Scott, 2012, "Domain wall nanoelectronics," Rev. Mod. Phys. **84**, 119–156.

Ceperley, D. M., 1995, "Path integrals in the theory of condensed helium," Rev. Mod. Phys. **67**, 279–355.

Chaikin, P. M., and T. C. Lubensky, 2000, *Principles of Condensed Matter Physics* (Cambridge University Press, Cambridge, England), Chaps. 9 and 10.

Chang, K., J. W. D. Villanova, J.-R. Ji, S. Das, F. Küster, S. Barraza-Lopez, P. Sessi, and S. S. P. Parkin, 2021, "Vortex-oriented ferroelectric domains in SnTe/PbTe monolayer lateral heterostructures," Adv. Mater. **33**, 2102267.

Chen, P., C. Paillard, H. J. Zhao, J. Íñiguez, and L. Bellaiche, 2022, "Deterministic control of ferroelectric polarization by ultrafast laser pulses," Nat. Commun. **13**, 2566.

Chen, P., C. Xu, S. Prokhorenko, Y. Nahas, B. Xu, and L. Bellaiche, 2023, "Electrical topological defects induced by terahertz laser pulses," Phys. Rev. B **107**, L060101.

Chen, P., H. J. Zhao, S. Prosandeev, S. Artyukhin, and L. Bellaiche, 2022, "Microscopic origin of the electric Dzyaloshinskii-Moriya interaction," Phys. Rev. B **106**, 224101.

Chen, P., *et al.*, 2020, "Atomic imaging of mechanically induced topological transition of ferroelectric vortices," Nat. Commun. **11**, 1840.

Chen, P., *et al.*, 2022, "Electrically driven motion, destruction, and chirality change of polar vortices in oxide superlattices," Sci. China Phys. Mech. Astron. **65**, 237011.

Chen, S., *et al.*, 2021, "Recent progress on topological structures in ferroic thin films and heterostructures," Adv. Mater. **33**, 2000857.

Chen, W. J., S. Yuan, L. L. Ma, Y. Ji, B. Wang, and Y. Zheng, 2018, "Mechanical switching in ferroelectrics by shear stress and its implications on charged domain wall generation and vortex memory devices," RSC Adv. **8**, 4434–4444.

Chen, W. J., Y. Zheng, and B. Wang, 2012, "Vortex domain structure in ferroelectric nanoplatelets and control of its transformation by mechanical load," Sci. Rep. **2**, 796.

Chen, W. J., Y. Zheng, and B. Wang, 2015, "Large and tunable polar-toroidal coupling in ferroelectric composite nanowires toward superior electromechanical responses," Sci. Rep. **5**, 11165.

Chen, Y. T., Y. L. Tang, Y. L. Zhu, Y. J. Wang, M. J. Han, M. J. Zou, Y. P. Feng, W. R. Geng, F. H. Gong, and X. L. Ma, 2020, "Periodic vortex-antivortex pairs in tensile strained PbTiO$_3$ films," Appl. Phys. Lett. **117**, 192901.

Cheng, R., M. Li, A. Sapkota, A. Rai, A. Pokhrel, T. Mewes, C. Mewes, D. Xiao, M. De Graef, and V. Sokalski, 2019, "Magnetic domain wall skyrmions," Phys. Rev. B **99**, 184412.

Cheong, S.-W., and M. Mostovoy, 2007, "Multiferroics: A magnetic twist for ferroelectricity," Nat. Mater. **6**, 13–20.

Chien, C. L., F. Q. Zhu, and J.-G. Zhu, 2007, "Patterned nanomagnets," Phys. Today **60**, No. 6, 40.

Chisholm, M. F., W. Luo, M. P. Oxley, S. T. Pantelides, and H. N. Lee, 2010, "Atomic-Scale Compensation Phenomena at Polar Interfaces," Phys. Rev. Lett. **105**, 197602.

Cho, D.-Y., *et al.*, 2007, "Ferroelectricity Driven by Y d^0-ness with Rehybridization in YMnO$_3$," Phys. Rev. Lett. **98**, 217601.

Choe, S.-B., Y. Acremann, A. Scholl, A. Bauer, A. Doran, J. Stöhr, and H. A. Padmore, 2004, "Vortex core-driven magnetization dynamics," Science **304**, 420–422.

Choi, K. J., *et al.*, 2004, "Enhancement of ferroelectricity in strained BaTiO$_3$ thin films," Science **306**, 1005–1009.

Choi, T., Y. Horibe, H. T. Yi, Y. J. Choi, W. Wu, and S.-W. Cheong, 2010, "Insulating interlocked ferroelectric and structural antiphase domain walls in multiferroic YMnO$_3$," Nat. Mater. **9**, 253–258.

Choudhury, N., L. Walizer, S. Lisenkov, and L. Bellaiche, 2011, "Geometric frustration in compositionally modulated ferroelectrics," Nature (London) **470**, 513–517.

Cohen, R. E., 1992, "Origin of ferroelectricity in perovskite oxides," Nature (London) **358**, 136–138.

Coleman, S., and E. Weinberg, 1973, "Radiative corrections as the origin of spontaneous symmetry breaking," Phys. Rev. D **7**, 1888–1910.

Cortés-Ortuño, D., W. Wang, M. Beg, R. A. Pepper, M.-A. Bisotti, R. Carey, M. Vousden, Th. Kluyver, O. Hovorka, and H. Fangohr, 2017, "Thermal stability and topological protection of skyrmions in nanotracks," Sci. Rep. **7**, 4060.

Cross, M., and H. Greenside, 2009, *Pattern Formation and Dynamics in Nonequilibrium Systems* (Cambridge University Press, Cambridge, England).

Cruz, M. P., Y. H. Chu, J. X. Zhang, P. L. Yang, F. Zavaliche, Q. He, P. Shafer, L. Q. Chen, and R. Ramesh, 2007, "Strain Control of Domain-Wall Stability in Epitaxial BiFeO$_3$ (110) Films," Phys. Rev. Lett. **99**, 217601.

Dagotto, E., 1994, "Correlated electrons in high-temperature superconductors," Rev. Mod. Phys. **66**, 763–840.

Dai, C., V. A. Stoica, S. Das, Z. Hong, L. W. Martin, R. Ramesh, J. W. Freeland, H. Wen, V. Gopalan, and L.-Q. Chen, 2022, "Tunable nanoscale evolution and topological phase transitions of a polar vortex supercrystal," Adv. Mater. **34**, 2106401.

Damodaran, A. R., *et al.*, 2017a, "Phase coexistence and electric-field control of toroidal order in oxide superlattices," Nat. Mater. **16**, 1003–1009.

Damodaran, A. R., *et al.*, 2017b, "Large polarization gradients and temperature-stable responses in compositionally-graded ferroelectrics," Nat. Commun. **8**, 14961.

Das, H., A. L. Wysocki, Y. Geng, W. Wu, and C. J. Fennie, 2014, "Bulk magnetoelectricity in the hexagonal manganites and ferrites," Nat. Commun. **5**, 2998.

Das, S., A. Ghosh, M. R. McCarter, S.-L. Hsu, Y.-L. Tang, A. R. Damodaran, R. Ramesh, and L. W. Martin, 2018, "Perspective: Emergent topologies in oxide superlattices," APL Mater. **6**, 100901.

Das, S., Z. Hong, M. McCarter, P. Shafer, Y.-T. Shao, D. A. Muller, L. W. Martin, and R. Ramesh, 2020, "A new era in ferroelectrics," APL Mater. **8**, 120902.

Das, S., *et al.*, 2019, "Observation of room-temperature polar skyrmions," Nature (London) **568**, 368–372.

Das, S., *et al.*, 2021, "Local negative permittivity and topological phase transition in polar skyrmions," Nat. Mater. **20**, 194–201.

Das, S., *et al.*, 2022, "Inherent spin-polarization coupling in a magnetoelectric vortex," Nano Lett. **22**, 3976–3982.

Dawber, M., P. Chandra, P. B. Littlewood, and J. F. Scott, 2003, "Depolarization corrections to the coercive field in thin-film ferroelectrics," J. Phys. Condens. Matter **15**, L393–L398.

Dawber, M., A. Gruverman, and J. F. Scott, 2006, "Skyrmion model of nano-domain nucleation in ferroelectrics and ferromagnets," J. Phys. Condens. Matter **18**, L71–L79.

Dawber, M., K. M. Rabe, and J. F. Scott, 2005, "Physics of thin-film ferroelectric oxides," Rev. Mod. Phys. **77**, 1083–1130.

Dawber, M., N. Stucki, C. Lichtensteiger, S. Gariglio, Ph. Ghosez, and J.-M. Triscone, 2007, "Tailoring the properties of artificially layered ferroelectric superlattices," Adv. Mater. **19**, 4153–4159.

De Guerville, F., I. Luk'yanchuk, L. Lahoche, and M. El Marssi, 2005, "Modeling of ferroelectric domains in thin films and superlattices," Mater. Sci. Eng. B **120**, 16–20.

Ding, L. L., Ye Ji, X. Y. Zhang, W. M. Xiong, W. J. Chen, B. M. Zhang, B. Wang, and Y. Zheng, 2019, "Characterization and control of vortex and antivortex domain defects in quadrilateral ferroelectric nanodots," Phys. Rev. Mater. **3**, 104417.

Di Rino, F., M. Sepliarsky, and M. G. Stachiotti, 2020, "Topology of the polarization field in PbTiO$_3$ nanoparticles of different shapes by atomic-level simulations," J. Appl. Phys. **127**, 144101.

Dolgov, O. V., D. A. Kirzhnits, and E. G. Maksimov, 1981, "On an admissible sign of the static dielectric function of matter," Rev. Mod. Phys. **53**, 81–93.

Donoway, E., Y. T. Shao, S. Das, Z. Hong, L. Caretta, M. McCarter, D. A. Muller, and R. Ramesh, 2021, "Emergent topological phase transition dynamics of polar skyrmions," Bull. Am. Phys. Soc. **Y55**, 00003, https://meetings.aps.org/Meeting/MAR21/Session/Y55.3.

Du, K., M. Zhang, C. Dai, Z. N. Zhou, Y. W. Xie, Z. H. Ren, H. Tian, L. Q. Chen, G. Van Tendeloo, and Z. Zhang, 2019, "Manipulating topological transformations of polar structures through real-time observation of the dynamic polarization evolution," Nat. Commun. **10**, 4864.

Dubovik, V. M., and V. V. Tugushev, 1990, "Toroid moments in electrodynamics and solid-state physics," Phys. Rep. **187**, 145–202.

Dubrovin, B. A., A. T. Fomenko, and S. P. Novikov, 1985, *Modern Geometry—Methods and Applications. Part II: The Geometry and Topology of Manifolds*, Graduate Texts in Mathematics Vol. 104 (Springer, New York).

Dupé, M., S. Heinze, J. Sinova, and B. Dupé, 2018, "Stability and magnetic properties of Fe double layers on Ir (111)," Phys. Rev. B **98**, 224415.

Dzyaloshinsky, I., 1958, "A thermodynamic theory of 'weak' ferromagnetism of antiferromagnetics," J. Phys. Chem. Solids **4**, 241–255.

Eliseev, E. A., A. N. Morozovska, S. V. Kalinin, Y. Li, J. Shen, M. D. Glinchuk, L.-Q. Chen, and V. Gopalan, 2009, "Surface effect on domain wall width in ferroelectrics," J. Appl. Phys. **106**, 084102.

Erb, K. C., and J. Hlinka, 2020, "Vector, bidirector, and Bloch skyrmion phases induced by structural crystallographic symmetry breaking," Phys. Rev. B **102**, 024110.

Ezawa, M., 2011, "Compact merons and skyrmions in thin chiral magnetic films," Phys. Rev. B **83**, 100408.

Feigelman, M. V., 1979, "Dipole forces and phase transition in a two-dimensional planar ferromagnet," Sov. Phys. JETP **49**, 395–398, http://jetp.ras.ru/cgi-bin/dn/e_049_02_0395.pdf.

Fernandez, A., M. Acharya, H.-G. Lee, J. Schimpf, Y. Jiang, D. Lou, Z. Tian, and L. W. Martin, 2022, "Thin-film ferroelectrics," Adv. Mater. **34**, 2108841.

Fert, A., V. Cros, and J. Sampaio, 2013, "Skyrmions on the track," Nat. Nanotechnol. **8**, 152–156.

Fiebig, M., 2005, "Revival of the magnetoelectric effect," J. Phys. D **38**, R123–R152.

Fiebig, M., Th. Lottermoser, D. Fröhlich, A. V. Goltsev, and R. V. Pisarev, 2002, "Observation of coupled magnetic and electric domains," Nature (London) **419**, 818–820.

Flërova, S. A., and O. E. Bochkov, 1981, "The influence of magnetic field on the phase boundary in BaTiO$_3$ crystals," JETP Lett. **33**, 34–36, http://jetpletters.ru/ps/1500/article_22925.pdf.

Flërova, S. A., and O. E. Bochkov, 1982, "The influence of a magnetic field on the behavior of BaTiO$_3$ crystals in the vicinity of a ferroelectric phase transition," Sov. Phys. Crystallogr. **27**, 122.

Fong, D. D., G. B. Stephenson, S. K. Streiffer, J. A. Eastman, O. Auciello, P. H. Fuoss, and C. Thompson, 2004, "Ferroelectricity in ultrathin perovskite films," Science **304**, 1650–1653.

Fröhlich, J., and Th. Spencer, 1981, "The Kosterlitz-Thouless transition in two-dimensional Abelian spin systems and the Coulomb gas," Commun. Math. Phys. **81**, 527–602.

Fu, H., and L. Bellaiche, 2003, "Ferroelectricity in Barium Titanate Quantum Dots and Wires," Phys. Rev. Lett. **91**, 257601.

Fujimura, N., T. Ishida, T. Yoshimura, and T. Ito, 1996, "Epitaxially grown YMnO$_3$ film: New candidate for nonvolatile memory devices," Appl. Phys. Lett. **69**, 1011–1013.

Gao, L., S. Prokhorenko, Y. Nahas, and L. Bellaiche, 2023, "Dynamical control of topology in ferroelectric skyrmions via twisted light," arXiv:2302.01402.

Gao, N., *et al.*, 2019, "Creation and annihilation of topological meron pairs in in-plane magnetized films," Nat. Commun. **10**, 5603.

Ghosez, Ph., E. Cockayne, U. V. Waghmare, and K. M. Rabe, 1999, "Lattice dynamics of BaTiO$_3$, PbTiO$_3$, and PbZrO$_3$: A comparative first-principles study," Phys. Rev. B **60**, 836–843.

Gómez-Ortiz, F., 2018, "Study of the topology of ferroelectric skyrmions," master's thesis (Universidad de Cantabria).

Gómez-Ortiz, F., H. Aramberri, J. M. López, P. García-Fernández, J. Íñiguez, and J. Junquera, 2023, "Kittel law and domain formation mechanism in PbTiO$_3$/SrTiO$_3$ superlattices," arXiv:2303.01755.

Gómez-Ortiz, F., P. García-Fernández, J. M. López, and J. Junquera, 2022a, "Berezinskii-Kosterlitz-Thouless phases in ultrathin PbTiO$_3$/SrTiO$_3$ superlattices," Phys. Rev. B **106**, 134106.

Gómez-Ortiz, F., P. García-Fernández, J. M. López, and J. Junquera, 2022b, "Melting of crystals of polarization vortices and chiral phase transitions in oxide superlattices," Phys. Rev. B **105**, L220103.

Gong, F.-H., *et al.*, 2021, "Atomic mapping of periodic dipole waves in ferroelectric oxide," Sci. Adv. **7**, eabg5503.

Govinden, V., S. Prokhorenko, Q. Zhang, S. Rijal, Y. Nahas, L. Bellaiche, and N. Valanoor, 2023, "Spherical ferroelectric solitons," Nat. Mater. (in press), 10.1038/s41563-023-01527-y.

Govinden, V., S. Rijal, Q. Zhang, Y. Nahas, L. Bellaiche, N. Valanoor, and S. Prokhorenko, 2023, "Stability of ferroelectric bubble domains," Phys. Rev. Mater. **7**, L011401.

Govinden, V., S. Rijal, Q. Zhang, D. Sando, S. Prokhorenko, Y. Nahas, L. Bellaiche, and N. Valanoor, 2021, "Controlling topological defect transitions in nanoscale lead zirconate titanate heterostructures," Phys. Rev. Mater. **5**, 124205.

Govinden, V., *et al.*, 2022, "Ferroelectric solitons crafted in epitaxial bismuth ferrite superlattices," arXiv:2209.08979.

Graf, M., H. Aramberri, P. Zubko, and J. Íñiguez, 2022, "Giant voltage amplification from electrostatically induced incipient ferroelectric states," Nat. Mater. **21**, 1252–1257.

Gregg, J. M., 2012, "Exotic domain states in ferroelectrics: Searching for vortices and skyrmions," Ferroelectrics **433**, 74–87.

Griffin, S. M., M. Lilienblum, K. T. Delaney, Y. Kumagai, M. Fiebig, and N. A. Spaldin, 2012, "Scaling Behavior and beyond Equilibrium in the Hexagonal Manganites," Phys. Rev. X **2**, 041022.

Grollier, J., D. Querlioz, K. Y. Camsari, K. Everschor-Sitte, S. Fukami, and M. D. Stiles, 2020, "Neuromorphic spintronics," Nat. Electron. **3**, 360–370.

Gruverman, A., D. Wu, H.-J. Fan, I. Vrejoiu, M. Alexe, R. J. Harrison, and J. F. Scott, 2008, "Vortex ferroelectric domains," J. Phys. Condens. Matter **20**, 342201.

Gui, Z., and L. Bellaiche, 2014, "Terahertz dynamics of ferroelectric vortices from first principles," Phys. Rev. B **89**, 064303.

Gui, Z., L.-W. Wang, and L. Bellaiche, 2015, "Electronic properties of electrical vortices in ferroelectric nanocomposites from large-scale *ab initio* computations," Nano Lett. **15**, 3224–3229.

Guo, M., *et al.*, 2021, "Toroidal polar topology in strained ferroelectric polymer," Science **371**, 1050–1056.

Guo, X., L. Zhou, B. Roul, Y. Wu, Y. Huang, S. Das, and Z. Hong, 2022, "Theoretical understanding of polar topological phase transitions in functional oxide heterostructures: A review," Small Methods **6**, 2200486.

Hadjimichael, M., *et al.*, 2021, "Metal-ferroelectric supercrystals with periodically curved metallic layers," Nat. Mater. **20**, 495–502.

Haeni, J. H., *et al.*, 2004, "Room-temperature ferroelectricity in strained SrTiO$_3$," Nature (London) **430**, 758–761.

Halperin, B. I., 2020, "APS Medal for Exceptional Achievement in Research: Topology and other tools in condensed matter physics," Rev. Mod. Phys. **92**, 045001.

Halperin, B. I., and D. R. Nelson, 1978, "Theory of Two-Dimensional Melting," Phys. Rev. Lett. **41**, 121–124.

Han, L., *et al.*, 2022, "High-density switchable skyrmion-like polar nanodomains integrated on silicon," Nature (London) **603**, 63–67.

Harris, M., 1999, "Taking the frustration out of ice," Nature (London) **399**, 311–312.

Hatcher, A., 2002, *Algebraic Topology* (Cambridge University Press, Cambridge, England).

He, Q., *et al.*, 2011, "Electrically controllable spontaneous magnetism in nanoscale mixed phase multiferroics," Nat. Commun. **2**, 225.

Hebard, A. F., and A. T. Fiory, 1980, "Evidence for the Kosterlitz-Thouless Transition in Thin Superconducting Aluminum Films," Phys. Rev. Lett. **44**, 291–294.

Hemberger, J., P. Lunkenheimer, R. Fichtl, H.-A. Krug von Nidda, V. Tsurkan, and A. Loidl, 2005, "Relaxor ferroelectricity and colossal magnetocapacitive coupling in ferromagnetic $CdCr_2S_4$," Nature (London) **434**, 364–367.

Herbut, I., 2007, *A Modern Approach to Critical Phenomena* (Cambridge University Press, Cambridge, England).

Herchig, R., and I. Ponomareva, 2017, "Unusual soft mode dynamics in ferroelectric $PbTiO_3$ nanowire under different mechanical boundary conditions," J. Appl. Phys. **122**, 214103.

Heron, J. T., *et al.*, 2014, "Deterministic switching of ferromagnetism at room temperature using an electric field," Nature (London) **516**, 370–373.

Hierro-Rodriguez, A., C. Quirós, A. Sorrentino, C. Blanco-Roldán, L. M. Alvarez-Prado, J. I. Martín, J. M. Alameda, E. Pereiro, M. Vélez, and S. Ferrer, 2017, "Observation of asymmetric distributions of magnetic singularities across magnetic multilayers," Phys. Rev. B **95**, 014430.

Hlinka, J., and P. Ondrejkovic, 2019, "Skyrmions in ferroelectric materials," in *Recent Advances in Topological Ferroics and their Dynamics*, Solid State Physics Vol. 70, edited by Robert L. Stamps and Helmut Schultheiß (Academic Press, New York), Chap. 4, pp. 143–169..

Hoffmann, M., F. P. G. Fengler, B. Max, U. Schroeder, S. Slesazeck, and Th. Mikolajick, 2019, "Negative capacitance for electrostatic supercapacitors," Adv. Energy Mater. **9**, 1901154.

Hohenberg, P. C., 1967, "Existence of long-range order in one and two dimensions," Phys. Rev. **158**, 383–386.

Holm, C., and W. Janke, 1994, "Monte Carlo study of topological defects in the 3D Heisenberg model," J. Phys. A **27**, 2553–2563.

Hong, J., G. Catalan, D. N. Fang, E. Artacho, and J. F. Scott, 2010, "Topology of the polarization field in ferroelectric nanowires from first principles," Phys. Rev. B **81**, 172101.

Hong, Z., S. Das, C. Nelson, A. Yadav, Y. Wu, J. Junquera, L.-Q. Chen, L. W. Martin, and R. Ramesh, 2021, "Vortex domain walls in ferroelectrics," Nano Lett. **21**, 3533–3539.

Hong, Z., *et al.*, 2017, "Stability of polar vortex lattice in ferroelectric superlattices," Nano Lett. **17**, 2246–2252.

Horibe, Y., *et al.*, 2014, "Color theorems, chiral domain topology, and magnetic properties of Fe_xTaS_2," J. Am. Chem. Soc. **136**, 8368–8373.

Hosten, O., and P. Kwiat, 2008, "Observation of the spin Hall effect of light via weak measurements," Science **319**, 787–790.

Huang, F.-T., and S.-W. Cheong, 2017, "Aperiodic topological order in the domain configurations of functional materials," Nat. Rev. Mater. **2**, 17004.

Huang, P., Th. Schönenberger, M. Cantoni, L. Heinen, A. Magrez, A. Rosch, F. Carbone, and H. M. Rønnow, 2020, "Melting of a skyrmion lattice to a skyrmion liquid via a hexatic phase," Nat. Nanotechnol. **15**, 761–767.

Imada, M., A. Fujimori, and Y. Tokura, 1998, "Metal-insulator transitions," Rev. Mod. Phys. **70**, 1039–1263.

Íñiguez, J., and D. Vanderbilt, 2002, "First-Principles Study of the Temperature-Pressure Phase Diagram of $BaTiO_3$," Phys. Rev. Lett. **89**, 115503.

Íñiguez, J., P. Zubko, I. Luk'yanchuk, and A. Cano, 2019, "Ferroelectric negative capacitance," Nat. Rev. Mater. **4**, 243–256.

Jia, C.-L., K. W. Urban, M. Alexe, D. Hesse, and I. Vrejoiu, 2011, "Direct observation of continuous electric dipole rotation in flux-closure domains in ferroelectric $Pb(Zr,Ti)O_3$," Science **331**, 1420–1423.

Jiang, J. C., X. Q. Pan, W. Tian, C. D. Theis, and D. G. Schlom, 1999, "Abrupt $PbTiO_3/SrTiO_3$ superlattices grown by reactive molecular beam epitaxy," Appl. Phys. Lett. **74**, 2851–2853.

Jin, S., T. H. Tiefel, M. McCormack, R. A. Fastnacht, R. Ramesh, and L. H. Chen, 1994, "Thousandfold change in resistivity in magnetoresistive LA-Ca-Mn-O films," Science **264**, 413–415.

José, J. V., 2012, *40 Years of Berezinskii-Kosterlitz-Thouless Theory* (World Scientific, Singapore).

Junquera, J., 2021, "Dzyaloshinskii-Moriya interaction turns electric," Nat. Mater. **20**, 291–292.

Junquera, J., and Ph. Ghosez, 2003, "Critical thickness for ferroelectricity in perovskite ultrathin films," Nature (London) **422**, 506–509.

Juraschek, D. M., Q. N. Meier, M. Trassin, S. E. Trolier-McKinstry, C. L. Degen, and N. A. Spaldin, 2019, "Dynamical Magnetic Field Accompanying the Motion of Ferroelectric Domain Walls," Phys. Rev. Lett. **123**, 127601.

Kamien, R. D., and R. A. Mosna, 2016, "The topology of dislocations in smectic liquid crystals," New J. Phys. **18**, 053012.

Kanazawa, N., Y. Onose, T. Arima, D. Okuyama, K. Ohoyama, S. Wakimoto, K. Kakurai, S. Ishiwata, and Y. Tokura, 2011, "Large Topological Hall Effect in a Short-Period Helimagnet MnGe," Phys. Rev. Lett. **106**, 156603.

Khan, A. I., D. Bhowmik, P. Yu, S. Joo Kim, I. Pan, R. Ramesh, and S. Salahuddin, 2011, "Experimental evidence of ferroelectric negative capacitance in nanoscale heterostructures," Appl. Phys. Lett. **99**, 113501.

Khan, A. I., K. Chatterjee, B. Wang, S. Drapcho, L. You, C. Serrao, S. R. Bakaul, R. Ramesh, and S. Salahuddin, 2015, "Negative capacitance in a ferroelectric capacitor," Nat. Mater. **14**, 182–186.

Khan, M. A., J. A. Caraveo-Frescas, and H. N. Alshareef, 2015, "Hybrid dual gate ferroelectric memory for multilevel information storage," Org. Electron. **16**, 9–17.

Kim, D. J., J. Y. Jo, Y. S. Kim, Y. J. Chang, J. S. Lee, Jong-Gul Yoon, T. K. Song, and T. W. Noh, 2005, "Polarization Relaxation Induced by a Depolarization Field in Ultrathin Ferroelectric $BaTiO_3$ Capacitors," Phys. Rev. Lett. **95**, 237602.

Kim, J., M. You, K.-E. Kim, K. Chu, and C.-H. Yang, 2019, "Artificial creation and separation of a single vortex-antivortex pair in a ferroelectric flatland," npj Quantum Mater. **4**, 29.

Kim, K. T., *et al.*, 2022, "Chiral structures of electric polarization vectors quantified by x-ray resonant scattering," Nat. Commun. **13**, 1769.

Kim, Y. C., T. J. Shin, S.-M. Hur, S. J. Kwon, and S. Y. Kim, 2019, "Shear-solvo defect annihilation of diblock copolymer thin films over a large area," Sci. Adv. **5**, eaaw3974.

King-Smith, R. D., and D. Vanderbilt, 1994, "First-principles investigation of ferroelectricity in perovskite compounds," Phys. Rev. B **49**, 5828–5844.

Kittel, C., 1966, *Introduction to Solid State Physics* (Wiley, Hoboken, NJ).

Kittel, Ch., 1946, "Theory of the structure of ferromagnetic domains in films and small particles," Phys. Rev. **70**, 965–971.

Kittel, Ch., 1949, "Physical theory of ferromagnetic domains," Rev. Mod. Phys. **21**, 541–583.

Kivelson, S. A., E. Fradkin, and V. J. Emery, 1998, "Electronic liquid-crystal phases of a doped Mott insulator," Nature (London) **393**, 550–553.

Klein, T., I. Joumard, S. Blanchard, J. Marcus, R. Cubitt, T. Giamarchi, and P. Le Doussal, 2001, "A Bragg glass phase in the vortex lattice of a type II superconductor," Nature (London) **413**, 404–406.

Kornev, I., H. Fu, and L. Bellaiche, 2004, "Ultrathin Films of Ferroelectric Solid Solutions under a Residual Depolarizing Field," Phys. Rev. Lett. **93**, 196104.

Kornev, I. A., H. Fu, and L. Bellaiche, 2006, "Properties of ferroelectric ultrathin films from first principles," J. Mater. Sci. **41**, 137–145.

Kornev, I. A., B.-K. Lai, I. Naumov, I. Ponomareva, H. Fu, and L. Bellaiche, 2008, "Domains in ferroelectric nanostructures from first principles," in *Handbook of Advanced Dielectric, Piezoelectric and Ferroelectric Materials*, Woodhead Publishing Series in Electronic and Optical Materials, edited by Zuo-Guang Ye (Woodhead Publishing, Cambridge, England), Chap. 19, pp. 570–599.

Kosterlitz, J. M., and D. J. Thouless, 1972, "Long range order and metastability in two dimensional solids and superfluids. (Application of dislocation theory)," J. Phys. C **5**, L124–L126.

Kosterlitz, J. M., and D. J. Thouless, 1973, "Ordering, metastability and phase transitions in two-dimensional systems," J. Phys. C **6**, 1181–1203.

Kosterlitz, M., 2016, "Kosterlitz-Thouless physics: A review of key issues," Rep. Prog. Phys. **79**, 026001.

Kubel, F., and H. Schmid, 1990, "Structure of a ferroelectric and ferroelastic monodomain crystal of the perovskite $BiFeO_3$," Acta Crystallogr. Sect. B **46**, 698–702.

Kumagai, Y., and N. A. Spaldin, 2013, "Structural domain walls in polar hexagonal manganites," Nat. Commun. **4**, 1540.

Kurumaji, T., T. Nakajima, M. Hirschberger, A. Kikkawa, Y. Yamasaki, H. Sagayama, H. Nakao, Y. Taguchi, T. Arima, and Y. Tokura, 2019, "Skyrmion lattice with a giant topological Hall effect in a frustrated triangular-lattice magnet," Science **365**, 914–918.

Laguta, V. V., M. D. Glinchuk, I. P. Bykov, Yu. L. Maksimenko, J. Rosa, and L. Jastrabík, 1996, "Impurity centers in $PbTiO_3$ single crystals: An electron-spin-resonance analysis," Phys. Rev. B **54**, 12353–12360.

Lahoche, L., I. Luk'yanchuk, and G. Pascoli, 2008, "Stability of vortex phases in ferroelectric easy-plane nano-cylinders," Integr. Ferroelectr. **99**, 60–66.

Lai, B.-K., I. Ponomareva, I. Kornev, L. Bellaiche, and G. Salamo, 2007a, "Thickness dependency of 180° stripe domains in ferroelectric ultrathin films: A first-principles-based study," Appl. Phys. Lett. **91**, 152909.

Lai, B.-K., I. Ponomareva, I. A. Kornev, L. Bellaiche, and G. J. Salamo, 2007b, "Domain evolution of $BaTiO_3$ ultrathin films under an electric field: A first-principles study," Phys. Rev. B **75**, 085412.

Lai, B.-K., I. Ponomareva, I. I. Naumov, I. Kornev, Huaxiang Fu, L. Bellaiche, and G. J. Salamo, 2006, "Electric-Field-Induced Domain Evolution in Ferroelectric Ultrathin Films," Phys. Rev. Lett. **96**, 137602.

Lammert, P. E., D. S. Rokhsar, and J. Toner, 1993, "Topology and Nematic Ordering," Phys. Rev. Lett. **70**, 1650–1653.

Landau, L., and E. Lifshitz, 1935, "On the theory of the dispersion magnetic permeability in ferromagnetic bodies," Phys. Z. Sowjetunion **8**, 153–169, https://www.sciencedirect.com/science/article/pii/B9780080105864500237?via%3Dihub.

Laughlin, R. B., 1988, "The relationship between high-temperature superconductivity and the fractional quantum Hall effect," Science **242**, 525–533.

Lee, J. H., K. Chu, K.-E. Kim, J. Seidel, and C.-H. Yang, 2016, "Out-of-plane three-stable-state ferroelectric switching: Finding the missing middle states," Phys. Rev. B **93**, 115142.

Lee, S.-H., C. Broholm, W. Ratcliff, G. Gasparovic, Q. Huang, T. H. Kim, and S.-W. Cheong, 2002, "Emergent excitations in a geometrically frustrated magnet," Nature (London) **418**, 856–858.

Li, Q., C. T. Nelson, S.-L. Hsu, A. R. Damodaran, L.-L. Li, A. K. Yadav, M. McCarter, L. W. Martin, R. Ramesh, and S. V. Kalinin, 2017, "Quantification of flexoelectricity in $PbTiO_3/SrTiO_3$ super-lattice polar vortices using machine learning and phase-field modeling," Nat. Commun. **8**, 1468.

Li, Q., *et al.*, 2021, "Subterahertz collective dynamics of polar vortices," Nature (London) **592**, 376–380.

Li, S., Y. J. Wang, Y. L. Zhu, Y. L. Tang, Y. Liu, J. Y. Ma, M. J. Han, B. Wu, and X. L. Ma, 2019, "Evolution of flux-closure domain arrays in oxide multilayers with misfit strain," Acta Mater. **171**, 176–183.

Li, S., Y. L. Zhu, Y. J. Wang, Y. L. Tang, Y. Liu, S. R. Zhang, J. Y. Ma, and X. L. Ma, 2017, "Periodic arrays of flux-closure domains in ferroelectric thin films with oxide electrodes," Appl. Phys. Lett. **111**, 052901.

Li, X., *et al.*, 2020, "Atomic-scale observations of electrical and mechanical manipulation of topological polar flux closure," Proc. Natl. Acad. Sci. U.S.A. **117**, 18954–18961.

Li, Y., N. Kanazawa, X. Z. Yu, A. Tsukazaki, M. Kawasaki, M. Ichikawa, X. F. Jin, F. Kagawa, and Y. Tokura, 2013, "Robust Formation of Skyrmions and Topological Hall Effect Anomaly in Epitaxial Thin Films of MnSi," Phys. Rev. Lett. **110**, 117202.

Li, Y., *et al.*, 2022, "Electrostatically driven polarization flop and strain-induced curvature in free-standing ferroelectric superlattices," Adv. Mater. **34**, 2106826.

Li, Z., *et al.*, 2017, "High-density array of ferroelectric nanodots with robust and reversibly switchable topological domain states," Sci. Adv. **3**, e1700919.

Lichtensteiger, C., P. Zubko, M. Stengel, P. Aguado-Puente, J.-M. Triscone, Ph. Ghosez, and J. Junquera, 2012, "Ferroelectricity in ultrathin-film capacitors," in *Oxide Ultrathin Films: Science and Technology*, edited by G. Pacchioni and S. Valeri (John Wiley & Sons, New York), Chap. 12, pp. 265–307.

Lin, S.-Z., *et al.*, 2014, "Topological defects as relics of emergent continuous symmetry and Higgs condensation of disorder in ferroelectrics," Nat. Phys. **10**, 970–977.

Lines, M. E., and A. M. Glass, 1977, *Principles and Applications of Ferroelectrics and Related Materials* (Oxford University Press, Oxford).

Lisenkov, S., and L. Bellaiche, 2007, "Phase diagrams of $BaTiO_3/SrTiO_3$ superlattices from first principles," Phys. Rev. B **76**, 020102(R).

Lisenkov, S., I. Ponomareva, and L. Bellaiche, 2009, "Unusual static and dynamical characteristics of domain evolution in ferroelectric superlattices," Phys. Rev. B **79**, 024101.

Liu, D., J. Wang, H. M. Jafri, X. Wang, X. Shi, D. Liang, C. Yang, X. Cheng, and H. Huang, 2022, "Phase-field simulations of vortex chirality manipulation in ferroelectric thin films," npj Quantum Mater. **7**, 34.

Liu, J., V. V. Laguta, K. Inzani, W. Huang, S. Das, R. Chatterjee, E. Sheridan, S. M. Griffin, A. Ardavan, and R. Ramesh, 2021,

"Coherent electric field manipulation of Fe^{3+} spins in $PbTiO_3$," Sci. Adv. **7**, eabf8103.

Liu, Y., J. Liu, H. Pan, X. Cheng, Z. Hong, B. Xu, L.-Q. Chen, C.-W. Nan, and Y.-H. Lin, 2022, "Phase-field simulations of tunable polar topologies in lead-free ferroelectric/paraelectric multilayers with ultrahigh energy-storage performance," Adv. Mater. **34**, 2108772.

Liu, Y., Y.-J. Wang, Y.-L. Zhu, C.-H. Lei, Y.-L. Tang, S. Li, S.-R. Zhang, J. Li, and X.-L. Ma, 2017, "Large scale two-dimensional flux-closure domain arrays in oxide multilayers and their controlled growth," Nano Lett. **17**, 7258–7266.

Liu, Z., B. Yang, W. Cao, E. Fohtung, and T. Lookman, 2017, "Enhanced Energy Storage with Polar Vortices in Ferroelectric Nanocomposites," Phys. Rev. Appl. **8**, 034014.

Loudet, J. C., P. Poulin, and P. Barois, 2001, "Edge dislocations of colloidal chains suspended in a nematic liquid crystal," Europhys. Lett. **54**, 175–181.

Louis, L., I. Kornev, G. Geneste, B. Dkhil, and L. Bellaiche, 2012, "Novel complex phenomena in ferroelectric nanocomposites," J. Phys. Condens. Matter **24**, 402201.

Lovesey, S. W., and G. van der Laan, 2018, "Resonant x-ray diffraction from chiral electric-polarization structures," Phys. Rev. B **98**, 155410.

Lu, G., S. Li, X. Ding, J. Sun, and E. K. H. Salje, 2021, "Tip-induced flexoelectricity, polar vortices, and magnetic moments in ferroelastic materials," J. Appl. Phys. **129**, 084104.

Lu, L., *et al.*, 2018, "Topological Defects with Distinct Dipole Configurations in $PbTiO_3$/$SrTiO_3$ Multilayer Films," Phys. Rev. Lett. **120**, 177601.

Luk'yanchuk, I., A. Sené, and V. M. Vinokur, 2018, "Electrodynamics of ferroelectric films with negative capacitance," Phys. Rev. B **98**, 024107.

Luk'yanchuk, I., Y. Tikhonov, A. Razumnaya, and V. M. Vinokur, 2020, "Hopfions emerge in ferroelectrics," Nat. Commun. **11**, 2433.

Luk'yanchuk, I. A., L. Lahoche, and A. Sené, 2009, "Universal Properties of Ferroelectric Domains," Phys. Rev. Lett. **102**, 147601.

Ma, J. Y., *et al.*, 2020, "Real-time observation of phase coexistence and a_1/a_2 to flux-closure domain transformation in ferroelectric films," Acta Mater. **193**, 311–317.

Ma, L. L., Y. Ji, W. J. Chen, J. Y. Liu, Y. L. Liu, B. Wang, and Y. Zheng, 2018, "Direct electrical switching of ferroelectric vortices by a sweeping biased tip," Acta Mater. **158**, 23–37.

Maier, P. G., and F. Schwabl, 2004, "Ferromagnetic ordering in the two-dimensional dipolar *XY* model," Phys. Rev. B **70**, 134430.

Maleev, S. V., 1976, "Dipole forces in two-dimensional and layered ferromagnets," Sov. Phys. JETP **43**, 1240, http://www.jetp.ras.ru/cgi-bin/dn/e_043_06_1240.pdf.

Malozemoff, A. P., and J. C. Slonczewski, 1979, *Magnetic Domain Walls in Bubble Materials* (Academic Press, New York).

Mangeri, J., Y. Espinal, A. Jokisaari, S. Pamir Alpay, S. Nakhmanson, and O. Heinonen, 2017, "Topological phase transformations and intrinsic size effects in ferroelectric nanoparticles," Nanoscale **9**, 1616–1624.

Manipatruni, S., D. E. Nikonov, C.-C. Lin, T. A. Gosavi, H. Liu, B. Prasad, Y.-L. Huang, E. Bonturim, R. Ramesh, and I. A. Young, 2019, "Scalable energy-efficient magnetoelectric spin-orbit logic," Nature (London) **565**, 35–42.

Mannhart, J., and D. G. Schlom, 2010, "Oxide interfaces—An opportunity for electronics," Science **327**, 1607–1611.

Manton, N., and P. Sutcliffe, 2004, *Topological Solitons*, Cambridge Monographs on Mathematical Physics (Cambridge University Press, Cambridge, England).

Martelli, P.-W., S. M. Mefire, and I. A. Luk'yanchuk, 2015, "Multi-domain switching in the ferroelectric nanodots," Europhys. Lett. **111**, 50001.

Martin, L. W., 2021, "Whirls and swirls of polarization," Science **371**, 992–993.

McDonald, S. A., G. Konstantatos, S. Zhang, P. W. Cyr, E. J. D. Klem, L. Levina, and E. H. Sargent, 2005, "Solution-processed PbS quantum dot infrared photodetectors and photovoltaics," Nat. Mater. **4**, 138–142.

McQuaid, R. G. P., L. J. McGilly, P. Sharma, A. Gruverman, and J. M. Gregg, 2011, "Mesoscale flux-closure domain formation in single-crystal $BaTiO_3$," Nat. Commun. **2**, 404.

Mehta, R. R., B. D. Silverman, and J. T. Jacobs, 1973, "Depolarization fields in thin ferroelectric films," J. Appl. Phys. **44**, 3379–3385.

Mermin, N. D., 1967, "Absence of ordering in certain classical systems," J. Math. Phys. (N.Y.) **8**, 1061–1064.

Mermin, N. D., 1979, "The topological theory of defects in ordered media," Rev. Mod. Phys. **51**, 591–648.

Mermin, N. D., and H. Wagner, 1966, "Absence of Ferromagnetism or Antiferromagnetism in One- or Two-Dimensional Isotropic Heisenberg Models," Phys. Rev. Lett. **17**, 1133–1136.

Meyer, B., and David Vanderbilt, 2002, "*Ab initio* study of ferroelectric domain walls in $PbTiO_3$," Phys. Rev. B **65**, 104111.

Mikheykin, A. S., E. S. Zhukova, V. I. Torgashev, A. G. Razumnaya, Y. I. Yuzyuk, B. P. Gorshunov, A. S. Prokhorov, A. E. Sashin, A. A. Bush, and M. Dressel, 2014, "Lattice anharmonicity and polar soft mode in ferrimagnetic m-type hexaferrite $BaFe_{12}O_{19}$ single crystal," Eur. Phys. J. B **87**, 232.

Mineev, V. P., 1998, *Topologically Stable Defects and Solitons in Ordered Media*, Classic Reviews in Physics (Taylor & Francis, London).

Moessner, R., and A. P. Ramirez, 2006, "Geometrical frustration," Phys. Today **59**, No. 2, 24–29.

Moffatt, H. K., and R. L. Ricca, 1992, "Helicity and the Călugăreanu invariant," Proc. R. Soc. A **439**, 411–429.

Monastyrsky, M., 1999, *Riemann, Topology, and Physics* (Birkhäuser, Boston).

Moon, K., H. Mori, K. Yang, S. M. Girvin, A. H. MacDonald, L. Zheng, D. Yoshioka, and S.-C. Zhang, 1995, "Spontaneous interlayer coherence in double-layer quantum Hall systems: Charged vortices and Kosterlitz-Thouless phase transitions," Phys. Rev. B **51**, 5138–5170.

Moriya, T., 1960, "Anisotropic superexchange interaction and weak ferromagnetism," Phys. Rev. **120**, 91–98.

Morozovska, A. N., E. A. Eliseev, S. V. Kalinin, and R. Hertel, 2021, "Flexosensitive polarization vortices in thin ferroelectric films," Phys. Rev. B **104**, 085420.

Morozovska, A. N., R. Hertel, S. Cherifi-Hertel, V. Y. Reshetnyak, E. A. Eliseev, and D. R. Evans, 2021, "Chiral polarization textures induced by the flexoelectric effect in ferroelectric nanocylinders," Phys. Rev. B **104**, 054118.

Mudry, Chris, 2014, *Lecture Notes on Field Theory in Condensed Matter Physics* (World Scientific, Singapore).

Mühlbauer, S., B. Binz, F. Jonietz, C. Pfleiderer, A. Rosch, A. Neubauer, R. Georgii, and P. Böni, 2009, "Skyrmion lattice in a chiral magnet," Science **323**, 915–919.

Müller, K. A., and W. Berlinger, 1986, "Microscopic probing of order-disorder versus displacive behavior in $BaTiO_3$ by Fe^{3+} EPR," Phys. Rev. B **34**, 6130–6136.

Müller, K. A., and H. Burkard, 1979, "$SrTiO_3$: An intrinsic quantum paraelectric below 4 K," Phys. Rev. B **19**, 3593–3602.

Mundy, J. A., *et al.*, 2022, "Liberating a hidden antiferroelectric phase with interfacial electrostatic engineering," Sci. Adv. **8**, eabg5860.

Nagaosa, N., and Y. Tokura, 2013, "Topological properties and dynamics of magnetic skyrmions," Nat. Nanotechnol. **8**, 899–911.

Nahas, Y., S. Prokhorenko, and L. Bellaiche, 2016, "Frustration and Self-Ordering of Topological Defects in Ferroelectrics," Phys. Rev. Lett. **116**, 117603.

Nahas, Y., S. Prokhorenko, I. Kornev, and L. Bellaiche, 2016, "Topological Point Defects in Relaxor Ferroelectrics," Phys. Rev. Lett. **116**, 127601.

Nahas, Y., S. Prokhorenko, I. Kornev, and L. Bellaiche, 2017, "Emergent Berezinskii-Kosterlitz-Thouless Phase in Low-Dimensional Ferroelectrics," Phys. Rev. Lett. **119**, 117601.

Nahas, Y., S. Prokhorenko, L. Louis, Z. Gui, I. Kornev, and L. Bellaiche, 2015, "Discovery of stable skyrmionic state in ferroelectric nanocomposites," Nat. Commun. **6**, 8542.

Nahas, Y., S. Prokhorenko, Q. Zhang, V. Govinden, N. Valanoor, and L. Bellaiche, 2020, "Topology and control of self-assembled domain patterns in low-dimensional ferroelectrics," Nat. Commun. **11**, 5779.

Nahas, Y., *et al.*, 2020, "Inverse transition of labyrinthine domain patterns in ferroelectric thin films," Nature (London) **577**, 47–51.

Nakahara, M., 2003a, *Geometry, Topology, and Physics*, 2nd ed., Graduate Student Series in Physics (Institute of Physics Publishing, Bristol, England).

Nakahara, M., 2003b, *Geometry, Topology and Physics* (Taylor & Francis, London).

Narayan, B., J. S. Malhotra, R. Pandey, K. Yaddanapudi, P. Nukala, B. Dkhil, A. Senyshyn, and R. Ranjan, 2018, "Electrostrain in excess of 1% in polycrystalline piezoelectrics," Nat. Mater. **17**, 427–431.

Nataf, G. F., M. Guennou, J. M. Gregg, D. Meier, J. Hlinka, E. K. H. Salje, and J. Kreisel, 2020, "Domain-wall engineering and topological defects in ferroelectric and ferroelastic materials," Nat. Rev. Phys. **2**, 634–648.

Naumov, I., and H. Fu, 2007, "Vortex-to-Polarization Phase Transformation Path in Ferroelectric Pb(ZrTi)O$_3$ Nanoparticles," Phys. Rev. Lett. **98**, 077603.

Naumov, I. I., L. Bellaiche, and H. Fu, 2004, "Unusual phase transitions in ferroelectric nanodisks and nanorods," Nature (London) **432**, 737–740.

Naumov, I. I., and H. Fu, 2008, "Cooperative Response of Pb(ZrTi)O$_3$ Nanoparticles to Curled Electric Fields," Phys. Rev. Lett. **101**, 197601.

Nelson, C. T., *et al.*, 2011, "Spontaneous vortex nanodomain arrays at ferroelectric heterointerfaces," Nano Lett. **11**, 828–834.

Nelson, D. R., 1988, "Vortex Entanglement in High-T_c Superconductors," Phys. Rev. Lett. **60**, 1973–1976.

Nelson, D. R., and B. I. Halperin, 1979, "Dislocation-mediated melting in two dimensions," Phys. Rev. B **19**, 2457–2484.

Neubauer, A., C. Pfleiderer, B. Binz, A. Rosch, R. Ritz, P. G. Niklowitz, and P. Böni, 2009, "Topological Hall Effect in the *a* Phase of MnSi," Phys. Rev. Lett. **102**, 186602.

Nguyen, K. X., *et al.*, 2020, "Transferring orbital angular momentum to an electron beam reveals toroidal and chiral order," arXiv:2012.04134.

Noheda, B., D. E. Cox, G. Shirane, J. A. Gonzalo, L. E. Cross, and S.-E. Park, 1999, "A monoclinic ferroelectric phase in the Pb(Zr$_{1-x}$Ti$_x$)O$_3$ solid solution," Appl. Phys. Lett. **74**, 2059–2061.

Ohtomo, A., and H. Y. Hwang, 2004, "A high-mobility electron gas at the LaAlO$_3$/SrTiO$_3$ heterointerface," Nature (London) **427**, 423–426.

Omari, K. A., and T. J. Hayward, 2014, "Chirality-Based Vortex Domain-Wall Logic Gates," Phys. Rev. Appl. **2**, 044001.

Onoda, M., S. Murakami, and N. Nagaosa, 2004, "Hall Effect of Light," Phys. Rev. Lett. **93**, 083901.

Onsager, L., 1949, "Statistical hydrodynamics," Nuovo Cimento **6**, 279–287.

Ortiz, G., E. Cobanera, and Z. Nussinov, 2012, "Dualities and the phase diagram of the p-clock model," Nucl. Phys. **B854**, 780–814.

Pappas, C., E. Lelièvre-Berna, P. Falus, P. M. Bentley, E. Moskvin, S. Grigoriev, P. Fouquet, and B. Farago, 2009, "Chiral Paramagnetic Skyrmion-like Phase in MnSi," Phys. Rev. Lett. **102**, 197202.

Pappas, D., Z. G. Fthenakis, and I. Ponomareva, 2018, "All-mechanical polarization control and anomalous (electro)mechanical responses in ferroelectric nanowires," Nano Lett. **18**, 5996–6001.

Park, J. P., P. Eames, D. M. Engebretson, J. Berezovsky, and P. A. Crowell, 2003, "Imaging of spin dynamics in closure domain and vortex structures," Phys. Rev. B **67**, 020403.

Parkin, S. S. P., M. Hayashi, and L. Thomas, 2008, "Magnetic domain-wall racetrack memory," Science **320**, 190–194.

Peierls, R., 1935, "Some typical properties of solids," Ann. Inst. Henri Poincaré **5**, 177–222, http://www.numdam.org/item/AIHP_1935__5_3_177_0/.

Peng, D., X. Yang, W. Jiang, and X. Tian, 2021, "Molecular dynamics simulations of void-mediated polarization vortex domain switching in compressed BaTiO$_3$ nanofilm," J. Appl. Phys. **130**, 034101.

Pereira Gonçalves, M. A., C. Escorihuela-Sayalero, P. Garca-Fernández, J. Junquera, and J. Íñiguez, 2019, "Theoretical guidelines to create and tune electric skyrmion bubbles," Sci. Adv. **5**, eaau7023.

Peters, J. J. P., G. Apachitei, R. Beanland, M. Alexe, and A. M. Sanchez, 2016, "Polarization curling and flux closures in multiferroic tunnel junctions," Nat. Commun. **7**, 13484.

Ponomareva, I., and L. Bellaiche, 2006, "Influence of the growth direction on properties of ferroelectric ultrathin films," Phys. Rev. B **74**, 064102.

Ponomareva, I., and L. Bellaiche, 2008, "Nature of Dynamical Coupling between Polarization and Strain in Nanoscale Ferroelectrics from First Principles," Phys. Rev. Lett. **101**, 197602.

Ponomareva, I., L. Bellaiche, and R. Resta, 2007, "Dielectric Anomalies in Ferroelectric Nanostructures," Phys. Rev. Lett. **99**, 227601.

Ponomareva, I., I. I. Naumov, and L. Bellaiche, 2005, "Low-dimensional ferroelectrics under different electrical and mechanical boundary conditions: Atomistic simulations," Phys. Rev. B **72**, 214118.

Ponomareva, I., I. I. Naumov, I. Kornev, H. Fu, and L. Bellaiche, 2005a, "Modelling of nanoscale ferroelectrics from atomistic simulations," Curr. Opin. Solid State Mater. Sci. **9**, 114–121.

Ponomareva, I., I. I. Naumov, I. Kornev, H. Fu, and L. Bellaiche, 2005b, "Atomistic treatment of depolarizing energy and field in ferroelectric nanostructures," Phys. Rev. B **72**, 140102.

Pontryagin, L. S., 1986, *Topological Groups*, 3rd ed., Classics of Soviet Mathematics Vol. 1 (Gordon and Breach, New York).

Popov, S. A., N. A. Tikhomirova, and S. A. Phlerova, 1985, "Interaction of moving domain boundaries with a magnetic field in Gd$_2$(MoO$_4$)$_3$," Sov. Phys. Crystallogr. **30**, 608–609.

Posadas, A.-B., M. Lippmaa, F. J. Walker, M. Dawber, C. H. Ahn, and J. M. Triscone, 2007, "Growth and novel applications of epitaxial oxide thin films," in *Physics of Ferroelectrics: A Modern Perspective*, Topics in Applied Physics Vol. 105, edited by K. M. Rabe, C. H. Ahn, and J.-M. Triscone (Springer, Berlin), Chap. 6, pp. 219–304.

Prokhorenko, S., Y. Nahas, and L. Bellaiche, 2017, "Fluctuations and Topological Defects in Proper Ferroelectric Crystals," Phys. Rev. Lett. **118**, 147601.

Prokhorenko, S., Y. Nahas, Q. Zhang, V. Govinden, N. Valanoor, and L. Bellaiche, 2023, "Motion and teleportation of polar bubbles in ultra-thin ferroelectrics," arXiv:2303.13883.

Prosandeev, S., A. R. Akbarzadeh, and L. Bellaiche, 2009, "Discovery of Incipient Ferrotoroidics from Atomistic Simulations," Phys. Rev. Lett. **102**, 257601.

Prosandeev, S., and L. Bellaiche, 2006, "Properties of Ferroelectric Nanodots Embedded in a Polarizable Medium: Atomistic Simulations," Phys. Rev. Lett. **97**, 167601.

Prosandeev, S., and L. Bellaiche, 2007a, "Asymmetric screening of the depolarizing field in a ferroelectric thin film," Phys. Rev. B **75**, 172109.

Prosandeev, S., and L. Bellaiche, 2007b, "Characteristics and signatures of dipole vortices in ferroelectric nanodots: First-principles-based simulations and analytical expressions," Phys. Rev. B **75**, 094102.

Prosandeev, S., and L. Bellaiche, 2007c, "Influence of crystallographic steps on properties of ferroelectric ultrathin films: An *ab initio* study," Appl. Phys. Lett. **91**, 072901.

Prosandeev, S., and L. Bellaiche, 2008a, "Controlling Double Vortex States in Low-Dimensional Dipolar Systems," Phys. Rev. Lett. **101**, 097203.

Prosandeev, S., and L. Bellaiche, 2008b, "Order parameter in complex dipolar structures: Microscopic modeling," Phys. Rev. B **77**, 060101(R).

Prosandeev, S., and L. Bellaiche, 2009, "Hypertoroidal moment in complex dipolar structures," J. Mater. Sci. **44**, 5235–5248.

Prosandeev, S., J. Grollier, D. Talbayev, B. Dkhil, and L. Bellaiche, 2021, "Ultrafast Neuromorphic Dynamics Using Hidden Phases in the Prototype of Relaxor Ferroelectrics," Phys. Rev. Lett. **126**, 027602.

Prosandeev, S., I. Kornev, and L. Bellaiche, 2007, "Tensors in ferroelectric nanoparticles: First-principles-based simulations," Phys. Rev. B **76**, 012101.

Prosandeev, S., I. A. Kornev, and L. Bellaiche, 2011, "Phase Transitions in Epitaxial (-110) BiFeO$_3$ Films from First Principles," Phys. Rev. Lett. **107**, 117602.

Prosandeev, S., S. Lisenkov, and L. Bellaiche, 2010, "Kittel Law in BiFeO$_3$ Ultrathin Films: A First-Principles-Based Study," Phys. Rev. Lett. **105**, 147603.

Prosandeev, S., A. Malashevich, Z. Gui, L. Louis, R. Walter, I. Souza, and L. Bellaiche, 2013, "Natural optical activity and its control by electric field in electrotoroidic systems," Phys. Rev. B **87**, 195111.

Prosandeev, S., A. Malashevich, I. P. Raevski, and L. Bellaiche, 2015, "Dynamical magnetoelectric effects associated with ferroelectric domain walls," Phys. Rev. B **91**, 100101.

Prosandeev, S., I. Ponomareva, I. Kornev, and L. Bellaiche, 2008, "Control of Vortices by Homogeneous Fields in Asymmetric Ferroelectric and Ferromagnetic Rings," Phys. Rev. Lett. **100**, 047201.

Prosandeev, S., I. Ponomareva, I. Kornev, I. Naumov, and L. Bellaiche, 2006, "Controlling Toroidal Moment by Means of an Inhomogeneous Static Field: An *Ab Initio* Study," Phys. Rev. Lett. **96**, 237601.

Prosandeev, S., I. Ponomareva, I. Naumov, I. Kornev, and L. Bellaiche, 2008, "Original properties of dipole vortices in zero-dimensional ferroelectrics," J. Phys. Condens. Matter **20**, 193201.

Prosandeev, S., S. Prokhorenko, Y. Nahas, and L. Bellaiche, 2019, "Prediction of a novel topological multidefect ground state," Phys. Rev. B **100**, 140104.

Prosandeev, S., S. Prokhorenko, Y. Nahas, J. Grollier, D. Talbayev, B. Dkhil, and L. Bellaiche, 2022, "Ultrafast activation and tuning of topological textures in ferroelectric nanostructures," Adv. Electron. Mater. **8**, 2200808.

Prosandeev, S., S. Prokhorenko, Y. Nahas, Y. Yang, C. Xu, J. Grollier, D. Talbayev, B. Dkhil, and L. Bellaiche, 2023, "Designing polar textures with ultrafast neuromorphic features from atomistic simulations," Neuromorph. Comput. Eng. **3**, 012002.

Prosandeev, S., *et al.*, 2016, "Ferroelectric vortices and related configurations," in *Nanoscale Ferroelectrics and Multiferroics: Key Processing and Characterization Issues, and Nanoscale Effects*, edited by M. Alguero, J. M. Gregg, and Liliana Mitoseriu (John Wiley & Sons, New York), Chap. 22, pp. 700–728.

Pullar, R. C., 2012, "Hexagonal ferrites: A review of the synthesis, properties and applications of hexaferrite ceramics," Prog. Mater. Sci. **57**, 1191–1334.

Quindeau, A., I. Fina, X. Marti, G. Apachitei, P. Ferrer, C. Nicklin, E. Pippel, D. Hesse, and M. Alexe, 2015, "Four-state ferroelectric spin-valve," Sci. Rep. **5**, 9749.

Rabe, K. M., 2005, "Theoretical investigations of epitaxial strain effects in ferroelectric oxide thin films and superlattices," Curr. Opin. Solid State Mater. Sci. **9**, 122–127.

Radzihovsky, L., and J. Toner, 1999, "Smectic liquid crystals in random environments," Phys. Rev. B **60**, 206–257.

Rajaraman, R., 1987, *Solitons and Instantons: An Introduction to Solitons and Instantons in Quantum Field Theory*, North-Holland Personal Library Vol. 15 (North-Holland, Oxford).

Ramesh, R., and D. G. Schlom, 2019, "Creating emergent phenomena in oxide superlattices," Nat. Rev. Mater. **4**, 257–268.

Ramirez, A. P., and B. Skinner, 2020, "Dawn of the topological age?," Phys. Today **73**, No. 9, 30–36.

Ravichandran, J., *et al.*, 2014, "Crossover from incoherent to coherent phonon scattering in epitaxial oxide superlattices," Nat. Mater. **13**, 168–172.

Ren, W., and L. Bellaiche, 2011, "Prediction of the Magnetotoroidic Effect from Atomistic Simulations," Phys. Rev. Lett. **107**, 127202.

Resnick, D. J., J. C. Garland, J. T. Boyd, S. Shoemaker, and R. S. Newrock, 1981, "Kosterlitz-Thouless Transition in Proximity-Coupled Superconducting Arrays," Phys. Rev. Lett. **47**, 1542–1545.

Resta, R., and D. Vanderbilt, 2007, "Theory of polarization: A modern approach," in *Physics of Ferroelectrics: A Modern Perspective*, Topics in Applied Physics Vol. 105, edited by K. M. Rabe, C. H. Ahn, and J.-M. Triscone (Springer, Berlin), Chap. 2, pp. 31–68.

Reyren, N., *et al.*, 2007, "Superconducting interfaces between insulating oxides," Science **317**, 1196–1199.

Rijal, S., Y. Nahas, S. Prokhorenko, and L. Bellaiche, 2023, "Dynamics of polar vortex crystallization," arXiv:2302.07380.

Rodriguez, B. J., X. S. Gao, L. F. Liu, W. Lee, I. I. Naumov, A. M. Bratkovsky, D. Hesse, and M. Alexe, 2009, "Vortex polarization states in nanoscale ferroelectric arrays," Nano Lett. **9**, 1127–1131.

Romera, M., *et al.*, 2018, "Vowel recognition with four coupled spin-torque nano-oscillators," Nature (London) **563**, 230–234.

Rondinelli, J. M., and N. A. Spaldin, 2011, "Structure and properties of functional oxide thin films: Insights from electronic-structure calculations," Adv. Mater. **23**, 3363–3381.

Rößler, U. K., A. N. Bogdanov, and C. Pfleiderer, 2006, "Spontaneous skyrmion ground states in magnetic metals," Nature (London) **442**, 797–801.

Rowley, S. E., Y.-S. Chai, S.-P. Shen, Y. Sun, A. T. Jones, B. E. Watts, and J. F. Scott, 2016, "Uniaxial ferroelectric quantum criticality in multiferroic hexaferrites $BaFe_{12}O_{19}$ and $SrFe_{12}O_{19}$," Sci. Rep. **6**, 25724.

Runge, K., Y. Nozaki, Y. Otani, H. Miyajima, B. Pannetier, T. Matsuda, and A. Tonomura, 1996, "High-resolution observation of magnetization processes in $2~\mu m \times 2~\mu m \times 0.04~\mu m$ Permalloy particles," J. Appl. Phys. **79**, 5075–5077.

Ruotolo, A., V. Cros, B. Georges, A. Dussaux, J. Grollier, C. Deranlot, R. Guillemet, K. Bouzehouane, S. Fusil, and A. Fert, 2009, "Phase-locking of magnetic vortices mediated by antivortices," Nat. Nanotechnol. **4**, 528–532.

Salahuddin, S., and S. Datta, 2008, "Use of negative capacitance to provide voltage amplification for low power nanoscale devices," Nano Lett. **8**, 405–410.

Sánchez-Santolino, G., *et al.*, 2023, "A 2D ferroelectric vortex lattice in twisted $BaTiO_3$ freestanding layers," arXiv:2301.04438.

Sayedaghaee, S. O., Ch. Paillard, S. Prosandeev, B. Xu, and L. Bellaiche, 2020, "Strain-induced resonances in the dynamical quadratic magnetoelectric response of multiferroics," npj Comput. Mater. **6**, 60.

Sayedaghaee, S. O., B. Xu, S. Prosandeev, Ch. Paillard, and L. Bellaiche, 2019, "Novel Dynamical Magnetoelectric Effects in Multiferroic $BiFeO_3$," Phys. Rev. Lett. **122**, 097601.

Schilling, A., D. Byrne, G. Catalan, K. G. Webber, Y. A. Genenko, G. S. Wu, J. F. Scott, and J. M. Gregg, 2009, "Domains in ferroelectric nanodots," Nano Lett. **9**, 3359–3364.

Schilling, A., S. Prosandeev, R. G. P. McQuaid, L. Bellaiche, J. F. Scott, and J. M. Gregg, 2011, "Shape-induced phase transition of domain patterns in ferroelectric platelets," Phys. Rev. B **84**, 064110.

Schlom, D. G., L.-Q. Chen, C.-B. Eom, K. M. Rabe, S. K. Streiffer, and J.-M. Triscone, 2007, "Strain tuning of ferroelectric thin films," Annu. Rev. Mater. Res. **37**, 589–626.

Schlom, D. G., L.-Q. Chen, C. J. Fennie, V. Gopalan, D. A. Muller, X. Pan, R. Ramesh, and R. Uecker, 2014, "Elastic strain engineering of ferroic oxides," MRS Bull. **39**, 118–130.

Schulz, T., R. Ritz, A. Bauer, M. Halder, M. Wagner, C. Franz, C. Pfleiderer, K. Everschor, M. Garst, and A. Rosch, 2012, "Emergent electrodynamics of skyrmions in a chiral magnet," Nat. Phys. **8**, 301–304.

Scott, J. F., 1974, "Soft-mode spectroscopy: Experimental studies of structural phase transitions," Rev. Mod. Phys. **46**, 83–128.

Scott, J. F., A. Gruverman, D. Wu, I. Vrejoiu, and M. Alexe, 2008, "Nanodomain faceting in ferroelectrics," J. Phys. Condens. Matter **20**, 425222.

Seidel, J., R. K. Vasudevan, and N. Valanoor, 2016, "Topological structures in multiferroics—Domain walls, skyrmions and vortices," Adv. Electron. Mater. **2**, 1500292.

Seki, S., and M. Mochizuki, 2016, *Skyrmions in Magnetic Materials*, Springer Briefs in Physics (Springer International Publishing, Cham, Switzerland).

Shafer, P., *et al.*, 2018, "Emergent chirality in the electric polarization texture of titanate superlattices," Proc. Natl. Acad. Sci. U.S.A. **115**, 915–920.

Shao, Q., Y. Liu, G. Yu, S. K. Kim, X. Che, C. Tang, Q. L. He, Y. Tserkovnyak, J. Shi, and K. L. Wang, 2019, "Topological Hall effect at above room temperature in heterostructures composed of a magnetic insulator and a heavy metal," Nat. Electron. **2**, 182–186.

Shao, Y.-T., *et al.*, 2021, "Probing the dynamics of ferroelectric topological oscillators with the electron beam," Microsc. Microanal. **27**, 690–692.

Shao, Y.-T., *et al.*, 2023, "Emergent chirality in a polar meron to skyrmion phase transition," Nat. Commun. **14**, 1355.

Shi, Q., *et al.*, 2022, "The role of lattice dynamics in ferroelectric switching," Nat. Commun. **13**, 1110.

Shimada, T., S. Tomoda, and T. Kitamura, 2010a, *Ab initio* study of ferroelectric closure domains in ultrathin $PbTiO_3$ films," Phys. Rev. B **81**, 144116.

Shimada, T., S. Tomoda, and T. Kitamura, 2010b, "First-principles study on ferroelectricity at $PbTiO_3$ surface steps," J. Phys. Condens. Matter **22**, 355901.

Shimada, T., Y. Wang, T. Hamaguchi, K. Kasai, K. Masuda, L. V. Lich, T. Xu, J. Wang, and H. Hirakata, 2021, "Emergence of nontrivial polar topologies hidden in singular stress field in $SrTiO_3$: Topological strain-field engineering," J. Phys. Condens. Matter **33**, 505301.

Shinjo, T., T. Okuno, R. Hassdorf, K. Shigeto, and T. Ono, 2000, "Magnetic vortex core observation in circular dots of Permalloy," Science **289**, 930–932.

Shirane, G., 1974, "Neutron scattering studies of structural phase transitions at Brookhaven," Rev. Mod. Phys. **46**, 437–449.

Shitrit, N., I. Yulevich, E. Maguid, D. Ozeri, D. Veksler, V. Kleiner, and E. Hasman, 2013, "Spin-optical metamaterial route to spin-controlled photonics," Science **340**, 724–726.

Sichuga, D., and L. Bellaiche, 2011, "Epitaxial $Pb(Zr, Ti)O_3$ Ultrathin Films under Open-Circuit Electrical Boundary Conditions," Phys. Rev. Lett. **106**, 196102.

Sichuga, D., W. Ren, S. Prosandeev, and L. Bellaiche, 2010, "Chiral Patterns of Tilting of Oxygen Octahedra in Zero-Dimensional Ferroelectrics and Multiferroics: A First Principle-Based Study," Phys. Rev. Lett. **104**, 207603.

Skyrme, T. H. R., 1961, "A non-linear field theory," Proc. R. Soc. A **260**, 127–138.

Spaldin, N. A., and R. Ramesh, 2019, "Advances in magnetoelectric multiferroics," Nat. Mater. **18**, 203–212.

Spanier, E. H., 1966, *Algebraic Topology* (Springer, New York).

Spanier, J. E., A. M. Kolpak, J. J. Urban, I. Grinberg, L. Ouyang, W. S. Yun, A. M. Rappe, and H. Park, 2006, "Ferroelectric phase transition in individual single-crystalline $BaTiO_3$ nanowires," Nano Lett. **6**, 735–739.

Stachiotti, M. G., 2004, "Ferroelectricity in $BaTiO_3$ nanoscopic structures," Appl. Phys. Lett. **84**, 251–253.

Stachiotti, M. G., and M. Sepliarsky, 2011, "Toroidal Ferroelectricity in $PbTiO_3$ Nanoparticles," Phys. Rev. Lett. **106**, 137601.

Stengel, M., and D. Vanderbilt, 2016, "First-principles theory of flexoelectricity," in *Flexoelectricity in Solids: From Theory To Applications*, edited by A. K. Tagantsev and P. V. Yudin (World Scientific, Singapore), Chap. 2, pp. 31–110.

Stephanovich, V. A., I. A. Luk'yanchuk, and M. G. Karkut, 2003, "Domain proximity and ferroelectric transition in ferro-paraelectric superlattices," Ferroelectrics **291**, 169–175.

Stephanovich, V. A., I. A. Luk'yanchuk, and M. G. Karkut, 2005, "Domain-Enhanced Interlayer Coupling in Ferroelectric/Paraelectric Superlattices," Phys. Rev. Lett. **94**, 047601.

Stephenson, G. B., and K. R. Elder, 2006, "Theory for equilibrium 180° stripe domains in $PbTiO_3$ films," J. Appl. Phys. **100**, 051601.

Stepkova, V., P. Marton, and J. Hlinka, 2015, "Ising lines: Natural topological defects within ferroelectric Bloch walls," Phys. Rev. B **92**, 094106.

Stoica, V. A., *et al.*, 2019, "Optical creation of a supercrystal with three-dimensional nanoscale periodicity," Nat. Mater. **18**, 377–383.

Streiffer, S. K., J. A. Eastman, D. D. Fong, C. Thompson, A. Munkholm, M. V. Ramana Murty, O. Auciello, G. R. Bai, and G. B. Stephenson, 2002, "Observation of Nanoscale 180° Stripe Domains in Ferroelectric PbTiO₃ Thin Films," Phys. Rev. Lett. **89**, 067601.

Strkalj, N., E. Gradauskaite, J. Nordlander, and M. Trassin, 2019, "Design and manipulation of ferroic domains in complex oxide heterostructures," Materials **12**, 3108.

Sun, Y., *et al.*, 2019, "Subunit cell–level measurement of polarization in an individual polar vortex," Sci. Adv. **5**, eaav4355.

Susarla, S., P. García-Fernández, C. Ophus, S. Das, P. Aguado-Puente, M. McCarter, P. Ercius, L. W. Martin, R. Ramesh, and J. Junquera, 2021, "Atomic scale crystal field mapping of polar vortices in oxide superlattices," Nat. Commun. **12**, 6273.

Tadapatri, P., K. S. Krishnamurthy, and W. Weissflog, 2012, "Patterned flexoelectric instability in a bent-core nematic liquid crystal," Soft Matter **8**, 1202–1214.

Tagantsev, A. K., and E. B. Sonin, 1989, "Linear singularities and their motion in improper ferroelectrics," Ferroelectrics **98**, 297–300.

Tan, C., *et al.*, 2021, "Engineering polar vortex from topologically trivial domain architecture," Nat. Commun. **12**, 4620.

Tan, G.-L., and W. Li, 2015, "Ferroelectricity and ferromagnetism of *M*-type lead hexaferrite," J. Am. Ceram. Soc. **98**, 1812–1817.

Tang, Y., Y. Zhu, B. Wu, Y. Wang, L. Yang, Y. Feng, M. Zou, W. Geng, and X. Ma, 2021, "Periodic polarization waves in a strained, highly polar ultrathin SrTiO₃," Nano Lett. **21**, 6274–6281.

Tang, Y. L., Y. L. Zhu, and X. L. Ma, 2021, "Topological polar structures in ferroelectric oxide films," J. Appl. Phys. **129**, 200904.

Tang, Y. L., *et al.*, 2015, "Observation of a periodic array of flux-closure quadrants in strained ferroelectric PbTiO₃ films," Science **348**, 547–551.

Tang, Y.-Y., Y. Xie, Y. Ai, W.-Q. Liao, P.-F. Li, T. Nakamura, and R.-G. Xiong, 2020, "Organic ferroelectric vortex-antivortex domain structure," J. Am. Chem. Soc. **142**, 21932–21937.

Theis, Th. N., and P. M. Solomon, 2010, "It's time to reinvent the transistor!," Science **327**, 1600–1601.

Thiel, S., G. Hammerl, A. Schmehl, C. W. Schneider, and J. Mannhart, 2006, "Tunable quasi-two-dimensional electron gases in oxide heterostructures," Science **313**, 1942–1945.

Tian, G., W. Yang, D. Chen, Z. Fan, Z. Hou, M. Alexe, and X. Gao, 2019, "Topological domain states and magnetoelectric properties in multiferroic nanostructures," Natl. Sci. Rev. **6**, 684–702.

Tian, G., W. D. Yang, X. S. Gao, and J.-M. Liu, 2021, "Emerging phenomena from exotic ferroelectric topological states," APL Mater. **9**, 020907.

Tikhonov, Y., *et al.*, 2020, "Controllable skyrmion chirality in ferroelectrics," Sci. Rep. **10**, 8657.

Tikhonov, Y., *et al.*, 2022, "Polarization topology at the nominally charged domain walls in uniaxial ferroelectrics," Adv. Mater. **34**, 2203028.

Tinte, S., and M. G. Stachiotti, 2001, "Surface effects and ferroelectric phase transitions in BaTiO₃ ultrathin films," Phys. Rev. B **64**, 235403.

Tokura, Y., and N. Nagaosa, 2000, "Orbital physics in transition-metal oxides," Science **288**, 462–468.

Torrejon, J., *et al.*, 2017, "Neuromorphic computing with nanoscale spintronic oscillators," Nature (London) **547**, 428–431.

Torres-Pardo, A., A. Gloter, P. Zubko, N. Jecklin, C. Lichtensteiger, C. Colliex, J.-M. Triscone, and O. Stéphan, 2011, "Spectroscopic mapping of local structural distortions in ferroelectric PbTiO₃/SrTiO₃ superlattices at the unit-cell scale," Phys. Rev. B **84**, 220102.

Toulouse, G., 1980, "A lecture on the topological theory of defects in ordered media: How the old theory was leading to paradoxes, and how their resolution comes within the larger frameworks of homotopy theory," in *Modern Trends in the Theory of Condensed Matter*, edited by A. Pekalski, P. Pekalski, and A. Jerzy (Springer, Berlin), pp. 188–194.

Toulouse, G., and M. Kléman, 1976, "Principles of a classification of defects in ordered media," J. Phys. (Paris), Lett. **37**, 149–151.

Trebin, H.-R., 1982, "The topology of non-uniform media in condensed matter physics," Adv. Phys. **31**, 195–254.

Turing, A. M., 1952, "The chemical basis of morphogenesis," Phil. Trans. R. Soc. B **237**, 37–72.

Uehara, M., S. Mori, C. H. Chen, and S.-W. Cheong, 1999, "Percolative phase separation underlies colossal magnetoresistance in mixed-valent manganites," Nature (London) **399**, 560–563.

Valasek, J., 1921, "Piezo-electric and allied phenomena in rochelle salt," Phys. Rev. **17**, 475–481.

Vanderbilt, D., 2018, *Berry Phases in Electronic Structure Theory: Electric Polarization, Orbital Magnetization and Topological Insulators* (Cambridge University Press, Cambridge, England).

Vanderbilt, D., and R. D. King-Smith, 1993, "Electric polarization as a bulk quantity and its relation to surface charge," Phys. Rev. B **48**, 4442–4455.

van der Laan, G., S. L. Zhang, and T. Hesjedal, 2021, "Depth profiling of 3D skyrmion lattices in a chiral magnet—A story with a twist," AIP Adv. **11**, 015108.

Vasiliev, A. Yu., A. E. Tarkhov, L. I. Menshikov, P. O. Fedichev, and U. R. Fischer, 2014, "Universality of the Berezinskii-Kosterlitz-Thouless type of phase transition in the dipolar *XY*-model," New J. Phys. **16**, 053011.

Vasin, M. G., V. N. Ryzhov, and V. M. Vinokur, 2018, "Berezinskii-Kosterlitz-Thouless and Vogel-Fulcher-Tammann criticality in *XY* model," arXiv:1712.00757.

Villanova, J. W., P. Kumar, and S. Barraza-Lopez, 2020, "Theory of finite-temperature two-dimensional structural transformations in group-IV monochalcogenide monolayers," Phys. Rev. B **101**, 184101.

Volovik, G. E., and V. P. Mineev, 1977, "Investigation of singularities in superfluid He³ in liquid crystals by the homotopic topology methods," Zh. Eksp. Teor. Fiz. **72**, 2256–2274, http://jetp.ras.ru/cgi-bin/dn/e_045_06_1186.pdf.

von Korff Schmising, C., M. Bargheer, M. Kiel, N. Zhavoronkov, M. Woerner, T. Elsaesser, I. Vrejoiu, D. Hesse, and M. Alexe, 2007, "Coupled Ultrafast Lattice and Polarization Dynamics in Ferroelectric Nanolayers," Phys. Rev. Lett. **98**, 257601.

Wachowiak, A., J. Wiebe, M. Bode, O. Pietzsch, M. Morgenstern, and R. Wiesendanger, 2002, "Direct observation of internal spin structure of magnetic vortex cores," Science **298**, 577–580.

Wadhawan, V. K., 2000, *Introduction to Ferroic Materials* (CRC Press, London).

Walter, R., S. Prokhorenko, Z. Gui, Y. Nahas, and L. Bellaiche, 2016, "Electrical control of chiral phases in electrotoroidic nanocomposites," Adv. Electron. Mater. **2**, 1500218.

Walter, R., S. Prokhorenko, Z. Gui, Y. Nahas, L.-W. Wang, and L. Bellaiche, 2018, "Temperature and electric field control of the bandgap in electrotoroidic nanocomposites by large-scale *ab initio* methods," Ferroelectrics **535**, 93–105.

Wang, Bo, Elhanan Maguid, Kexiu Rong, Michael Yannai, Vladimir Kleiner, and Erez Hasman, 2019, "Photonic Topological Spin Hall Effect Mediated by Vortex Pairs," Phys. Rev. Lett. **123**, 266101.

Wang, J., and M. Kamlah, 2009, "Intrinsic switching of polarization vortex in ferroelectric nanotubes," Phys. Rev. B **80**, 012101.

Wang, J., *et al.*, 2003, "Epitaxial BiFeO$_3$ multiferroic thin film heterostructures," Science **299**, 1719–1722.

Wang, P. S., and H. J. Xiang, 2014, "Room-Temperature Ferrimagnet with Frustrated Antiferroelectricity: Promising Candidate toward Multiple-State Memory," Phys. Rev. X **4**, 011035.

Wang, R. V., *et al.*, 2009, "Reversible Chemical Switching of a Ferroelectric Film," Phys. Rev. Lett. **102**, 047601.

Wang, Y. J., D. Chen, Y. L. Tang, Y. L. Zhu, and X. L. Ma, 2014, "Origin of the Bloch-type polarization components at the 180° domain walls in ferroelectric PbTiO$_3$," J. Appl. Phys. **116**, 224105.

Wang, Y. J., Y. L. Tang, Y. L. Zhu, and X. L. Ma, 2023, "Entangled polarizations in ferroelectrics: A focused review of polar topologies," Acta Mater. **243**, 118485.

Wang, Y. J., *et al.*, 2020, "Polar meron lattice in strained oxide ferroelectrics," Nat. Mater. **19**, 881–886.

Wang, Y.-J., Y.-L. Zhu, and X.-L. Ma, 2017, "Chiral phase transition at 180° domain walls in ferroelectric PbTiO$_3$ driven by epitaxial compressive strains," J. Appl. Phys. **122**, 134104.

Watanabe, Y., 1998, "Theoretical stability of the polarization in a thin semiconducting ferroelectric," Phys. Rev. B **57**, 789–804.

Watanabe, Y., 2005, in *Ferroelectric Thin Films: Basic Properties and Device Physics for Memory Applications*, edited by M. Okuyama and Y. Ishibashi (Springer, Berlin).

Wei, X.-K., C.-L. Jia, T. Sluka, B.-X. Wang, Z.-G. Ye, and N. Setter, 2016, "Néel-like domain walls in ferroelectric Pb(Zr, Ti)O$_3$ single crystals," Nat. Commun. **7**, 12385.

Wen, X. G., and Q. Niu, 1990, "Ground-state degeneracy of the fractional quantum Hall states in the presence of a random potential and on high-genus Riemann surfaces," Phys. Rev. B **41**, 9377–9396.

Whitehead, J. H. C., 1947, "An expression of Hopf's invariant as an integral," Proc. Natl. Acad. Sci. U.S.A. **33**, 117–123.

Wilczek, F., 2016, "Particle physics and condensed matter: The saga continues," Phys. Scr. **T168**, 014003.

Wojdeł, J. C., and J. Íñiguez, 2014, "Ferroelectric Transitions at Ferroelectric Domain Walls Found from First Principles," Phys. Rev. Lett. **112**, 247603.

Wolf, S. A., D. U. Gubser, W. W. Fuller, J. C. Garland, and R. S. Newrock, 1981, "Two-Dimensional Phase Transition in Granular NbN Films," Phys. Rev. Lett. **47**, 1071–1074.

Wu, H., J. Leng, X. Teng, T. Su, Q. Li, J. Li, J. Wu, D. Xu, and Y. Zhu, 2019, "Characterizing the interactions of edge dislocation dipole in hexagonal close packed Ti-Al alloys," Mater. Des. **164**, 107559.

Wu, P., X. Ma, Y. Li, V. Gopalan, and L.-Q. Chen, 2012, "Dipole spring ferroelectrics in superlattice SrTiO$_3$/BaTiO$_3$ thin films exhibiting constricted hysteresis loops," Appl. Phys. Lett. **100**, 092905.

Wu, Z., N. Huang, Z. Liu, J. Wu, W. Duan, and B.-L. Gu, 2007, "Unusual vortex structure in ultrathin Pb(Zr$_{0.5}$Ti$_{0.5}$)O$_3$ films," J. Appl. Phys. **101**, 014112.

Wu, Z., N. Huang, Z. Liu, J. Wu, W. Duan, B.-L. Gu, and X.-W. Zhang, 2004, "Ferroelectricity in Pb(Zr$_{0.5}$Ti$_{0.5}$)O$_3$ thin films: Critical thickness and 180° stripe domains," Phys. Rev. B **70**, 104108.

Wurfel, P., I. P. Batra, and J. T. Jacobs, 1973, "Polarization Instability in Thin Ferroelectric Films," Phys. Rev. Lett. **30**, 1218–1221.

Xu, C., Y. Nahas, S. Prokhorenko, H. Xiang, and L. Bellaiche, 2020, "Berezinskii-Kosterlitz-Thouless phase in two-dimensional ferroelectrics," Phys. Rev. B **101**, 241402.

Xue, F., X. S. Gao, and J.-M. Liu, 2009, "Monte Carlo simulation on the size effect in ferroelectric nanostructures," J. Appl. Phys. **106**, 114103.

Yadav, A. K., *et al.*, 2016, "Observation of polar vortices in oxide superlattices," Nature (London) **530**, 198–201.

Yadav, A. K., *et al.*, 2019, "Spatially resolved steady-state negative capacitance," Nature (London) **565**, 468–471.

Yang, T., C. Dai, Q. Li, H. Wen, and L.-Q. Chen, 2021, "Condensation of collective polar vortex modes," Phys. Rev. B **103**, L220303.

Yasuda, K., R. Wakatsuki, T. Morimoto, R. Yoshimi, A. Tsukazaki, K. S. Takahashi, M. Ezawa, M. Kawasaki, N. Nagaosa, and Y. Tokura, 2016, "Geometric Hall effects in topological insulator heterostructures," Nat. Phys. **12**, 555–559.

Yin, J., *et al.*, 2021, "Nanoscale bubble domains with polar topologies in bulk ferroelectrics," Nat. Commun. **12**, 3632.

Yin, X., Z. Ye, J. Rho, Y. Wang, and X. Zhang, 2013, "Photonic spin Hall effect at metasurfaces," Science **339**, 1405–1407.

Young, A. P., 1979, "Melting and the vector Coulomb gas in two dimensions," Phys. Rev. B **19**, 1855–1866.

Yu, E., J. McCaldin, and T. McGill, 1992, "Band offsets in semiconductor heterojunctions," in *Solid State Physics*, Vol 46, edited by H. Ehrenreich and D. Turnbull (Academic Press, New York), pp. 2–146.

Yu, X. Z., W. Koshibae, Y. Tokunaga, K. Shibata, Y. Taguchi, N. Nagaosa, and Y. Tokura, 2018, "Transformation between meron and skyrmion topological spin textures in a chiral magnet," Nature (London) **564**, 95–98.

Yu, X. Z., Y. Onose, N. Kanazawa, J. H. Park, J. H. Han, Y. Matsui, N. Nagaosa, and Y. Tokura, 2010, "Real-space observation of a two-dimensional skyrmion crystal," Nature (London) **465**, 901–904.

Yuan, S., W. J. Chen, L. L. Ma, Y. Ji, W. M. Xiong, J. Y. Liu, Y. L. Liu, B. Wang, and Y. Zheng, 2018, "Defect-mediated vortex multiplication and annihilation in ferroelectrics and the feasibility of vortex switching by stress," Acta Mater. **148**, 330–343.

Zeches, R. J., *et al.*, 2009, "A strain-driven morphotropic phase boundary in BiFeO$_3$," Science **326**, 977–980.

Zhang, H.-Y., X.-J. Song, X.-G. Chen, Z.-X. Zhang, Y.-M. You, Y.-Y. Tang, and R.-G. Xiong, 2020, "Observation of vortex domains in a two-dimensional lead iodide perovskite ferroelectric," J. Am. Chem. Soc. **142**, 4925–4931.

Zhang, Q., R. Herchig, and I. Ponomareva, 2011, "Nanodynamics of Ferroelectric Ultrathin Films," Phys. Rev. Lett. **107**, 177601.

Zhang, Q., S. Prokhorenko, Y. Nahas, L. Xie, L. Bellaiche, A. Gruverman, and N. Valanoor, 2019, "Deterministic switching of ferroelectric bubble nanodomains," Adv. Funct. Mater. **29**, 1808573.

Zhang, Q., L. Xie, G. Liu, S. Prokhorenko, Y. Nahas, X. Pan, L. Bellaiche, A. Gruverman, and N. Valanoor, 2017, "Nanoscale bubble domains and topological transitions in ultrathin ferroelectric films," Adv. Mater. **29**, 1702375.

Zhao, H. J., P. Chen, S. Prosandeev, S. Artyukhin, and L. Bellaiche, 2021, "Dzyaloshinskii-Moriya-like interaction in ferroelectrics and antiferroelectrics," Nat. Mater. **20**, 341–345.

Zheng, Y., and W. J. Chen, 2017, Characteristics and controllability of vortices in ferromagnetics, ferroelectrics, and multiferroics," Rep. Prog. Phys. **80**, 086501.

Zhong, W., R. D. King-Smith, and D. Vanderbilt, 1994, "Giant LO-TO Splittings in Perovskite Ferroelectrics," Phys. Rev. Lett. **72**, 3618–3621.

Zhong, W., and D. Vanderbilt, 1996, "Effect of quantum fluctuations on structural phase transitions in SrTiO$_3$ and BaTiO$_3$," Phys. Rev. B **53**, 5047–5050.

Zhu, R., *et al.*, 2022, "Dynamics of Polar Skyrmion Bubbles under Electric Fields," Phys. Rev. Lett. **129**, 107601.

Zubko, P., S. Gariglio, M. Gabay, Ph. Ghosez, and J.-M. Triscone, 2011, "Interface physics in complex oxide heterostructures," Annu. Rev. Condens. Matter Phys. **2**, 141–165.

Zubko, P., N. Jecklin, A. Torres-Pardo, P. Aguado-Puente, A. Gloter, C. Lichtensteiger, J. Junquera, O. Stéphan, and J.-M. Triscone, 2012, "Electrostatic coupling and local structural distortions at interfaces in ferroelectric/paraelectric superlattices," Nano Lett. **12**, 2846–2851.

Zubko, P., J. C. Wojdeł, M. Hadjimichael, S. Fernandez-Pena, A. Sené, I. Luk'yanchuk, J.-M. Triscone, and J. Íñiguez, 2016, "Negative capacitance in multidomain ferroelectric superlattices," Nature (London) **534**, 524–528.

See Supplemental Material at http://link.aps.org/supplemental/10.1103/RevModPhys.95.025001 for a description of the methods and a figure with a timeline including some important milestones in the research of complex polar textures in electric polar materials.

SUPPLEMENTAL MATERIAL FOR "TOPOLOGICAL PHASES IN POLAR OXIDE NANOSTRUCTURES"

Javier Junquera

Departamento de Ciencias de la Tierra y Física de la Materia Condensada,
Universidad de Cantabria,
Cantabria Campus Internacional,
Avenida de los Castros s/n,
39005 Santander,
Spain

Yousra Nahas, Sergei Prokhorenko, and Laurent Bellaiche

Physics Department and Institute for Nanoscience and Engineering,
University of Arkansas,
Fayetteville, Arkansas 72701,
USA

Jorge Íñiguez

Materials Research and Technology Department,
Luxembourg Institute of Science and Technology,
5 avenue des Hauts-Fourneaux,
L-4362 Esch/Alzette,
Luxembourg
Department of Physics and Materials Science,
University of Luxembourg,
41 Rue du Brill, Belvaux L-4422,
Luxembourg

Darrell G. Schlom

Department of Materials Science and Engineering,
Cornell University,
Ithaca, New York 14853,
USA
Kavli Institute at Cornell for Nanoscale Science,
Ithaca, New York 14853,
USA
Leibniz-Institut für Kristallzüchtung,
Max-Born-Str. 2, 12489 Berlin,
Germany

Long-Qing Chen

Department of Materials Science and Engineering,
Materials Research Institute,
The Pennsylvania State University,
University Park, Pennsylvania 16802,
USA

Sayeef Salahuddin

Department of Electrical Engineering and Computer Sciences,
University of California,
Berkeley, Berkeley, CA 94720,
USA.
Lawrence Berkeley National Laboratory,
1 Cyclotron Road,
Berkeley, CA 94720,
USA.

David A. Muller

School of Applied and Engineering Physics,
Cornell University,

Ithaca, New York 14853,
USA
Kavli Institute at Cornell for Nanoscale Science,
Ithaca, New York 14853,
USA

Lane W. Martin

Department of Materials Science and Engineering,
University of California - Berkeley,
Berkeley, 94720,
USA
Materials Sciences Division,
Lawrence Berkeley National Laboratory,
Berkeley, 94720,
USA.

R. Ramesh

Department of Physics and Department of Materials Science and Engineering,
University of California - Berkeley,
Berkeley, 94720,
USA
Materials Sciences Division,
Lawrence Berkeley National Laboratory,
Berkeley, 94720,
USA.

I. METHODS

In the hundred years since the original discovery of ferroelectricity in Rochelle salt (Valasek, 1921), numerous significant discoveries and technological manifestations of these materials have been demonstrated (Das *et al.*, 2018). The striking new discoveries of polar skyrmions and vortices within the family of well-known perovskite ferroelectrics, has been driven by the emergence of three scientific advances in the past decade, all of which are central to this review. The first is the ability of materials synthesis approaches to control and tailor artificially designed materials at the atomic scale, as exemplified by the creation of epitaxial superlattices by molecular beam epitaxy (MBE), reflection high-energy electron diffraction (RHEED)-assisted pulsed laser deposition (PLD), and ultrahigh vacuum sputtering (Martin and Rappe, 2016; Ramesh and Schlom, 2019). The second is the development of a wide variety of probes using X-rays, electrons, neutrons, and near-field techniques that are now enabling researchers to study physical phenomena at at unprecedented length, energy, and/or time scales (Li *et al.*, 2019). The final piece is the dramatic advancements in $ab-initio$ and mesoscale phase-field computational approaches coupled with the exponential increase in computing power which has enabled predictions of both ground states and excited states not just in a few atom ensemble, but cells approaching realistic dimensions (Ghosez and Junquera, 2022). A brief summary of these areas are provided in the following, but we urge the interested reader to explore recent reviews on this subject for additional details (Seidel *et al.*, 2016).

A. Advanced experimental approaches

1. Advanced synthesis

It is our ability to tune and manipulate the interplay among fundamental degrees of freedom that gives rise to the exotic phenomena and new states of matter that have so often caught the attention of the scientific community. Nonetheless, despite considerable interest in the exotic topologies noted above and theoretical predictions of their formation, the experimental methodologies required to control these degrees of freedom and, in turn, produce such features have only been developed relatively recently. At the most basic level, such transformative observations require advances in synthesis that enable atomic-scale control of cation/anion chemistries and defect structures, application of large strains via epitaxial lattice mismatch with a substrate, and the ability to create artificial heterostructures engineered down to the unit cell (Fig. 1). Such efforts in complex oxides have intensified over the past decade, particularly in the condensed-matter physics and materials-science communities, wherein researchers have taken cues from semiconductor heteroepitaxy to enable many fundamental and

applied discoveries.

Of particular relevance to the creation of complex oxide heterostructures with atomic layering control is the ability to assess their evolution in real time as they are being grown. Reflection high-energy electron diffraction (RHEED) is quite powerful in this regard because the components of RHEED lie well out of the way of the deposition process. RHEED provides feedback with atomic-level sensitivity on the film phase, orientation, crystalline perfection, smoothness, surface termination, and growth rate. Employing RHEED during growth was critical to achieving the growth of semiconductor heterostructures MBE with atomic-level thickness control as well as an *in situ* means to calibrate the deposition rate of end-member compounds with $\sim 1\%$ accuracy, enabling superlattices and quantum wells with atomically accurate thickness to be grown (Joyce *et al.*, 1986; Wood, 1981).

It is the powerful combination of *in situ* real-time feedback from RHEED with MBE, PLD, and most recently sputtering that has led to the interface abruptness and unit-cell thickness control ((Jiang *et al.*, 1999; Koster *et al.*, 2015; Podkaminer *et al.*, 2016)) that underlie the successful experimental realization of topological textures in complex oxide heterostructures. The benefits of RHEED to improve the growth of complex oxides by MBE were harnessed first, including its use to calibrate (Haeni *et al.*, 2000; Iijima *et al.*, 1992; Nie *et al.*, 2014; Sun *et al.*, 2018; Terashima *et al.*, 1990), and the use of RHEED to gain clues about interface rearrangements that can occur during growth (Nie *et al.*, 2014). The technical challenges of utilizing RHEED in higher pressure deposition processes such as PLD have been overcome using differential pumping (Karl and Stritzker, 1992; Rijnders *et al.*, 1997). Similarly, for magnetron sputtering, where magnetic fields can easily distort the RHEED images, RHEED has also been successfully implemented (Podkaminer *et al.*, 2016).

MBE, long used in the synthesis of exacting semiconductor heterostructures, has been used for more than three decades now to produce oxide materials (Schlom, 2015). Today, MBE growth of oxides enables precise chemical control of materials and so-called reactive MBE (Schlom and Harris, 1995), hybrid MBE (Brahlek *et al.*, 2017; Prakash and Jalan, 2019), suboxide MBE (Adkison *et al.*, 2020; Vogt *et al.*, 2021), and solid-source metal-organic MBE (Nunn *et al.*, 2021) approaches have expanded the range of elemental species that can be included in multi-component materials. While MBE offers the ability to produce extremely high-quality films (MacManus-Driscoll *et al.*, 2020), it comes at a price (both monetary and complexity of use). PLD, on the other hand, provides a generally less costly setup and one that is rapidly adjustable to explore new materials, but also one prone to defect production due to the inherently non-equilibrium nature of

the growth process and high kinetic energy of the typical adatom species (Damodaran *et al.*, 2014; Saremi *et al.*, 2018, 2016). Given time and care, however, all of these techniques provide a pathway to high quality materials, as has been benchmarked for prototypical oxide systems (Breckenfeld *et al.*, 2013a, 2012, 2013c; Hosoda *et al.*, 2013; MacManus-Driscoll *et al.*, 2020; Oh *et al.*, 2011; Schlom, 2015; Warusawithana *et al.*, 2013). The vast majority of this work has focused on perovskite oxides compounds wherein the oxygen sublattice provides an excellent structural and chemical framework (within which the cations are inserted mainly into interstitial sites) for the construction of superlattices. The A-site cations occupy body-centred positions within a corner-sharing network of BO_6 octahedra and it is possible, in superlattice structures, to systematically swap out, vary, or even impose gradients in the A- and B-site cations to produce a plethora of thermodynamic responses.

Thin-film epitaxy, in general, allows researchers to manipulate the ground state of materials, and to control the interactions between spin, charge, orbital, and lattice degrees of freedom. Today, researchers readily make use of thin-film epitaxy to strain engineer materials [Fig. 1(a)] (Choi *et al.*, 2004; Haeni *et al.*, 2004; Schlom *et al.*, 2007, 2014; Warusawithana *et al.*, 2009; Zeches *et al.*, 2009), exploit octahedral rotations to alter bond angles and thus affect properties [Fig. 1(b)] (Rondinelli *et al.*, 2012; Rondinelli and Spaldin, 2011), stabilize non-equilibrium materials via epitaxial constraints [Fig. 1(c)] (Bruinsma, R. and Zangwill, A., 1986; Damodaran *et al.*, 2012; Flynn, 1986; Jesser, 1969; Kaul *et al.*, 2004; Machlin and Chaudhari, 1980; Zunger and Wood, 1989), create exotic strain states and nanostructures in epitaxial nanocomposites [Fig. 1(d)] (MacManus-Driscoll *et al.*, 2008; Mohaddes-Ardabili *et al.*, 2004; Zheng *et al.*, 2004a,b), produce novel properties via interface engineering [Fig. 1(e)] (Bousquet *et al.*, 2008; Bozovic *et al.*, 1994; Iijima *et al.*, 1992; Ohtomo *et al.*, 2002; Specht *et al.*, 1998; Tenne *et al.*, 2006; Warusawithana *et al.*, 2003), drive exotic effects via dimensional confinement [Fig. 1(f)] (Dawley *et al.*, 2020; Lee *et al.*, 2013), alter carrier concentrations utilizing modulation doping (Dingle *et al.*, 1978; Kajdos *et al.*, 2013) or polarization doping [Fig. 1(g)] (Falson and Kawasaki, 2018; Harrison *et al.*, 1978; Nakagawa *et al.*, 2006; Ohtomo and Hwang, 2004; Tasker, 1979; Tsukazaki *et al.*, 2010, 2007), or induce new properties via symmetry breaking [Fig. 1(h)] (Mundy *et al.*, 2016; Warusawithana *et al.*, 2003).

Among these approaches, strain engineering [Fig. 1(a)] is the most common and describes the use of a substrate with a different lattice constant than that of the thin film. The result is a biaxial strain which is imposed on the thin film—within limits of strain and film thickness—so that strain-relaxing defects (e.g., dislocations, cracks or sometimes point defects) (Boullay *et al.*, 2009; Breckenfeld
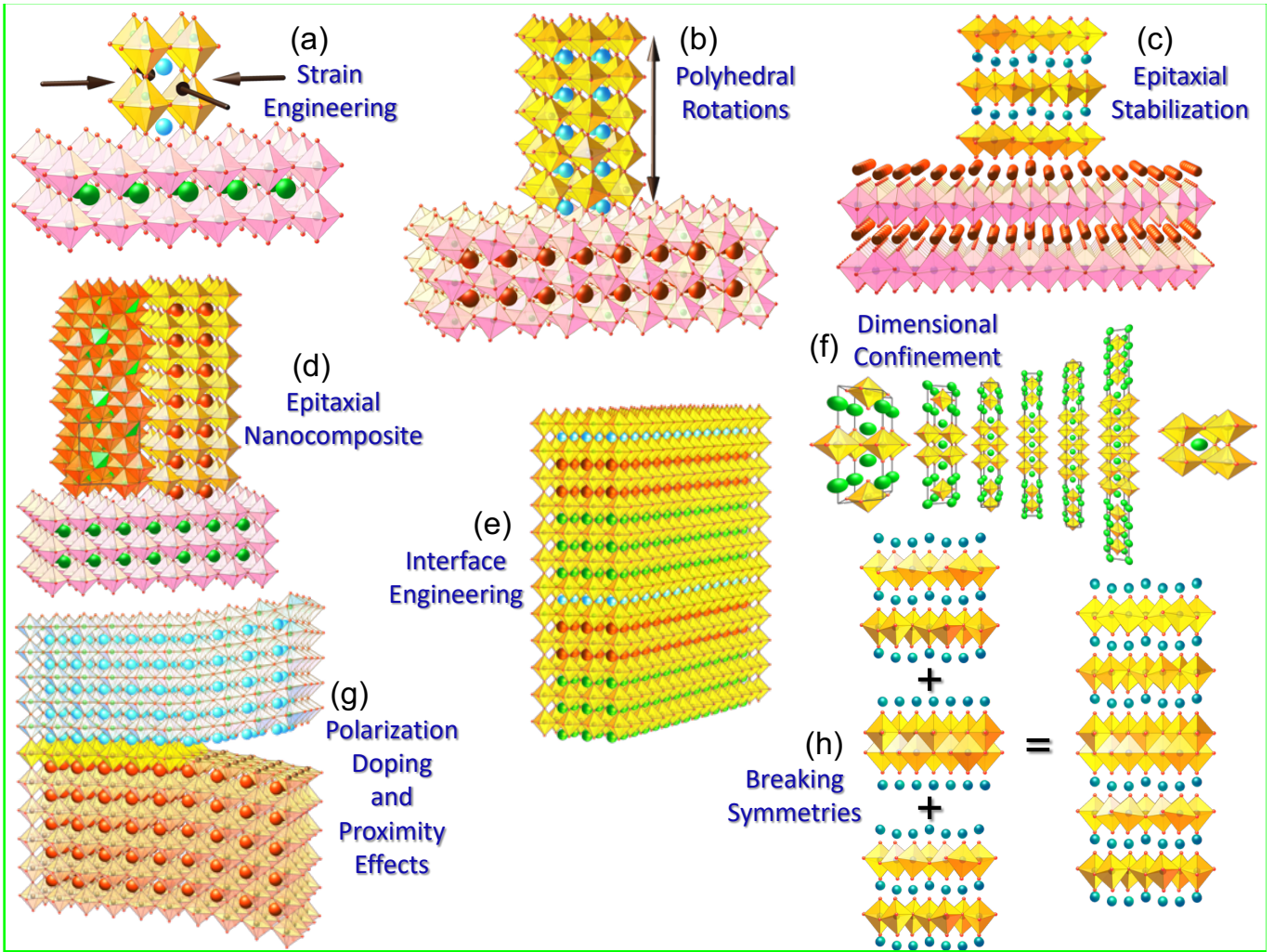
FIG. 1 Approaches used in vacuum thin-film deposition techniques to create epitaxial heterostructures that can give rise to emergent phenomena. These include (a) strain engineering through lattice mismatch; (b) engineering bond angles by interfacing competing polyhedral rotation patterns that decay over a length shown by the vertical arrow; (c) epitaxial stabilization of otherwise metastable phases; (d) epitaxial nanocomposites created using the principles of epitaxy along the out-of-plane direction as well as the in-plane directions; (e) interface engineering to integrate different materials with atomic-layer precision and abruptness to exploit interfacial phenomena; (f) dimensional confinement using epitaxy to reduce the dimensionality of a normally 3D material by confining a thin layer of it between barrier materials; (g) polarization doping and proximity effects in which the spontaneous polarization in one layer is used to modulate carrier concentrations, mobilities, or spins in the adjacent layer; (h) breaking symmetry at interfaces, for example, by breaking mirror symmetry. (a) and (d)-(g) are reproduced from Ref. (Ramesh and Schlom, 2019).

et al., 2013b; Damodaran *et al.*, 2014; Donner *et al.*, 2011; Klenov *et al.*, 2003) are minimized. Although strain engineering has been used to improve the performance of the materials in semiconductor devices (Nguyen *et al.*, 1992; Welser *et al.*, 1994), if applied to oxides, strain engineering can do more than simply enhance an existing property. In oxides, strain engineering can perturb the energy landscape to such an extent that a metastable polymorph (or hidden ground state) becomes the ground state. The resultant phase may have properties that are absent in the bulk form of the material (*i.e.*, hidden ground states with unparalleled properties can be unleashed) (Schlom

et al., 2014). Examples include unleashing ferroelectric order (Haeni *et al.*, 2004; Warusawithana *et al.*, 2009), multiferroic order (Goian *et al.*, 2020; Lee *et al.*, 2010), or superconductivity (Ruf *et al.*, 2021) in systems where such effects are absent in the ground state.

A close relative of strain engineering is rotation of the oxygen coordination polyhedra in response to an imposed strain or the competition between coordination polyhedra rotation patterns across an interface [Fig. 1(b)]. Such rotation of the coordination polyhedra occurs in framework structures when under-constrained oxygen coordination polyhedra are free to rotate. The most com-

mon example in thin-film epitaxy today is interfaces between perovskites with competing octahedral rotation patterns (Rondinelli et al., 2012; Rondinelli and Spaldin, 2011). The length over which an octahedral rotation pattern decays and transitions into another octahedral rotation pattern depends on the perovskites involved, but is typically on the order of a nanometer or two. Beyond this length, which is indicated by the vertical arrow in [Fig. 1(b)], the new rotation pattern has set in and only the strain imposed by the substrate remains. The bond angles in the active layers of the resulting heterostructure may be controlled by selecting among the rotation patterns of substrates, constituent layers, and the thicknesses of those layers (Liao et al., 2016; Moon et al., 2014; Rondinelli et al., 2012). This polyhedral rotation phenomenon likely extends beyond (001)-oriented perovskite heterostructures. It should occur more generally at epitaxial interfaces between framework structures with corner-linked coordination polyhedra. Likely examples include interfaces between framework silicates (e.g., feldspars and zeolites) with corner-linked SiO_4 or AlO_4 tetrahedra or materials where the corner-linked rotations of rigid polyhedra result in negative thermal expansion (e.g., ZrW_2O_8, cordierite, and β-eucryptite) (Heine et al., 1999).

Also related is epitaxial stabilization [Fig. 1(c)] which refers to the process by which lattice-misfit strain energies and interfacial energies are exploited to favor a desired metastable phase over the equilibrium phase (Bruinsma, R. and Zangwill, A., 1986; Damodaran et al., 2012; Flynn, 1986; Jesser, 1969; Kaul et al., 2004; Machlin and Chaudhari, 1980; Zunger and Wood, 1989). The ideal substrate is isostructural with and well lattice matched to the metastable polymorph (Machlin and Chaudhari, 1980). Epitaxial stabilization provides a direct route to stabilizing a hidden-ground state and is applicable to a wide range of oxides. Because many oxide materials have a propensity for competing ground states, epitaxial stabilization of the targeted ground state can be essential. As with strain engineering, the key to the implementation of epitaxial stabilization is the availability and selection of appropriate substrates. Indeed, though the potential of epitaxial stabilization was realized over 50 years ago (Jesser, 1969), it is the development of appropriate substrates that has led to expanded use of this modality in complex oxides in recent years.

Yet another route to manipulate materials is the creation of epitaxial nanocomposites [Fig. 1(d)]. These are self-assembled nanocomposites in which one phase forms 1D rods in a matrix of the other phase (a so-called 1-3 composite) (Newnham et al., 1978), and both phases are epitaxially oriented with respect to the substrate. For this modality, epitaxy occurs not only in-plane (on the substrate), but also in the out-of-plane direction between the constituents of the nanocomposite. As a consequence, it is possible to impose large strains on films

that are thicker than the films within a conventional strained bilayer [Fig. 1(a)] (Huang et al., 2017; Zheng et al., 2004a).

Beside traditional strain and related effects, no other approach has been more influential for producing novel properties in materials than the production of artificial heterostructures and superlattices. Interface engineering [Fig. 1(e)] has garnered enormous interest in the last decade for use with complex oxides because of the potential for and realization of exotic phenomena, including emergent interfacial conduction, magnetic order, and superconductivity (Hwang et al., 2012; Mannhart and Schlom, 2010). Another example is $PbTiO_3/SrTiO_3$ superlattices, in which a new form of interfacial coupling is obtained based on antiferrodistortive rotations of the octahedra, wherein polarization resulting from the asymmetry in the rotation pattern is possible (Bousquet et al., 2008; Dawber et al., 2005). Such work has paved the way to the production of unexpected effects in ferroelectric materials and represents the foundation upon which the recent success in the realization of emergent dipolar topologies is based. Among interface engineering approaches, dimensional confinement [Fig. 1(f)] is achieved by the insertion of layers that restrict the spatial extent of an order parameter, for example, a superlattice in which conducting layers alternate with insulating layers that confine the mobile electrons.

Modulation doping is the dominant technique to realize 2D electron gases in conventional semiconductors by locating dopants remotely from an interface and using the energetics of band alignment to cause the carriers released by the remotely located dopants to spill over into the undoped material. There, the added carriers form a 2D electron gas with minimal ionized impurity scattering (Tsukazaki et al., 2007). Polarization doping [Fig. 1(g)] occurs naturally in, for example, cuprate superconductors as charge reservoir layers that donate their carriers to surrounding CuO_2 layers (Cava, 1990), but analogous electronic reconstruction can also occur at epitaxially engineered oxide interfaces, such as the $LaAlO_3$ and $SrTiO_3$ (Nakagawa et al., 2006; Ohtomo and Hwang, 2004; Reyren et al., 2007).

Interfaces also can be used to break symmetries by stacking layers in a particular sequence. This is where the ability to precisely control the sequence and kind of atomic layers that are grown using advanced vacuum deposition techniques comes into play. For example, the stacking sequence of alternating layers (A-B-A-B) contains mirror symmetry (at the positions of the A-planes and the B-planes) if the individual A- and B-layers possess mirror symmetry. In contrast, by the controlled addition of layer C to the aforementioned superlattice, the stacking sequence A-B-C-A-B-C breaks this symmetry (Sai et al., 2000; Tenne et al., 2006; Warusawithana et al., 2003). Another way to break mirror symmetry in stacked layers is to use layers that them-

selves lack mirror symmetry, such as the rumpled rare-earth layers in hexagonal rare-earth manganites including YMnO$_3$ (Yakel Jnr *et al.*, 1963) or hexagonal rare-earth ferrites including LuFeO$_3$ (Bossak *et al.*, 2004; Mundy *et al.*, 2016), which are geometric ferroelectrics (Ederer and Spaldin, 2004). This latter example is depicted in [Fig. 1(h)].

2. Electron-based techniques: Direct Imaging and Diffraction-Based

There are two main approaches to measuring polar order in materials using transmission electron microscopy (TEM). Direct imaging of atomic positions by aberration-corrected electron microscopy provides structural insights, but over a limited field of view, and with relatively low sensitivity. Diffraction-based methods, including scanning diffraction and dark-field imaging offer larger fields of view, and increased sensitivity, but with additional care needed to recognize or correct for artefacts (Figure 2). The imaging of electric or magnetic fields is possible with the new diffraction-based techniques. In the following, we will capture the principles of each imaging techniques as well as discuss their limitations. The gold standard for atomic-scale imaging of ferroelectric order has been by mapping lattice distortions from annular-dark-field STEM. This approach has a limited field of view, low sensitivity ($\sim$ 10 pm) and is slow. With the development of high-speed, high-dynamic range electron-microscope detectors that record the full momentum distribution for every position of a scanned, Å -scale electron beam, producing a 4-dimensional (4D) phase-space map, this can be overcome. In traditional diffraction, phase information is lost, but when the incident beam is shrunk to dimensions smaller than the spacing of interest in the sample, phase is encoded in the interference of overlapping diffracted beams, enabling a Berry-phase-like measurement of local multipolar order. This can be used to map polarization fields in polar textures under conditions where conventional microscopies lack sensitivity and resolution. Simultaneously measuring electric and polarization fields allowed us to directly image regions of negative differential capacitance at the core of ferroelectric vortex states. This unique approach is capable of determining chirality and topological order with sub-nanometer resolution in engineered ferroelectric heterostructures. The newest version of the detector runs at 10,000 frames per second with a maximum beam current per pixel of 200 pA, making high precision, high speed imaging possible from atomic to micron length scales (with further hardware improvements expected over the next 2 years). Direct imaging at the atomic scale will be boosted by the new high-brightness cold-field emission microscopes and with the ability to map composition (including oxygen-octahedral rotations) by X-ray fluorescence at sub-Å resolution. Electron energy loss spectroscopy (EELS) can also be carried out with atomic-scale precision. Atomic-resolution EELS is particularly suited to study the valence and crystal-field splitting at the Ti^{3+}/Ti^{+4} edge (Ohtomo *et al.*, 2002) along with spatially and chemically-resolved local density of states.

Conceptually, direct imaging is relatively straightforward - an electron microscope with sufficiently high spatial resolution should be able to resolve the positions of the atomic nuclei viewed in projection through a thin sample. The development of aberration correctors improved the resolution of microscopes to better than 100 pm, sufficient to isolate each column of atoms down most zone axes, including light elements such as oxygen (Jia *et al.*, 2003). Tracking shifts of these isolated columns is possible with a precision of about 5-10 % of the resolution, or 5-10 pm in absolute terms. Consequently structural distortions on this scale can be measured and mapped. Originally this was done using phase-contrast TEM to measure the displacement of the oxygen atoms with respect to their neighboring cations to determine the local polar order in ferroelectrics such as PZT (Jia *et al.*, 2008, 2007). Phase-contrast TEM unfortunately restricted the sample thickness to well under 10 nm in projection if multiple scattering artefacts were to be avoided as the phase wraps through 2π every few nanometers. These samples were both extremely difficult to prepare, and very limited in field of view so a more popular approach in the ferroelectric community has been to use HAADF-STEM (Nelson *et al.*, 2011). This technique relies on focusing the electron beam down to a small spot, scanning it across the sample and collecting the high-angle scattering on an annular detector that covers a sufficiently large solid angle as to produce an incoherent image, suppressing the phase contrast. The interpretation of the image is simpler and thicker samples can be used, but it is not completely free of artefacts, and substantial systematic errors in locating atom column positions can occur due to electron channeling as well as small local sample mistilts (Kimoto *et al.*, 2010). Channeling artefacts are minimal when the projected columns are well separated, and can become severe when neighboring projected columns are closer than 100 pm (Kimoto *et al.*, 2010). Nevertheless, these artefacts are still smaller than those found in phase contrast or annular bright field (ABF) images. ABF, and more recently integrated differential phase contrast (iDPC) images are used to qualitatively image light elements such as oxygen atoms (Sun *et al.*, 2019). However, as noted above, both are extremely sensitive to thickness and tilt, even to the point of creating the appearance of polarity in non-polar materials (Bürger *et al.*, 2020). At this point and for these reasons, we caution against using these methods for measurements of polarity or bonding, and discuss more robust alternatives such as multislice ptychography, described below.

The HAADF-STEM image is sensitive to the nuclear potential, with an atomic number dependence that scales as $Z^{1.5} - Z^{1.8}$ as the detector inner angle is increased. While useful for tracking cation positions, it also makes it very difficult to detect the oxygen columns, and the displacement of the cations is tracked instead. This approach works well for conventional displacive ferroelectrics (Nelson *et al.*, 2011), including for many of the topological textures discussed in this review (Yadav *et al.*, 2016, 2019; Zhang *et al.*, 2017). HAADF-STEM imaging also works well for hybrid improper ferroelectrics such as the hexagonal manganites, where the rotations of the oxygen atoms in the ferroelectric trimers are coupled to large displacements of the A-site cations (Holtz *et al.*, 2021, 2017). The displacement patterns measured from the strongly-scattering A-sites provide a good proxy for a local order parameter, and this has been used to quantitatively study the transition from continuous symmetry to discrete domain formation as a function of distance from vortex cores (Holtz *et al.*, 2017).

Directly imaging the displacement of individual atomic sites requires sampling the image with multiple pixels per atom column. This greatly limits the field of view that can be recorded in the time period where the microscope remains stable and aligned. Obtaining information over larger areas, and especially when statistically meaningful and representative data has prompted the development of diffraction-based methods. Diffraction-contrast based imaging is an old approach, but with the recent development of high-speed, high-dynamic-range direct electron detectors (Ozdol *et al.*, 2015; Tate *et al.*, 2016) it can now be applied in a quantitative and dose-efficient manner.

The principle of detecting polar order using dark-field imaging or electron diffraction is based on coherent multiple scattering effects that is a surprising benefit of the strong electron-sample interaction. In the kinematic diffraction limit all zone-axis diffraction patterns are centrosymmetric and therefore insensitive to polar order, i.e. the diffraction intensity of Bragg reflection (hkl) is the same as its inversion counterpart, or $I(hkl) = I(\bar{h}\bar{k}\bar{l})$ which is often referred as the Friedel symmetry (Friedel, 1913). The proof follows from the properties of the Fourier transform of a real potential and the approximation that the measured structure factors are the Fourier transforms of the scattering potential - essentially using a first Born approximation treatment of the scattering. While this is a good approximation for most X-ray diffraction experiments, the Friedel symmetry breaks down in polar and chiral crystals in the case of electron diffraction, where multiple scattering effects modify both the phase and amplitude of the structure factors. As a result, the charge redistribution associated with polarization in ferroelectric crystals leads to the breakdown of the Friedel's law when multiple scattering is involved. Thus, using the polarity-sensitive reflections for dark-field imaging will generate contrast even in the case of 180° domains (Tanaka and Honjo, 1964).

To accurately account for multiple scattering effects in electron diffraction patterns, two main approaches were developed: Bloch-wave and multislice methods. The Bloch-wave method, originated from Hans Bethe's thesis (Bethe, 1928), exploits the periodic symmetry of a perfect crystal with the resulting diffraction intensity depends on the number of diffracted beams included in the calculation. In the simplest case of two beams, one incident and one diffracted (0 and g), this can be solved analytically (Howie *et al.*, 1961). However, the two-beam theory still preserves the Friedel symmetry, which is contradictory to the early experimental observations (Goodman and Lehmpfuhl, 1968) and general solutions to Schrödinger's equation (Miyake and Uyeda, 1955). The development of three-beam and multi-beam theories was necessary to capture the noncentrosymmetric elements in an electron diffraction pattern (Guo *et al.*, 2018; Kambe, 1957; Zuo *et al.*, 1989). The development of three-beam theory (Kambe, 1957) introduces the three-phase invariant, which the two diffracted beams, g and h, forms a closed loop with the transmitted beam. This three-phase invariant is independent of the choice of origin, which sums to either 0 or π for centrosymmetric crystals (Gjønnes and Høier, 1971).

Because of the necessity for multiple scattering, one might expect this effect to rely on thick samples, but this is not the case and we can see the breaking of Friedel symmetry even in the thinnest case of polar monolayer materials such as MoS_2 and WS_2 (Deb *et al.*, 2020). This thin film limit gives us a good opportunity to understand the essential mechanisms of polar contrast. We start with the observation that the diffraction plane is a momentum space, and the shift of the beam in this space is a probability current flow (Lubk and Zweck, 2015). The thin-film limit allows us to expand the scattered signal in a Taylor-series, which in Fourier space becomes a series of scattering paths between sites on the reciprocal lattice starting at the original and with increasing numbers of steps, and the paths of interest that break Friedel symmetry in polar materials are the probability current flows in closed rings (Deb *et al.*, 2020). The lowest-order closed path is a three-member ring, and the phase acquired for the probability flow around the ring is the three-phase invariant, Ψ. Thus to leading order, the intensity of the measured diffraction beam intensity difference between the $+\mathbf{G}$ and $-\mathbf{G}$ beam is modulated by a term proportional to $\sin\Psi$ (Deb *et al.*, 2020). The center of mass of the pair of beams is proportional to $\mathbf{G}\sin\Psi$, which can be used as an order parameter to map local polar order (Nguyen *et al.*, 2020a) (Figure 2).

The dynamical diffraction effects are best captured by a convergent beam electron diffraction (CBED) pattern, which reflects the crystallographic symmetry and local polar order (Buxton *et al.*, 1976; Krajnak and Etheridge, 2020; LeBeau *et al.*, 2010; Morniroli and Steeds, 1992;
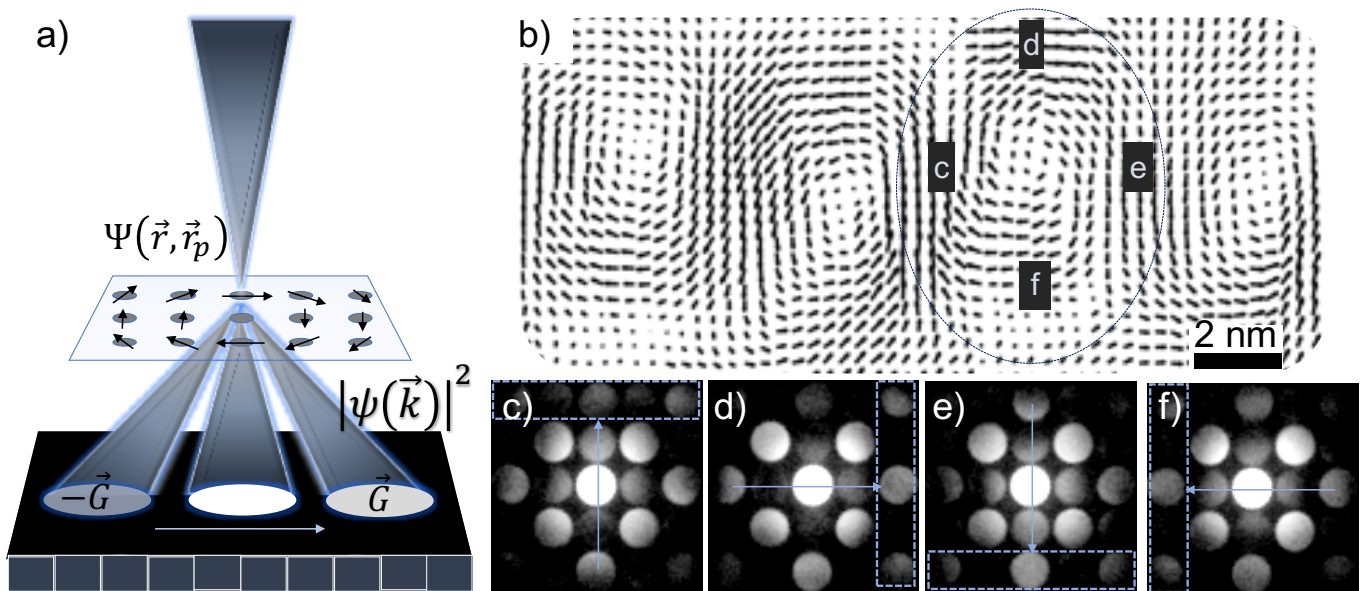
FIG. 2 Measuring Polarization Textures by Scanning Electron Diffraction (4D-STEM). (a) Schematic of 4D-STEM experimental setup. The incident electron beam $\Psi(\mathbf{r}, \mathbf{r}_p)$ is focused to a spot on the sample centered at probe position $\mathbf{r}_p$, just larger than a unit cell, where a convergent beam electron diffraction (CBED) pattern $|\psi(\mathbf{k})|^2$is is recorded on a detector placed in the diffraction plane. Polarity causes an asymmetry in intensities of the conjugate Friedel pairs of diffracted disks at $+\mathbf{G}$ and $-\mathbf{G}$, where $\mathbf{G}$ is a reciprocal lattice vector, indicated as light and dark gray disks. We utilize this asymmetry in probability current flow on the detector to map the polarization vortices in (b), formed in a PbTiO$_3$/SrTiO$_3$ superlattice. Panels (c)-(f) show individual diffraction patterns recorded at those respective positions around the selected vortex, highlighting the changes in intensity on the Friedel-sensitive diffraction beams. Adapted from Ref. (Nguyen *et al.*, 2020a; Yadav *et al.*, 2019).

Tanaka and Tsuda, 2011). CBED patterns are recorded using a focused probe with sizes of sub- to a few nm, with the Bragg spots broadened into disks from the increased probe convergence angle. Conventional CBED patterns consist of non-overlapping disks, which the intensity variations within the disk can be regarded as a function of incident wave direction also known as rocking curves. The rocking curves recorded in CBED patterns not only provides information about the crystallographic symmetry, but also allows for an accurate determination of the structure factors by matching with calculations and hence a precise measurement of the atomic positions and bonding charge densities (Nakashima *et al.*, 2011; Tsuda *et al.*, 2002; Zuo *et al.*, 1999). For ferroelectric crystals, along certain incident beam directions the projected polar direction can be retrieved from the intensity asymmetry lying in the mirror plane. Using the rich information in every CBED pattern recorded at each probe scanning position, we can map the domain configurations and local symmetry fluctuations in real space for ferroelectrics having various Bravais lattice ranging from tetragonal, rhombohedral, hexagonal, to even monoclinic or triclinic symmetries (Hayashida *et al.*, 2020; Kim *et al.*, 2013, 2015; Müller-Caspary *et al.*, 2019; Shao and Zuo, 2017a,b; Tsuda and Tanaka, 2013, 2017; Tsuda *et al.*, 2013).

While scanning electron diffraction is a powerful tech-

nique for mapping local symmetries and polar order, it is not until the development of fast direct electron detectors that made this technique even more widely applicable (McMullan *et al.*, 2014; Tate *et al.*, 2016). This is often referred as four-dimensional (4D) STEM, which records a diffraction pattern (k_x, k_y) at each real-space position (x, y) spanning over 4D phase space (Ophus, 2019; Zuo and Spence, 2016) (Figure 2). There are two major advantages in using a fast direct electron detector, acquisition speed and detector sensitivity. A simple comparison of the acquisition time for a 256×256 scan using a charge-coupled device (CCD) camera will take >4 hrs, while with fast detectors of >1k fps will require less than a few minutes to record a comparable data set. This allows for an experimental recording of polar textures over large fields of view which outruns mechanical instabilities in a TEM, as well as opens up possibilities for *in-situ* experiments or imaging beam sensitive polar textures such as skyrmions or merons. The improved dynamic range and signal-to-noise ratio in the diffraction patterns allows for a simultaneous determination of polar textures (Nguyen *et al.*, 2020a; Shao *et al.*, 2021) and strain fields (Béché *et al.*, 2009; Cooper *et al.*, 2016; Han *et al.*, 2018; Müller *et al.*, 2012; Ozdol *et al.*, 2015; Padgett *et al.*, 2020; Yuan *et al.*, 2019), as well as imaging electric or magnetic fields (Cao *et al.*, 2017; Nguyen *et al.*, 2020b; Zhang *et al.*, 2021) or even energy landscape (Das

et al., 2021; Yadav *et al.*, 2019).

A key advantage of the direct electron detectors is their ability to record the full momentum distribution, and since we have recorded the whole 4D-STEM dataset, it is now possible to disentangle polarization information from artefacts due to electron channeling or local crystal mistilts (Shao *et al.*, 2021), where the latter is inevitable across domain walls in perovskite ferroelectrics (Aizu, 1970; Floquet *et al.*, 1997; MacLaren *et al.*, 2015). As a consequence, techniques such as differential phase contrast measured from a quadrant detector or center-of-mass analysis lack the momentum resolution to separate crystal mistilt from genuine polar order, and are more useful as a proxy for mapping grain orientation (Caswell *et al.*, 2009).

The beam convergence sets the size of the sampled region, and for non-overlapping disks this can range from just larger than a unit cell to many unit cells, thus by adjusting this size the local order parameter can be averaged over a given volume, and the scan size and sampling interval adjusted to measure or large fields of view, with a precision often a hundred-fold better than direct imaging.

A new emerging method that offers promise for extending the range and precision of direct imaging is multislice electron ptychography (Chen *et al.*, 2021). Here the modern direct electron detectors collect 4D-STEM data sets from a highly-convergent electron beam focused down to a small spot. The phase information from overlapping disks is recovered by the ptychographic reconstruction to map out the underlying electrostatic potential. The inclusion of the multislice algorithm properly accounts for multiple scattering and crystal tilt, effectively eliminating these as potential artifacts. The method has achieved a lateral resolution of below 20 pm, limited not by the probe size, but by the thermal vibrations of the atoms themselves (Chen *et al.*, 2021). The precision with which individual atom columns can be measured is about 1 pm from a single scan, but more importantly is free from systematic channeling and tilt errors that complicate past direct imaging methods. Further, all atoms, including the light oxygen atoms are detected. Larger fields of view can be recorded by using a defocused coherent probe (Chen *et al.*, 2020) to reduce the number of patterns needed to sample a given region at atomic resolution.

Overall, the new detectors have greatly improved our ability and precision in measuring polarization, strain, energy landscape, electric and magnetic fields over large fields of view and are crucial to the characterization and fundamental understanding of complex 3D topological polar textures.

Another electron-microscope technique that is of considerable value for understanding the microscopic details of ferroelectric textures is EELS. In modern aberration-corrected instruments EELS can be used to map composition and bonding at the atomic scale (Muller, 2009; Muller *et al.*, 2008), including the electronic structure changes resulting from the local broken symmetries in the ferroelectric state (Torres-Pardo *et al.*, 2011). Here a spectrometer placed after the sample records the energy losses of the transmitted electron beam after it has been focused to a spot smaller than the atomic spacing and scanned across the sample. The energy transferred from the electron beam to the sample includes the excitation of core electrons to empty states on the same atomic site. The core-level binding energy that marks the EELS edge onset allows a unique elemental identification to be made, atom-column by atom-column. The shape of the edge itself reflects the underlying local partial density of states modified by the presence of a core hole (Rez and Muller, 2008). This is similar to the information obtained by x-ray absorption spectroscopy (XAS), and the same simulation tools can be used to model and interpret both sets of spectra - see the review by (Rez and Muller, 2008). In complex oxides, the localization introduced by the core hole makes it reasonably simple to fingerprint many of the local electronic configurations (Kourkoutis *et al.*, 2010), and crystal field theory and charge-transfer multiplets provide simple models to interpret features in the spectra from $3d$ transition metal sites (De Groot, 2005). Changes in formal valence and electronic charge redistribution can be spatially mapped in some case - particularly for $3d$ transition metals (Ohtomo *et al.*, 2002). As the symmetry is lowered by the distortions and off-centering of the B-site cation in displacive ferroelectrics like $PbTiO_3$, additional splittings of the d-orbital energy levels are introduced, and these are often sufficiently large to be detected in the EELS spectrum (Torres-Pardo *et al.*, 2011). The momentum transfer in EELS plays a similar role to polarization in XAS so, in principle, linear dichroism measurements should be possible, however the large range of in-plane momenta needed to form a small probe overwhelms any such changes. Although some in-plane vs out-of-plane anisotropy is possible to measure, the in-plane component can provide information only about the magnitude and not the direction of the electronic distortions.

EELS is also particularly useful for analysing light elements such as oxygen, and can be used to map the position and displacement of the oxygen anions directly. In multiferroic lutetium ferrite, the oxygen EELS signal shows the different bonding environments of the different oxygen sublattices, and as the core-hole effects are less pronounced on anions as compared to cations, band-like features in the unoccupied local density of states were mapped at atom-column by atom-column (Mundy *et al.*, 2012). The ability of EELS to decompose local electronic information by site, atomic species and angular momentum is helpful in constructing a microscopic picture of structure and bonding in ferroelectrics, and more closely couples experimental measurements to DFT and other

electronic structure theories.

3. Proximal probes: AFM/PFM; near field optical techniques

For polar/ferroelectric systems, scanning-probe-based microscopies, in particular, PFM and related techniques have become mainstream techniques for the study of ferroic order at the nanoscale over the last few decades. There are numerous reviews on the field [see for example, Refs. (Gruverman *et al.*, 2019; Kholkin *et al.*, 2007; Soergel, 2011)] and the current treatment is not meant to be an exhaustive review. Such approaches now readily allow researchers to image ferroic domain structures at length scales limited by the sharpness of the scanning-probe tips (10-30 nm). Among numerous important advances in the study of ferroic materials have been the development of methodologies that enable real-time or $in-operando$ studies of dynamic properties in such materials under applied fields. For example, switching spectroscopy PFM (SS-PFM) allows one to map switching parameters by acquiring the local PFM hysteresis loop at each point in a PFM image (Jesse *et al.*, 2006). Such an approach provides spectroscopic information on the spatial variations of the local switching parameters such as coercive bias, imprint, and nucleation bias. Therefore, it allows one to connect variations therein to topographic features in the material. Another technique, so-called band-excitation PFM (BE-PFM), works by exciting and monitoring the tip response within a continuous frequency band rather than at a single frequency and allows for quantitative measurements of energy dissipation through determination of the quality factor (Jesse *et al.*, 2007). This approach also provides information on the frequency dependence of the piezoelectric properties and switching parameters.

Such multimodal spectroscopy approaches are now opening up the possibility of probing the dynamics of ferroic systems at both the time- and length-scales required to glean useful information about real switching process. While exciting, these advances open up new challenges, namely that the size and the complexity of the dataset produced are such that ready human-based analysis is nearly impossible. In turn, researchers are now going beyond classic nanoscience fields and adapting lessons from social analytics, natural-language processing, and sentiment analysis, for example, where computational roadblocks are pervasive. Today, researchers are applying machine-learning and artificial neural networks to extract understandable/interpretable insight from these hyperspectral datasets (Agar *et al.*, 2018, 2019). While this provides immediate insight into ferroic physics, it also opens a door for connections to other measurement approaches (e.g., time-of-flight secondary-ion mass spectrometry, scanning Raman, electron energy loss spectroscopy, etc.).

At the same time, other tip-based approaches can also be used to locally probe ferroic order. For example, scanning near-field optical microscopy (SNOM) - developed across a similar time period as PFM - allows for high-resolution (sub-micron) spatial imaging with simultaneous optical interrogation of a material (Hermann and Gordon, 2018). As such, it is possible to complete near-field ellipsometric, infrared interferometry, photoluminescence, Raman, second-harmonic generation, and many other forms of study using these techniques. All in all, the advance of tip-based probes, provides a complimentary way for probing such exotic dipolar structures (and their consequential properties) at the nanoscale that extends what is possible with electron microscopy.

4. Synchrotron-based techniques

Modern light sources provide increasingly coherent and bright sources of radiation which are also revolutionizing the information we can extract from the materials wherein emergent dipolar phenomena may be possible. In particular, techniques such as hard X-ray diffraction - even using relatively basic bend magnets - now provide extremely bright radiation sources that, when combined with advanced detectors, enable rapid mapping of large swatches of reciprocal space in short time periods. For example, work on the $(PbTiO_3)_n/(SrTiO_3)_n$ superlattices have extensively drawn on the use of the PILATUS 100k pixel detector (Dectris) which provides large areas of reciprocal space and up to 10 millon counts per second to produce 3D reciprocal maps with high accuracy and speed. This has been essential to map the complex structures of emergent (and often long-range) order dipolar structures. Another technique, in particular useful in superlattices and systems with periodic emergent features, is resonant soft X-ray diffraction (RSXD). RSXD makes use of the spectroscopic sensitivity of resonances in the energy range of the radiation to the electronic character to probe spatial variations/patterns in order. While this technique has often been applied to magnetic materials (Wilkins *et al.*, 2003), researchers have applied this techniques to probe chirality and emergent phenomena in the dipolar textures of interest in this review (Lovesey and van der Laan, 2018; Shafer *et al.*, 2018). Finally, advances in ultra-fast pump-probe studies (wherein the pump can be light, THz, X-ray or other radiation) and the probe is X-ray are beginning to give insights into the evolution of ferroelectric and related materials (specific examples of emergent topologies will be described in detail in a later section) (Daranciang *et al.*, 2012; Grigoriev *et al.*, 2006; Jo *et al.*, 2011; Wen *et al.*, 2013).

1. First-principles simulations

For a simulation method to be *predictive*, it must rely on a fundamental theory that does not require experimental input about the materials of interest. This fundamental theory is of course quantum mechanics, where the Schrödinger equation for our materials of interest is typically solved within a computationally efficient and generally accurate approach: Density Functional Theory (DFT). DFT allows us to predict the behavior of materials subject to arbitrary boundary conditions (e.g., poor electrostatic screening, epitaxial strain), resolving the ensuing atomic-scale details (e.g., potentially non-trivial domain wall structures) even in situations that may be markedly different from the usual equilibrium state of the compound.

The application of DFT methods to ferroelectrics (Ghosez and Junquera, 2022) and ferroelectric domain walls (Iñiguez, 2020) are well reviewed in the literature. Among the works that laid the foundation for current studies of topological ferroelectrics, let us highlight: the investigation of ultra-thin ferroelectric thin films in monodomain (Junquera and Ghosez, 2003) and multidomain (Aguado-Puente and Junquera, 2008) states; the investigation of electrostatically-driven multidomain structures in $PbTiO_3/SrTiO_3$ superlattices and their behavior with epitaxial strain (Aguado-Puente and Junquera, 2012); and the elucidation of the internal Bloch-like structure of the 180° domain walls of $PbTiO_3$ (Wojdeł and Íñiguez, 2014), which is ultimately responsible for the topological features of the recently discovered skyrmion bubbles (Das *et al.*, 2019; Pereira Gonçalves *et al.*, 2019). Intestingly more efficient DFT methods have been designed to reduce the solution time for the electronic groundstate whilst preserving high accuracy. They have been used to simulate the polar morphologies and surface reconstructions of $PbTiO_3$ films on $SrTiO_3$ with system sizes over > 2000 atoms, including the influence of the oxygen rotations on the vortex structure (Baker and Bowler, 2020), or the origin of ferroelectric domain wall alignments with surface trenches (Baker and Bowler, 2021).

2. Atomistic effective potentials

Despite recent progress in software and hardware, DFT simulations are still computationally heavy. Hence, as soon as the length scale of our ferroelectric textures exceeds a few nanometers (about 300 atoms), they simply cannot be used. The computational challenge is even greater when we want to investigate behavior at finite temperatures, switching under applied fields, etc.

A way around this problem is to employ effective potentials that capture the basic interatomic couplings (e.g., those giving rise to the ferroelectric distortion)
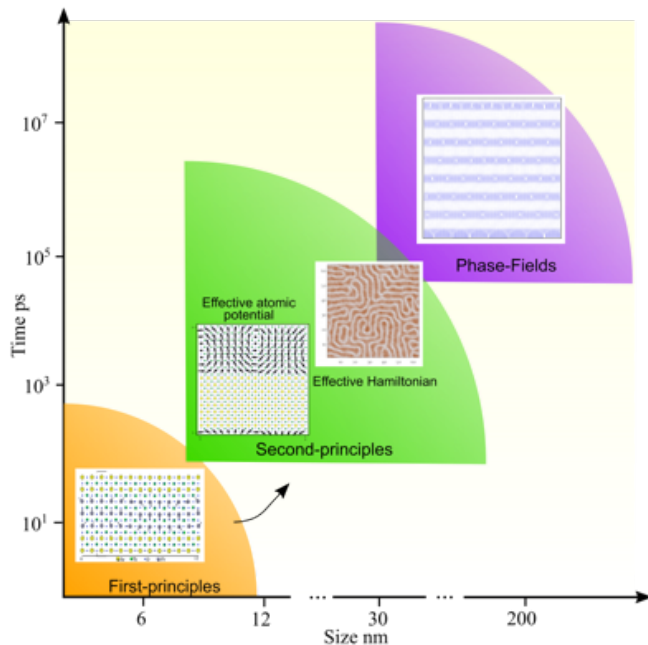

FIG. 3 Sketch with the different length and time scales affordable with the variety of key computational approaches presented in Sec. I.B. Black arrow indicates where some methods are parametrized from.

B. Key computational approaches

Ferroelectrics is a field where the synergistic interaction between theoretical simulation and experiment has led to enormous progress. This interplay – which started in the early 90's with the fundamental first-principles investigations of the origin of ferroelectricity in perovskite oxides such as $BaTiO_3$ and $PbTiO_3$ (Cohen, 1992) – has accelerated in the past years with the appearance or consolidation of methods that permit predictive large-scale simulations of multidomain configurations. As described elsewhere in this review, such techniques have been key for the pioneering prediction of non-trivial ferroelectric textures (Fu and Bellaiche, 2003); then, among many recent applications, they allowed us to predict and explain the occurrence of ferroelectric skyrmion bubbles in $PbTiO_3/SrTiO_3$ superlattices, exactly as observed experimentally (Das *et al.*, 2019; Pereira Gonçalves *et al.*, 2019). Given their critical role in the field, in the following we briefly describe these simulation techniques.

in a mathematically simple form, thus allowing us to run larger-scale simulations based on them. Such effective potentials – usually known as *force fields* in the broader simulations community – are ubiquitous in condensed-matter physics and computational materials science. However, to treat ferroelectrics and multiferroics, one often needs to reach a level of numerical accuracy (down to 1 meV per atom, or even better) and complexity (strongly anharmonic – non-linear – effects dominate the behavior) that go beyond what is usual in other fields. Hence, instead of using off-the-shelf methods, the ferroelectrics community has tended to adopt an original approach, either developing brand-new simulation techniques, or suitably modifying existing ones.

A first example of such atomistic approaches is the so-called "shell models", which were developed mimicking those initially introduced e.g. to interpret neutron and Raman measurements of phonons (Cowley, 1964; Migoni *et al.*, 1976). Shell models with parameters computed from first principles have been constructed for many important ferroelectric perovskites (Tinte *et al.*, 1999), including relaxors (Sepliarsky *et al.*, 2004) and multiferroics (Graf *et al.*, 2014). Applications include the investigation of topological multi-domain toroidal structures in $PbTiO_3$ nano-particles (Stachiotti and Sepliarsky, 2011).

A second example is the development of a first-principles-based "bond-valence" methods (Etxebarria *et al.*, 2005; Shin *et al.*, 2005), mimicking the homonymous phenomenological approach to estimate structural stability that is well-known in crystallography (Brown, 2009). For example, these methods have been successfully employed to investigate ferroelectric multidomain structures, and their switching properties (Liu *et al.*, 2016; Shin *et al.*, 2007); however, to the best of our knowledge, it has not been applied to topological problems yet.

Then, the best developed and most applied strategy for the theoretical investigation of ferroelectrics – including their topological features – is the so-called "effective Hamiltonian" approach. This scheme, which can be seen as an extension of the classic "ϕ^4" models (Radescu *et al.*, 1995), relies on a simplified atomistic description of the material, whereby only the (local) distortions that are relevant to the physics of interest (e.g., cell dipoles yielding the spontaneous polarization, tilts of the O_6 octahedra that characterize a perovskite structure, local and global strains) are considered in the model. Further, the interactions among these degrees of freedom are treated in a perturbative way, using a high-symmetry (e.g., the cubic perovskite) structure as reference and simplifying the mathematics by considering only the symmetry-allowed couplings. The parameters of the resulting model are computed from first principles, which provides us with a predictive scheme that permits statistical (e.g., Monte Carlo) and dynamical (e.g., molecular dynamics) simulations of relatively large systems [typically, over 10,000–100,000 atoms; and up to 1,000,000 atoms us-

ing hybrid schemes (Prokhorenko *et al.*, 2018)]. This approach was originally introduced in the mid-nineties, and applied to simple perovskites such as $BaTiO_3$ and $PbTiO_3$ (Krakauer *et al.*, 1999; Rabe, 2005; Waghmare and Rabe, 1997; Zhong *et al.*, 1994, 1995). The early 00's saw many extensions and development, for example, to treat solid solutions and chemical (dis)order (e.g., compounds like $PbZr_{1-x}Ti_xO_3$, where effective-Hamiltonian calculations were instrumental to elucidate the physics of its morphotropic phase boundary (Bellaiche *et al.*, 2000)), and to model magnetoelectric multiferroics (e.g., spins were incorporated to produce models for $BiFeO_3$, resulting in key insights into the properties of this all-important material (Kornev *et al.*, 2007)). By now, the successful applications of the effective-Hamiltonian approach to ferroelectrics are countless.

Of special interest here is the development, also carried out in the early 00's, to treat ferroelectric *nanostructures* using effective Hamiltonians, tackling the different mechanical and electrical boundary conditions that are typical of such cases (Ponomareva *et al.*, 2005a,b). These methods were later used to reproduce the striking nanostripe domains experimentally found in ultrathin ferroelectric films (Fong *et al.*, 2004; Streiffer *et al.*, 2002), and to predict novel ferroelectric states such as electric vortices (Naumov *et al.*, 2004), electric bubbles (Lai *et al.*, 2006), dipolar waves (Sichuga and Bellaiche, 2011), electric skyrmions (Nahas *et al.*, 2015) and electrical disclinations/merons (Lu *et al.*, 2018), all of which have been experimentally confirmed (Das *et al.*, 2019; Jia *et al.*, 2011; Lu *et al.*, 2018; Nelson *et al.*, 2011; Yadav *et al.*, 2016; Zhang *et al.*, 2017). Indeed, the effective-Hamiltonian approach has been the key theoretical method in the studies of topological ferroelectrics, and many of the seminal works just cited are reviewed elsewhere in this article.

Last but not least, during the last decade we have seen the emergence of a new scheme (called "second-principles") that aims at extending the effective-Hamiltonian approach by retaining all the atoms in the model (Escorihuela-Sayalero *et al.*, 2017; Wojdeł *et al.*, 2013) and even considering the relevant electronic bands if needed (García-Fernández *et al.*, 2016). Thus, the ambition is to develop simulation methods that can approach first-principles accuracy as much as needed. There is a caveat, though: second-principles techniques also rely on a reference structure, which yields computationally very efficient methods, but limits their application to effects where chemical bonds do not break or form. Fortunately, this is sufficient to tackle all the topological problems of interest here.

From the early stages, second-principles methods proved their value in studies of ferroelectric domain walls and topology-related problems, for a key reason: the domain walls are high-energy states whose internal structure (and associated energy landscape) can significantly differ from that of the domains. Hence, having a more

realistic model of the material, we are better equipped to investigate these specially challenging objects. Thus, the first novel application of the second-principles methods revealed the Bloch-like nature of the ferroelectric domain walls of PbTiO$_3$ (Wojdeł and Íñiguez, 2014). Note that this critical result had been missed by previous theoretical investigations, probably because the used models rely on a too-drastic simplification of the compound itself (as is the case of effective Hamiltonians, which are coarse grained) or its energy landscape (shell models and bond-valence models rely on simple and rigid interaction potentials). After this initial success, second-principles methods have been used to predict and explain electric skyrmions in PbTiO$_3$-based materials (Pereira Gonçalves et al., 2019), quantify their properties (e.g., their chirality (Shafer et al., 2018), their negative capacitance response (Yadav et al., 2019; Zubko et al., 2016)), propose practical ways to control them via external fields (Das et al., 2021), etc. Thus, despite many remaining challenges (e.g., constructing models in a customary way), second-principles methods clearly mark a way forward in the simulation of topological ferroelectrics.

More recently, and working along this line of multiscale simulations, a combination of neural-network quantum molecular dynamics with a molecular mechanic framework has been used to study topological defects and its response to electric and strain fields on PbTiO$_3$ nanowires embedded on a SrTiO$_3$ matrices (Linker et al., 2022a,b).

3. Phase-field methods

Despite all this success, the above (atomistic) methods are still limited in the length and time scales of the phenomena amenable to investigation. Today, using effective Hamiltonians (probably the most computationally efficient scheme among those just mentioned), one can achieve molecular dynamics simulations of 10^6 atoms evolving for periods of 10^{-9} seconds. However, this is still far from the length and time scales characteristic of some very interesting phenomena: for example, studying the movement of polar disclinations (merons) in labyrinth domain patterns will presumably require simulations of 10^9 atoms evolving during 10^{-8} seconds. Such order of magnitude difference of achievable and needed time scales calls for alternative methods to continue moving forward.

One of the computational methods that have been extensively employed to model the polar structures of ferroelectric thin films and superlattices is phase-field simulations (Chen, 2008; Chen and Zhao, 2022; Hu and Chen, 1997; Li et al., 2001; Schrade et al., 2007; Su and Landis, 2007; Wang et al., 2004, 2019a; Zheng et al., 2006). In this method, the thermodynamics of a system is described by its total free energy as a function of spontaneous electric polarization, mechanical displacement or

strain field, and electric potential gradient or electric field. In the phase-field method, the mechanical displacement and the electric potential are obtained by solving the mechanical and electrostatic equilibrium equations, while the spontaneous polarization is obtained by solving the time-dependent Ginzburg-Landau equation (Chandra and Littlewood, 2007). Typically, under a given set of electric and mechanical boundary conditions, an initial (non-equilibrium) distribution of electric potential, mechanical displacement, and spontaneous electric polarization is allowed to evolve, temporally and spatially, so as to reduce the total free energy of the system, towards an equilibrium state.

In most phase-field investigations, one works in the overdamped regime, assuming that the inertial momentum is immediately dissipated by the environment. However, it is perfectly possible to introduce inertial effects in the dynamic equations (Blinc and Žekš, 1974), and thus get access to shorter time scales and phonon-like features. Recent examples are given in Refs. (Akamatsu et al., 2018; Li et al., 2021).

The total polarization, mechanical displacement, and electric potential distributions that minimize the total free energy represents the equilibrium ferroelectric and ferroelastic domain configurations under the prescribed electric, mechanical, and polarization boundary conditions. We typically refer the spatial distribution of spontaneous electric polarization as the polar structure or ferroelectric domain structure, and the spatial distribution of spontaneous strain as the ferroelastic domain structure. Most of the experimentally observed spatial electrical polarization and mechanical displacement patterns and their length scales in a ferroelectric thin film or heterostructure can be understood based on the competition among the domain wall energy, the long-range electrostatic energy, and the elastic interaction energy, which can be obtained based on the spatial distributions of spontaneous polarization, mechanical displacements, and electric potential within a thin film or heterostructure (Chen, 2008; Wang et al., 2019a). One of the advantages of the phase-field approach is that it is rather straightforward to model and predict the formation and temporal evolution of complex polarization patterns while incorporating long-range elastic and electrostatic interaction energies as well as domain wall energies in a heterostructure with arbitrary crystal anisotropy. A unique advantage, compared to other computational methods described in this review, is the fact that one can isolate the individual contributions of strain energy, electrostatic energy and domain wall energy and study their relative importance in determining certain types of topological polar structures. It is also possible to incorporate charge carriers and dopants to investigate the polar structures in the presence of both ionic and electronic defects as well as their evolution under external stimuli, e.g., light excitation (Shi and Chen, 2020; Yang and Chen,

2021). Therefore, it is a natural method for exploring and understanding the thermodynamic driving forces underlying the formation of complicated topological polarization patterns such as polarization vortex and skyrmion lattices, as well as regular domain structures and their stability and temporal evolution dynamics under external thermal, mechanical and electric stimuli (Balakrishna and Huber, 2015; Balke *et al.*, 2012; Cheataf and Zheng, 2015; Das *et al.*, 2019; Hong and Chen, 2019; Hong *et al.*, 2017, 2021; Nelson *et al.*, 2011; Winchester *et al.*, 2015; Xue *et al.*, 2018; Yadav *et al.*, 2016). Finally, one can easily extend the phase-field model of polar structures to heterostructures or composites of ferroelectric and ferromagnetic systems to model the coupled topological polar and magnetic systems within the same system (Chu *et al.*, 2015; Hu *et al.*, 2017, 2018, 2020; Wang *et al.*, 2019b).

In principle, phase-field models can be formulated at different length scales for the same system in analogy with microscopic observations of a domain structure at different spatial resolution. However, just like in any other computational method, it is extremely challenging to formulate a phase-field model at very large length scales, e.g., tens of microns, while simultaneously at very high spatial resolution, e.g., resolving domain walls around one nanometer of thickness. Despite such limitations, a lot has been accomplished by fitting the usual phase-field potentials to a more fundamental theory, and then run studies of complex ferroelectric textures. This is, in essence, what was done in Ref. (Das *et al.*, 2019), where second-principles results were used as input to construct a new Ginzburg-Landau potential for $PbTiO_3$, capable of capturing the Bloch character of the ferroelectric domain walls in this material (the key feature behind the occurrence of skyrmions). Note that the existing Landau parameters used for $PbTiO_3$ do not capture (predict) this feature, and it was thanks to the synergy between atomistic (second-principles) and continuum approaches that the new Ginzburg-Landau potentials – and their later application to study non-trivial topological structures in $PbTiO_3$-based compounds – were made possible.

II. OVERVIEW OF THE DAWN OF NON-TRIVIAL TEXTURES IN FERROIC MATERIALS. TIMELINE FIGURE
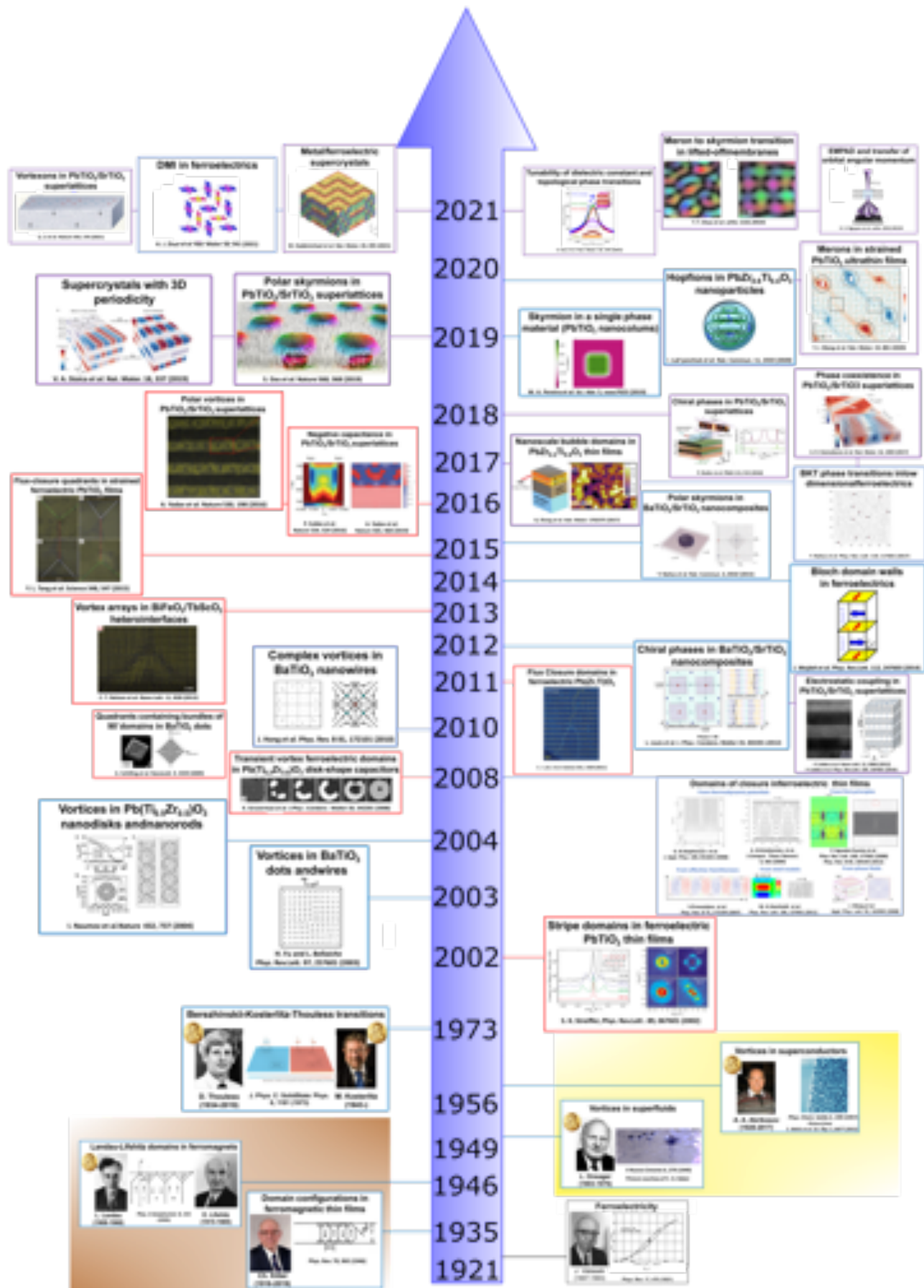
FIG. 4   Timeline with some key breakthroughs regarding the study of novel non-trivial topological phases in polar oxide nanostructures. Panels surrounded by a solid red (blue) line refer to experimental (theoretical) developments, while those surrounded by a solid magenta line correspond to combined experimental/theoretical studies.

REFERENCES

Adkison, K M, S.-L. Shang, B. J. Bocklund, D. Klimm, D. G Schlom, and Z.-K. Liu (2020), "Suitability of binary oxides for molecular-beam epitaxy source materials: A comprehensive thermodynamic analysis," APL Mater. **8**, 081110.

Agar, J C, Y. Cao, B. Naul, S. Pandya, S. van der Walt, A. I. Luo, J. T. Maher, N. Balke, S. Jesse, S. V. Kalinin, Rama K. Vasudevan, and L. W. Martin (2018), "Machine detection of enhanced electromechanical energy conversion in PbZr$_{0.2}$Ti$_{0.8}$O$_3$ thin films," Adv. Mater. **30**, 1800701.

Agar, J C, B. Naul, S. Pandya, S. van der Walt, J. Maher, Y. Ren, L.-Q. Chen, S. V. Kalinin, R. K. Vasudevan, Y. Cao, J. S. Bloom, and L. W. Martin (2019), "Revealing ferroelectric switching character using deep recurrent neural networks," Nat. Commun. **10**, 4809.

Aguado-Puente, P, and J. Junquera (2008), "Ferromagnetic-clike closure domains in ferroelectric ultrathin films: First-principles simulations," Phys. Rev. Lett. **100**, 177601.

Aguado-Puente, P, and J. Junquera (2012), "Structural and energetic properties of domains in PbTiO$_3$/SrTiO$_3$ superlattices from first principles," Phys. Rev. B **85**, 184105.

Aizu, K (1970), "Determination of the state parameters and formulation of spontaneous strain for ferroelastics," J. Phys. Soc. Jpn. **28**, 706–716.

Akamatsu, H, Y. Yuan, V. A. Stoica, G. Stone, T. Yang, Z. Hong, S. Lei, Y. Zhu, R. C. Haislmaier, J. W. Freeland, L.-Q. Chen, H. Wen, and V. Gopalan (2018), "Light-activated Gigahertz ferroelectric domain dynamics," Phys. Rev. Lett. **120**, 096101.

Baker, J S, and D. R. Bowler (2020), "Polar morphologies from first principles: PbTiO$_3$ films on SrTiO$_3$ substrates and the p($2\times\lambda$) surface reconstruction," Adv. Theory Simul. **3**, 2000154.

Baker, J S, and D. R. Bowler (2021), "Origin of ferroelectric domain wall alignment with surface trenches in ultrathin films," Phys. Rev. Lett. **127**, 247601.

Balakrishna, A R, and J. E. Huber (2015), "Scale effects and the formation of polarization vortices in tetragonal ferroelectrics," Appl. Phys. Lett. **106**, 092906.

Balke, N, B. Winchester, W. Ren, Y. H. Chu, A. N. Morozovska, E. A. Eliseev, M. Huijben, R. K. Vasudevan, P. Maksymovych, J. Britson, S. Jesse, I. Kornev, R. Ramesh, L. Bellaiche, L. Q. Chen, and S. V. Kalinin (2012), "Enhanced electric conductivity at ferroelectric vortex cores in BiFeO$_3$," Nat. Phys. **8**, 81–88.

Bellaiche, L, A. García, and D. Vanderbilt (2000), "Finite-temperature properties of Pb(Zr$_{1-x}$Ti$_x$)O$_3$ alloys from first principles," Phys. Rev. Lett. **84**, 5427–5430.

Bethe, H (1928), "Theorie der beugung von elektronen an kristallen," Ann. Phys. **392**, 55–129.

Blinc, R, and B. Zekš (1974), *Soft modes in ferroelectrics and antiferroelectrics*, Selected topics in solid state physics (North-Holland Pub. Co., Amsterdam).

Bossak, A A, I. E. Graboy, O. Y. Gorbenko, A. R. Kaul, M. S. Kartavtseva, V. L. Svetchnikov, and H. W. Zandbergen (2004), "XRD and HREM studies of epitaxially stabilized hexagonal orthoferrites RFeO$_3$ (R = Eu − Lu)," Chem. Mater. **16**, 1751–1755.

Boullay, P, V. Dorcet, O. Pérez, C. Grygiel, W. Prellier, B. Mercey, and M. Hervieu (2009), "Structure determination of a brownmillerite Ca$_2$Co$_2$O$_5$ thin film by precession electron diffraction," Phys. Rev. B **79**, 184108.

Bousquet, E, M. Dawber, N. Stucki, C. Lichtensteiger, P. Hermet, S. Gariglio, J.-M. Triscone, and Ph. Ghosez (2008), "Improper ferroelectricity in perovskite oxide artificial superlattices," Nature **452**, 732–736.

Bozovic, I, J. N. Eckstein, G. F. Virshup, A. Chaiken, M. Wall, R. Howell, and M. Fluss (1994), "Atomic-layer engineering of cuprate superconductors," J. Supercond. **7**, 187–195.

Brahlek, M, A. S. Gupta, J. Lapano, J. Roth, H.-T. Zhang, L. Zhang, R. Haislmaier, and R. Engel-Herbert (2017), "Frontiers in the growth of complex oxide thin films: Past, present, and future of hybrid MBE," Adv. Funct. Mater. **28**, 1702772.

Breckenfeld, E, N. Bronn, J. Karthik, A. R. Damodaran, S. Lee, N. Mason, and L. W. Martin (2013a), "Effect of growth induced (non)stoichiometry on interfacial conductance in LaAlO$_3$/SrTiO$_3$," Phys. Rev. Lett. **110**, 196804.

Breckenfeld, E, A. B. Shah, and L. W. Martin (2013b), "Strain evolution in non-stoichiometric heteroepitaxial thin-film perovskites," J. Mater. Chem. C **1**, 8052–8059.

Breckenfeld, E, R. Wilson, J. Karthik, A. R. Damodaran, D. G. Cahill, and L. W. Martin (2012), "Effect of growth induced (non)stoichiometry on the structure, dielectric response, and thermal conductivity of SrTiO$_3$ thin films," Chem. Mater. **24**, 331–337.

Breckenfeld, E, R. B. Wilson, and L. W. Martin (2013c), "Effect of growth induced (non)stoichiometry on the thermal conductivity, permittivity, and dielectric loss of LaAlO$_3$ films," Appl. Phys. Lett. **103**, 082901.

Brown, I D (2009), "Recent developments in the methods and applications of the bond valence model," Chem. Rev. **109** (12), 6858–6919.

Bruinsma, R,, and Zangwill, A. (1986), "Structural transitions in epitaxial overlayers," J. Phys. France **47**, 2055–2073.

Buxton, B F, J. A. Eades, J. W. Steeds, and G. M. Rackham (1976), "The Symmetry of Electron Diffraction Zone Axis Patterns," Proc. R. Soc. London. Ser. A **281**, 171–194.

Béché, A, J. L. Rouvière, L. Clément, and J. M. Hartmann (2009), "Improved precision in strain measurement using nanobeam electron diffraction," Appl. Phys. Lett. **95**, 123114.

Bürger, J, Th. Riedl, and J. K. N. Lindner (2020), "Influence of lens aberrations, specimen thickness and tilt on differential phase contrast stem images," Ultramicroscopy **219**, 113118.

Cao, M C, Y. Han, Z. Chen, Y. Jiang, K. X. Nguyen, E. Turgut, G. D. Fuchs, and D. A Muller (2017), "Theory and practice of electron diffraction from single atoms and extended objects using an EMPAD," Microscopy **67**, i150–i161.

Caswell, T A, P. Ercius, M. W. Tate, A. Ercan, S. M. Gruner, and D. A. Muller (2009), "A high-speed area detector for novel imaging techniques in a scanning transmission electron microscope," Ultramicroscopy **109**, 304–311.

Cava, R J (1990), "Structural chemistry and the local charge picture of copper oxide superconductors," Science **247**, 656–662.

Chandra, P, and P. B. Littlewood (2007), "A Landau primer for ferroelectrics," in *Physics of Ferroelectrics: A Modern Perspective* (Springer Berlin Heidelberg, Berlin, Heidelberg) pp. 69–116.

Cheataf, W J, and Y. Zheng (2015), "Vortex switching in ferroelectric nanodots and its feasibility by a homogeneous

electric field: Effects of substrate, dislocations and local clamping force," Acta Mater. **88**, 41–54.

Chen, L-Q (2008), "Phase-field method of phase transitions/domain structures in ferroelectric thin films: A review," J. Am. Ceram. Soc. **91**, 1835–1844.

Chen, L-Q, and Y. Zhao (2022), "From classical thermodynamics to phase-field method," Prog. Mater. Sci. **124**, 100868.

Chen, Z, Y. Jiang, Y.-T. Shao, M. E. Holtz, M. Odstrčil, M. Guizar-Sicairos, I. Hanke, S. Ganschow, D. G. Schlom, and D. A. Muller (2021), "Electron ptychography achieves atomic-resolution limits set by lattice vibrations," Science **372**, 826–831.

Chen, Z, M. Odstrcil, Y. Jiang, Y. Han, M.-H. Chiu, L.-J. Li, and D. A. Muller (2020), "Mixed-state electron ptychography enables sub-angstrom resolution imaging with picometer precision at low dose," Nat. Commun. **11**, 2994.

Choi, K J, M. Biegalski, Y. L. Li, A. Sharan, J. Schubert, R. Uecker, P. Reiche, Y. B. Chen, X. Q. Pan, V. Gopalan, L.-Q. Chen, D. G. Schlom, and C. B. Eom (2004), "Enhancement of ferroelectricity in strained $BaTiO_3$ thin films," Science **306** (5698), 1005–1009.

Chu, P, Y. L. Xie, Y. Zhang, J. P. Chen, D. P. Chen, Z. B. Yan, and J.-M. Liu (2015), "Real-space anisotropic dielectric response in a multiferroic skyrmion lattice," Sci. Rep. **5**, 8318.

Cohen, R E (1992), "Origin of ferroelectricity in perovskite oxides," Nature **358**, 136–138.

Cooper, D, T. Denneulin, N. Bernier, A. Béché, and J.-L. Rouvière (2016), "Strain mapping of semiconductor specimens with nm-scale resolution in a transmission electron microscope," Micron **80**, 145–165.

Cowley, R A (1964), "Lattice dynamics and phase transitions of strontium titanate," Phys. Rev. **134**, A981–A997.

Damodaran, A R, E. Breckenfeld, Z. Chen, S. Lee, and L. W. Martin (2014), "Enhancement of ferroelectric Curie temperature in $BaTiO_3$ films via strain-induced defect dipole alignment," Adv. Mater. **26**, 6341–6347.

Damodaran, A R, S. Lee, J. Karthik, S. MacLaren, and L. W. Martin (2012), "Temperature and thickness evolution and epitaxial breakdown in highly strained $BiFeO_3$ thin films," Phys. Rev. B **85**, 024113.

Daranciang, D, M. J. Highland, H. Wen, S. M. Young, N. C. Brandt, H. Y. Hwang, M. Vattilana, F. Nicoul, M.and Quirin, J. Goodfellow, T. Qi, I. Grinberg, D. M. Fritz, M. Cammarata, D. Zhu, H. T. Lemke, D. A. Walko, E. M. Dufresne, Y. Li, J. Larsson, D. A. Reis, K. Sokolowski-Tinten, K. A. Nelson, A. M. Rappe, P. H. Fuoss, G. B. Stephenson, and A. M. Lindenberg (2012), "Ultrafast photovoltaic response in ferroelectric nanolayers," Phys. Rev. Lett. **108**, 087601.

Das, S, A. Ghosh, M. R. McCarter, S.-L. Hsu, Y.-L. Tang, A. R. Damodaran, R. Ramesh, and L. W. Martin (2018), "Perspective: Emergent topologies in oxide superlattices," APL Mater. **6**, 100901.

Das, S, Z. Hong, V. A. Stoica, M. A. P. Gonçalves, Y. T. Shao, E. Parsonnet, E. J. Marksz, S. Saremi, M. R. McCarter, A. Reynoso, C. J. Long, A. M. Hagerstrom, D. Meyers, V. Ravi, B. Prasad, H. Zhou, Z. Zhang, H. Wen, F. Gómez-Ortiz, P. García-Fernández, J. Bokor, J. Íñiguez, J. W. Freeland, N. D. Orloff, J. Junquera, L. Q. Chen, S. Salahuddin, D. A. Muller, L. W. Martin, and R. Ramesh (2021), "Local negative permittivity and topological phase transition in polar skyrmions," Nat. Mater. **20**, 194–201.

Das, S, Y. L. Tang, Z. Hong, M. A. P. Gonçalves, M. R. McCarter, C. Klewe, K. X. Nguyen, F. Gómez-Ortiz, P. Shafer, E. Arenholz, V. A. Stoica, S.-L. Hsu, B. Wang, C. Ophus, J. F. Liu, C. T. Nelson, S. Saremi, B. Prasad, A. B. Mei, D. G. Schlom, J. Íñiguez, P. García-Fernández, D. A. Muller, L. Q. Chen, J. Junquera, L. W. Martin, and R. Ramesh (2019), "Observation of room-temperature polar skyrmions," Nature **568**, 368–372.

Dawber, M, K. M. Rabe, and J. F. Scott (2005), "Physics of thin-film ferroelectric oxides," Rev. Mod. Phys. **77**, 1083–1130.

Dawley, N M, E. J. Marksz, A. M. Hagerstrom, G. H. Olsen, M. E. Holtz, V. Goian, C. Kadlec, J. Zhang, X. Lu, J. A. Drisko, R. Uecker, S. Ganschow, C. J. Long, J. C. Booth, S. Kamba, C. J. Fennie, D. A. Muller, N. D. Orloff, and D. G. Schlom (2020), "Targeted chemical pressure yields tuneable millimetre-wave dielectric," Nat. Mater. **19**, 176–181.

De Groot, Frank (2005), "Multiplet effects in X-ray spectroscopy," Coord. Chem. Rev. **249**, 31–63.

Deb, P, M. C. Cao, Y. Han, M. E. Holtz, S. Xie, J. Park, R. Hovden, and D. A Muller (2020), "Imaging Polarity in Two Dimensional Materials by Breaking Friedel's Law," Ultramicroscopy **215**, 113019.

Dingle, R, H. L. Störmer, A. C. Gossard, and W. Wiegmann (1978), "Electron mobilities in modulation-doped semiconductor heterojunction superlattices," Appl. Phys. Lett. **33**, 665–667.

Donner, W, C. Chen, M. Liu, A. J. Jacobson, Y.-L. Lee, M. Gadre, and D. Morgan (2011), "Epitaxial strain-induced chemical ordering in $La_{0.5}Sr_{0.5}CoO_{3-\delta}$ films on $SrTiO_3$," Chem. Mater. **23**, 984–988.

Ederer, C, and N. A. Spaldin (2004), "A new route to magnetic ferroelectrics," Nat. Mater. **3**, 849–851.

Escorihuela-Sayalero, C, J. C. Wojdeł, and J. Íñiguez (2017), "Efficient systematic scheme to construct second-principles lattice dynamical models," Phys. Rev. B **95**, 094115.

Etxebarria, I, J. M. Perez-Mato, A. García, P. Blaha, K. Schwarz, and J. Rodriguez-Carvajal (2005), "Comparison of empirical bond-valence and first-principles energy calculations for a complex structural instability," Phys. Rev. B **72**, 174108.

Falson, J, and M. Kawasaki (2018), "A review of the quantum Hall effects in MgZnO/ZnO heterostructures," Rep. Prog. Phys. **81**, 056501.

Floquet, N, C. M. Valot, M. T. Mesnier, J. C. Niepce, L. Normand, A. Thorel, and R. Kilaas (1997), "Ferroelectric domain walls in $BaTiO_3$: Fingerprints in XRPD diagrams and quantitative HRTEM image analysis," J. Phys. III France **7**, 1105–1128.

Flynn, C P (1986), "Strain-assisted epitaxial growth of new ordered compounds," Phys. Rev. Lett. **57**, 599–602.

Fong, D D, G. B. Stephenson, S. K. Streiffer, J. A. Eastman, O. Auciello, P. H. Fuoss, and C. Thompson (2004), "Ferroelectricity in ultrathin perovskite films," Science **304**, 1650–1653.

Friedel, G (1913), "Sur les symétries cristallines que peut révéler la diffraction des rayons X." Comptes Rendus, Acad. Sci. (Paris) **157**, 1533–1536.

Fu, H, and L. Bellaiche (2003), "Ferroelectricity in barium titanate quantum dots and wires," Phys. Rev. Lett. **91**, 257601.

García-Fernández, P, J. C. Wojdeł, J. Íñiguez, and J. Junquera (2016), "Second-principles method for materials sim-

ulations including electron and lattice degrees of freedom," Phys. Rev. B **93**, 195137.

Ghosez, Ph, and J. Junquera (2022), "Modeling of ferroelectric oxide perovskites: From first to second principles," Annu. Rev. Condens. Matter Phys. **13**, null.

Gjønnes, J, and R. Høier (1971), "The application of non-systematic many-beam dynamic effects to structure factor determination," Acta Crystallogr. Sec. A **27**, 313–316.

Goian, V, R. Held, E. Bousquet, Y. Yuan, A. Melville, H. Zhou, V. Gopalan, Ph. Ghosez, N. A. Spaldin, D. G. Schlom, and S. Kamba (2020), "Making EuO multiferroic by epitaxial strain engineering," Commun. Mater. **1**, 74.

Goodman, P, and G. Lehmpfuhl (1968), "Observation of the breakdown of Friedel's law in electron diffraction and symmetry determination from zero-layer interactions," Acta Cryst. A **24**, 339–347.

Graf, M, M. Sepliarsky, M. Stachiotti, and S. Tinte (2014), "Development of an atomic level model for $BiFeO_3$ from first-principles," Ferroelectrics **461**, 61–67.

Grigoriev, A, D.-H. Do, D. M. Kim, C.-B. Eom, B. Adams, E. M. Dufresne, and P. G. Evans (2006), "Nanosecond domain wall dynamics in ferroelectric $Pb(Zr, Ti)O_3$ thin films," Phys. Rev. Lett. **96**, 187601.

Gruverman, A, M. Alexe, and D. Meier (2019), "Piezoresponse force microscopy and nanoferroic phenomena," Nat. Commun. **10**, 1661.

Guo, Y, Ph. N. H. Nakashima, and J. Etheridge (2018), "Three-beam convergent-beam electron diffraction for measuring crystallographic phases," IUCrJ **5**, 753–764.

Haeni, J H, P. Irvin, W. Chang, R. Uecker, P. Reiche, Y. L. Li, S. Choudhury, W. Tian, M. E. Hawley, B. Craigo, A. K. Tagantsev, X. Q. Pan, S. K. Streiffer, L. Q. Chen, S. W. Kirchoefer, J. Levy, and D. G. Schlom (2004), "Room-temperature ferroelectricity in strained $SrTiO_3$," Nature **430** (7001), 758–761.

Haeni, JH, C.D. Theis, and D.G. Schlom (2000), "RHEED intensity oscillations for the stoichiometric growth of $SrTiO_3$ thin films by reactive molecular beam epitaxy," J. Electroceramics **4**, 385–391.

Han, Y, K. Nguyen, M. Cao, P. Cueva, S. Xie, M. W. Tate, P. Purohit, S. M. Gruner, J. Park, and D. A Muller (2018), "Strain Mapping of Two-Dimensional Heterostructures with Subpicometer Precision," Nano Lett. **18**, 3746–3751.

Harrison, W A, E. A. Kraut, J. R. Waldrop, and R. W. Grant (1978), "Polar heterojunction interfaces," Phys. Rev. B **18**, 4402–4410.

Hayashida, T, Y. Uemura, K. Kimura, S. Matsuoka, D. Morikawa, S. Hirose, K. Tsuda, T. Hasegawa, and T. Kimura (2020), "Visualization of ferroaxial domains in an order-disorder type ferroaxial crystal," Nat. Commun. **11**, 4582.

Heine, V, P. R. L. Welche, and M. T. Dove (1999), "Geometrical origin and theory of negative thermal expansion in framework structures," J. Am. Ceram. Soc. **82**, 1793–1802.

Hermann, R J, and M. J. Gordon (2018), "Nanoscale optical microscopy and spectroscopy using near-field probes," Annu. Rev. Chem. Biomol. Eng. **9**, 365–387.

Holtz, M E, E. S. Padgett, R. Steinhardt, Ch. M. Brooks, D. Meier, D. G. Schlom, D. A. Muller, and J. A. Mundy (2021), "Dimensionality-induced change in topological order in multiferroic oxide superlattices," Phys. Rev. Lett. **126**, 157601.

Holtz, M E, K. Shapovalov, J. A. Mundy, C. S. Chang, Z. Yan,

E. Bourret, D. A. Muller, D. Meier, and A. Cano (2017), "Topological defects in hexagonal manganites: Inner structure and emergent electrostatics," Nano Lett. **17**, 5883–5890.

Hong, Z, and L.-Q. Chen (2019), "Switchable polar spirals in tricolor oxide superlattices," Acta Mater. **164**, 493–498.

Hong, Z, A. R. Damodaran, F. Xue, S.-L. Hsu, J. Britson, A. K. Yadav, C. T. Nelson, J.-J Wang, J. F. Scott, L. W. Martin, R. Ramesh, and L.-Q. Chen (2017), "Stability of polar vortex lattice in ferroelectric superlattices," Nano Lett. **17** (4), 2246–2252.

Hong, Z, S. Das, C. Nelson, A. Yadav, Y. Wu, J. Junquera, L.-Q. Chen, L. W. Martin, and R. Ramesh (2021), "Vortex domain walls in ferroelectrics," Nano Lett. **21**, 3533–3539.

Hosoda, M, C. Bell, Y. Hikita, and H. Y. Hwang (2013), "Compositional and gate tuning of the interfacial conductivity in $LaAlO_3/LaTiO_3/SrTiO_3$ heterostructures," Appl. Phys. Lett. **102**, 091601.

Howie, A, M. J. Whelan, and N. F. Mott (1961), "Diffraction contrast of electron microscope images of crystal lattice defects - ii. the development of a dynamical theory," Proc. R. Soc. London. Ser. A **263**, 217–237.

Hu, H-L, and L.-Q. Chen (1997), "Computer simulation of $90°$ ferroelectric domain formation in two-dimensions," Mater. Sci. Eng. A **238**, 182–191.

Hu, J-M, C.-G. Duan, C.-W. Nan, and L.-Q. Chen (2017), "Understanding and designing magnetoelectric heterostructures guided by computation: progresses, remaining questions, and perspectives," Npj Comput. Mater. **3**, 18.

Hu, J-M, T. Yang, and L.-Q. Chen (2018), "Strain-mediated voltage-controlled switching of magnetic skyrmions in nanostructures," Npj Comput. Mater. **4**, 62.

Hu, J-M, T. Yang, and L.-Q. Chen (2020), "Stability and dynamics of skyrmions in ultrathin magnetic nanodisks under strain," Acta Mater. **183**, 145–154.

Huang, J, J. L. MacManus-Driscoll, and H. Wang (2017), "New epitaxy paradigm in epitaxial self-assembled oxide vertically aligned nanocomposite thin films," J. Mater. Res. **32**, 4054–4066.

Hwang, H Y, Y. Iwasa, M. Kawasaki, B. Keimer, N. Nagaosa, and Y. Tokura (2012), "Emergent phenomena at oxide interfaces," Nat. Mater. **11**, 103–113.

Iijima, K, T. Terashima, Y. Bando, K. Kamigaki, and H. Terauchi (1992), "Atomic layer growth of oxide thin films with perovskite-type structure by reactive evaporation," J. Appl. Phys. **72**, 2840–2845.

Iñiguez, J (2020), "First-principles studies of structural domain walls," in *Domain Walls: From Fundamental Properties to Nanotechnology Concepts*, edited by D. Meier, J. Seidel, M. Gregg, and R. Ramesh (Oxford University Press, New York, NY) pp. 36–75.

Jesse, S, A. P. Baddorf, and S. V. Kalinin (2006), "Switching spectroscopy piezoresponse force microscopy of ferroelectric materials," Appl. Phys. Lett. **88**, 062908.

Jesse, S, S. V. Kalinin, R. Proksch, A. P. Baddorf, and B. J. Rodriguez (2007), "The band excitation method in scanning probe microscopy for rapid mapping of energy dissipation on the nanoscale," Nanotechnology **18**, 435503.

Jesser, WA (1969), "A theory of pseudomorphism in thin films," Mater. Sci. Eng. **4**, 279–286.

Jia, C L, M. Lentzen, and K. Urban (2003), "Atomic-resolution imaging of oxygen in perovskite ceramics," Science **299**, 870–873.

Jia, C-L, S.-B. Mi, K. Urban, I. Vrejoiu, M. Alexe, and D. Hesse (2008), "Atomic-scale study of electric dipoles near charged and uncharged domain walls in ferroelectric films," Nat. Mater. **7**, 57–61.

Jia, C-L, V. Nagarajan, J.-Q. He, L. Houben, T. Zhao, R. Ramesh, K. Urban, and R. Waser (2007), "Unit-cell scale mapping of ferroelectricity and tetragonality in epitaxial ultrathin ferroelectric films," Nat. Mater. **6**, 64–69.

Jia, C-L, K. W. Urban, M. Alexe, D. Hesse, and I. Vrejoiu (2011), "Direct observation of continuous electric dipole rotation in flux-closure domains in ferroelectric Pb(Zr, Ti)O$_3$," Science **331**, 1420–1423.

Jiang, J C, X. Q. Pan, W. Tian, C. D. Theis, and D. G. Schlom (1999), "Abrupt PbTiO$_3$ /SrTiO$_3$ superlattices grown by reactive molecular beam epitaxy," Appl. Phys. Lett. **74**, 2851–2853.

Jo, J Y, P. Chen, R. J. Sichel, S. J. Callori, J. Sinsheimer, E. M. Dufresne, M. Dawber, and P. G. Evans (2011), "Nanosecond dynamics of ferroelectric/dielectric superlattices," Phys. Rev. Lett. **107**, 055501.

Joyce, B A, P. J. Dobson, J. H. Neave, K. Woodbridge, J. Zhang, P. K. Larsen, and B. Bôlger (1986), "Rheed studies of heterojunction and quantum well formation during mbe growth — from multiple scattering to band offsets," Surf. Sci. **168**, 423–438.

Junquera, J, and Ph. Ghosez (2003), "Critical thickness for ferroelectricity in perovskite ultrathin films," Nature **422**, 506–509.

Kajdos, A P, D. G. Ouellette, T. A. Cain, and S. Stemmer (2013), "Two-dimensional electron gas in a modulation-doped SrTiO$_3$/Sr(Ti, Zr)O$_3$ heterostructure," Appl. Phys. Lett. **103**, 082120.

Kambe, K (1957), "Study of simultaneous reflexion in electron diffraction by crystals i. theoretical treatment," J. Phys. Soc. Jpn. **12**, 13–25.

Karl, H, and B. Stritzker (1992), "Reflection high-energy electron diffraction oscillations modulated by laser-pulse deposited YBa$_2$Cu$_3$O$_{7-x}$," Phys. Rev. Lett. **69**, 2939–2942.

Kaul, A R, O. Yu. Gorbenko, and A. A. Kamenev (2004), "The role of heteroepitaxy in the development of new thin-film oxide-based functional materials," Russ. Chem. Rev. **73**, 861–880.

Kholkin, A L, S. V. Kalinin, A. Roelofs, and A. Gruverman (2007), "Review of ferroelectric domain imaging by piezoresponse force microscopy," in *Scanning Probe Microscopy: Electrical and Electromechanical Phenomena at the Nanoscale*, edited by S. Kalinin and A. Gruverman (Springer New York, New York, NY) pp. 173–214.

Kim, K-H, D. A. Payne, and J. M. Zuo (2013), "Determination of fluctuations in local symmetry and measurement by convergent beam electron diffraction: applications to a relaxor-based ferroelectric crystal after thermal annealing," J. Appl. Crystallogr. **46**, 1331–1337.

Kim, K-H, D. A. Payne, and J.-M. Zuo (2015), "Determination of 60° polarization nanodomains in a relaxor-based ferroelectric single crystal," Appl. Phys. Lett. **107**, 162902.

Kimoto, K, T. Asaka, X. Yu, T. Nagai, Y. Matsui, and K. Ishizuka (2010), "Local crystal structure analysis with several picometer precision using scanning transmission electron microscopy," Ultramicroscopy **110**, 778–782.

Klenov, D O, W. Donner, B. Foran, and S. Stemmer (2003), "Impact of stress on oxygen vacancy ordering in epitaxial (La$_{0.5}$Sr$_{0.5}$)CoO$_{3-\delta}$ thin films," Appl. Phys. Lett. **82**, 3427–3429.

Kornev, I A, S. Lisenkov, R. Haumont, B. Dkhil, and L. Bellaiche (2007), "Finite-temperature properties of multiferroic BiFeO$_3$," Phys. Rev. Lett. **99**, 227602.

Koster, G, M. Huijben, and G. Rijnders (2015), in *Epitaxial Growth of Complex Metal Oxides*, Woodhead Publishing Series in Electronic and Optical Materials, edited by G. Koster, M. Huijben, and G. Rijnders (Woodhead Publishing, Cambridge) p. iv.

Kourkoutis, L F, H. L. Xin, T. Higuchi, Y. Hotta, J. H. Lee, Y. Hikita, D. G. Schlom, H. Y. Hwang, and D. A. Muller (2010), "Atomic-resolution spectroscopic imaging of oxide interfaces," Philos. Mag. **90**, 4731–4749.

Krajnak, M, and J. Etheridge (2020), "A symmetry-derived mechanism for atomic resolution imaging," Proc. Natl. Acad. Sci. USA **117**, 27805–27810.

Krakauer, H, R. Yu, C.-Z. Wang, K. M. Rabe, and U. V. Waghmare (1999), "Dynamic local distortions in KNbO$_3$," J. Phys.: Condens. Matter **11**, 3779–3787.

Lai, B-K, I. Ponomareva, I. I. Naumov, I. Kornev, Huaxiang Fu, L. Bellaiche, and G. J. Salamo (2006), "Electric-field-induced domain evolution in ferroelectric ultrathin films," Phys. Rev. Lett. **96**, 137602.

LeBeau, J M, S. D. Findlay, L. J. Allen, and S. Stemmer (2010), "Position averaged convergent beam electron diffraction: Theory and applications," Ultramicroscopy **110**, 118–125.

Lee, C-H, N. D. Orloff, T. Birol, Y. Zhu, V. Goian, E. Rocas, R. Haislmaier, E. Vlahos, J. A. Mundy, L. F. Kourkoutis, Y. Nie, M. D. Biegalski, J. Zhang, M. Bernhagen, N. A. Benedek, Y. Kim, J. D. Brock, R. Uecker, X. X. Xi, V. Gopalan, D. Nuzhnyy, S. Kamba, D. A. Muller, I. Takeuchi, J. C. Booth, C. J. Fennie, and D. G. Schlom (2013), "Exploiting dimensionality and defect mitigation to create tunable microwave dielectrics," Nature **502**, 532–536.

Lee, J H, L. Fang, E. Vlahos, X. Ke, Y. W. Jung, L. F. Kourkoutis, J.-W. Kim, Ph. J. Ryan, T. Heeg, M. Roeckerath, V. Goian, M. Bernhagen, R. Uecker, P. C. Hammel, K. M. Rabe, S. Kamba, J. Schubert, J. W. Freeland, D. A. Muller, C. J. Fennie, P. Schiffer, V. Gopalan, E. Johnston-Halperin, and D. G. Schlom (2010), "A strong ferroelectric ferromagnet created by means of spin–lattice coupling," Nature **466**, 954–958.

Li, Q, S. D. Marks, S. Bean, M. Fisher, D. A. Walko, A. D. DiChiara, X. Chen, K. Imura, N. K. Sato, M. Liu, P. G. Evans, and H. Wen (2019), "Simultaneous scanning near-field optical and X-ray diffraction microscopy for correlative nanoscale structure–property characterization," J. Synchrotron Radiat. **26**, 1790–1796.

Li, Q, V. A. Stoica, M. Paściak, Y. Zhu, Y. Yuan, T. Yang, M. R. McCarter, S. Das, A. K. Yadav, S. Park, C. Dai, H. J. Lee, Y. Ahn, S. D. Marks, S. Yu, C. Kadlec, T. Sato, M. C. Hoffmann, M. Chollet, M. E. Kozina, S. Nelson, D. Zhu, D. A. Walko, A. M. Lindenberg, P. G. Evans, L.-Q. Chen, R. Ramesh, L. W. Martin, V. Gopalan, J. W. Freeland, J. Hlinka, and H. Wen (2021), "Subterahertz collective dynamics of polar vortices," Nature **592**, 376–380.

Li, Y L, S. Y. Hu, Z. K. Liu, and L. Q. Chen (2001), "Phase-field model of domain structures in ferroelectric thin films," Appl. Phys. Lett. **78**, 3878–3880.

Liao, Z, M. Huijben, Z. Zhong, N. Gauquelin, S. Macke, R. J. Green, S. Van Aert, J. Verbeeck, G. Van Tendeloo, K. Held, G. A. Sawatzky, G. Koster, and G. Rijnders (2016), "Controlled lateral anisotropy in correlated man-

ganite heterostructures by interface-engineered oxygen octahedral coupling," Nat. Mater. **15** (4), 425–431.

Linker, T, S. Fukushima, R. V. Kalia, A. Krishnamoorthy, A. Nakano, K. Nomura, K. Shimamura, F. Shimojo, and P. Vashishta (2022a), "Towards computational polar-topotronics: Multiscale neural-network quantum molecular dynamics simulations of polar vortex states in SrTiO$_3$/PbTiO$_3$ nanowires," Front. Nanotechnol. **4**, 884149.

Linker, T, K. Nomura, A. Aditya, S. Fukshima, R. K. Kalia, A. Krishnamoorthy, A. Nakano, P. Rajak, K. Shimmura, F. Shimojo, and P. Vashishta (2022b), "Exploring far-from-equilibrium ultrafast polarization control in ferroelectric oxides with excited-state neural network quantum molecular dynamics," Sci. Adv. **8**, eabk2625.

Liu, S, I. Grinberg, and A. M. Rappe (2016), "Intrinsic ferroelectric switching from first principles," Nature **534** (7607), 360–363.

Lovesey, S W, and G. van der Laan (2018), "Resonant x-ray diffraction from chiral electric-polarization structures," Phys. Rev. B **98**, 155410.

Lu, L, Y. Nahas, M. Liu, H. Du, Z. Jiang, S. Ren, D. Wang, L. Jin, S. Prokhorenko, C.-L. Jia, and L. Bellaiche (2018), "Topological defects with distinct dipole configurations in PbTiO$_3$/SrTiO$_3$ multilayer films," Phys. Rev. Lett. **120**, 177601.

Lubk, A, and J. Zweck (2015), "Differential phase contrast: An integral perspective," Phys. Rev. A **91**, 023805.

Machlin, ES, and P Chaudhari (1980), "Theory of pseudomorphic stabilization of metastable phases in thin film form," Synthesis and Properties of Metastable Phases , 11–29.

MacLaren, I, L. Q. Wang, D. McGrouther, A. J. Craven, S. McVitie, R. Schierholz, A. Kovács, J. Barthel, and R. E. Dunin-Borkowski (2015), "On the origin of differential phase contrast at a locally charged and globally charge-compensated domain boundary in a polar-ordered material," Ultramicroscopy **154**, 57–63.

MacManus-Driscoll, J L, M. P. Wells, C. Yun, J.-W. Lee, C.-B. Eom, and D. G. Schlom (2020), "New approaches for achieving more perfect transition metal oxide thin films," APL Mater. **8**, 040904.

MacManus-Driscoll, J L, P. Zerrer, H. Wang, H. Yang, J. Yoon, A. Fouchet, R. Yu, M. G. Blamire, and Q. Jia (2008), "Strain control and spontaneous phase ordering in vertical nanocomposite heteroepitaxial thin films," Nat. Mater. **7**, 314–320.

Mannhart, J, and D. G. Schlom (2010), "Oxide interfaces—an opportunity for electronics," Science **327**, 1607–1611.

Martin, L W, and A. M. Rappe (2016), "Thin-film ferroelectric materials and their applications," Nat. Rev. Mater. **2**, 16087.

McMullan, G, A.R. Faruqi, D. Clare, and R. Henderson (2014), "Comparison of optimal performance at 300 keV of three direct electron detectors for use in low dose electron microscopy," Ultramicroscopy **147**, 156–163.

Migoni, R, H. Bilz, and D. Bäuerle (1976), "Origin of Raman scattering and ferroelectricity in oxidic perovskites," Phys. Rev. Lett. **37**, 1155–1158.

Miyake, S, and R. Uyeda (1955), "Friedel's law in the dynamical theory of diffraction," Acta Crystallogr. **8**, 335–342.

Mohaddes-Ardabili, L, H. Zheng, S. B. Ogale, B. Hannoyer, W. Tian, J. Wang, S. E. Lofland, S. R. Shinde, T. Zhao, Y. Jia, L. Salamanca-Riba, D. G. Schlom, M. Wuttig, and R. Ramesh (2004), "Self-assembled single-crystal fer-

romagnetic iron nanowires formed by decomposition," Nat. Mater. **3**, 533–538.

Moon, E J, P. V. Balachandran, B. J. Kirby, D. J. Keavney, R. J. Sichel-Tissot, C. M. Schlepütz, E. Karapetrova, X. M. Cheng, J. M. Rondinelli, and S. J. May (2014), "Effect of interfacial octahedral behavior in ultrathin manganite films," Nano Lett. **14**, 2509–2514.

Morniroli, J P, and J. W. Steeds (1992), "Microdiffraction as a tool for crystal structure identification and determination," Ultramicroscopy **45**, 219–239.

Muller, D A (2009), "Structure and bonding at the atomic scale by scanning transmission electron microscopy," Nat. Mater. **8**, 263–270.

Muller, D A, L. Fitting Kourkoutis, M. Murfitt, J. H. Song, H. Y. Hwang, J. Silcox, N. Dellby, and O. L. Krivanek (2008), "Atomic-scale chemical imaging of composition and bonding by aberration-corrected microscopy," Science **319**, 1073–1076.

Müller-Caspary, K, T. Grieb, J. Müßener, N. Gauquelin, P. Hille, J. Schörmann, J. Verbeeck, S. Van Aert, M. Eickhoff, and A. Rosenauer (2019), "Electrical polarization in AlN/GaN nanodisks measured by momentum-resolved 4D scanning transmission electron microscopy," Phys. Rev. Lett. **122**, 106102.

Mundy, J A, Ch. M. Brooks, M. E. Holtz, J. A. Moyer, H. Das, A. F. Rébola, J. T. Heron, J. D. Clarkson, S. M. Disseler, Z. Liu, A. Farhan, R. Held, R. Hovden, E. Padgett, Q. Mao, H. Paik, R. Misra, L. F. Kourkoutis, E. Arenholz, A. Scholl, J. A. Borchers, W. D. Ratcliff, R. Ramesh, C. J. Fennie, P. Schiffer, D. A. Muller, and D. G. Schlom (2016), "Atomically engineered ferroic layers yield a room-temperature magnetoelectric multiferroic," Nature **537**, 523–527.

Mundy, J A, Q. Y. Mao, C. M. Brooks, D. G. Schlom, and D. A. Muller (2012), "Atomic-resolution chemical imaging of oxygen local bonding environments by electron energy loss spectroscopy," Appl. Phys. Lett. **101**, 042907.

Müller, K, A. Rosenauer, M. Schowalter, J. Zweck, R. Fritz, and K. Volz (2012), "Strain measurement in semiconductor heterostructures by scanning transmission electron microscopy," Microsc. Microanal. **18**, 995–1009.

Nahas, Y, S. Prokhorenko, L. Louis, Z. Gui, I. Kornev, and L. Bellaiche (2015), "Discovery of stable skyrmionic state in ferroelectric nanocomposites," Nat. Commun. **6**, 8542.

Nakagawa, N, H. Y. Hwang, and D. A. Muller (2006), "Why some interfaces cannot be sharp," Nat. Mater. **5**, 204–209.

Nakashima, PhN H, A. E. Smith, J. Etheridge, and B. C. Muddle (2011), "The bonding electron density in aluminum," Science **331**, 1583–1586.

Naumov, I I, L. Bellaiche, and H. Fu (2004), "Unusual phase transitions in ferroelectric nanodisks and nanorods," Nature **432**, 737–740.

Nelson, C T, B. Winchester, Y. Zhang, S.-J. Kim, A. Melville, C. Adamo, C. M. Folkman, S.-H. Baek, C.-B. Eom, D. G. Schlom, L.-Q. Chen, and X. Pan (2011), "Spontaneous vortex nanodomain arrays at ferroelectric heterointerfaces," Nano Lett. **11**, 828–834.

Newnham, RE, D.P. Skinner, and L.E. Cross (1978), "Connectivity and piezoelectric-pyroelectric composites," Mater. Res. Bull. **13**, 525–536.

Nguyen, K X, Y. Jiang, M. C. Cao, P. Purohit, A. K. Yadav, P. García-Fernández, M. W. Tate, C. S. Chang, P. Aguado-Puente, J. Íñiguez, F. Gómez-Ortiz, S. M. Gruner, J. Junquera, L. W. Martin, R. Ramesh, and D. A. Muller (2020a), "Transferring orbital angular momentum to an electron

beam reveals toroidal and chiral order," arXiv:2012.04134 [cond-mat.mtrl-sci].

Nguyen, K X, E. Turgut, M. C. Cao, J. Glaser, Z. Chen, M. J. Stolt, S. Jin, G. D. Fuchs, and D. A. Muller (2020b), "Disentangling magnetic and grain contrast in polycrystalline fege thin films using $4 - D$ Lorentz scanning transmission electron microscopy," arXiv:2001.06900 [cond-mat.mtrl-sci].

Nguyen, LD, A.S. Brown, M.A. Thompson, and L.M. Jelloian (1992), "50-nm self-aligned-gate pseudomorphic AlInAs/GaInAs high electron mobility transistors," IEEE Trans. Electron Devices **39**, 2007–2014.

Nie, Y F, Y. Zhu, C.-H. Lee, L. F. Kourkoutis, J. A. Mundy, J. Junquera, Ph. Ghosez, D. J. Baek, S. Sung, X. X. Xi, K. M. Shen, D. A. Muller, and D. G. Schlom (2014), "Atomically precise interfaces from non-stoichiometric deposition," Nat. Commun. **5**, 4530.

Nunn, W, J. Yue, A. K. Manjeshwar, and B. Jalan (2021), "Novel mbe approach for highly conducting epitaxial ruo$_2$ films," Bull. Am. Phys. Soc. **A55**, 00005.

Oh, D-W, J. Ravichandran, C.-W. Liang, W. Siemons, B. Jalan, Ch. M. Brooks, M. Huijben, D. G. Schlom, S. Stemmer, L. W. Martin, A. Majumdar, R. Ramesh, and D. G. Cahill (2011), "Thermal conductivity as a metric for the crystalline quality of SrTiO$_3$ epitaxial layers," Appl. Phys. Lett. **98**, 221904.

Ohtomo, A, and H. Y. Hwang (2004), "A high-mobility electron gas at the LaAlO$_3$/SrTiO$_3$ heterointerface," Nature **427**, 423–426.

Ohtomo, A, D. A. Muller, J. L. Grazul, and H. Y. Hwang (2002), "Artificial charge-modulation in atomic-scale perovskite titanate superlattices," Nature **419**, 378–380.

Ophus, C (2019), "Four-dimensional scanning transmission electron microscopy $(4D - STEM)$: From scanning nanodiffraction to ptychography and beyond," Microsc. Microanal. **25**, 563–582.

Ozdol, V B, C. Gammer, X. G. Jin, P. Ercius, C. Ophus, J. Ciston, and A. M. Minor (2015), "Strain mapping at nanometer resolution using advanced nano-beam electron diffraction," Appl. Phys. Lett. **106** (25), 253107.

Padgett, E, M. E. Holtz, P. Cueva, Y.-T. Shao, E. Langenberg, D. G. Schlom, and D. A. Muller (2020), "The exit-wave power-cepstrum transform for scanning nanobeam electron diffraction: robust strain mapping at subnanometer resolution and subpicometer precision," Ultramicroscopy **214**, 112994.

Pereira Gonçalves, M A, C. Escorihuela-Sayalero, P. Garca-Fernández, J. Junquera, and J. Íñiguez (2019), "Theoretical guidelines to create and tune electric skyrmion bubbles," Sci. Adv. **5**, eaau7023.

Podkaminer, J P, J. J. Patzner, B. A. Davidson, and C. B. Eom (2016), "Real-time and in situ monitoring of sputter deposition with rheed for atomic layer controlled growth," APL Mater. **4**, 086111.

Ponomareva, I, I. I. Naumov, and L. Bellaiche (2005a), "Low-dimensional ferroelectrics under different electrical and mechanical boundary conditions: Atomistic simulations," Phys. Rev. B **72**, 214118.

Ponomareva, I, I. I. Naumov, I. Kornev, H. Fu, and L. Bellaiche (2005b), "Atomistic treatment of depolarizing energy and field in ferroelectric nanostructures," Phys. Rev. B **72**, 140102.

Prakash, A, and B. Jalan (2019), "Molecular beam epitaxy for oxide electronics," in *Molecular Beam Epitaxy*, Chap. 26

(John Wiley & Sons, Ltd) pp. 423–452.

Prokhorenko, S, K. Kalke, Y. Nahas, and L. Bellaiche (2018), "Large scale hybrid Monte Carlo simulations for structure and property prediction," npj Comput. Mater. **4**, 80.

Rabe, K M (2005), "Theoretical investigations of epitaxial strain effects in ferroelectric oxide thin films and superlattices," Curr. Opin. Solid State Mat. Sci. **9** (3), 122–127.

Radescu, S, I Etxebarria, and J M Perez-Mato (1995), "The landau free energy of the three-dimensional ϕ^4 in wide temperature intervals," J. Phys.: Condens. Matter **7**, 585–595.

Ramesh, R, and D. G. Schlom (2019), "Creating emergent phenomena in oxide superlattices," Nat. Rev. Mater. **4**, 257–268.

Reyren, N, S. Thiel, A. D. Caviglia, L. Fitting Kourkoutis, G. Hammerl, C. Richter, C. W. Schneider, T. Kopp, A.-S. Rüetschi, D. Jaccard, M. Gabay, D. A. Muller, J.-M. Triscone, and J. Mannhart (2007), "Superconducting interfaces between insulating oxides," Science **317**, 1196–1199.

Rez, P, and D. A. Muller (2008), "The theory and interpretation of electron energy loss near-edge fine structure," Annu. Rev. Mater. Res. **38**, 535–558.

Rijnders, G J H M, G. Koster, D. H. A. Blank, and H. Rogalla (1997), "In situ monitoring during pulsed laser deposition of complex oxides using reflection high energy electron diffraction under high oxygen pressure," Appl. Phys. Lett. **70**, 1888–1890.

Rondinelli, J M, S. J. May, and J. W. Freeland (2012), "Control of octahedral connectivity in perovskite oxide heterostructures: An emerging route to multifunctional materials discovery," MRS Bull. **37**, 261–270.

Rondinelli, J M, and N. A. Spaldin (2011), "Structure and properties of functional oxide thin films: Insights from electronic-structure calculations," Adv. Mater. **23**, 3363–3381.

Ruf, J P, H. Paik, N. J. Schreiber, H. P. Nair, L. Miao, J. K. Kawasaki, J. N. Nelson, B. D. Faeth, Y. Lee, B. H. Goodge, B. Pamuk, C. J. Fennie, L. F. Kourkoutis, D. G. Schlom, and K. M. Shen (2021), "Strain-stabilized superconductivity," Nat. Commun. **12**, 59.

Sai, N, B. Meyer, and D. Vanderbilt (2000), "Compositional inversion symmetry breaking in ferroelectric perovskites," Phys. Rev. Lett. **84**, 5636–5639.

Saremi, S, A. Dasgupta, R. Gao, and L. W. Martin (2018), "New facets for the role of defects in ceramics," Am. Ceram. Soc. Bull. **97**, 16–23.

Saremi, S, R. Xu, L. R. Dedon, J. A. Mundy, S.-L. Hsu, Z. Chen, A. R. Damodaran, S. P. Chapman, J. T. Evans, and L. W. Martin (2016), "Enhanced electrical resistivity and properties via ion bombardment of ferroelectric thin films," Adv. Mater. **28**, 10750–10756.

Schlom, D G (2015), "Perspective: Oxide molecular-beam epitaxy rocks!" APL Mater. **3**, 062403.

Schlom, D G, L.-Q. Chen, C.-B. Eom, K. M. Rabe, S. K. Streiffer, and J.-M. Triscone (2007), "Strain tuning of ferroelectric thin films," Annu. Rev. Mater. Res. **37**, 589–626.

Schlom, D G, L.-Q. Chen, C. J. Fennie, V. Gopalan, D. A. Muller, X. Pan, R. Ramesh, and R. Uecker (2014), "Elastic strain engineering of ferroic oxides," MRS Bull. **39**, 118–130.

Schlom, D G, and J. S. Harris (1995), "6 - MBE growth of high tc superconductors," in *Molecular Beam Epitaxy*, edited by Robin F.C. Farrow (William Andrew Publishing, Park Ridge, NJ) pp. 505–622.

Schrade, D, R. Mueller, B.X. Xu, and D. Gross (2007),

"Domain evolution in ferroelectric materials: A continuum phase field model and finite element implementation," Comput. Meth. Appl. Mech. Eng. **196**, 4365–4374.

Seidel, J, R. K. Vasudevan, and N. Valanoor (2016), "Topological structures in multiferroics – domain walls, skyrmions and vortices," Adv. Electron. Mater. **2**, 1500292.

Sepliarsky, M, Z. Wu, A. Asthagiri, and R. E. Cohen (2004), "Atomistic model potential for $PbTiO_3$ and PMN by fitting first principles results," Ferroelectrics **301**, 55–59.

Shafer, P, P. García-Fernández, P. Aguado-Puente, A. R. Damodaran, A. K. Yadav, C. T. Nelson, S.-L. Hsu, J. C. Wojdeł, J. Íñiguez, L. W. Martin, E. Arenholz, J. Junquera, and R. Ramesh (2018), "Emergent chirality in the electric polarization texture of titanate superlattices," Proc. Natl. Acad. Sci. U.S.A. **115**, 915–920.

Shao, Y-T, S. Das, Z. Hong, R. Xu, S. Chandrika, F. Gómez-Ortiz, P. García-Fernández, L.-Q. Chen, H. Y. Hwang, J. Junquera, L. W. Martin, R. Ramesh, and D. A. Muller (2021), "Emergent chirality in a polar meron to skyrmion phase transition," arXiv:2101.04545 [cond-mat.mes-hall].

Shao, Y-T, and J.-M. Zuo (2017a), "Lattice-rotation vortex at the charged monoclinic domain boundary in a relaxor ferroelectric crystal," Phys. Rev. Lett. **118**, 157601.

Shao, Y-T, and J.-M. Zuo (2017b), "Nanoscale symmetry fluctuations in ferroelectric barium titanate, $BaTiO_3$," Acta Crystallogr. Sec. B **73**, 708–714.

Shi, Y, and L.-Q. Chen (2020), "Spinodal electronic phase separation during insulator-metal transitions," Phys. Rev. B **102**, 195101.

Shin, Y-H, V. R. Cooper, I. Grinberg, and A. M. Rappe (2005), "Development of a bond-valence molecular-dynamics model for complex oxides," Phys. Rev. B **71**, 054104.

Shin, Y-H, I. Grinberg, I.-W. Chen, and A. M. Rappe (2007), "Nucleation and growth mechanism of ferroelectric domain-wall motion," Nature **449**, 881–884.

Sichuga, D, and L. Bellaiche (2011), "Epitaxial Pb(Zr, Ti)O$_3$ ultrathin films under open-circuit electrical boundary conditions," Phys. Rev. Lett. **106**, 196102.

Soergel, E (2011), "Piezoresponse force microscopy (PFM)," J. Phys. D: Appl. Phys. **44**, 464003.

Specht, E D, H.-M. Christen, D. P. Norton, and L. A. Boatner (1998), "X-ray diffraction measurement of the effect of layer thickness on the ferroelectric transition in epitaxial $KTaO_3$/$KNbO_3$ multilayers," Phys. Rev. Lett. **80**, 4317–4320.

Stachiotti, M G, and M. Sepliarsky (2011), "Toroidal ferroelectricity in $PbTiO_3$ nanoparticles," Phys. Rev. Lett. **106**, 137601.

Streiffer, S K, J. A. Eastman, D. D. Fong, C. Thompson, A. Munkholm, M. V. Ramana Murty, O. Auciello, G. R. Bai, and G. B. Stephenson (2002), "Observation of nanoscale 180° stripe domains in ferroelectric $PbTiO_3$ thin films," Phys. Rev. Lett. **89**, 067601.

Su, Y, and C. M. Landis (2007), "Continuum thermodynamics of ferroelectric domain evolution: Theory, finite element implementation, and application to domain wall pinning," J. Mech. Phys. Solids **55**, 280–305.

Sun, H Y, Z. W. Mao, T. W. Zhang, L. Han, T. T. Zhang, X. B. Cai, X. Guo, Y. F. Li, Y. P. Zang, W. Guo, J. H. Song, D. X. Ji, C. Y. Gu, C. Tang, Z. B. Gu, N. Wang, Y. Zhu, D. G. Schlom, Y. F. Nie, and X. Q. Pan (2018), "Chemically specific termination control of oxide interfaces via layer-by-layer mean inner potential engineering," Nat. Commun. **9**, 2965.

Sun, Y, A. Y. Abid, C. Tan, C. Ren, M. Li, N. Li, P. Chen, Y. Li, J. Zhang, X. Zhong, J. Wang, M. Liao, K. Liu, X. Bai, Y. Zhou, D. Yu, and P. Gao (2019), "Subunit cell–level measurement of polarization in an individual polar vortex," Sci. Adv. **5**, eaav4355.

Tanaka, M, and G. Honjo (1964), "Electron optical studies of barium titanate single crystal films," J. Phys. Soc. Jpn. **19**, 954–970.

Tanaka, M, and K. Tsuda (2011), "Convergent-beam electron diffraction," J. Electron Microsc. **60**, S245–S267.

Tasker, P W (1979), "The stability of ionic crystal surfaces," J. Phys. C **12**, 4977–4984.

Tate, M W, P. Purohit, D. Chamberlain, K. X. Nguyen, R. Hovden, C. S. Chang, P. Deb, E. Turgut, J. T. Heron, D. G. Schlom, D. C. Ralph, G. D. Fuchs, K. S. Shanks, H. T. Philipp, D. A. Muller, and S. M. Gruner (2016), "High dynamic range pixel array detector for scanning transmission electron microscopy," Microsc. Microanal. **22**, 237–249.

Tenne, D A, A. Bruchhausen, N. D. Lanzillotti-Kimura, A. Fainstein, R. S. Katiyar, A. Cantarero, A. Soukiassian, V. Vaithyanathan, J. H. Haeni, W. Tian, D. G. Schlom, K. J. Choi, D. M. Kim, C. B. Eom, H. P. Sun, X. Q. Pan, Y. L. Li, L. Q. Chen, Q. X. Jia, S. M. Nakhmanson, K. M. Rabe, and X. X. Xi (2006), "Probing nanoscale ferroelectricity by ultraviolet Raman spectroscopy," Science **313**, 1614–1616.

Terashima, T, Y. Bando, K. Iijima, K. Yamamoto, K. Hirata, K. Hayashi, K. Kamigaki, and H. Terauchi (1990), "Reflection high-energy electron diffraction oscillations during epitaxial growth of high-temperature superconducting oxides," Phys. Rev. Lett. **65**, 2684–2687.

Tinte, S, M. G. Stachiotti, M. Sepliarsky, R. L. Migoni, and C. O. Rodriguez (1999), "Atomistic modelling of $BaTiO_3$ based on first-principles calculations," J. Phys.: Condens. Matter **11**, 9679–9690.

Torres-Pardo, A, A. Gloter, P. Zubko, N. Jecklin, C. Lichtensteiger, C. Colliex, J.-M. Triscone, and O. Stéphan (2011), "Spectroscopic mapping of local structural distortions in ferroelectric $PbTiO_3$/$SrTiO_3$ superlattices at the unit-cell scale," Phys. Rev. B **84**, 220102.

Tsuda, K, Y. Ogata, K. Takagi, T. Hashimoto, and M. Tanaka (2002), "Refinement of crystal structural parameters and charge density using convergent-beam electron diffraction – the rhombohedral phase of $LaCrO_3$," Acta Crystallogr. Sec. A **58**, 514–525.

Tsuda, K, and M. Tanaka (2013), "Convergent-beam electron diffraction study of the local structure of the tetragonal phase of $PbTiO_3$," Appl. Phys. Express **6**, 101501.

Tsuda, K, and M. Tanaka (2017), "Nanometer-scale local structural study of the paraelectric cubic phase of $KNbO_3$ by convergent-beam electron diffraction," Jpn. J. Appl. Phys. **56**, 10PB09.

Tsuda, K, A. Yasuhara, and M. Tanaka (2013), "Two-dimensional mapping of polarizations of rhombohedral nanostructures in the tetragonal phase of $BaTiO_3$ by the combined use of the scanning transmission electron microscopy and convergent-beam electron diffraction methods," Appl. Phys. Lett. **103**, 082908.

Tsukazaki, A, S. Akasaka, K. Nakahara, Y. Ohno, H. Ohno, D. Maryenko, A. Ohtomo, and M. Kawasaki (2010), "Observation of the fractional quantum Hall effect in an oxide," Nat. Mater. **9**, 889–893.

Tsukazaki, A, A. Ohtomo, T. Kita, Y. Ohno, H. Ohno, and M. Kawasaki (2007), "Quantum Hall effect in polar oxide heterostructures," Science **315**, 1388–1391.

Valasek, J (1921), "Piezo-electric and allied phenomena in rochelle salt," Phys. Rev. **17**, 475–481.

Vogt, P, F. V. E. Hensling, K. Azizie, C. S. Chang, D. Turner, J. Park, J. P. McCandless, H. Paik, B. J. Bocklund, G. Hoffman, O. Bierwagen, D. Jena, H. G. Xing, S. Mou, D. A. Muller, S.-L. Shang, Z.-K. Liu, and D. G. Schlom (2021), "Adsorption-controlled growth of Ga_2O_3 by suboxide molecular-beam epitaxy," APL Mater. **9**, 031101.

Waghmare, U V, and K. M. Rabe (1997), "Ab initio statistical mechanics of the ferroelectric phase transition in $PbTiO_3$," Phys. Rev. B **55**, 6161–6173.

Wang, J, S.-Q. Shi, L.-Q. Chen, Y. Li, and T.-Y. Zhang (2004), "Phase-field simulations of ferroelectric/ferroelastic polarization switching," Acta Mater. **52**, 749–764.

Wang, J-J, B. Wang, and L.-Q. Chen (2019a), "Understanding, predicting, and designing ferroelectric domain structures and switching guided by the phase-field method," Annu. Rev. Mater. Res. **49**, 127–152.

Wang, J-J, T.-N. Yang, J. A. Zorn, E. Wang, J. Irwin, S. Lindemann, M. S. Rzchowski, J.-M. Hu, C.-B. Eom, and L.-Q. Chen (2019b), "Strain anisotropy and magnetic domain structures in multiferroic heterostructures: High-throughput finite-element and phase-field studies," Acta Mater. **176**, 73–83.

Warusawithana, M P, Ch. Cen, Cha. R. Sleasman, J. C. Woicik, Y. Li, L. F. Kourkoutis, J. A. Klug, H. Li, Ph. Ryan, L.-P. Wang, M. Bedzyk, D. A. Muller, L.-Q. Chen, J. Levy, and D. G. Schlom (2009), "A ferroelectric oxide made directly on silicon," Science **324**, 367–370.

Warusawithana, M P, E. V. Colla, J. N. Eckstein, and M. B. Weissman (2003), "Artificial dielectric superlattices with broken inversion symmetry," Phys. Rev. Lett. **90**, 036802.

Warusawithana, M P, C. Richter, J. A. Mundy, P. Roy, J. Ludwig, S. Paetel, T. Heeg, A. A. Pawlicki, L. F. Kourkoutis, M. Zheng, M. Lee, B. Mulcahy, W. Zander, Y. Zhu, J. Schubert, J. N. Eckstein, D. A. Muller, C. Stephen Hellberg, J. Mannhart, and D. G. Schlom (2013), "$LaAlO_3$ stoichiometry is key to electron liquid formation at $LaAlO_3$/$SrTiO_3$ interfaces," Nat. Commun. **4**, 2351.

Welser, J, J. L. Hoyt, and J. F. Gibbons (1994), "Electron mobility enhancement in strained-si n-type metal-oxide-semiconductor field-effect transistors," IEEE Electron Device Lett. **15** (3), 100–102.

Wen, H, P. Chen, M. P. Cosgriff, D. A. Walko, J. H. Lee, C. Adamo, R. D. Schaller, J. F. Ihlefeld, E. M. Dufresne, D. G. Schlom, P. G. Evans, J. W. Freeland, and Y. Li (2013), "Electronic origin of ultrafast photoinduced strain in $BiFeO_3$," Phys. Rev. Lett. **110**, 037601.

Wilkins, S B, P. D. Hatton, M. D. Roper, D. Prabhakaran, and A. T. Boothroyd (2003), "Soft x-ray resonant magnetic diffraction," Phys. Rev. Lett. **90**, 187201.

Winchester, B, N. Balke, X. X. Cheng, A. N. Morozovska, S. Kalinin, and L. Q. Chen (2015), "Electroelastic fields in artificially created vortex cores in epitaxial $BiFeO_3$ thin films," Appl. Phys. Lett. **107**, 052903.

Wojdeł, J C, P. Hermet, M. P. Ljungberg, Ph. Ghosez, and J. Íñiguez (2013), "First-principles model potentials for lattice-dynamical studies: general methodology and example of application to ferroic perovskite oxides," J. Phys.: Condens. Matter **25** (30), 305401.

Wojdeł, J C, and J. Íñiguez (2014), "Ferroelectric transitions at ferroelectric domain walls found from first principles," Phys. Rev. Lett. **112**, 247603.

Wood, C E C (1981), "RED intensity oscillations during MBE of GaAs," Surf. Sci. **108** (2), L441–L443.

Xue, F, N. Wang, X. Wang, Y. Ji, S.-W. Cheong, and L.-Q. Chen (2018), "Topological dynamics of vortex-line networks in hexagonal manganites," Phys. Rev. B **97**, 020101.

Yadav, A K, C. T. Nelson, S. L. Hsu, Z. Hong, J. D. Clarkson, C. M. Schlepütz, A. R. Damodaran, P. Shafer, E. Arenholz, L. R. Dedon, D. Chen, A. Vishwanath, A. M. Minor, L. Q. Chen, J. F. Scott, L. W. Martin, and R. Ramesh (2016), "Observation of polar vortices in oxide superlattices," Nature **530**, 198–201.

Yadav, A K, K. X. Nguyen, Z. Hong, P. García-Fernández, P. Aguado-Puente, C. T. Nelson, S. Das, B. Prasad, D. Kwon, S. Cheema, A. I. Khan, C. Hu, J. Íñiguez, J. Junquera, L.-Q. Chen, D. A. Muller, R. Ramesh, and S. Salahuddin (2019), "Spatially resolved steady-state negative capacitance," Nature **565**, 468–471.

Yakel Jnr, H L, W. C. Koehler, E. F. Bertaut, and E. F. Forrat (1963), "On the crystal structure of the manganese(iii) trioxides of the heavy lanthanides and yttrium," Acta Crystallogr. **16**, 957–962.

Yang, T N, and L. Q. Chen (2021), "Dynamical phase-field model of coupled electronic and structural processes," To be published.

Yuan, R, J. Zhang, and J.-M. Zuo (2019), "Lattice strain mapping using circular hough transform for electron diffraction disk detection," Ultramicroscopy **207**, 112837.

Zeches, R J, M. D. Rossell, J. X. Zhang, A. J. Hatt, Q. He, C.-H. Yang, A. Kumar, C. H. Wang, A. Melville, C. Adamo, G. Sheng, Y.-H. Chu, J. F. Ihlefeld, R. Erni, C. Ederer, V. Gopalan, L. Q. Chen, D. G. Schlom, N. A. Spaldin, L. W. Martin, and R. Ramesh (2009), "A strain-driven morphotropic phase boundary in $BiFeO_3$," Science **326**, 977–980.

Zhang, H, Y.-T. Shao, R. Chen, X. Chen, S. Susarla, J. T. Reichanadter, L. Caretta, X. Huang, N. S. Settineri, Z. Chen, J. Zhou, E. Bourret-Courchesne, P. Ercius, J. Yao, J. B. Neaton, D. A. Muller, R. J. Birgeneau, and R. Ramesh (2021), "A room temperature polar ferromagnetic metal," arXiv:2106.00833 [cond-mat.mtrl-sci].

Zhang, Q, L. Xie, G. Liu, S. Prokhorenko, Y. Nahas, X. Pan, L. Bellaiche, A. Gruverman, and N. Valanoor (2017), "Nanoscale bubble domains and topological transitions in ultrathin ferroelectric films," Adv. Mater. **29**, 1702375.

Zheng, H, J. Wang, S. E. Lofland, Z. Ma, L. Mohaddes-Ardabili, T. Zhao, L. Salamanca-Riba, S. R. Shinde, S. B. Ogale, F. Bai, D. Viehland, Y. Jia, D. G. Schlom, M. Wuttig, A. Roytburd, and R. Ramesh (2004a), "Multiferroic $BaTiO_3$/$CoFe_2O_4$ nanostructures," Science **303**, 661–663.

Zheng, H, J. Wang, L. Mohaddes-Ardabili, M. Wuttig, L. Salamanca-Riba, D. G. Schlom, and R. Ramesh (2004b), "Three-dimensional heteroepitaxy in self-assembled $BaTiO_3$/$CoFe_2O_4$ nanostructures," Appl. Phys. Lett. **85**, 2035–2037.

Zheng, Y, B. Wang, and C. H. Woo (2006), "Simulation of interface dislocations effect on polarization distribution of ferroelectric thin films," Appl. Phys. Lett. **88**, 092903.

Zhong, W, D. Vanderbilt, and K. M. Rabe (1994), "Phase transitions in $BaTiO_3$ from first principles," Phys. Rev. Lett. **73**, 1861–1864.

Zhong, W, D. Vanderbilt, and K. M. Rabe (1995), "First-

principles theory of ferroelectric phase transitions for perovskites: The case of BaTiO$_3$," Phys. Rev. B **52**, 6301–6312.

Zubko, P, J. C. Wojdeł, M. Hadjimichael, S. Fernandez-Pena, A. Sené, I. Luk'yanchuk, J.-M. Triscone, and J. Íñiguez (2016), "Negative capacitance in multidomain ferroelectric superlattices," Nature **534**, 524–528.

Zunger, A, and D.M. Wood (1989), "Structural phenomena in coherent epitaxial solids," J. Cryst. Growth **98**, 1–17.

Zuo, J M, R. Høier, and J. C. H. Spence (1989), "Three-beam and many-beam theory in electron diffraction and its use for structure-factor phase determination in non-centrosymmetric crystal structures," Acta Crystallogr. Sec. A **45**, 839–851.

Zuo, J M, M. Kim, M. O'Keeffe, and J. C. H. Spence (1999), "Direct observation of d-orbital holes and $Cu-Cu$ bonding in Cu_2O," Nature **401**, 49–52.

Zuo, J M, and J. C. H. Spence (2016), *Advanced Transmission Electron Microscopy: Imaging and Diffraction in Nanoscience* (Springer, New York).